TECHNISCHE UNIVERSITÄT DRESDEN

Fakultät Umweltwissenschaften

Thema der Dissertation

Genesis, conservation and deformation of ice-rich mountain permafrost:
Driving factors, mapping and geodetic monitoring

Dissertation zur Erlangung des akademischen Grades
Doktoringenieur (Dr.-Ing)

vorgelegt von

Dipl. Ing. Kenner, Robert

geboren am 11.03.1986 in Dresden

Gutachter:

Herr Prof. Dr. Manfred Buchroithner
Technische Universität Dresden

Herr Prof. Dr. Wilfried Haeberli
Universität Zürich (Emeritus)

Herr Prof. Dr. Martin Hoelzle
Universität Fribourg

Dresden, 29.01.2018

Table of Contents

Abstract:

This thesis analyses ice-rich mountain permafrost with regard to its genesis, distribution, deformation and interaction with other environmental factors. The processes influencing ground ice formation in ice-rich and ice-poor mountain permafrost are highlighted. Factors influencing the presence of ice-rich permafrost are identified and their individual or combined effect on frozen ground is determined. Based on these findings, a new permafrost distribution map of Switzerland was created, which specifies permafrost temperature and ice contents and considers rock glacier creep paths. The deformation of rock glaciers is investigated with newly developed monitoring systems and concepts. This enables a better understanding of the processes leading to rock glacier acceleration at different time scales.

Keywords: Ice-rich permafrost, Mountain permafrost mapping, Ground ice genesis, Rock glacier acceleration, Glacier, Mass movements, Geodetic monitoring, Time-lapse photography, Terrestrial laser scanning

1. **Introduction**

Mountain permafrost refers to ground in alpine terrain with temperatures permanently below 0°C . As mountain permafrost is sensitive to climate changes and influences slope stability (Davies *et al.*, 2001; Gruber and Haeberli, 2007), it affects the safety of inhabitants and infrastructure in alpine regions and is thus the object of scientific investigations. Mountain permafrost commonly occurs worldwide in mountain regions which show mean annual air temperatures of close to 0° or below (Haeberli *et al.*, 1993). The exact distribution, the controlling factors and the thermal and geomorphologic characteristics of mountain permafrost are however complex. The three dimensionality and the topographical diversity can lead to variations of permafrost occurrence on an extremely small scale (Staub, 2015). Mountain permafrost ground can differ largely in landform type, underground characteristics and temperatures (PERMOS, 2016). Ground ice content is another variable property of mountain permafrost. Ice-rich mountain permafrost is characterized by pores spaces in soil that are completely filled or even oversaturated with ice, the latter is specified as excess ice (Ferrians Jr, 1989). Ice-rich permafrost shows differences to ice-poor permafrost regarding its thermal conductivity and heat capacity (Schneider *et al.*, 2012) and often exists at lower elevations and in different landforms than ice-poor permafrost. The capability of excess ground ice to induce creep allows the formation of rock glaciers, permafrost specific landforms which can initiate potentially hazardous mass wasting processes like rock fall or debris flows (Stoffel *et al.*, 2005; Delaloye *et al.*, 2010b).

The studies summarized in this dissertation focus on ice-rich permafrost, investigate its genesis and identify the factors controlling its conservation and creep velocity. The results will accentuate the considerable differences to ice-poor permafrost. Although these differences were already considered by some authors, a broad spectrum of permafrost literature does not distinguish between ice-rich and ice-poor permafrost or underestimates the relevance of these differences, as is discussed in the following literature review.

Permafrost is defined exclusively as a thermal state (ground having a temperature of 0°C or below for at least 2 consecutive years (Ferrians Jr, 1989). Consequently, descriptions and explanations of (ice-rich) permafrost have mainly focused on thermal processes, such as conductive, convective or radiation heat transfer between atmosphere, ground surface and the ground as well as latent heat effects (Frauenfelder and Kääb, 2000; Hoelzle *et al.*, 2001; Etzelmüller and Frauenfelder, 2009). These thermal processes are strongly influenced by the soil properties and especially by the ground ice content (Schneider *et al.*, 2012). Numerical

models used for the calculation of ground temperatures, such as the coupled heat and mass transfer model (CoupModel) (Jansson and Karlberg, 2004; Jansson, 2012) or the Snowpack model (Haberkorn *et al.*, 2015; Luethi *et al.*, 2017) simulate these processes in a detailed soil stratigraphy, and take into account the ground ice content. This is crucial to successfully reproduce the thermal ground conditions at a specific terrain point (Scherler *et al.*, 2013). If the ground-ice content is known, the largest challenges arise from realistically modelling advective air or water flow within blocky active layers (Scherler *et al.*, 2013). Whereas 1D modelling produces relatively good results, larger uncertainties occur when including the spatial distribution or long term temporal evolution of permafrost. In the case of 1D permafrost models, the ground-ice content is an input variable and can influence whether the model output yields long term stable permafrost conditions or not. This implies that the model itself is not able to specify the locations at which ice-rich permafrost is present. The genesis of ice-rich permafrost can thus not be explained by the thermal processes considered in the model. This problem is reflected by large uncertainties in permafrost maps and by discrepancies between them and ground truths (Figure 1). Permafrost maps (Keller *et al.*, 1998; Gruber and Hoelzle, 2001; Boeckli *et al.*, 2012) are mainly empirically based expressions of permafrost likelihood. The areas of uncertainty within the maps (zones indicated with "Permafrost possible/likely" or permafrost probability between 0 and 1) cover not only the majority of the permafrost area in Switzerland but also large parts of non-permafrost ground (Chapter 3.5). However, there are still permafrost sites which are not captured by these maps (Chapter 3.5). Furthermore, individual approaches of permafrost distribution modelling reveal quite large differences (Hoelzle *et al.*, 2001). The problem of lacking accuracy in permafrost distribution mapping is commonly explained by local effects such as intra talus ventilation (Delaloye and Lambiel, 2005; Wicky and Hauck, 2016), the creep of rock glaciers (Boeckli *et al.*, 2012) or insulating effects of snow (Haeberli, 1975; Keller, 1992). The considerable and widespread vagueness of permafrost maps raises the question, whether these explanations are sufficient. **Why is mainly low-elevation, ice-rich mountain permafrost neglected by 3D permafrost modelling? How does the massive ground ice develop?**

As long as these questions remain unclear, modelling or reconstruction of the temporal evolution of permafrost is affected by uncertainties. If a model is not able to predict the genesis of ice-rich permafrost, how can it forecast its future development? A popular method of climate reconstruction is to compare the frontal elevations of active and relict rock glaciers (Kerschner, 1978; Haeberli, 1983; Chueca, 1992; Payne, 1998; Frauenfelder and Kääb, 2000; Marchenko, 2001; Putnam and Putnam, 2009; Scotti *et al.*, 2013).
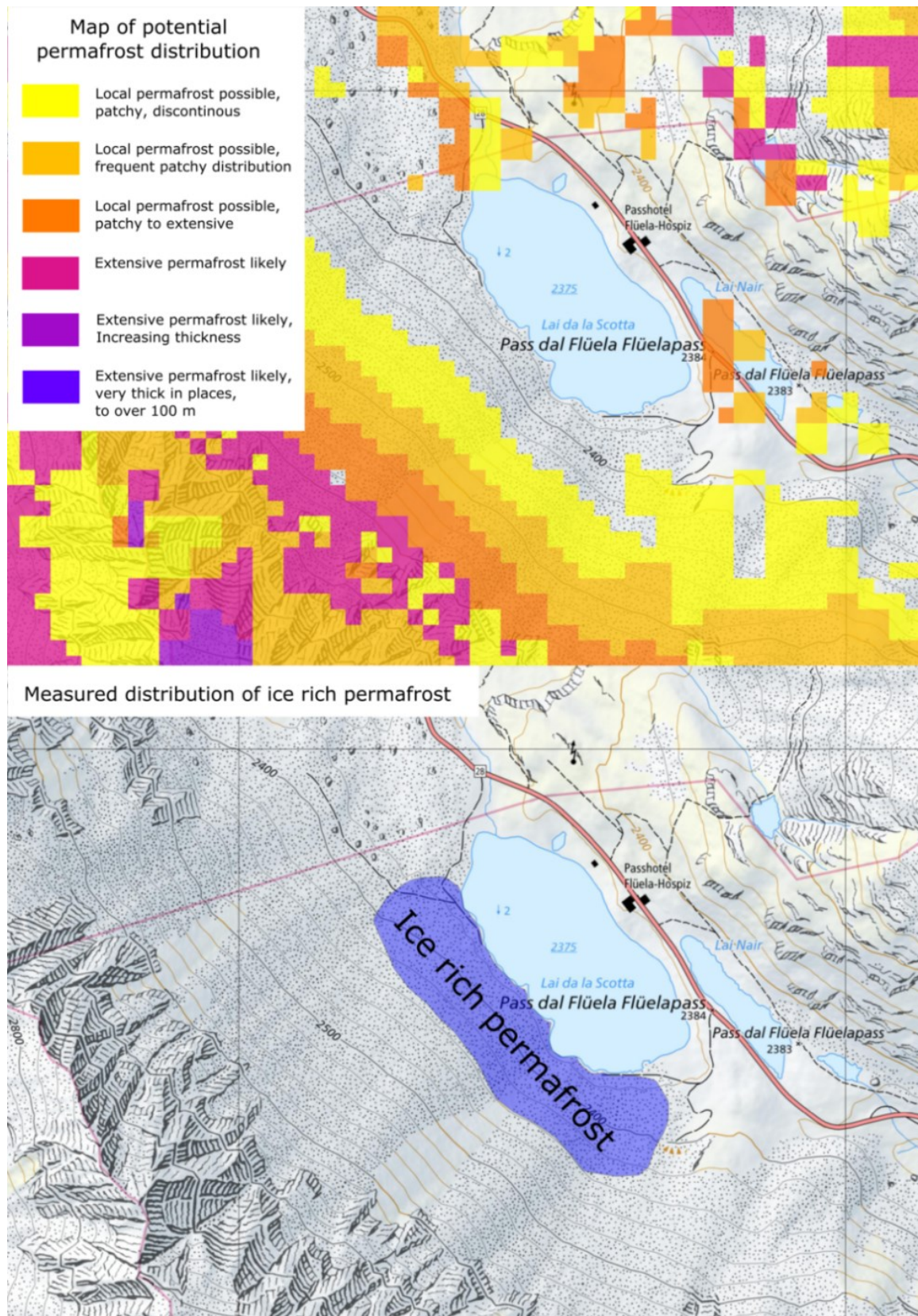
Figure 1: Top: Map of potential permafrost distribution provided by the Swiss Federal Office for the Environment (map.geo.admin.ch). Bottom: Measured permafrost distribution at the same site (see Chapter 3.3 for details). An insufficient consideration of processes leading to the genesis of ice-rich permafrost can lead to considerable discrepancies in the modelling of permafrost distribution (Map: pixmaps © (2017) swisstopo (5704 000 000)).

This approach is again based on the thermal processes mentioned above, which are considered as being decisive for the front elevations of rock glaciers. Suspiciously, the differences in frontal elevations of active and relict rock glaciers differ considerably between neighbouring regions (Frauenfelder and Kääb, 2000) despite a similar climate evolution. Are differences in rock glacier front elevations indeed an equivalent of climate change? **The studies in the second part of this dissertation investigate whether the thermal processes considered by current permafrost models are alone sufficient to explain ice-rich permafrost or if there are other important processes.**

Permafrost related deformation processes have attracted increasing interest during the last decades (Haeberli, 1985; Arenson et al., 2002; Kaufmann and Ladstädter, 2003; Lambiel and Delaloye, 2004; Strozzi et al., 2004; Kääb et al., 2007; Delaloye et al., 2008; Delaloye et al., 2010a; Bollmann et al., 2012). Most of these authors report about an acceleration trend of rock glacier deformation velocity over the last two decades. Naturally this acceleration seemed to be linked to climate change and many authors draw a direct connection to permafrost warming caused by a higher plasticity of ice under warmer temperatures (Kääb et al., 2007; Ikeda et al., 2008; Nickus et al., 2015). However, there is no absolute certainty about the source of the acceleration. Correlations between mean annual air- or ground temperatures and deformation velocities are rather weak (Kellerer-Pirklbauer and Kaufmann, 2012; Nickus et al., 2015) or absent (Roer et al., 2005). This might be linked to the fact that most rock glaciers in the Alps show temperatures very close to $0°C$ (PERMOS, 2016) and a further warming would lead to ice melt instead of higher plasticity. Furthermore, the plasticity of the rock glacier body, which changes relatively slowly over time, does not seem well suited to explain the velocity changes of rock glaciers, which often show high annual and seasonal velocity variations (Delaloye et al., 2010a). Studies explaining rock glacier movements by plastic deformation reported remarkably high rock glacier plasticity values, over five times higher than those of glacier ice (Ikeda et al., 2008). **This dissertation investigates whether plastic deformation is the right model to explain rock glacier movements and whether ground temperature is the factor controlling their velocity.**

In combination with the densification of infrastructure in alpine regions, the increasing dynamics of rock glaciers in the European Alps are causing a higher hazard and damage potential. The protection of inhabited valleys against natural hazards released in permafrost areas, such as rock fall or debris flows, requires detailed knowledge on the surface movements taking place. The same applies for the construction of sustainable infrastructure

such as cable cars or avalanche defence structures in permafrost areas (Bommer *et al.*, 2010). To investigate such movements, geodetic monitoring of the ground surface is required. **The increasing number of potentially hazardous instabilities related to ice-rich permafrost represent a challenge for practitioners in terms of monitoring effort and financing. To address these problems, a couple of monitoring concepts are presented within this dissertation, covering a wide range of applications.** Monitoring concepts and automatized post processing algorithms were designed and optimized for various tasks, covering small scale monitoring for the purposes of hazard prevention or scientific investigations as well as large scale estimations of permafrost creep. With the development and implementation of a low cost and low tech monitoring system, further improvements in data quality, accessibility, resolution and cost efficiency could be achieved. These results might not only be of interest for research but also for practitioners. Part 1 of this dissertation focusses on the geodetic monitoring methods, Part 2 will discuss processes linked to ice-rich permafrost.

Part one

Monitoring of ice-rich permafrost induced mass wasting processes

Terrestrial laser scanning at Ritigraben (Grächen VS), 20.8.2014 (Photo: Marcia Phillips).

2. Terrestrial laser scanning: Introduction

Terrestrial laser scanning is a key technology, used in almost all monitoring tasks carried out in the following studies. The methodical basements for these applications were explained by Kenner *et al.* (2014). Although this earlier study is not part of this dissertation, some parts are cited here, as they are a good introduction of the method and are relevant for the understanding of the subsequent work.

2.1 Basics and data processing

Terrestrial laser scanning (TLS) is based on the time of flight measurement of directed laser impulses. It provides point clouds with resolutions of up to a couple of centimetres. The point clouds can be transformed into a common coordinate system by either applying a least squares matching of control points included in the scans or running the iterative-closest-point (ICP) algorithm (Chen and Medioni, 1991) on the point clouds. The further processing when applying TLS to monitor of mass movements is described by Kenner *et al.* (2014):

" *In the next step, elevation rasters were generated from the TLS point clouds. The raster resolution values were defined by averaging the z components of the points within one cell. The raster resolution was chosen to be close to the point cloud resolution. […] To fill cells without data, we used a nearest-neighbour interpolation. The elevation values of multi-temporal raster surfaces were subtracted from each other. In the resulting difference-raster, deformations or rapid mass movements could easily be identified. Deposit or erosion volumes were defined by adding up the difference-raster values over a specified spatial extent.*

To calculate horizontal creep rates between the measurement campaigns, a high-pass filter was applied to the raster surfaces. Using a filter panel of 5 × 5 to 10 × 10 m, all large scale topography information was filtered out, leaving only the high frequency surface structure of the rock glacier. The resulting surfaces were grey-value scaled depending on their new z-value and saved as ordinary geo-referenced image files with the same extent and resolution for each image. As the surface structure of a rock glacier and hence the grey value pattern of the images mostly do not change in spite of slow creep, a correlation could be calculated between the multi temporal images. This was done by defining the shift of pattern between the images within patches of a given size using the particle imaging velocimetry method introduced by Roesgen and Totaro (1995). Translation vector components u in x-direction and v in y-direction were saved for each patch and converted from image to map units.

Taking into account the amount of time between the measurements, we calculated creep velocity and direction for each patch. The more common way to produce correlatable images out of raster data is to illuminate them using a hill-shade effect. We opted for the high pass filter, as it provides consistently good contrast in every exposition and inclination whereas hill-shade illumination can cause correlation errors (Bollmann et al., 2012). "

2.2 Accuracy analysis

An extensive accuracy analysis was carried out by Kenner et al. (2014), starting with the accuracy of vertical movements (difference DEMs):

" The aim of our accuracy analysis was not to define the accuracy of DEMs but to define a level of significance (LOS) for change detection between raster datasets. As described in Kenner et al. (2011), the LOS of surface movements is highly dependent on the spatial extent of the movement. The larger the extent of a movement, the higher the LOS of the movement signal in the difference-raster (spatial out-filtering of errors). Hence, one single accuracy specification for the complete monitoring task is insufficient. Instead, the accuracy should be given in dependency of the extent of the movement. We therefore used a technique based on matching repetition of unchanged terrain between two measurement campaigns. Using the stable parts of the difference-raster we calculated the arithmetic mean error (ARM) for the surroundings of each cell. The calculation extent varied depending on the spatial extent of the surface movements of interest. Each single ARM value removes all single cell random errors within its calculation extent. These errors play no role for the detection of an extensive change (spatial out-filtering). However ARM values conserve the important systematic large scale errors in their area. We calculated the absolute mean (ABM) of all ARM values to obtain a value that represents all extent-dependent large scale errors over the whole dataset. Adding the standard deviation (STDEV) of all ARM values to extent-dependent ABM, we obtained the value los. los is a mathematical specification of the LOS concept, representing the smallest detectable vertical movement with a horizontal spatial extent that corresponds to the calculation extent of ARM values. Figure 6 shows a simplified 1D concept of this procedure."
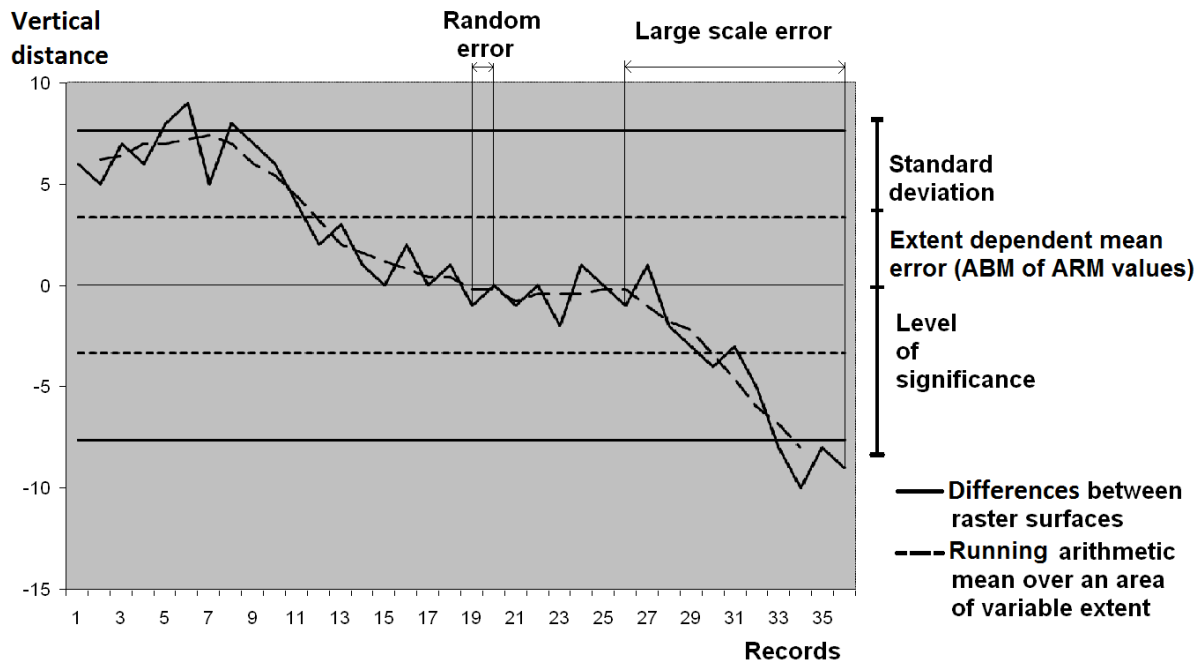
Figure 6 from Kenner et al. (2014): Sketch showing the definition of the level of significance in difference-raster.

Additionally the accuracy of the defined creep rates was analysed in Kenner et al. (2014):

"To define a level of accuracy for the calculated creep rates we used two different approaches. The first and most significant way was to use control points measured by differential real time kinematic GPS. [...] We calculated horizontal creep rates for each of the GPS points and reduced the values accordingly to the period of time between the ALS and TLS measurements. Due to the higher accuracy, the GPS creep rates were treated as true values. Hence we calculated residuals between every GPS creep vector and the closest image-based creep vector. [...] ABM and STDEV of the polar residuals quantify the obtained accuracy. This approach is analogous to the procedure described in the previous section. In this case the extent dependency of the mean error is realized by the size of the correlation window. To obtain accuracy for annual creep rates, the magnitude has to be divided through the number of years between the measurements.

An estimation of accuracy without additional datasets was based on determining the plausibility of the resulting vector fields. A horizontal offset between the input data sets should be evident in a homogeneous and unidirectional shift of stable terrain and can be removed. LOS arises out of the smallest shift rates that can be displayed in a directed and plausible vector field. Calculations below this level result in chaotic vector fields with high frequency changes of magnitude and direction."

To realize an objective and automated evaluation of the plausibility of a translation vector field, Kenner et al. (2014) developed a filter algorithm:

"Inevitably there are some large errors in most of the creep vector fields obtained. They are mainly single mismatches and larger areas with faulty correlations due to major changes of structure, shadow effects or homogeneity of surface pattern. The different superficial extension of these two kinds of errors makes it difficult to eliminate them fully automatically without a considerable loss of data. We obtained the best results with a relatively simple filter procedure. In the regular raster structure of the vector field we calculated STDEV of the angle for the 3×3 surroundings of each single vector. This calculation is difficult due to the discontinuous function of angle units. STDEV between neighbouring vectors of 360°, 1° and 2° cannot be calculated in the common way. We therefore calculated the mean vector v_m of the 3×3 surrounding first:

$$v_m = \sum_{i=1}^{9} \frac{v_i}{|v_i|}$$

where v_m is the mean vector of a 3×3 vector array;

v_i are the single vectors within the 3×3 vector array;

i is the running index .

In the next step we calculated the azimuth of v_m and obtained the mean value for the standard deviation. The single differences for the standard deviation between azimuth v_i and azimuth v_m (ΔA) were defined by a case-by-case analysis for ΔA < 180° (=ΔA) and ΔA >180° (=360 − ΔA). For the STDEV value obtained we defined a threshold of 20° for the maximum acceptable STDEV value of a 3×3 filter panel. All other vectors were eliminated. This led to a complete capture of all faulty correlations, but also affected a buffer zone of correct correlations around the incorrect ones. For example the entire 3×3 surroundings of a single mismatch lie above the given threshold. To counter this effect we performed a 3×3 dilatation on the elimination zone to recover the well-matched areas.
In the course of an iterative process the same procedure would also be possible using the length of the creep vectors as a disqualifier instead of the angle. However one iteration with angle values was sufficient here."

Kenner et al. (2014) found, that the accuracy values defined by using GPS reference data were identical with the smallest remaining creep vectors after the application of the filter algorithm. The filter algorithm was therefore considered as good accuracy estimation. At three different sites, the study defined surface displacements with a level of significance of a few cm in both, horizontal and vertical direction.

2.3 Conclusions and outlook

Terrestrial laser scanning has proved to be a suitable method to monitor local mass wasting processes. However there is not a single method that could cover all monitoring tasks connected with alpine mass movements. Terrestrial laser scanning can fail, for example due to the lack of appropriate scan positions which provide a good measurement geometry and as short as possible scan ranges. Considerable challenges arise from large scale movements, covering areas of multiple square kilometres. The first study in Part 1 of the thesis therefore evaluates other available measurement systems and present a measurement concept focusing on the monitoring of extensive areas with numerous different mass wasting processes. Such an approach is probably rather of interest for administrative hazard management tasks than for case-specific engineering. For the latter, the second study of Part 1 presents an interesting solution in form of a low tech and low cost method. This method allows the acquisition of surprisingly accurate and robust deformation data, in a very high spatial and temporal resolution. The only data components required are monoscopic images taken by an automatic in-situ camera and a digital terrain model.

3. Integration of space-borne DInSAR data in a multi-method monitoring concept for alpine mass movements

Robert Kenner[1], Giulia Chinellato[2], Christian Iasio[2], David Mosna[3], Giovanni Cuozzo[2], Elisa Benedetti[4], Maria Grazia Visconti[5], Michele Manunta[6], Marcia Phillips[1], Volkmar Mair[3], Andreas Zischg[7], Benni Thiebes[2], Claudia Strada[3]

[1] WSL Institute for Snow and Avalanche Research SLF;
[2] European Academy of Bolzano/Bozen (EURAC);
[3] Office for Geology and building materials testing, Autonomous Province of Bolzano, Italy;
[4] Sapienza University of Rome
[5] Politecnico di Milano
[6] National Research Council of Italy, Institute for Electromagnetic Sensing of the Environment (IREA)
[7] University of Bern, Institute of Geography, Oeschger Centre for Climate Change Research, Mobiliar Lab for Natural Risks

Personal contributions:

Robert Kenner: Paper concept and realization; TLS acquisition and processing; Post-processing concept; Data consolidation; Data analysis; Discussion; Fieldwork

Giulia Chinellato: GNSS data acquisition and preparation; Data management; Fieldwork; Project coordination (takeover from Christian Iasio)

Christian Iasio: Project Idea; Project coordination (handover to Giulia Chinellato); Fieldwork

David Mosna: Reporting; Fieldwork

Giovanni Cuozzo: Scientific assistance for DInSAR processing

Elisa Benedetti: GNSS Processing

Maria Grazia Visconti: GNSS Processing

Michele Manunta: DInSAR Processing

Marcia Phillips: Project idea and acquistition, Scientific assistance; Fieldwork

Volkmar Mair: Scientific assistance; SAR Tiepoint design

Andreas Zischg: Reporting

Benni Thiebes: Scientific assistance (takeover from Giulia Chinellato)

Claudia Strada: Coordination between international project partners

Abstract

This study presents the results of an experimental application of a multi-method measurement concept for the monitoring of alpine mass movements. Satellite-borne differential interferometric synthetic aperture radar (DInSAR) was applied as the key technology. To improve the information contents of the DInSAR displacement data for an individual mass movement, a complementary measurement was carried out with a three dimensional measurement system. The information on the 3D movement characteristics obtained by this complementary measurement was used to extrapolate subsequent DInSAR measurements to 3D. Terrestrial laser scanning (TLS) and Global Navigation Satellite System (GNSS) data were tested as complementary 3D measurement systems. The deviations between the single measurement systems were mainly controlled by the error budgets of the different methods. An exception were short term GNSS single point time series which included small scale surface movements that were not captured by the other methods. TLS proved to be the most suitable complementary method. A single TLS repeat measurement was sufficient to create a mask, which enables the projection of DInSAR displacement data to 3D. The application of satellite-borne DInSAR in alpine terrain is challenging; signal decorrelation is a problem due to fast terrain movements and snow coverage and can cause failure of the measurement system.

3.1 Introduction

The densification of infrastructure and settlement areas in the European Alps requires careful consideration of natural hazards and the activity of geomorphological processes, in particular in the light of climate change. Alpine mass movements like landslides, permafrost creep or rock slope failures are the source of potentially hazardous processes. They can show a low activity for decades or even centuries without being seriously hazardous – before unexpectedly accelerating. Some of these accelerations can be forecasted or at least detected in real time if the mass wasting zone is monitored on a long term basis. These include for example rock glacier creep surges (Delaloye *et al.*, 2013; Kenner *et al.*, 2014), accelerations of landslides and deep seated gravitational slope deformations (Angeli *et al.*, 2000) or rock fall events (Abellán *et al.*, 2010; Kenner *et al.*, 2011).

However, decision makers in natural hazard prevention are confronted with a considerable number of critical mass movement processes in alpine environments, which are often insufficiently documented. Long term monitoring tasks using classical monitoring methods are in many cases associated with high costs. This may force the natural hazard managers into a mode of reactionary operation. In many cases potentially dangerous mass movements are only focused on after the occurrence of larger events, which is suboptimal in terms of hazard prevention (Tobler *et al.*, 2012). A cost-efficient long term monitoring system, mostly working in a self-operating mode over regions of hundreds of square kilometers, with cm accuracy and capturing changes in existing mass movement processes or even detecting new ones, would clearly help decision makers. This is the point on which the current study was based on. Our aim was to develop a measurement concept that enable a supra-regional, long term monitoring of as many individual mass movements as possible.

Numerous measurement technologies are currently used for monitoring tasks in alpine terrain (table 1). They can be classified into in-situ and remote sensing methods but also into single point tracking systems or those enabling data acquisition over wide areas. The information content of the data obtained varies substantially according to the measurement system. Mass movement processes were traditionally monitored using total stations (Veulliet *et al.*, 2009). Air-borne photogrammetry has been used for several decades for long term monitoring tasks (Kääb, 1999; Kaufmann and Ladstädter, 2003; Fabris *et al.*, 2005). In recent years, this method has been applied more frequently and facilitated by the development of air-borne digital sensors (ADS), the availability of drone-borne photogrammetry (Eisenbeiß, 2009; Bühler *et al.*, 2012) and software improvements.

Table 1: Most frequently applied monitoring technologies for mass movements in alpine terrain

	GNSS	Total Station	Terrestrial laser scanning	Air-borne laser scanning	Air-borne photogrammetry	Terrestrial Radar	Space-borne SAR
Platform	Terrestrial: On site	Terrestrial: On site	Terrestrial: Ground base close to site	Remote: Aeroplane/ Helicopter	Remote: Aeroplane/Drone	Terrestrial: Ground base close to site	Remote: Satellite
Highest achievable spatial resolution	Single Point measurement	Single Point measurement	few cm	> 50cm	> 25cm	> 1 m @1 km	> 1m
Spatial coverage	Local	Local	Local	Regional	Supra-regional	Local	Supra-regional
Dimensionality	Direct 3D point coordinates	Direct 3D point coordinates	Direct 3D surface coordinates	Direct 3D surface coordinates	Indirect 3D surface coordinates	Direct 1D coordinate differences	Direct 1D coordinate differences
Highest achievable accuracy	>mm	mm	>cm	dm	sub-dm	mm	mm
Image information	Not available	Not available	Referenced images	Not available	Multiband image information	Not available	Not available
Natural radiation	Independent	Independent	Independent	Independent	Dependent	Independent	Independent
Topographical effects	Satellite shadowing	Surface shadowing	Surface shadowing	No influence	In steep terrain	Surface shadowing and layover	Surface shadowing and layover
Vegetation	No Influence	No influence	Influence	Influence	Influence	Influence	Influence
Effort (time for data acquisition, logistics, costs)	High, Manual measurement on every single point	High, Manual measurement on every single point	Medium, remote sensing over long ranges, Close to site access required	High, Long flight time, expensive	Medium, Efficient area coverage, expensive	Medium, Automatic operation, heavy equipment,	Low, Automatic operation, efficient, reasonable prices

Meanwhile GNSS measurements have become a widely used additional method to the classical surveying techniques (Lambiel and Delaloye, 2004; Wirz *et al.*, 2015). Since the beginning of the 2000s, laser scanning technology has developed rapidly and allowed the terrestrial and air-borne acquisition of widespread 3D terrain data (Bauer *et al.*, 2003; Sailer *et al.*, 2012; Kenner *et al.*, 2014). This was a notable development, especially for monitoring inaccessible and steep terrain areas. Simultaneously, radar technology proved to be a very powerful method for high accuracy applications in mass movement monitoring (Strozzi *et al.*, 2005; Colesanti and Wasowski, 2006; Gischig *et al.*, 2009; Kos *et al.*, 2013), allowing to monitor millimeter scale deformations of the ground surface over areas of up to hundreds of square kilometers. Table 1 gives an overview of the characteristics of these technologies. Several of the methods have been applied by Strozzi *et al.* (2010) for the monitoring of a rock slide in high alpine terrain. This study provides additional information about the characteristics of the methods and differences between them.

Based on this evaluation of measurement systems, our study focuses on satellite-borne differential interferometric synthetic aperture radar (DInSAR) as a key technology to realize the aim of a self-operating large scale monitoring concept providing centimeter accuracy. Space-borne DInSAR is an established method to detect and monitor large scale surface displacements. Similarly it can be used to monitor numerous small scale displacements distributed over areas of several hundred square kilometres (Pritchard and Simons, 2002). In the last decade, a large number of case studies successfully applied DInSAR methods for detecting and monitoring ground deformations in alpine environments, and in particular in permafrost-affected areas (Strozzi *et al.*, 2004; Barboux *et al.*, 2012; Echelard *et al.*, 2013; Barboux *et al.*, 2015). A comprehensive overview of differential InSAR and the application of the method to alpine environments and the detection of ground deformations is provided by Barboux et al. (2015).

However all these studies also underline several limitations of DInSAR, making it difficult to rely exclusively on DInSAR data when analyzing and monitoring a mass movement; the one-dimensionality of movement measurements has to be mentioned here in particular. We tried to overcome this weakness by embedding DInSAR measurements into a monitoring concept that can implement the results of a complementary measurement system if necessary. A locally and temporally limited application of such complementary data provides 3D movement information on individual mass movements to understand their general movement characteristics. The complementary data should enable the operator to draw

clear conclusions from further DInSAR measurements and also monitor complex movement processes using DInSAR only.

3.2 Study site

The study was carried out at a test site located above Pontresina in the Upper Engadin valley, Grisons (Switzerland). The monitoring area includes three individual active rock glaciers in a West oriented mountain cirque called Foura da l'amd Ursina. The rock glacier complex henceforth referred to as Ursina (Figure 2) ranges between 2700 and 2900 m asl. The steep surrounding ridges and rock walls reach elevations over 3000 m and are subject to intermittent rock fall. The lowest rock glacier has a steep front in the top of the Val Giandains gully, which is the source area of potential debris flows. A protection dam was built at the base of the gully above Pontresina in 2003.
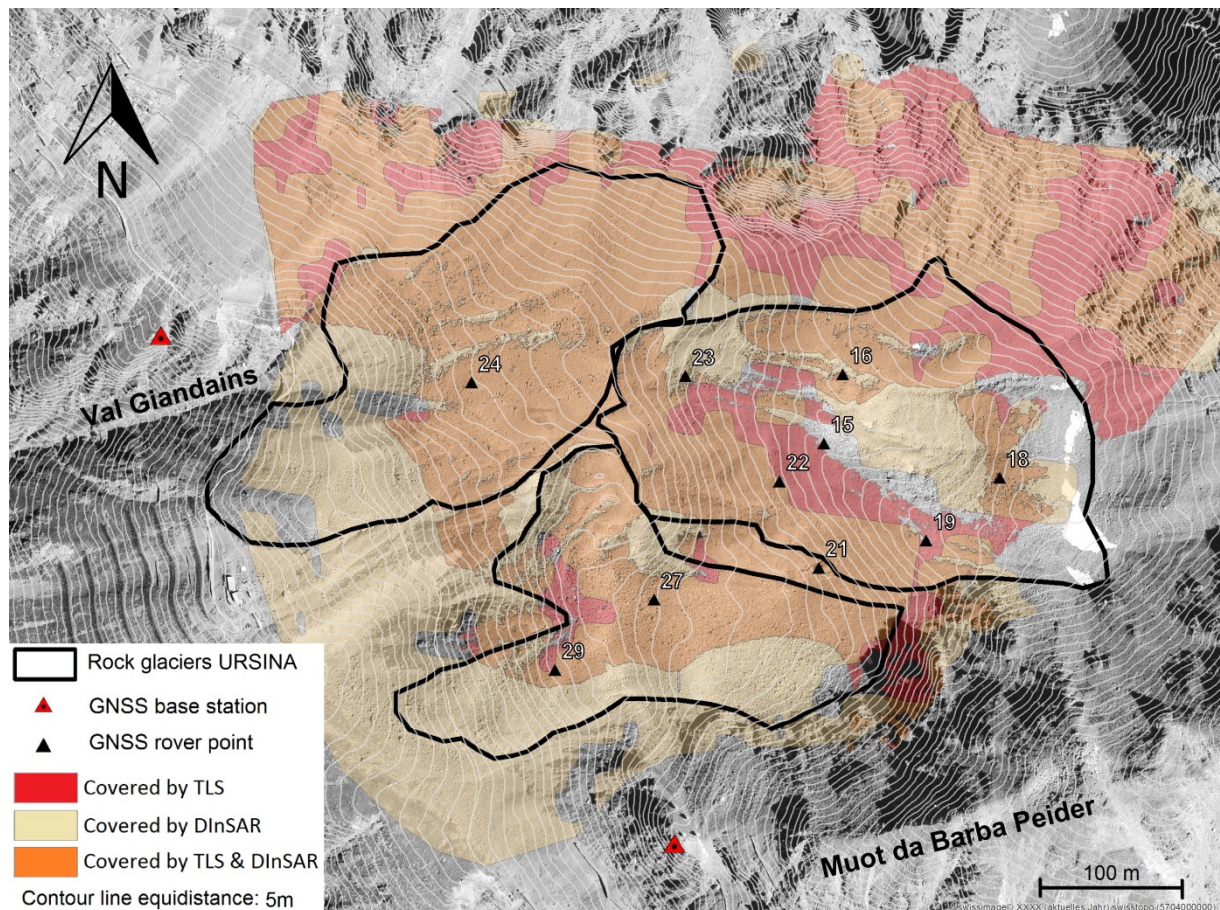
Figure 2: Study site Ursina with measurement configurations. The area covered by DInSAR includes only these regions in which displacement rates or a proof of stability could be deduced from DInSAR data.

3.3 Methods

3.3.1 Monitoring concept

Satellite-borne differential interferometric synthetic aperture radar (DInSAR) (Skolnik, 1980; Bamler and Hartl, 1998) provides data on surface changes over areas of several hundred square kilometers with up to mm accuracy and a minimum of effort for the recipient of the data.

However, there are also considerable problems using DInSAR. The InSAR-specific effects regarding overlay, foreshortening and shadowing (Speck *et al.*, 2007) prevent the complete surface coverage. Fast surface movements can lead to a decorrelation of multi-temporal InSAR images (Bingyuan *et al.*, 2008). Closed snow- and dense vegetation cover entirely prevent the capture of surface movements using DInSAR. However, the major disadvantage of DInSAR is that surface changes are only displayed one dimensionally along the line of sight (LOS) of the satellite, making it difficult to infer the type of movement and its exact kinematic characteristics. Additional information is therefore necessary to correctly interpret DInSAR data. This information can be obtained via a spatially and temporally limited reconnaissance campaign using a different measurement system that provides information on the 3D surface kinematics. The three dimensional interpretability of the DInSAR signal can thus be established for individual sites by referencing it to the reconnaissance campaign. Ideally DInSAR measurements, supported by process information obtained from such local reconnaissance campaigns can then be used to perform an autarkical long term monitoring and provide estimations of the 3D kinematics. The complementary measurement system applied for the reconnaissance campaign must be embedded in the measurement geometry of DInSAR and be suitable to acquire information on the unknown detailed process kinematics. We therefore defined requirements for the complementary measurement system:

- The reconnaissance campaign is temporally limited, so a high accuracy is required to capture even slow movements

- Measurement results should be provided in direct 3D

- If not already available, a digital elevation model (DEM) should be derivable from the measurement data to determine slope and to project the DInSAR data onto

- In some cases the moving terrain is not accessible and must be monitored remotely

Terrestrial laser scanning (TLS) offers adequate solutions for all these issues but depends on an unchanging surface structure for creep detection (see 3.4.) and its accuracy is limited to a few cm. These limitations can be narrowed, if necessary, using single point measurements such as GNSS or terrestrial surveying with a total station. Both provide a higher accuracy - up to mm (table 1) and capture movements based on the tracking of individual points. Their disadvantages include the need for accessible terrain and the spatially sporadic data records in contrast to the area-covering TLS method. In our pilot study we tested both TLS and GNSS as complementary methods to DInSAR.

3.3.2 Reference framework

Each of the measurement systems used has its own reference system. GNSS and DInSAR operate within the World Geodetic System 1984 (WGS84) but their registration can differ e.g. due to satellite orbit uncertainties. The TLS data are referenced in a local frame of control points. To create coherence between the measurements these reference frames must be linked. We therefore installed two local terrestrial control points. Theoretically a third linking point would be necessary to join the reference frames exactly; however, due to the limited spatial extent of the study site and the high temporal stability of the reference frames we could neglect the remaining deviations between the reference frames. The linking reference points were set on stable bedrock and were equipped with an artificial InSAR reflector, a GNSS antenna base and a TLS reflector (Figure 3). The linking points acted as stable reference points for the TLS and DInSAR measurements and the GNSS base stations were located on them. The InSAR corner reflectors consist of an orthogonal open aluminium trihedral with a short edge length of 57 cm. This size results in a theoretical radar cross section of approximately 20 dB for the COSMO-SkyMed© X-band data used. To reduce the weight of the reflector and to facilitate snow melt, a regular grid of circular holes was drilled in the 3 mm aluminium plates. The hole diameter of 6 mm does not interfere with the wavelength used by the satellite system. The TLS reflectors consist of metal plates laminated with retro-reflecting foil. In addition to the linking points four other reflectors were used to define the TLS reference frame. They were mounted on stable bedrock at various distances from the scan position, i.e. shorter distances for the positioning and longer ones for the orientation of the scanner.

Figure 3: Example of a multi-functional control point. The TLS reflector target (bottom right), the InSAR Corner and on it the basement for the GNSS reference station with attached GNSS antenna.

3.3.3 GNSS

Relative GNSS measurements were carried out using two base stations in stable terrain and one rover for the data acquisition in the mass wasting zone. The double frequency sensors Leica Viva GS10 and Leica GS530 were used. A network of GNSS measurement platforms was installed, taking into account the expected surface kinematics and the geometrical GNSS requirements (i.e. satellite visibility, baseline length). The platforms consisted of measurement poles mounted on large boulders; 14 measurement points were defined in addition to the base stations (Figure 2). One GNSS campaign was carried out in summer 2012 and three during the summers 2013 and 2014 (table 2). To obtain highly accurate results, each point was measured in static mode for at least 30 minutes with a 5 second sampling rate.

Table 2: Dates of the measurement campaigns.

	TLS	GNSS	DInSAR
2009	Sep, 11	-	-
2010	Aug, 04	-	-
2011	Aug, 18	-	-
2012	Sep, 18	Sep, 18	Jul, 21; Aug, 06; Aug, 22; Sep, 07; Sep, 23
2013	Aug, 29	Jul, 24-25; Aug, 29 Sep, 23.	Jul, 24; Aug, 09; Aug, 22; Aug, 25; Sep, 07; Sep, 10; Sep, 14; Sep, 09
2014	Aug, 15	Jul, 09; Aug, 18-19 Sep, 30	Jul, 15; Jul, 23; Aug, 16; Aug, 25; Aug, 28; Sep, 13; Sep, 29, Oct, 03; Oct, 12

The post-processing of the collected GNNS data was performed using the 'Leica Geo Office' software, by Leica Geosystems. Baselines of all rover points to both base stations were calculated and the relative coordinates of these points were defined. The comparison of the baselines from two different base stations allowed the identification of large errors. Random errors of single points were minimized by calculating a least squares adjustment of the GPS network baselines. In order to refer the local net to the global reference system the base stations were connected to permanent reference stations belonging to the Swiss geodetic network (SWIPOS). The results of two measurement campaigns A and B were referred against each other by correcting the point coordinates of the repeat measurement B by the deviation A-B of the barycenter between the local reference stations. The degree of precision between two measurement campaigns is equivalent to the accuracy of the displacement values. This precision was equivalent to the remaining deviation of the reference station coordinates between two measurement campaigns, after they have been corrected by Barycenter bias (accuracy specifications are given in the Results section).

For calculating displacement velocities from the GNSS data we carried out a pre-selection of rover points. A few of these rover points showed movements below the level of significance, a few others could not be measured during each campaign due to logistic reasons and thus show data gaps. Both types of rover points were therefore excluded from the calculation. For the remaining points a mean velocity per measurement interval was defined.

3.3.4 TLS

Annual TLS measurements have been carried out for the entire site since 2009. Shorter measurement intervals showed no significant movement results. The instruments used were a Riegl LPM321, and from 2013 onwards a Riegl VZ6000. Both scanner systems are

specified for long range applications (for technical details see: www.riegl.com). Measurements were carried out from a single fixed scan platform on the mountain ridge Mout da Barba Peider (Figure 2). The scans were performed with a resolution of < 10 cm (range dependent). Referenced images of the scan areas were taken using the camera integrated in the scanners. To reference the data, six retro-reflecting reference points including the reference frame linking points were scanned at a very high resolution. The absolute coordinates (WGS84) of the reference points were defined in advance, using a Leica TPS1200 total station.

The point clouds acquired were filtered to remove outliers and to homogenize the spatial resolution. To achieve an optimal relative referencing of the multi-temporal scans, the iterative closest point (ICP) algorithm was applied to match unchanged terrain parts in the scan (Chen and Medioni, 1991). Subsequently the set of relative registered point clouds was transformed into global coordinates using the least squares adjustment of all observations into grid based digital elevation models (DEM) with 20 cm resolution. Small data gaps were filled using a 3x3 cell mean interpolation.

Horizontal 2D displacements (i.e. rock glacier creep) were derived from the multi-temporal DEM using the surface structure of the blocky terrain. The DEM grids were filtered using a high pass filter which removed information about the raw topography from the grid and only conserved the high frequency surface structure (blocks and boulders). These surface models were grey value scaled to visualize the surface pattern and saved as images. Subsequently image patches of 10x10 m were matched using the particle imaging velocimetry correlating method introduced by Roesgen and Totaro (1995). This algorithm produced a 2D displacement vector for each patch. The resulting vector field was filtered to eliminate faulty correlations (Kenner *et al.*, 2014).

Regarding the vertical component of the displacement, a simple difference DTM would show the surface change on a specified location in the reference system. The GNSS and DInSAR methods track the movement of a single surface point or surface patch instead. This methodical difference would not allow a direct comparison of the vertical displacement components between the different measurement systems. An additional processing step was therefore applied to the TLS data. Initially, the DEMs of the first measurement t_1 and a repeat measurement t_2 and the horizontal 2D displacement vector field between both measurements were used. For the initial position of each horizontal 2D displacement vector, the elevation value was defined by calculating a weighted average between the four closest cell centres of DEM t_1 surrounding the point. Subsequently the displacement value was

added to the initial positions of the displacement vectors and the elevation calculation was applied to this second set of points using the DEM t_2. Both elevations were subtracted to define the change in elevation for each point pair. This elevation difference represents the dZ component of the final 3D displacement vector field. Figure 4 summarizes this procedure. An accuracy analysis of the TLS measurements at this site was previously carried out by Kenner *et al.* (2014), detailing a methical approach to define accuracy specifications for TLS displacement measurements in position and elevation (accuracy specifications are given in the Results section blow).
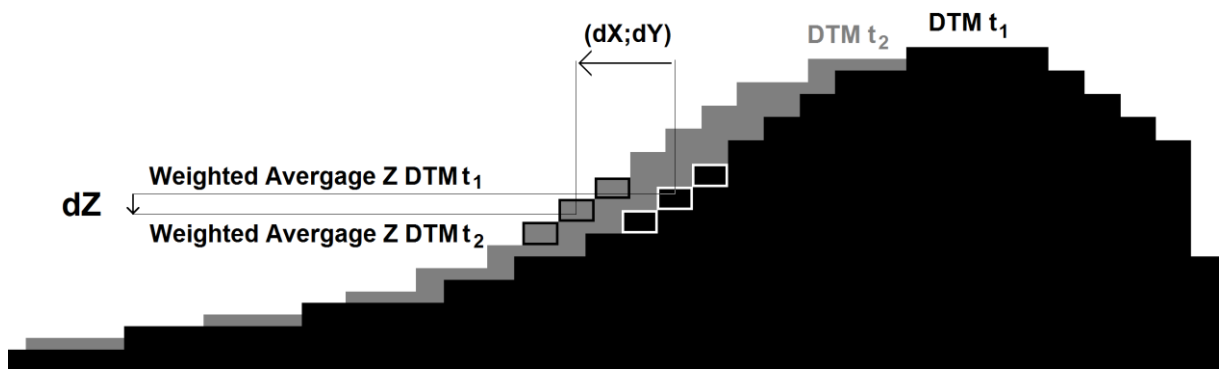
Figure 4: Sketch showing the mode of extracting the z component of a movement from two TLS DTMs.

3.3.5 DInSAR

The spatial and temporal resolution of space-borne SAR imagery were important characteristics on which the selection of a satellite system was based on. Additional analyses were carried out including a topographical analysis, applying distortion masks to simulate the layover, shadowing and foreshortening effects. Based on this, the satellite platform COSMO-SkyMed, operated by the Italian Space Agency and the Italian Ministry of Defense was selected. It consists of four satellites with a revisit time of 8-16 days. To capture the West oriented mountain cirque, descending orbits were used with a resulting off-nadir angle of 30.620 degrees. The SAR acquisition was carried out in stripmap mode with a nominal spatial resolution of 3 m.

Multi-temporal DInSAR uses stacks of SAR images acquired with the same geometry and exploits the redundant information of phase difference to measure ground displacements. The available techniques can be grouped in two main classes: Persistent Scatterers (PS; Ferretti et al., 2001) and Small BAseline Subsets (SBAS; Berardino et al., 2002). Both

methods can deliver displacements along the line of sight (LOS) direction with accuracy in the order of a few millimetres per year (Pasquali et al., 2014). In a recent paper, Barboux et al. (2015) applied PS and SBAS interferometry based on TerraSAR-X for the monitoring of Swiss rock glaciers. One central finding of the aforementioned study was that SBAS interferometry was able to detect maximum displacements ten times larger than PS interferometry (3.5 cm/a versus 35 cm/a for SBAS) but inaccurate measurements due to phase unwrapping errors were already observed for velocity rates larger than 20 cm/a. Referring to the creep velocities of up to 25 cm/a we chose the SBAS technique developed by CNR IREA of Naples (Lanari *et al.*, 2004) for our data analysis. This technique uses the surface structure as natural scatter and allows an analysis of the study area with a high spatial resolution. The study site, showing a complete absence of vegetation and widespread rocks and boulders, was particularly suited for the application of this algorithm.

The influence of atmospheric distortions such as refraction in SAR images declines with an increasing number of images. To achieve a high accuracy, multi-interferometry of SAR data requires a minimum of 20 images to effectively remove the distortions by applying spatial and temporal filtering operations (Colesanti *et al.*, 2003). The implementation of our concept showed that due to the short snow free period at this elevation, only 5 images could be captured in 2012, 8 in 2013 and 9 in 2014. This not only affected the accuracy of the results, but also the resolution of spatially differential movements. The spatial resolution of the generated surface velocity maps was thus adapted to the significance of the data and lowered to 15 m x 21 m.

Geometrical or electrical changes in the properties of the Earth's surface between data acquired at different times are potential sources of temporal decorrelation. If the temporal decorrelation between two consecutive images is high (usually a threshold of 0.7 is used), no reliable interferogram or deformation map can be created. Moreover, if the deformation along the LOS is greater than half the wavelength (i.e. 1.55 cm in the COSMO-SkyMed data) aliasing problems can occur. Similar problems arise for parts of a scene covered by snow. In our study area, the snow-free period only lasted for 3-4 months each year and thus hindered the determination of interannual displacements.

3.3.6 Integration of multi methodical measurement results

To compare the results acquired with GNSS and TLS, each GNSS displacement vector was linked to the mean of all TLS displacement records in its 15 m x 15 m surroundings. The deviation between both solutions was calculated for each data pair in all three spatial

components. Subsequently the mean absolute error deviation was specified for each directional component.

To allow a comparison of the DInSAR monitoring results and the results obtained from TLS and GNSS, the 3D movement information of the latter had to be projected on the line of sight (LOS) of the SAR satellite. In a Cartesian coordinate system both the displacement and the LOS of the radar sensor are represented by a 3D vector. The scalar product of the displacement vector $\vec{a} = (a_x, a_y, a_z)$ and the unit vector $\hat{b} = (b_x, b_y, b_z)$ of the radar LOS results in the projection of $\vec{a}$ on $\hat{b}$. The TLS and GNSS displacement vectors were projected on the SAR LOS to achieve comparability between the different datasets.

The GNSS measurements were carried out with a similar temporal resolution as the DInSAR measurements and were used as comparative data. All DInSAR displacement values in a 15 m radius around each GNSS point were averaged and linked to the GNSS displacement result. These values were normalized by time and then directly compared to define the absolute accuracy of DInSAR monitoring results.

So far, data from different measurement systems were only compared with each other. In the next step the three dimensional information of a TLS reference measurement is linked to DInSAR results of another measurement period, to extrapolate these DInSAR results into 3D. The information content of the DInSAR is thus clearly improved. To do this, TLS displacement data was transformed into an extrapolation mask for DInSAR in the following way: TLS displacement vectors $\vec{a}$ for the monitoring period 2013-14 were projected onto the LOS of the SAR sensor. This projection is called $\vec{c}$. Subsequently all three spatial displacement components of $\vec{a}$ were expressed as a fraction of the length of the vector $\vec{c}$ (equations 1-3).

(1) $a_x = u \cdot |\vec{c}|$
(2) $a_y = v \cdot |\vec{c}|$
(3) $a_z = w \cdot |\vec{c}|$

Using the vector specific fraction parameters u, v and w a 1D DInSAR displacement value can be extrapolated to 3D under the assumption that the creep directions remain constant. We extrapolated the DInSAR displacements in summer 2013 to 3D by splitting each DInSAR displacement value into the components *dx, dy* and *dz* by multiplication with the mean fraction parameters of all TLS vectors in their 15x15 m vicinity.

In a following step, the reliability of the DInSAR derived 3D dataset was tested. Although TLS and DInSAR datasets were now both available in 3D, they could not be compared

directly due to their different temporal resolution. TLS measurements were taken with an annual resolution, whereas no interannual DInSAR processing was possible. However, the relative spatial distribution of the creep velocity was assumed to be similar between the different but temporally close observation periods of both datasets. This implies that the ratio in velocity between a fast moving zone and a slow moving zone should be approximately the same for both methods. Although the relative velocity pattern remained constant, the absolute displacement values differed between different observation periods due to: a) temporal creep velocity differences and b) different durations of the monitoring intervals.

To eliminate this scale difference between both datasets, the TLS displacement vectors were scaled on the DInSAR vectors. The scaling factor was defined using the ratio of the mean norm of all DInSAR displacement vectors and the mean norm of all TLS displacement vectors. Subsequently root mean square error and mean absolute deviation between the datasets were calculated.

3.4 Results

3.4.1 Results and comparability of GNSS and TLS

The individual results of GNSS and TLS measurements were plausible and coherent. TLS captured highly differential surface movements with a high area covering resolution (Figure 5). GNSS single point measurements confirmed the vector field obtained by TLS and provided a higher temporal resolution during the summer months (Figure 6).

The 3D mean absolute error (MAE) between displacement records of GNSS and TLS was found to be 3.7 cm and the root mean square error (RMSE) 3.4 cm. There is no significant difference in the deviation for the single directional components. The deviations are slightly higher than the TLS precision of 3.3 cm for the position, and 3 cm for the elevation and clearly greater than the GNSS precision of 2 mm on the East-, 0.8 mm on the North- and 6 mm on the elevation component.
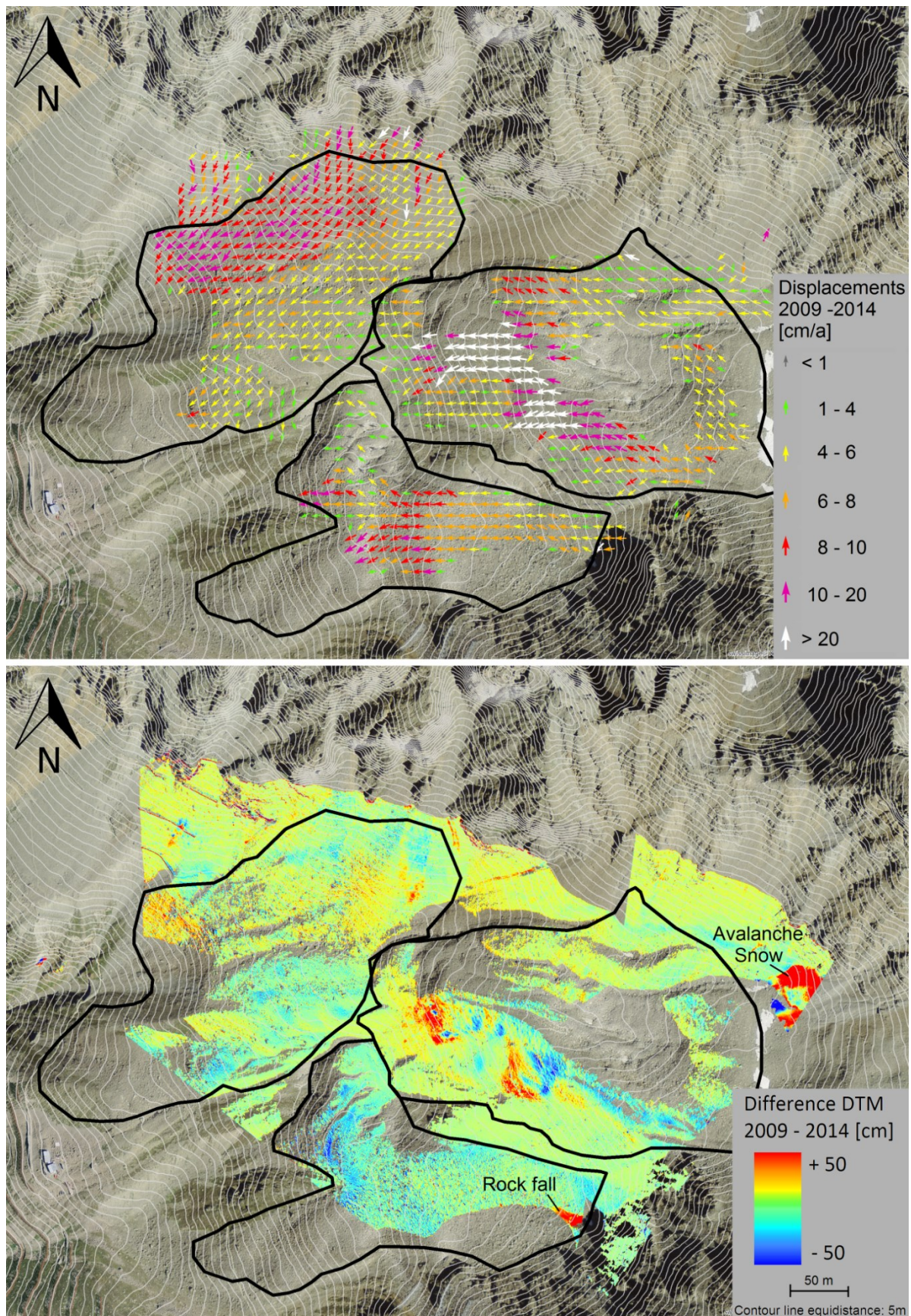
Figure 5: Results of the TLS measurements between 2009 and 2014. Horizontal 2D creep rates are shown for visualization. The vertical differences represent the differences between the DTMs.
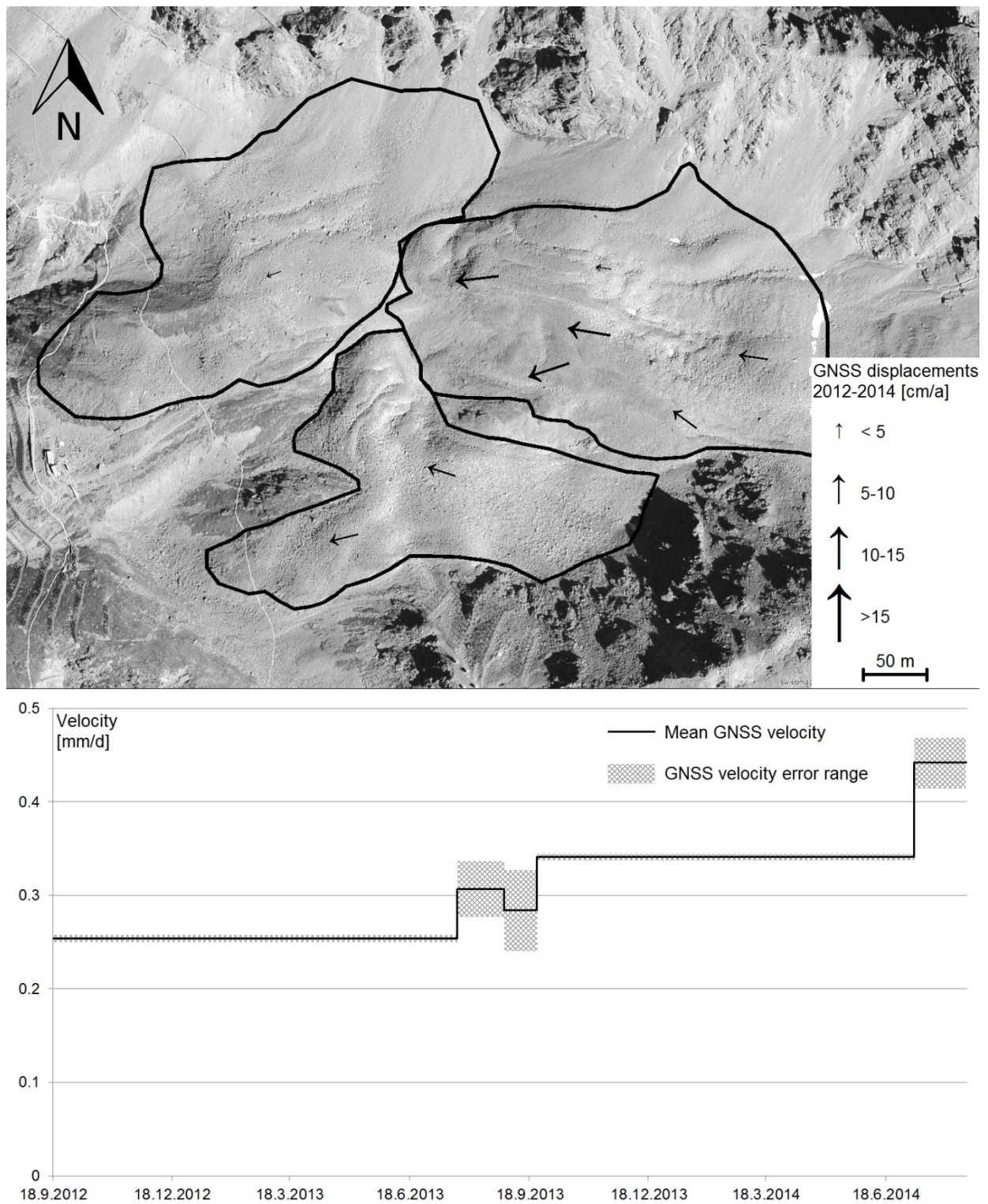
Figure 6: Velocities of the GPS point displacements during the monitoring period 2012-2014, in spatial resolution (top) and temporal resolution (bottom).

3.4.2 Results, validation and integration of DInSAR measurements

The rock glacier movement at Foura da l'amd Ursina could also be verified with the satellite-borne DInSAR measurements. As mentioned in the method section the DInSAR displacement solutions only exist for individual summer seasons and not on a full annual basis. A first comparison shows that the zones of mass movements detected by DInSAR are almost the same as the zones detected by terrestrial laser scanning. These zones correspond to the geomorphologically defined spatial extent of the rock glaciers (Figure 7). DInSAR captured the mass movement area with a similar reliability as TLS at this site, yet with a lower spatial resolution. Unfortunately, movement rates could not be quantified in some of the fast moving zones of the rock glacier complex by DInSAR. No correlation between the limited number of SAR images could be established here by the DInSAR processing.
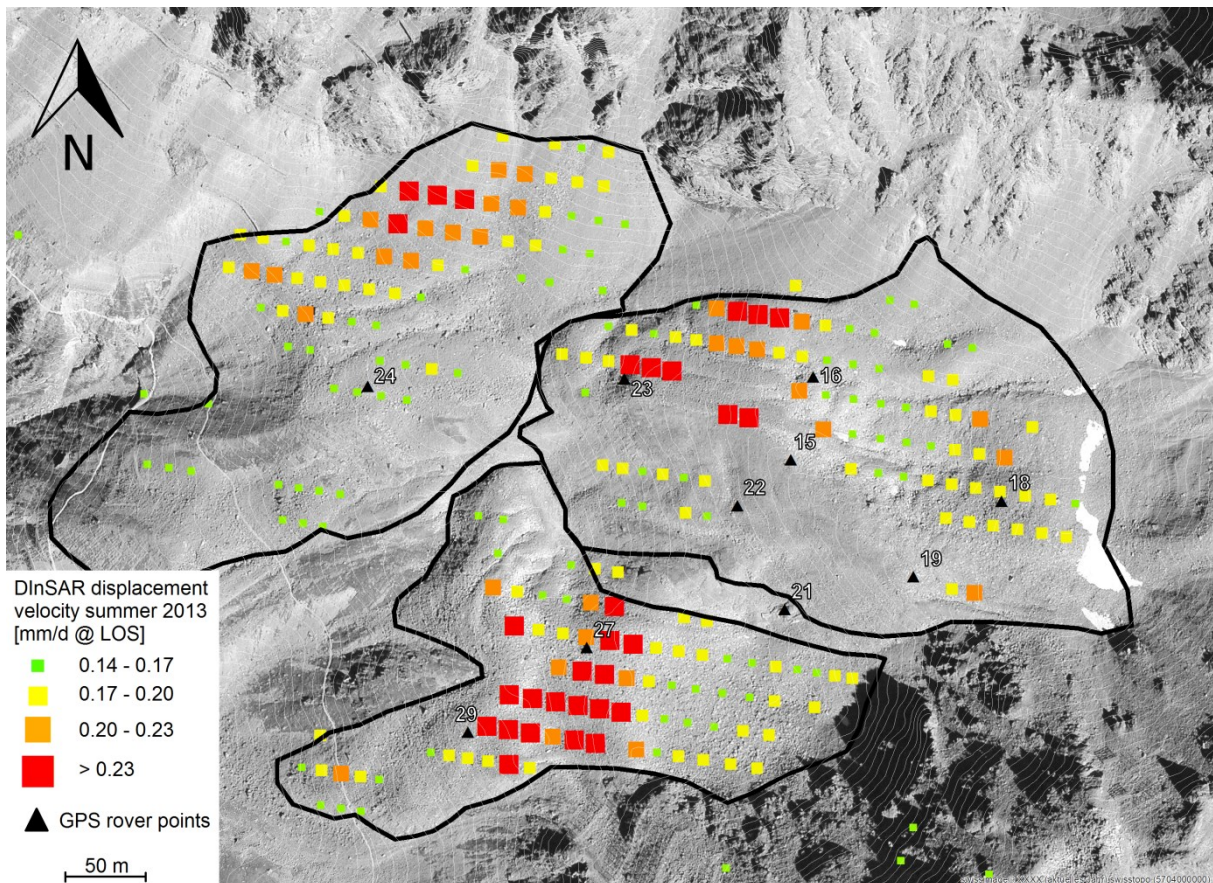
Figure 7: Mean velocity of the rock glaciers in the direction of the line of sight of the SAR sensor. Addionally the locations of the GNSS rover points are mapped.

As a couple of GNSS basements are located in these fast moving zones the comparison of GNSS and DInSAR displacement results is based on a small statistical baseline. This comparison was intended to give an estimation of accuracy and reliability on the DInSAR results. However, we obtained differences between both methods that cannot be explained by the error budgets alone. Figure 8 shows the differences of GNSS and DInSAR displacement records projected on the LOS of the radar sensor. The values are given in mm per day and are based on the monitoring period 2013 (61 days for GNSS and 76 days for DInSAR) (table 2). Although the 3D GNSS displacements include larger error influences compared to the 2D solutions, they are probably more relevant in this figure, as the elevation component of the movement is disproportionately strong represented in the LOS projection. Parts of the differences between GNSS and DInSAR are related to measurement errors. The error bars for the GNSS measurements are included in Figure 8.

Velocity in the line of sight of the radar [mm/d]

Records

Legend:
- GNSS accuracy 3D @ LOS
- GNSS accuracy 2D @ LOS
- DInSAR
- GNSS 3D @ LOS
- GNSS 2D @ LOS
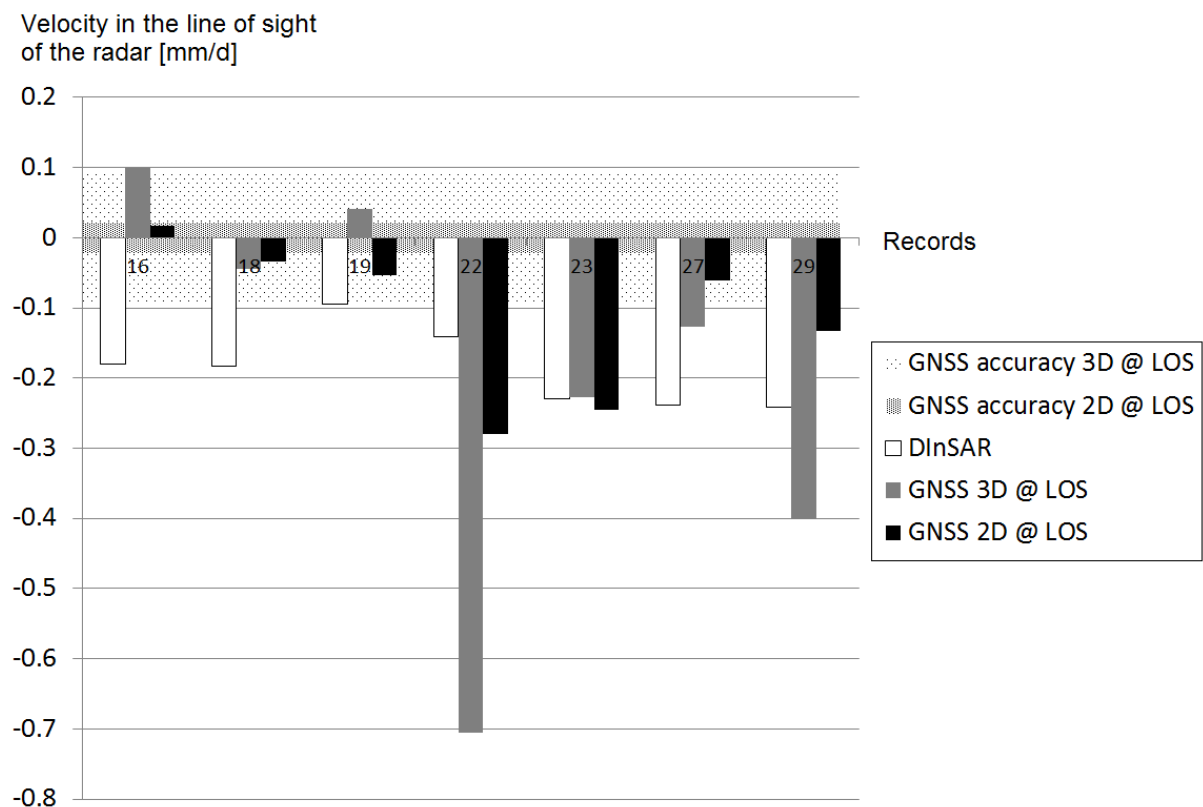
Figure 8: Differences between GNSS displacements projected in the line of sight of the radar and the surrounding DInSAR displacement values; the values are based on the summer monitoring period 2013 (61 days for GNSS and 76 days for DInSAR). Systematic deviations are evident.

Certainly also the DInSAR results show sub-optimal accuracy. This is likely due to the relatively low number of available acquisitions; as a rule of thumb, an accurate SBAS analysis requires 20-25 images – however, for our analyses, a lower number of images was available. Another problematic issue is the uneven distribution of the images over time. Moreover, the analysed deformation phenomena are characterised by fast ground displacements (i.e. in relation to the X-band wavelength) and high spatial (Figure 5) and temporal (Figure 6) heterogeneity. These conditions are not ideal for DInSAR applications and lead to errors in the phase unwrapping, particularly in fast moving areas. Another error source contributing to the deviations between GNSS and DInSAR in Figure 8, is the spatial averaging of the DInSAR displacements over a 15m radius around each GNSS monitoring point. While the GPS value represents the displacement of one point, DInSAR represents the displacement of a large area surrounding this point. However, also GNSS points that are surrounded by homogeneous DInSAR displacement values (Figure 7, e.g. point 18 and 27) show high deviations (Figure 8). Another explanation for the deviations is therefore, that the GNSS single point measurements include small scale surface movements that superimpose the large scale rock glacier creep and disturb the creep signal, especially for short measurement periods (Wirz *et al.*, 2014). These small scale effects e.g. the toppling or subsiding of single rocks are not included in the DInSAR signal that is achieved by the correlation of larger surface patches. An accuracy assessment using single point measurements is therefore only reasonable for a longer monitoring period.

The 3D vector field extrapolated from DInSAR displacement values with the help of the TLS extrapolation mask showed visually plausible results (Figure 9). Unfortunately, large parts of the moving area are not included in the dataset: on the one hand the areas of DInSAR decorrelation and on the other the areas in the TLS shadow. The comparison with the scaled TLS 3D vectors resulted in an MAE of 1.1 cm and a RMSE of 1.5 cm. The highest displacement values within the reference period, i.e. the DInSAR monitoring period of 2013, were around 6cm. We can therefore consider the relative velocity pattern of TLS and DInSAR as significantly coherent.

Figure 9: 3D Vector field extrapolated from DInSAR measurements using a TLS extrapolation mask.

3.5 Discussion

Space-borne DInSAR is an established method to detect and monitor large scale surface displacements or numerous small scale displacements that are distributed over large areas. One aim of this pilot study was to identify an appropriate complementary method for large scale DInSAR data at local scales and for a limited time period to provide 3D movement information of individual mass movements. TLS and GNSS were tested as complementary methods. When comparing TLS and GNSS directly, we found consistent results; the deviations between both were mainly controlled by the measurement precision of the TLS system. Static GNSS showed the higher precision, thus providing the possibility of a higher temporal measurement resolution or rather shorter significant monitoring intervals. When comparing GNSS to DInSAR deviations of different magnitude and algebraic sign occured. Phase unwrapping errors might be one explanation for these devations. As the comparison period of both methods corresponds to time scales of weeks to a couple of months, short term surface movements, which are not captured by DInSAR might also contribute to the deviations. Small scale surface movements of the blocky surface (toppling, subsidence or

41

acceleration of single boulders) induced by the creep process may have distorted the signal of the large scale creep process in the GNSS single point measurements (Wirz *et al.*, 2014). The differing algebraic sign of the deviations supports this second hypothesis. In the short term, the deviations between both measurement systems occasionally reached magnitudes higher than the creep process itself and caused a total misalignment with the DInSAR results. An accuracy analysis of the DInSAR results using GNSS data was difficult due to the unknown origin of these deviations. However these deviations are random and become less significant with increasingly long measurement periods. Therefore the phenomenon was not observed in the comparison of GNSS and TLS, as these results were compared over a much longer time span. The GNSS advantage of high accuracy associated with higher temporal resolution was nevertheless almost invalid. Instead, the weakness of GNSS in relation to TLS became more relevant: this is mainly the very low spatial resolution of the data. It is highly improbable that meaningful conclusions can be drawn from the GNSS displacements mapped in the upper section of Figure 6 regarding the rest of the rock glacier complex. Nevertheless, it is still possible to derive an overview of the seasonal creep velocity signal for the entire site out of the GNSS data by using the spatial redundancy of multiple GNSS monitoring points to filter out the small-scale distortions (lower section of Figure 6).

TLS was the more convincing complementary method to DInSAR in this study. It allowed the creation of an area-wide 3D extrapolation mask for the DInSAR displacements and showed a high degree of relative conformity with them. This is due to the similar procedure of displacement tracking of these methods. Both correlate surface patterns of several square meters to detect movements. In contrast to GNSS measurements, small-scale surface movements were therefore not captured; the movement signal rather represents the movement of the entire rock glacier body instead. Moreover, TLS has the great advantage of being a remote sensing method avoiding time consuming and potentially dangerous work directly on the difficult terrain of the monitored object. However, in contrast to GNSS, TLS fails due to visibility disruptions by cloudage, fog, snow coverage or terrain shadows.

For this study site, space-borne DInSAR measurements did not meet all the expectations of our study. This was mainly due to the loss of SAR image correlation caused by a) the long period of snow coverage and b) the too low frequency of SAR image acquisitions in relation to the rock glacier movement. As both issues are valid for many high alpine mass movement zones, this must be considered as being a characteristic limitation of the method. The long snow period not only prevents the capture of inter-annual deformation time series, it also

lowers the spatial resolution and accuracy of intra-seasonal results. The decorrelation in fast moving terrain parts can theoretically be limited with shorter measurement intervals. However, the planning of data acquisition is subject to restrictions by the provider and this study used the highest temporal resolution available. Our study area is small and not representative for all alpine mass movements. It is therefore likely, that other problems and restrictions may occur when applying this concept to other alpine sites. In particular, shadow effects inherent to the remote techniques TLS and DInSAR might play a much more important role at other sites.

Apart from these limitations, DInSAR delivered reliable and plausible results and was in general suitable for our measurement concept. The common reference frame proved to be stable for all three methods and allowed data comparability. The DInSAR extrapolation mask created using the 3D TLS information allowed a simple 3D projection of the radar data. In contrast to the original DInSAR deformations, these 3D vector fields can be interpreted intuitively and allow a rapid recognition of potentially hazardous accelerations: Depending on the SAR geometry, the raw DInSAR displacements results show sometimes just a small fraction of the actual movement; the movement velocity and so the absolute magnitude of a possible acceleration are strongly underestimated. This can lead to misinterpretations regarding the risk assessment. The 3D extrapolation allows the estimation of the real velocity and acceleration values. Moreover, the comparison with the TLS monitoring results showed that the DInSAR method captured spatial velocity differences with a similar reliability as TLS.

3.6 Conclusions

Summarising, the applied measurement concept is a sufficient way of rationalising the monitoring efforts for selected mass movements. This selection is mainly based on the applicability of spaceborne DInSAR measurements regarding overlay, foreshortening and shadowing as well as the duration of Snow coverage and the continuous availability of SAR images in a sufficient frequency. Furthermore the movement directions of the mass movement have to stay constant and the application of TLS or other terrestrial measurement systems must be feasible. Apart from this limitations the initially defined requirements cost-efficiency, long term monitoring, self-operating mode and large scale application with cm accuracy are fulfilled.

Additionally we can draw the following conclusions:

- Referring to the initially defined requirements, TLS was shown to be the more suitable complementary measurement method for DInSAR. The reasons are the similar tracking method for surface displacements, the high spatial resolution and the efficient remote sensing. It should be noted that there may be different results for other sites.

- On short time scales up to months, GNSS and DInSAR displacement values show large deviations. They are probably the result of small scale surface movements included in the GNSS signal or originate from error sources which could not be identified within this study.

- Space-borne DInSAR showed considerable limitations in alpine terrain due to a short measurement season (long snow coverage), spatially differential creep velocities and complex terrain. This led to spatial and temporal data gaps and a reduced accuracy and spatial resolution.

- Nevertheless, reliable and valid 3D results could be extrapolated from the DInSAR records with the help of a single TLS repeat measurement. These results are easy to interpret and include considerably more information.

- Considering its limitations, a suitable practical application for space-borne DInSAR in combination with a complementary reconnaissance method is the monitoring of extensive, slightly active, long term mass movements that require observation. Furthermore, the area wide acquisition and analysis of DInSAR data allows to detect hitherto unknown mass movements which can then be investigated using the presented monitoring concept to facilitate the early recognition of hazardous areas.

4. Monitoring mass movements using georeferenced time-lapse photography: Ritigraben rock glacier, western Swiss Alps

Robert Kenner[1], Marcia Phillips[1], Philippe Limpach[2], Jan Beutel[3], Martin Hiller[1]

[1] WSL Institute for Snow and Avalanche Research SLF, Davos Switzerland
[2] ETH Zürich, Institute of Geodesy and Photogrammetry
[3] ETH Zürich, Computer Engineering and Networks Laboratory

Personal contributions:

Robert Kenner: Paper concept and realization; Image processing idea and algorithm code; TLS acquisition and processing; Data analysis and discussion

Marcia Phillips: Idea and realization of automatic in situ camera; Scientific assistance

Phillippe Limpach: GNSS Processing

Jan Beutel: Design of the GNSS Sensor

Martin Hiller: Technical support for the automatic camera and data transmission

Abstract

An automatic method was developed to monitor rock glacier kinematics. Displacements derived from monoscopic time-lapse images were scaled and projected into the Swiss Coordinate System CH1903. We tested this method at the front of the rapidly creeping Ritigraben rock glacier, where time-lapse pictures of the rock glacier front were taken by an automatic camera with a temporal resolution of 3 hours. The images were automatically processed using a Matlab algorithm. The output data were spatially resolved creep velocities between successive images and mean relative velocities over time. The digital elevation model used for the projection of the time-lapse data was acquired using terrestrial laser scanning (TLS). The resulting horizontal displacement velocities and accelerations were validated against GPS data measured at one point on the rock glacier front. The high temporal resolution of the time-lapse image velocities provided new insights on the kinematics of the rock glacier front, which could not have been discerned with the GPS or TLS measurements applied. The Ritigraben study site is particularly suitable for our approach due to the temporally constant movement directions. Snow coverage and fog are disturbing factors which can lead to failure of the method.

4.1 Introduction

Potentially hazardous mass movements such as debris flows and rockfall are a major challenge in populated alpine regions (Pradhan and Buchroithner, 2012). The long-term monitoring of such processes is expensive and complicated, especially in inaccessible mountain terrain. In addition, current climate conditions are contributing towards an increase in the displacement velocities of loose rock material in alpine permafrost environments (Kääb et al., 2007; Delaloye et al., 2010a; Kenner et al., 2017a), due to phenomena such as warming permafrost substrates and active layer thickening (Zenklusen Mutter et al., 2010; PERMOS, 2013), combined with intensifying rainfall in summer (Scherrer et al., 2016). This development multiplies monitoring tasks and leads to rising costs and logistic challenges, especially in long alpine valleys with numerous lateral sediment providers such as rock glaciers or moraines. Simple low-cost solutions allowing observation of velocities and changes in the kinematics of mass movements are therefore of great interest for the safety managers of exposed transport lines and settlements.

Monoscopic time-lapse photography has long been established as a simple and effective low-tech monitoring method (Bozzini et al., 2012), and is often used to visualize mass wasting processes (Delaloye et al., 2013; van Herwijnen et al., 2013). Time-lapse photography gives a visual impression of the processes occurring and allows an approximation of process kinematics and their extent. In addition, the timing of events such as rock slope failures or debris flows can be established.

Monoplotting, i.e. the projection of photographs onto a digital terrain model (DTM), is often used to georeference image information for further analysis, e.g. for snow line tracking (Schröter and Buchroithner, 2015) or to establish rock glacier extents (Scapozza et al., 2014). This study presents a combination of time-lapse photography and monoplotting, with the aim to quantify displacement velocities of a moving sediment mass and to determine accelerations or changing velocity patterns. Previous studies mainly focused on stereo image pairs to realize this (Kaufmann, 2012; Neyer et al., 2014; Teng et al., 2017), but a few studies already applied a similar approach to monitor glaciers (Maas et al., 2010) or landslides (Travelletti et al., 2012). We are tracking displacements of an active and potentially hazardous rock glacier front on monoscopic time-lapse images taken by an automatic camera, which are then projected in global coordinates using a monoplotting approach and finally scaled based on a reference measurement with an area-covering 3D measurement system such as terrestrial laser scanning. This procedure was implemented in a fully automatic algorithm and can provide displacement data at a high spatial and temporal

resolution. The results are validated against GPS data from a permanent monitoring station on the rock glacier front.

4.2 Site description

The method presented here was tested on the active, ice-rich Ritigraben rock glacier in the western Swiss Alps above Grächen in Canton Valais (Figure 10). The rock glacier front is located at around 2600 m a.s.l and flows into the upper end of the WNW oriented 30-40° steep Ritigraben gully at a rate of around 2 m per year. Rock fall periodically occurs here and rock debris accumulates in the gully, where debris flows are regularly released. In the 1990s large debris flows also released directly from the rock glacier tongue in the top of the Ritigraben gully, damaging roads and infrastructure below (Lugon and Stoffel, 2010; Stoffel, 2010). The Plattja rock ridge to the south of the gully is stable and there are two steel pylons (Plattja chairlift) at its eastern end, on the edge of the cliff above the Ritigraben gully. The time-lapse camera described below is attached to one of these pylons (Figure 10) and the GPS device is located in the topmost southeastern corner of the gully on a large rock moving with the rock glacier (Figures 10 and 11). The chairlift pylons and cables are visible in the top right part of Figure 11 and the displaced foundation of a former chairlift pylon which was located on the rock glacier is visible near the centre of the photograph (black arrow), giving a first impression of the dynamics of the rock glacier. In the Ritigraben gully the rock glacier surface is very rough and consists of large boulders with a maximum size of a few cubic metres (Figure 11). The deformation velocity patterns and their driving factors are analysed in detail by (Kenner *et al.*, 2017a).
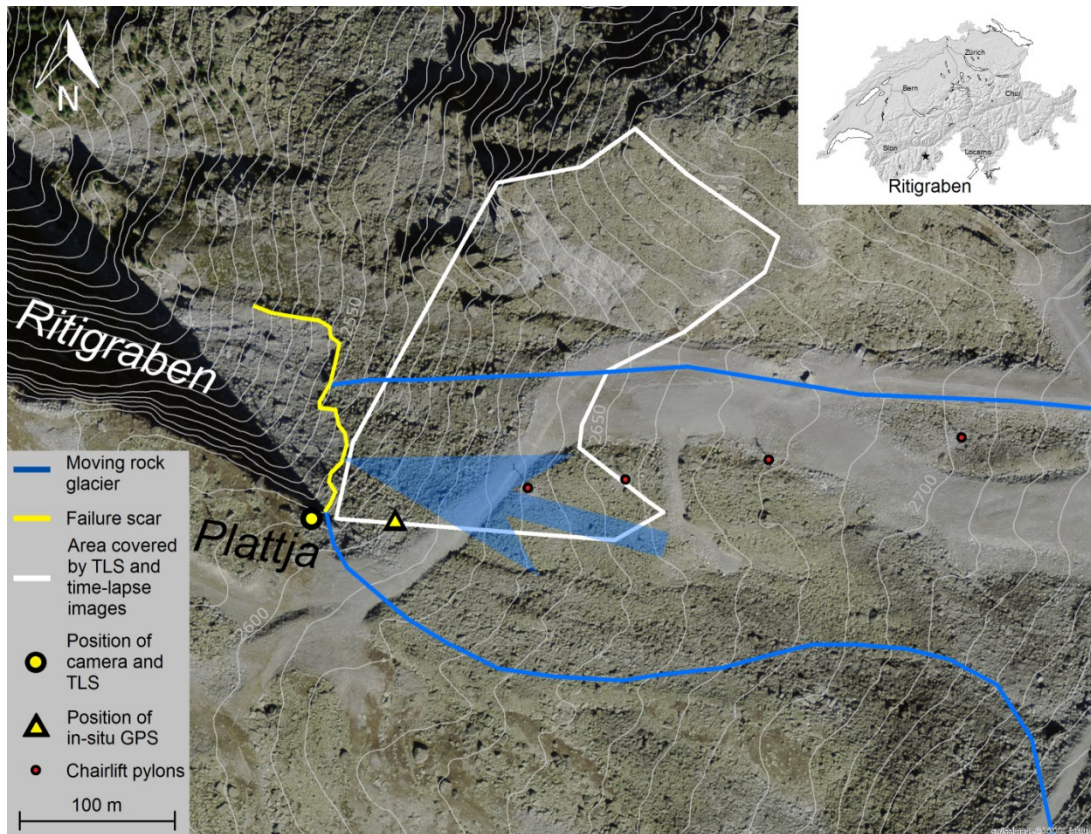
Figure 10: Orthophoto of the front of the Ritigraben rock glacier with the measurement setup. Equidistance: 10m, see legend for more details. Inset: map of Switzerland showing the location of Ritigraben. Swissimage© 2016 swisstopo (DV 033594).
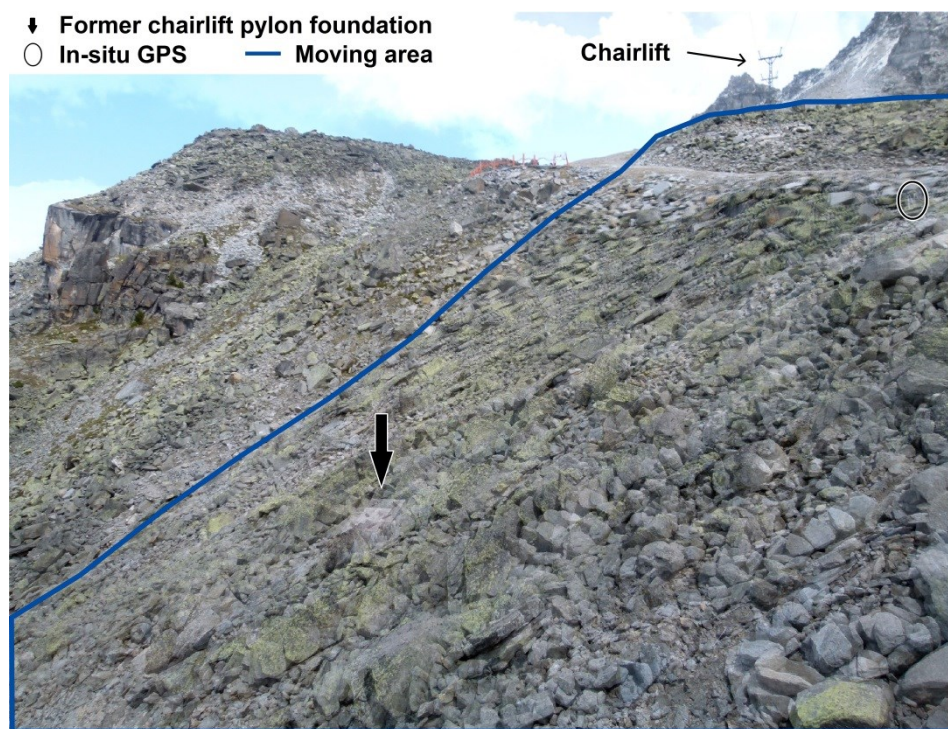
Figure 11: Two overlying time-lapse images of the Ritigraben rock glacier front taken in July and October 2015. The area of movement is outlined in blue. The former chairlift pylon foundation is shown (black vertical arrow), as is the chairlift and the GPS device.

4.3 Methods

4.3.1 Terrestrial laser scanning

Terrestrial laser scanning (TLS) has been carried out once annually at the study site since 2012 (Table 3) to monitor the creep behaviour of the Ritigraben rock glacier. The scans were carried out from the Plattja ridge south of the Ritigraben gully (Figures 10 and 14) using a Riegl VZ6000 long range laser scanner. The resolution of the resulting point clouds was higher than 10 cm and they were transformed into digital elevation models (DEMs) with a 20 cm resolution. Elevation changes were tracked by calculating difference DEMs. To calculate the horizontal component of the creep movement (position displacements), the surface structure was extracted from the DEM using a high pass filter and creep rates were then obtained by matching surface structure patterns as described by Kenner *et al.* (2014). The spatial resolution of these creep rate vector fields was approximately 5 m. Faulty correlations were eliminated by applying a filter kernel to the vector field. This filter algorithm is explained in detail in section 3.3., where it is applied to a vector field obtained from time-lapse photography.

Table 3: Measurement dates

Datasets	Acquisition dates
TLS	12.07.2012; 13.09.2013; 20.08.2014; 11.08.2015
GPS	Since 20.07.2012; Sampling: L1-GPS 30 sec.; 120 sec. inclinometer
Time-lapse photography	Since 03.07.2015; every 3 hours

Figure 12: Photographs of the time-lapse camera on the pylon (left), the terrestrial laser scanner next to the pylon (centre) and the GPS device (right).

4.3.2 Continuous differential L1-GPS

The L1-GPS device used here is a custom built GPS data logger with an integrated two-axis inclinometer, ruggedized for long-term outdoor use (Wirz *et al.*, 2014). It is located on a large boulder of the rock glacier on the orographic left part of the rock glacier front (Figures 10 and 14). The device uses a commodity u-blox LEA-6T L1-GPS receiver, an active Trimble Bullet III antenna, two Murata SCA830-D07 inclinometers and a Sensirion SHT 21 temperature and humidity sensor IC, powered by a 12V solar system (30Wp, 33Ah). All electronics and the antenna are integrated inside the top of a 1 m long fiberglass tube mounted on a steel base. This provides maximum protection, minimizes cabling and elevates the sensitive GPS antenna above the snow cover. The length of the tube increases the radial distance of the GPS antenna from the rotation axis of the block. Tilting of the block can cause significant displacements of the antenna, superimposing the creep signal. These effects can at least partly be corrected by the inclinometer measurements; however the unknown dimensions of the block can cause uncertainties.

The GPS logger is configured for continuous operation with static sampling intervals (Table 3). The logger data is collected annually and fed into a database and post processing toolchain. For double-differencing differential GPS processing a reference position with an identical GPS receiver setup is used. This reference is located at a stable position with a baseline distance of 5.845 km and an elevation difference of 102 m (WGS86: N 46.12350, E 7.82129).

The GPS data is processed with the Bernese GNSS Software (Dach *et al.*, 2007) in a fully automated processing chain. The processing is based on single frequency differential carrier phase techniques. In this context, daily static coordinates are computed.

To calculate velocities from the GPS position data, the coordinate time series was first filtered using a running mean over 10 days, the period we found to be sufficiently long to remove most of the GPS measurement noise. Within the filtered series, velocities were calculated between the first and the last position values of a 10 day window which was moved along the time series with a daily increment.

4.3.3 Automatic calculation of global displacement data from time-lapse photography

A MATLAB algorithm was developed, which calculates translation vector fields (TVF) between subsequent images of a time lapse series, automatically corrects offsets between the photographs, deletes translation vectors with faulty correlations, georeferences the TVF, scales the magnitude of the vectors from image to metric units, reorients the vectors within the global coordinate system, resamples the TVF to a regular grid in the global coordinate system and calculates velocities, velocity time series and accelerations.

Feature tracking between subsequent images

A time-lapse camera (Panasonic Lumix DMC FZ100) was installed on a steel chairlift pylon on the stable Plattja ridge above the southern edge of the upper Ritigraben, opposite the detachment zone of the rock glacier (Figures 10 and 12a). The camera is equipped with a solar panel and takes photographs of the rock glacier front every three hours (Table 1). The images are registered using an eyefi SD card and transmitted via WLAN from the card to a mobile modem (Netmodule router NB1600). They are then transferred to an online server. The orientation of the camera is fixed and all photographs have approximately the same extent (Figure 11). Changes in the structure of the rock glacier front can be tracked automatically using the particle imaging velocimetry method introduced by Roesgen and Totaro (1995). This algorithm correlates small patches of the photographs and calculates translation vectors for image patterns that have moved within the images.

These translation vector fields (TVF) are the basis for the automatic monitoring method introduced in this paper. The TVF were calculated with a resolution of 75 pixels and the correlation window size was 150 x 150 pixels. The translation vectors thus form a regular grid on the image. In their initial state, the TVF refer to image coordinates.

Error correction of the translation vector fields

Slight camera movements caused by thermal influences or wind can lead to distortions in the TVF. There can be orientation changes if the camera moves around one of its axes or positioning changes if the whole camera is relocated. Together with orientation changes, also the radial distortion of individual object points can change. As changes in orientation were very small in our case, this error was not measurable in our setup and neglectable. Additionally, orientation changes lead to image wide constant offsets between subsequent photographs. If the camera moves around the y-axis it leads to a rotation of the image. In

contrast to orientation changes, positioning changes will cause differential distortions in the TVF which are difficult to correct.

Due to the stability of the mounting point, no position errors occurred. Equally, no rotation was evident and is probably uncommon in general, as this would require a torsion of the mounting structure, which is rather unlikely. The main errors affecting our measurements were occasionally occurring offsets, which became apparent via homogeneous and mono-directional TVF over the entire image extent.

We identified offsets between chronologically successive images by defining a reference patch within the images, located in stable rock areas. If translation vectors appear in these areas, they define the vertical and horizontal components of an offset. The whole TVF was therefore corrected using these values.

Another error occurs in parts of the image where patterns change rapidly (e.g. sky, fast rock slides and rockfall). Here the TVF is chaotic and contains mismatches. Faulty correlations were eliminated by applying a 3x3 deleting kernel to the gridded TVF. If the standard deviation of the vector directions within the kernel exceeded 10° (empirically defined value), the central vector was deleted. To restore erroneously deleted values surrounding zones with faulty correlations, a 3x3 dilation was subsequently applied (Kenner *et al.*, 2014).

Georeferencing of the translation vector fields

The georeferencing of the translation vectors was realized by creating a transformation mask based on the 2015 TLS point cloud. The high resolution point cloud (< 10 cm) of the rock glacier front was captured from a position 2 m south of the camera with a similar perspective as that in the time-lapse photographs. To reference the laser scan point cloud on the photographs, reflecting reference points were temporarily installed on the rock glacier: one at the point representing the image centre, one on the left end of the line bisecting the image horizontally and another on the camera box. Using these three points, a Cartesian camera coordinate system was defined with the y-axis originating in the focal point of the camera and going through the image centre, the x-axis running orthogonal to the y-axis and lying in the plane defined by the three reference points and the z-axis perpendicular to x and y (Figure 13).
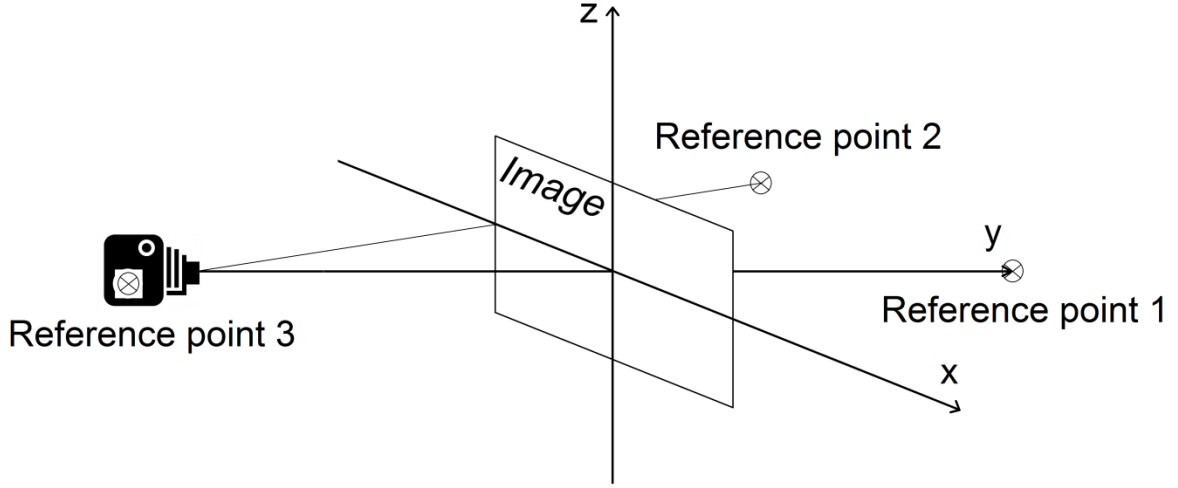
Figure 13: Sketch showing the definition of the camera coordinate system using reflecting control points.

After the point cloud was transformed into Cartesian camera coordinates, a second transformation into image coordinates was applied by calculating a central projection of the point cloud from the position of the camera using:

$$x_i = c \cdot \frac{x_c}{z_c} \cdot s + a$$

$$y_i = c \cdot \frac{y_c}{z_c} \cdot s + a$$

where x_i; y_i are image coordinates, x_c; y_c; z_c are camera coordinates, c is the focal length of the camera, s is the scale factor and a the additional constant between both coordinate systems. After the point cloud was projected onto the images, it was transformed into a 3-band raster dataset with 1/10 of the photo resolution, containing information on the global x, y and z coordinates of the original laser scanning points. If one raster cell contained more than 1 TLS point the coordinate information was averaged, which led to a smoother representation of the surface. Each translation vector was then georeferenced by assigning the global coordinate information from the underlying raster cell to it.

Orientation and scaling of the translation vector fields

Although the TVF were georeferenced now, they still contained displacement values in image units (pixels) and a displacement direction was missing. Thus, further masks for the scaling and orientation of the translation vectors were created. To do this, we compared image-based TVF $A = \overrightarrow{(a_{ij})}$ (in image units) and TLS creep vectors $B = \overrightarrow{(b_{ij})}$ (in global units).

As the measurement periods of both methods differ, B (annual basis) was normalized on A (5 month basis) using the continuous GPS time series:

$$B_{timelapse\_period} = \frac{B_{annual} \cdot \Delta\_GPS_{timelapse\_period}}{\Delta\_GPS_{annual}}$$

Each $\overrightarrow{a_{ij}}$ was then linked to a distance weighted mean value $\vec{b}$ of the $\overrightarrow{b_{ij}}$ surrounding it. The scaling factor for $\overrightarrow{a_{ij}}$, s_{ij}, was simply obtained by $s_{ij} = \frac{|\vec{b}|}{|\overrightarrow{a_{ij}}|}$. The azimuth az_{ij} for $\overrightarrow{a_{ij}}$ was adopted from $\vec{b}$. As a result, we obtained the scaling mask $S = (s_{ij})$ and the azimuth mask $AZ = (az_{ij})$ which allow to attribute each image-based translation vector of any TVF with an individual universally valid scaling factor and azimuth.

The image-based TVF now contained horizontal 2D displacements of the rock glacier surface in metric units; however their spatial resolution was still affected by the central projection of the camera (Figure 14). Therefore the TVF was resampled in a regular grid with a defined spatial resolution of 2.5 m. Vectors in parts of the TVF with originally higher resolutions were merged by weighted averaging.

Calculation of velocity time series

As the algorithm processes any number of chronologically successive images, it not only calculates surface displacements but also velocities, velocity time series and accelerations. The time-lapse between the images is used to calculate mean daily creep velocities for every translation vector. These spatially variable creep velocities are summarized to a mean relative velocity, on the basis of a reference velocity defined by the first two images within the series. Each velocity vector between images i and i+1 is expressed as a fraction of the velocity vector at the same location between images 1 and 2, expressed as a percentage. The spatial mean of these values can be based on a strongly varying number of single vectors, depending on how many have passed the filter algorithm; the number of vectors the mean velocity is based on is therefore outputted, specifying the statistical basement of the mean velocity. The time series of the relative velocity are shown in chart form and the absolute velocities are produced as vector fields in shapefile format. Similar outputs are also available for acceleration values.
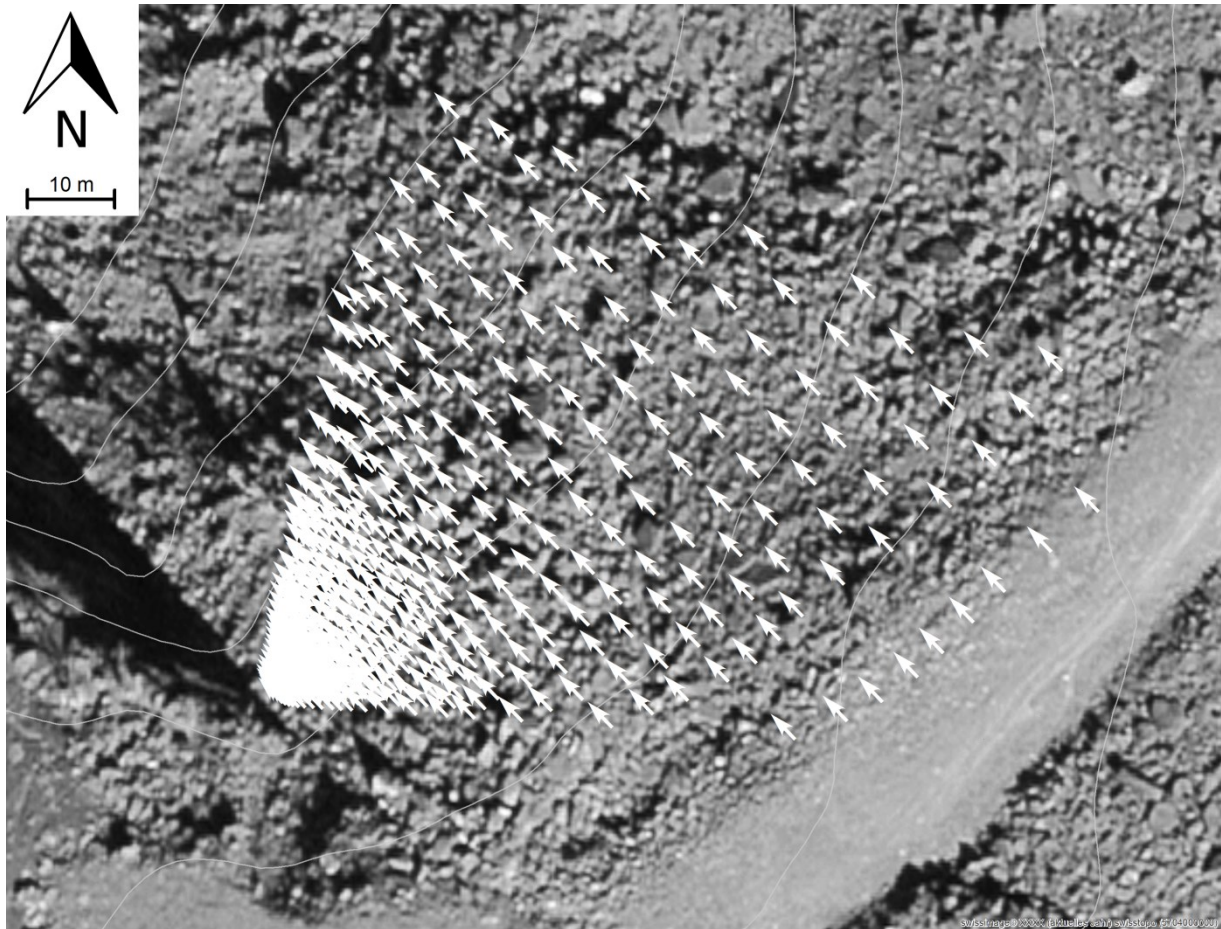
Figure 14: Raw translation vector field prior to resampling and scaling, showing the influence of the central projection on its spatial resolution. Swissimage© 2016 swisstopo (DV 033594).

4.3.4 Accuracy analyses

Sensitivity of the approach to different error sources

The method presented here produces two kind of output, spatially and temporally resolved absolute displacement data and a relative velocity time series. The relative velocity time series is only affected by errors originating from the image quality. This refers to factors such as the stability of the camera frame, the geometry of the photograph (distance and angle to the moving object), the image resolution and the light and contrast conditions in the photograph. The actual accuracy reached here becomes evident in the reproduction of unchanged terrain parts or in the reproducibility of the velocity time series.

The absolute displacement values are affected by more error sources. As they are based on the TLS measurements (basis for the scaling mask), the TLS accuracy is a limiting factor. Additionally, georeferencing errors and the spatial resolution of the scaling mask play a role.

Georeferencing is important to attribute the correct scaling factor from the scaling mask to each translation vector. A high spatial resolution of the scaling mask reduces the error introduced when interpolating the scaling factors surrounding a translation vector. Visual checks of the georeferencing results were carried out by overlaying the images with the projected point cloud used to define the georeferencing mask. A comparison of characteristic objects in the point cloud and the image revealed that the georeferencing error is within the range of a few pixels. This corresponds to less than 10 cm georeferencing error within the movement zone. Considering that the spatial resolution of the scaling mask is 4.75 m, such a small georeferencing error is not very relevant. Also a higher resolution of the scaling mask would have limited benefits: the rock glacier movement is spatially quite homogeneous and except from the boundary zones of the movement there is little change in velocity within a radius of 4.75 m.

Accuracy of TLS and GPS measurements

A comprehensive accuracy analysis for TLS measurements on alpine mass movements was carried out by Kenner *et al.* (2014) for comparable study sites with creeping permafrost features. This study gives a reliable rule of thumb for the accuracy estimation of TLS derived creep vector fields: offsets between the underlying DEMs become evident in homogeneous vector fields outside the moving areas. Provided that there are no such offsets, the smallest deformation vectors remaining after the application of the filter algorithm give a good approximation of the accuracy obtained for the deformation values. Kenner *et al.* (2014) specified that the accuracy commonly reached for TLS derived translation vectors on rock glaciers is around 2-3 cm. In the case of Ritigraben, there is no offset between the scanned DEMs and the smallest remaining vectors are 3 cm.

The daily GPS coordinates are estimated with an error (standard deviation) of approximately 1-2 mm in the horizontal and 2-3 mm in the vertical component. Hence, the accuracy of the GPS method is around one order of magnitude higher than that of TLS and it provides a much higher temporal resolution, however only at a point scale.

Accuracy of the displacement data obtained from time-lapse image processing

The accuracy of the relative creep velocity data obtained with time-lapse photography was analysed by comparing relative velocity time series of two image time series within the same monitoring period (3.7.2015 to 19.11.2015). Both time series consisted of images with an approximately weekly resolution but the acquisition time of the individual photographs differed by a few hours, yet by less than 24 hours. Only the first two images of both data

series were identical, as they define the reference velocity (100%) for the subsequent relative velocity values. Data from both time series was treated as being comparable, although the acquisition time differed slightly. The root mean square error (RMSE) between both velocity time series was calculated to quantify the internal robustness of the method, i.e. the reproducibility of the results. Using this procedure the effects of different lighting conditions or small movements of the camera (e.g. induced by vibrations of the pylon) within the time series could be analysed.

We also compared the image-based velocity time series with the GPS-based one. The relative velocities from time-lapse images were transformed into absolute velocities by fixing the initial relative velocity (100%) between the first two images to the absolute velocity value obtained by the GPS measurements during the same period. All subsequent relative velocities in the time series were transformed by referring to this initial absolute velocity. Apart from the initial value, the further progression of the image-based absolute velocity time series is therefore independent from the GPS time series.

4.4 Results and Discussion

The TLS measurements show an unchanged geometry of the rock glacier body with constant movement directions during the period 2012 to 2015. A detailed analysis of the rock glacier deformation velocity can be found in (Kenner *et al.*, 2017a).

Two synchronous time series of the relative velocity based on different images with varying lighting conditions (different shadow patterns, cloud cover) showed a high degree of consistency (Figure 15). The RMSE between them is 5.6 % relative velocity, referring to an initial absolute velocity (mean velocity between the first two images) of 4.0 mm/day. This good reproducibility implies a high level of robustness despite different lighting conditions or small changes in the camera orientation. Travelletti *et al.* (2012), who monitored a landslide with a similar method reported larger influences by these factors. This might be caused by longer measurement ranges and a less clearly defined surface structure. However, also our offset correction and the different way of filtering the vector fields probably reduced these error influences here.
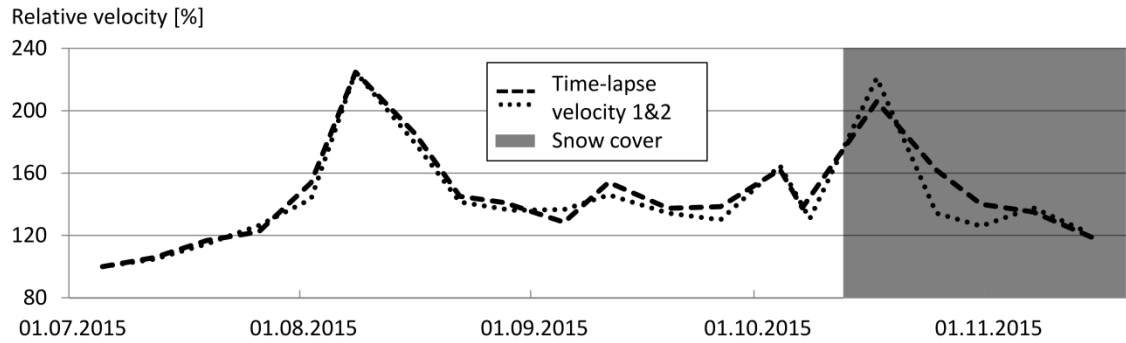
Relative velocity [%]

Figure 15: Rock glacier velocities derived from 2 differential time-lapse image series.

When compared to the GPS measurements, the velocities based on time-lapse images are reasonable and show similar magnitudes. Figure 16 displays the spatial mean of the relative velocity of the rock glacier front for the complete time-lapse data series acquired in summer 2015, supplemented by GPS velocities. Both velocity charts show a similar overall progression but velocity variations at time scales of days to one week are not reflected in the GPS time series (Figure 16). This is caused by methodical differences: The time-lapse method has a fixed level of significance for which surface displacements can be tracked. This level of significance is independent from the length of the time-lapse between the images. Hence, short term accelerations can be tracked at any temporal resolution if the velocity is high enough. In contrast, L1 GPS measurements rely on redundancy to reach their full potential in accuracy. This implies a limitation for the temporal resolution of significant GPS velocities, as measurements over a certain time period have to be integrated to obtain the required redundancy. Generally it is difficult to differentiate between short term accelerations and GPS measurement errors (Wirz *et al.*, 2014) and the definition of the optimal temporal resolution for GPS based velocity time series is therefore challenging. Our GPS velocities are derived with a temporal resolution of 10 days and are additionally smoothed by a running mean. Velocity maxima of short term accelerations are therefore smaller or absent in the GPS time series compared to the time-lapse image based velocities. These systematic differences became evident in particular between August 9th and 10th 2015. In this short period the rock glacier front accelerated 16-fold, as is clearly shown by the time-lapse velocity chart (Figure 16, inset) and is visible to the naked eye in the images. This velocity peak is however strongly smoothed in the GPS velocity data.

An additional difference between the GPS and image based velocities becomes evident in the mean seasonal displacement values. The seasonal acceleration of the rock glacier (Kenner *et al.*, 2017a), which can be particularly well distinguished in July and at the

beginning of August (Figure 16), is less pronounced in the GPS velocity values than in the image based ones. This might be caused by the spatial resolution of the datasets. While the image based velocity time series is calculated over the whole rock glacier front, the GPS time series is based on a point measurement. The GPS sensor is located in a relatively slow sector of the rock glacier front, which probably shows more homogeneous velocities than most of the other parts captured by the time-lapse camera.
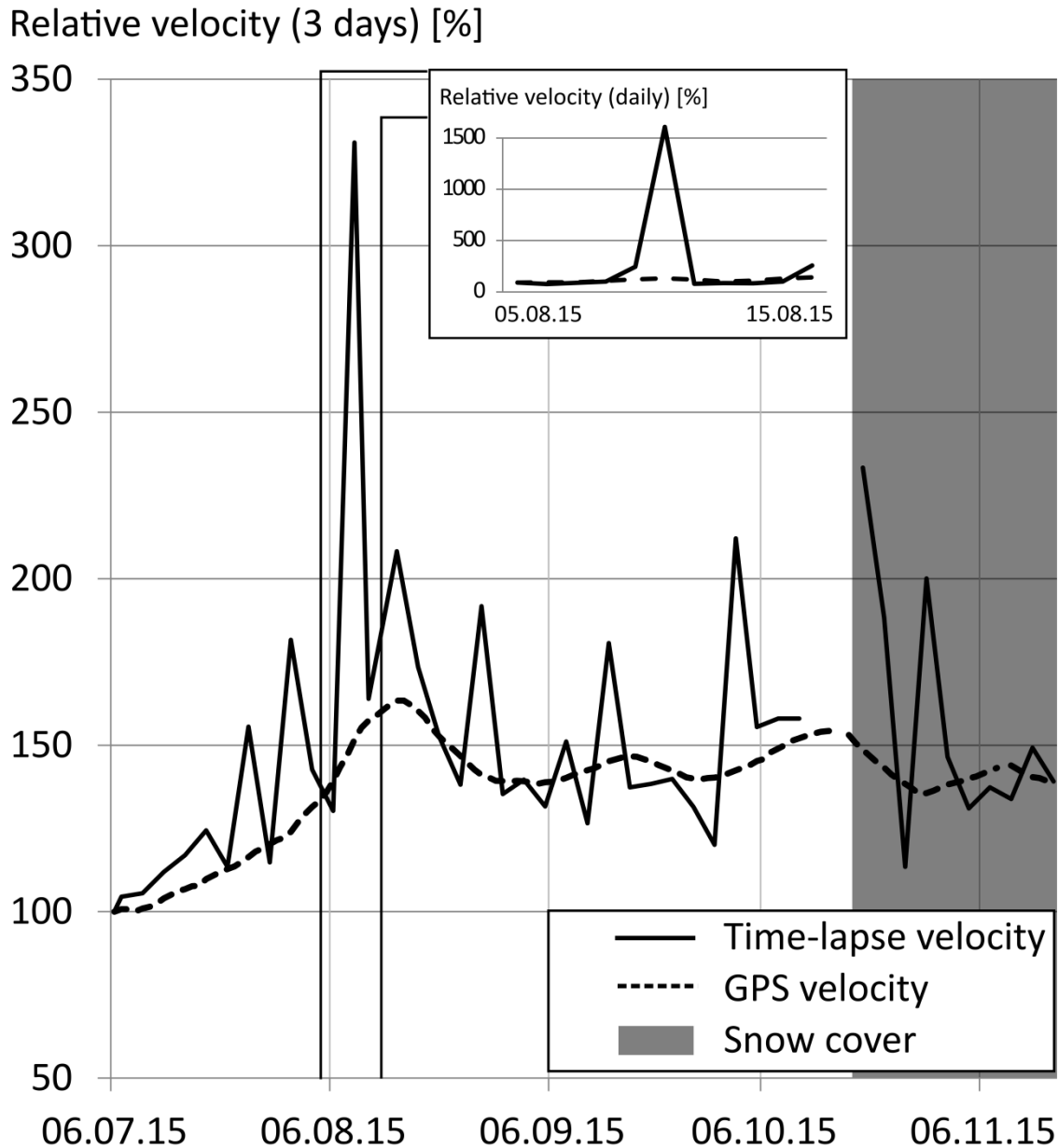

Figure 16: Comparison of creep velocities derived from GPS and time-lapse photography with a 3 day temporal resolution. The inset contains a close up of the period 05.-15.08.2015 with daily resolution, showing a strong acceleration between 9 and 10 August.

Generally, moderate deviations between both systems show that the time-lapse algorithm produced reasonable velocities, even during a period with a slowly melting, thin snow cover of around 20 cm in autumn 2015 (Figure 16). However, problems occurred when calculating velocities between images with large differences in snow cover, e.g. the differences before and after a snowfall (time-lapse data gap in Figure 16). Equally, a thick snow cover covering most of the boulders in the moving zone leads to failure of the time-lapse image method. Surface tracking of images from subsequent summer periods were not possible, as the surface structure moved to strong during the winter. However, images acquired with a time lag of several weeks could be processed. This might not be possible for sites with stronger surface changes (Travelletti *et al.*, 2012).

Figure 17 shows the absolute velocities at the rock glacier front for 8 periods of around 7 days between 10.07.2015 and 02.09.2015. The spatially varying velocity patterns over the rock glacier front become evident. For example, in Figure 17a, the fastest movements occur directly at the failure scar, whilst in Figure 17h, the fastest zone is in the upper part of the rock glacier front. Such high-frequency measurements are not feasible using manual measurement campaigns. The different extents of the TVF in Figure 17 have methodical reasons. In the upper part of the rock glacier front the angle of projection of the terrain in the images is glancing, so creep velocities can only be determined during periods with high overall displacements here (e.g. Figure 17e). Due to the varying extent of the TVF, it is important to calculate the relative velocity on the basis of single vectors and not on the basis of an overall mean velocity.

A further benefit of the time-lapse image monitoring method is that the images are accessible online and the processing can be carried out in near real time. The method therefore has the potential to be applied for early-warning purposes. In addition to displacement data, the images provide visual information on the movement process, on rapid mass movements like rockfall or slides and on environmental conditions such as weather or snow coverage.

The main limitations of the time-lapse method are induced by the requirement that the creep directions and the geometry of the mass wasting area remain approximately constant, as fixed azimuths and georeferencing masks are used. This is certainly the case on the rapidly creeping rock glacier front in the steep and narrow Ritigraben gully. However it is not necessarily the case for other mass movements.
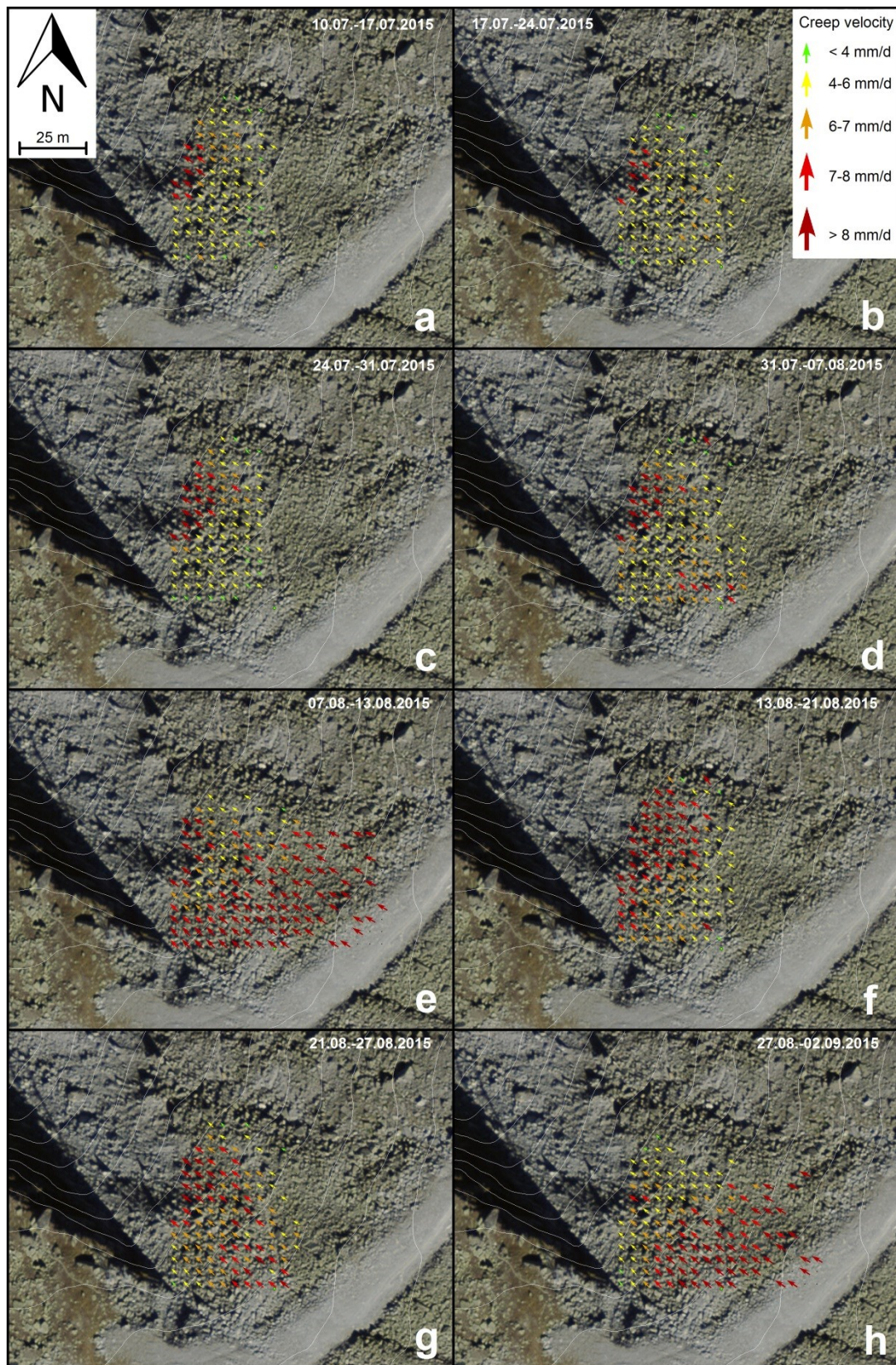
Figure 17: Spatial velocity distribution for selected 7 day periods in summer 2015 (July 10 to September 9 2015). Swissimage© 2016 swisstopo (DV 033594).

4.5 Conclusions

Time-lapse photography has proved to be a reliable monitoring system for an alpine mass movement with temporally uniform movement directions and limited changes in overall geometry. Once calibrated by a 3D measurement such as TLS, time-lapse photography provides highly resolved temporal and spatial information on the absolute and relative velocities of the mass movement. This information is useful to determine local or overall accelerations of the moving mass, which often point towards the preparatory phase of a rockfall or debris flow event. For individual cases, time-lapse photography monitoring can therefore be suitable to substitute other, more expensive long-term monitoring systems. We conclude that:

- Displacement vectors derived from time-lapse images can be successfully georeferenced, scaled and oriented using displacement data from a reference period acquired with a 3D measurement system such as terrestrial laser scanning.

- After calibration, time-lapse image monitoring functions independently.

- The complete processing of the time-lapse images can be automated in near real time, with vector shapefiles and velocity time charts as output data.

- Time-lapse image monitoring provides significant velocity data at a very high temporal resolution and captures short term accelerations that are not registered to this extent by permanent GPS measurements.

- Ideally, the camera orientation should be orthogonal to the moving surface to avoid shadow effects and glancing intersections

- At the Ritigraben site, different lighting conditions do not substantially influence the results of the time-lapse monitoring.

- Strong changes in snow coverage lead to failure of the method, whilst a thin and constant snow cover has little influence.

- The visual impression of the images complements the automatic displacement values with information on fast movements not captured by the algorithm and also allows observation of weather/snow conditions.

Acknowledgements

Part two

Genesis and factors influencing ice-rich mountain permafrost

Rock fall on a snow covered rock glacier at Parpaner Weisshorn, Tschiertschen-Praden (eastern Swiss Alps), 02.12.2016 (Photo: T. Meissen).

5. Estimating the effect of different influencing factors on rock glacier development in two regions in the Swiss Alps

R. Kenner[1], J. Magnusson [1,2]

[1] WSL Institute for Snow and Avalanche Research SLF, Davos Dorf, Switzerland
[2] Norwegian Water Resources and Energy Directorate (NVE), Oslo, Norway

Personal contributions:

Robert Kenner: All aspects of the study and the paper, except the calculation of the wind sheltering index

Jan Magnusson: Calculation of the wind sheltering index

Abstract

To elucidate the factors that influence rock glacier distribution, we created a rock glacier inventory for two regions in the Swiss Alps (the Albula Alps and the Glarner Alps) and identified their spatial characteristics by adding topographical and meteorological data to a GIS. We evaluated the influence of mean annual precipitation (MAP), mean annual air temperature, head wall erosion, glacier coverage, lithology, slope, aspect, elevation and snow cover on rock glacier occurrence and characteristics, taking into account the interactions between these factors. MAP, lithology and head wall erosion significantly influenced rock glacier distribution, and the interaction of precipitation and lithology seemed to play a key role. Wind-driven snow redistribution influenced rock glacier frequency on hillslopes with different aspects. Rock glaciers interact with all of the factors analysed and exhibit complex relations with their regional environments.

5.1 Introduction

The origin and development of excess ice in rock glaciers are important issues of mountain permafrost research. Explanations range from ice segregation in fine material to burial of surface snow and ice by rock fall material and integration of glacier ice (Haeberli and Vonder Mühll, 1996; Clark et al., 1998; Berthling, 2011). Although all of these processes may contribute to rock glacier genesis (Haeberli *et al.*, 2006), rock glacier development and the influence of external factors are still poorly understood. For example, the maximum values of mean annual air temperature (MAAT) that preserve permafrost in rock glaciers and talus slopes vary, depending on the study site and landform (Chueca, 1992; Payne, 1998; Marchenko, 2001). Consequently, additional factors may influence rock glacier genesis and spatial distribution, such as topography, lithology or aspect (Johnson et al., 2007). Elevation changes in rock glacier distribution through time have been commonly attributed to changes in MAAT (Haeberli, 1983; Chueca, 1992; Payne, 1998; Sailer and Kerschner, 1999; Frauenfelder and Kääb, 2000; Frauenfelder *et al.*, 2001). These studies have deduced a long-term MAAT signal from the elevation distribution of active and relict rock glacier fronts, which raises the question as to whether the elevation pattern of rock glacier fronts over time is in fact controlled by air temperature only. Because rock glaciers may develop over thousands of years (Haeberli et al., 1998), their response periods are probably much longer than existing observation records of influencing factors, which themselves show large temporal variations. This is why the long-term effects of temporally variable influencing factors on rock glacier development remain insufficiently understood.

The aim of this study is to identify the influence of different environmental factors on the characteristics, frequency and spatial distribution of rock glaciers in two regions of the Swiss Alps. We hypothesised that the heterogeneous development of rock glaciers in different regions represents the long-term effect of spatially variable influencing factors. We used a GIS-based approach that seeks spatial correlation between rock glacier occurrence, size, state and morphology with environmental parameters identified in the literature. The Swiss Alps are an optimal study site for this approach as they provide heterogeneous external conditions over small areas. First, we present the GIS and make some theoretical pre-considerations, before we analyse the effect of the individual factors on rock glaciers.

5.2 Composition and characteristics of the GIS

5.2.1 Influencing factors

We initially defined the factors that may influence the development of rock glaciers, based on the literature (Morris, 1981; Ikeda and Matsuoka, 2006; Johnson *et al.*, 2007; Frauenfelder *et al.,* 2008). Then we grouped them into temporally variable factors (head wall erosion rate, glacier coverage, MAAT, mean annual precipitation (MAP), snow cover) and temporally stable factors (elevation, aspect, slope and lithology (sedimentary rock vs metamorphic/crystalline rock)). The timescale considered here for the attribute stability is the Holocene Epoch.

5.2.2 Influencing factor proxies

Two indirect indicators (proxies) of influencing factors are noted: aspect and elevation. This means that the distribution of rock glaciers depends on another factor that is highly correlated with the obvious one. The dependency on aspect results mainly from the variable duration and intensity of solar radiation upon different aspects. Aspect is therefore used as a proxy for insolation because: (1) the distribution of rock glaciers according to aspect has been analysed in several studies of Swiss rock glaciers (Gruber and Hoelzle, 2001; Nyenhuis *et al.*, 2005; Noetzli *et al.*, 2007).; (2) aspect is easier to interpret and to categorise than solar radiation values; and (3) potential insolation energy specifications as provided by GIS analysis tools give a false accuracy. They depend, for example, on unknown variables like cloud coverage, which often differs between morning and afternoon (Stubenrauch *et al.*, 2012), which in turn disturbs the spatial solar radiation balance and the absolute insolation values. Factors like slope and shadow effects that are not considered by aspect are randomly distributed and neglected due to the high number of rock glacier records.

The dependency of rock glacier distribution on elevation results mainly from its dependency on air temperature. We used elevation data as a temperature proxy since they have a much higher resolution than the MeteoSwiss MAAT grid data (Table 4).

5.2.3 Study regions

Two study regions were chosen in the Swiss Alps: the Glarner Alps and the Albula Alps (Figure 18). The Glarner Alps are part of the Alpine North Slope and are characterised by a high precipitation regime. The central and eastern parts of this mountain range consist of sedimentary rock, whereas metamorphic/crystalline rock occurs in the western parts. The Albula Alps represent an inner alpine region with a relatively continental climate. The majority of the Albula Alps consists of metamorphic or crystalline rock, and the southern and western parts of sedimentary rock (see Figure 19).
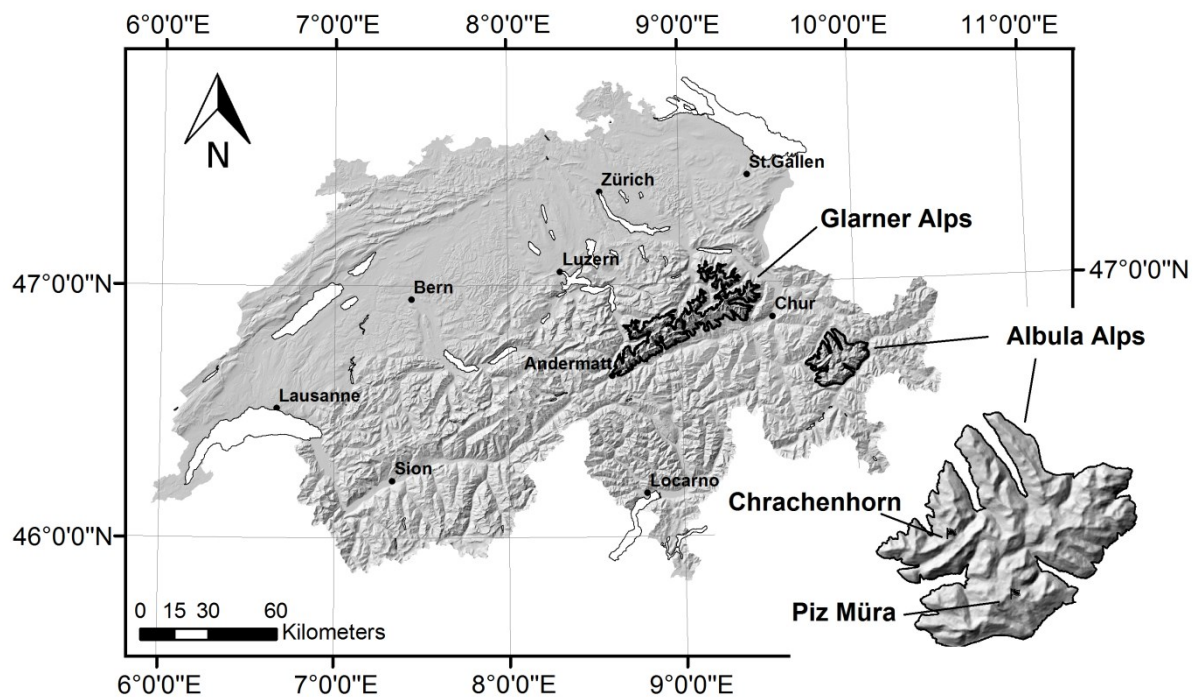
Figure 18: Location map of the study sites: the Glarner Alps and the Albula Alps in Switzerland. Inset shows the location of two wind measurement stations (Chrachenhorn and Piz Müra) in the Albula Alps.

5.2.4 GIS data input

The sources of topographical, meteorological and land cover data used for the GIS analysis are given in Table 4. Additional data were derived manually from the Swissimage orthophotographs provided by Swisstopo (Table 4). Study areas were first delimited by the surrounding valley bottoms. Regions below 2000 m asl were excluded to obtain a similar distribution of elevation between the study regions.

Rock glaciers were defined with polygons identifying clearly visible creeping features on the orthophotographs (e.g. transverse or longitudinal ridges and furrows, and steep front or side walls). Rock glaciers were divided into 'relict' and 'active' categories by analysing the rock

71

glacier morphology and vegetation cover. Relict ones were identified where vegetation cover was evident, in particular at their fronts and at the front of creeping lobes superimposed on the rock glacier body. Analysis of infrared aerial images aided identification of vegetation. Relict rock glaciers also showed rounded, eroded creep forms with signs of subsidence. The transition from active to relict rock glacier state is not sharply defined and a long period of inactivity probably separates them (Barsch, 1996). However, remote sensing methods cannot distinguish between relict and inactive rock glaciers still containing ice. Hence, we include inactive rock glaciers in the category of relict rock glaciers. In the case of relict rock glaciers with superimposed active rock glaciers in the upper parts, the extent of the active rock glacier was included in the area of the relict one.
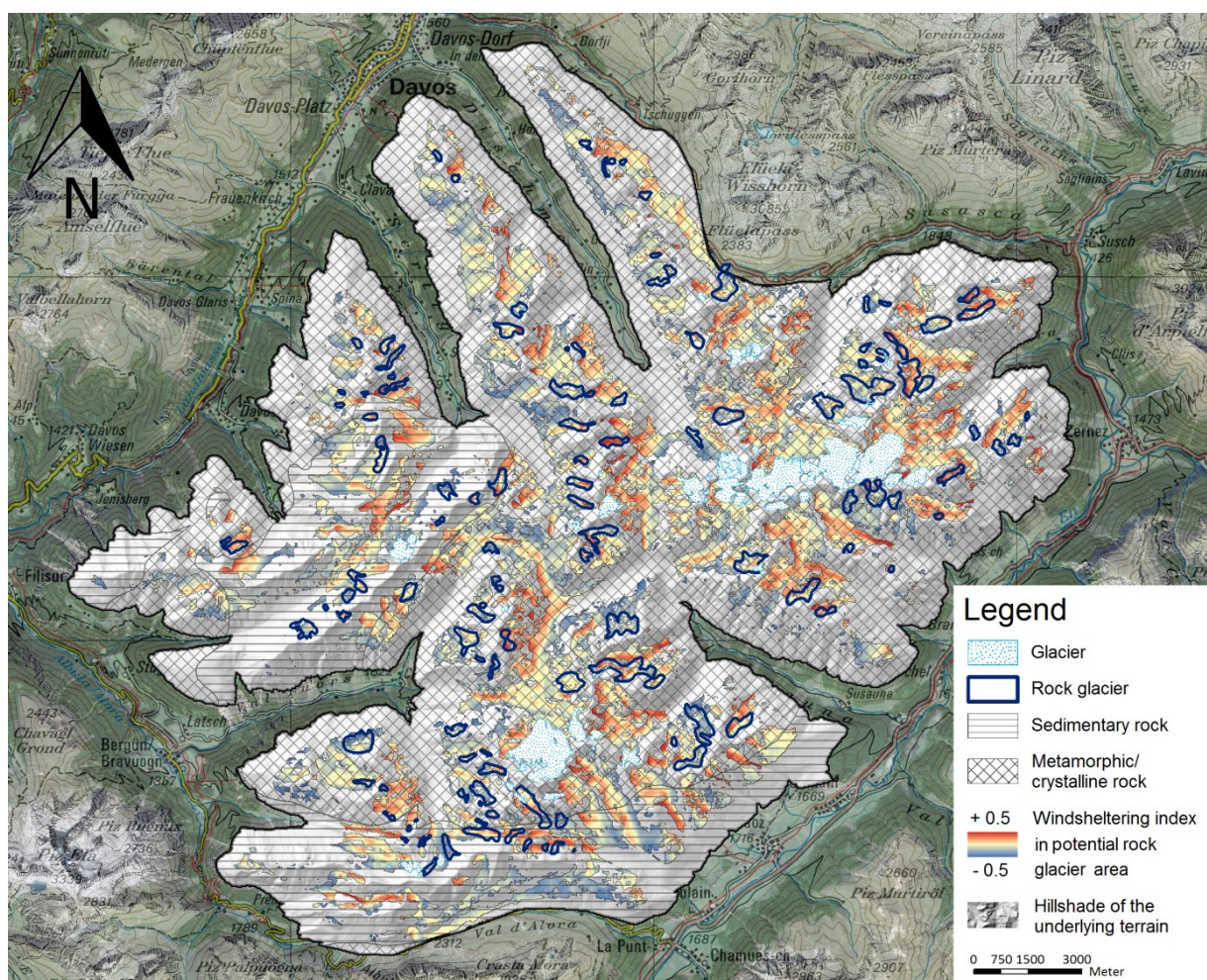
Figure 19: Rock glacier distribution in the Albula Alps. The area currently occupied by glaciers and the distribution of the lithology classes are indicated. For the potential rock glacier area (see Fig. 20), the wind sheltering indices are shown in the background. In areas unfavourable for rock glaciers, the background is mapped as grey hillshade. Swissimage© 2014 swisstopo (DV 033594), DTM-AV DOM-AV © 2015 Eidg. Vermessungsdirektion (DV033531).

Table 4: Datasets used for the GIS analysis.

Data Layer	Description	Provider / Reference
SWISSIMAGE	Orthophoto with 50 cm resolution	Swisstopo (Loup, 2008)
DEM25	Digital elevation model with 25 m resolution	Swisstopo (Swisstopo, 2005)
Aspect from DEM25	Aspect grid created from the DEM25	-
Slope from DEM25	Slope grid created from the DEM25	-
VECTOR25	Vector dataset of land cover	Swisstopo (Swisstopo, 2007)
GeoCover	Vectorized Geological map of Switzerland	Swisstopo
Norm Precipitation Grid	Mean annual precipitation from 1961 to 1990 with 2 km resolution	MeteoSwiss
Norm Temperature Grid	Mean annual air temperature from 1961 to 1990 with 2 km resolution	MeteoSwiss (Begert *et al.*, 2003)
Global radiation of mountain weather stations	Weather stations: Pilatus; Piz Martegnas; Crap Masegn; Col du grand St. Bernard; Motta Naluns	MeteoSwiss

Because it was impracticable to estimate the volumes of every rock glacier record in this study, we used the two-dimensional (2D) rock glacier area (projected on the Swiss coordinate grid) as a proxy for the relative size of rock glaciers. The total number of rock glaciers in the study areas is 239, including 75 relict rock glaciers in the Albula Alps (see Table 6).

The head wall (i.e. the rock wall which supplies rock material to the rock glacier) was defined as the area lying in the slope line directly above the rock glacier and having a slope angle of at least 40°. Talus slopes reach maximum angles of around 40° and rock movements above this threshold result in rock fall or rock avalanches (Carson, 1977) which can cover snow patches. The area of the head walls was defined in three dimensions (3D).

5.2.5 Correlations between influencing factors

Correlations between the influencing factors (e.g. MAP and elevation) can lead to ambiguities in their analysis. The very different spatial resolution of the input data-sets (Table 4) hinders the interpretation of correlation coefficients. We therefore focus on citing established relations between influencing factors and discuss their relevance for the study:

The dependency of MAAT on elevation is described by the lapse rate. We used elevation as a proxy for MAAT.

MAP also depends on elevation. At elevations between 2000 and 3000 m asl, MAP increases with elevation (Brutsaert, 2005). This relation is not relevant for the analysis because (1) rock glaciers tend to occur in continental environments in the Alps, and (2) high MAP values are unfavourable for rock glacier development (Barsch, 1996; Dramis *et al.*, 2003). MAP increases with elevation and can therefore control the upper elevational border for rock glaciers (e.g. by glaciation). MAAT, however, decreases with increasing elevation and will therefore influence the lower elevational border for rock glaciers.

Snow cover distribution is only analysed at local scales in this study. An unproven but possible dependency of snow cover and aspect is considered as critical. All other combinations are treated as having no relevant dependencies for this study.

5.2.6 Distribution and frequency of influencing factor characteristics

The characteristics of influencing factors are defined as specifications or specification intervals of an influencing factor (e.g. W-N sector for aspect / 2000–2100 m asl for elevation). The spatial distribution and frequency of these characteristics can be influenced by many complex sources. They can therefore differ between two regions (e.g. the frequency of occurrence of W-N slopes differs between the Albula Alps and the Glarner Alps) and between two specifications of another factor (e.g. the distribution of snow differs for individual aspect sectors).

Unequal distributions of influencing factor characteristics can falsify the analysis of the influence of individual factors on rock glaciers. Hence, unequally distributed influencing factors must be detected and normalised before analysis. This problem mainly concerns the distribution of factors of high spatial variability (i.e. MAAT, elevation, aspect, slope, glacier coverage) within one specification of factors of low spatial variability (i.e. regions with different precipitation regimes and lithologies). Therefore, these distributions were calculated for all factors that were spatially highly variable. For example, the frequency of occurrence of W-N, N-E, E-S and S-W slopes was calculated for both the Glarner and the Albula Alps. The frequencies were compared between both regions and categorised as being equally or unequally distributed. The frequencies of specifications of an equally distributed factor differ by less than 5 per cent of the basic population (e.g. all aspects). Head wall erosion was omitted in this test, as its effect on rock glacier distribution was analysed in a special way.

As specified in Table 5, the characteristics of all factors are equally distributed between the lithology classes of one region, and therefore do not influence the effect of lithology. However, all factor characteristics except MAAT and slopes below 30° are unequally distributed between the regions and must be treated carefully.

Table 5. Distributions of influencing factor characteristics (ED – equal distribution, UD – unequal distribution).

	MAP	**MAAT**	**Elevation**	**Aspect**	**Slope < 30°**	**Snow cover**	**Glacier coverage**
Lithology	ED	ED	ED	ED	ED	ED	ED
Region	UD (tab. 6, li.9)	ED	UD (tab. 6, li.12)	UD (tab. 6, li. 24-27)	ED (tab. 6, li. 31)	UD	UD

5.3 Analysis of influencing factors

Two basic concepts are used to analyse the influence of individual factors on rock glaciers. First, we analysed rock glacier characteristics in two environments that differ by only one influencing factor. However, there are cases where at least one other influencing factor also varies. Second, we defined a potential rock glacier area that is reduced in a stepwise manner by factors adverse to rock glacier occurrence, such as glaciation. Using this area as a basic unit for defining rock glacier frequency, the effect (e.g. of glacier coverage or steep slopes) can be excluded from the following analysis of other influencing factors.

The results of the GIS analysis are summarised in Table 6 and schematically illustrated in Figure 20, to facilitate understanding of the workflow.

Table 6. Results of the GIS analysis. PRGA = Potential rock glacier area; MAAT = mean annual air temperature.

Line		Garner Alps	Glarner Alps metam./cryst. rock	Glarner Alps sedimentary rock	Albula Alps	Albula Alps metam./cryst. rock	Albula Alps sedimentary rock	Albula Alps relict rock glaciers
1	Total area [km2] Albula > 2000 m a.s.l./Glarner Alps > 2000 m a.s.l	715.8	189.4	526.5	361.0	275.9	85.1	361.0
2	PRGA: Slope < 30° and no glacier and Albula > 2300 m a.s.l. / Glarner Alps > 2100 m a.s.l. and "no convexity" [% total area]	16.7	20.1	15.7	31.9	33.5	26.6	-
3	Number of rock glaciers	40	29	11	124	101	23	75
4	Rock glacier surface (absolute) [km^2]	2.1	1.7	0.3	13.6	11.8	1.8	14.1
5	Rock glacier surface (relative to PRGA) [%]	1.7	4.5	0.4	11.7	12.8	8.0	3.9
6	Mean size of rock glaciers [m^2]	53'500	64'400	24'900	109'300	116'700	76'600	188'100
7	Largest rock glacier [m^2]	185'701	185'701	53'912	658'859	658'859	216'212	975'709
8	Rock glacier surface relative to head wall [%]				130			175
9	Mean annual precipitation [mm]	1764	1677	1783	950	961	904	-
10	Mean annual precipitation rock glacier [mm]	1720	-	-	971	-	-	-
11	Spatial average of MAAT (normalized by elevation) [°C]	1.9	-	-	0.7 (1.4)	-	-	-
12	Mean elevation of the region [m a.s.l.]	2380	2409	2370	2482	2490	2456	2482
13	Elevational belt of rock glaciers (mean) [m a.s.l.]	2030-2780 (2500)	2180-2780 (2540)	2030-2720 (2260)	2260-3110 (2650)	2260-3110 (2650)	2350-2920 (2640)	2070-2910 (2456)
14	Elevational belt of rock glaciers S-Aspect (mean) [m a.s.l.]	2030-2780 (2560)	-	-	2319-3110 (2747)	-	-	-
15	Elevational belt of rock glaciers N-Aspect (mean) [m a.s.l.]	2050-2760 (2465)	-	-	2260-3030 (2620)	-	-	-
16	Rock glacier area in aspect W-N [% of total rock glacier area]	29	-	-	46	-	-	-
17	Rock glacier area in aspect N-E [% of total rock glacier area]	14	-	-	29	-	-	-
18	Rock glacier area in aspect E-S [% of total rock glacier area]	36	-	-	10	-	-	-
19	Rock glacier area in aspect S-W [% of total rock glacier area]	21	-	-	14	-	-	-
20	Rock glacier area in aspect W-N [% of PRGA in W-N]	1.3	-	-	15.6	-	-	-
21	Rock glacier area in aspect N-E [% of PRGA in N-E]	0.5	-	-	9.6	-	-	-
22	Rock glacier area in aspect E-S [% of PRGA in E-S]	0.6	-	-	3.5	-	-	-
23	Rock glacier area in aspect S-W [% of PRGA in S-W]	0.6	-	-	5.1	-	-	-
24	PRGA in aspect W-N [% of line 2]	15	-	-	25	-	-	-
25	PRGA in aspect N-E [% of line 2]	20	-	-	26	-	-	-
26	PRGA in aspect E-S [% of line 2]	40	-	-	25	-	-	-
27	PRGA in aspect S-W [% of line 2]	25	-	-	24	-	-	-
28	Glacier surface [km^2] (% total area)	62.8 (17.4)	-	-	8.6 (1.2)	-	-	-
29	Glacier surface [% (km^2) of PRGA incl. glacier]	13 (30.8)	-	-	5 (7.4)	-	-	-
30	Slope of 95% of rock glacier surface without front/side walls and without scree slope below the head wall (mean) [°]	0 - 27 (18)	0 - 27 (18)	0 - 27 (18)	0 - 28 (18)	0 - 28 (18)	0 - 28 (18)	-
31	Slopes <30°/30°-40°/>40° [% of total area line 1]		53/25/22			55/32/13		
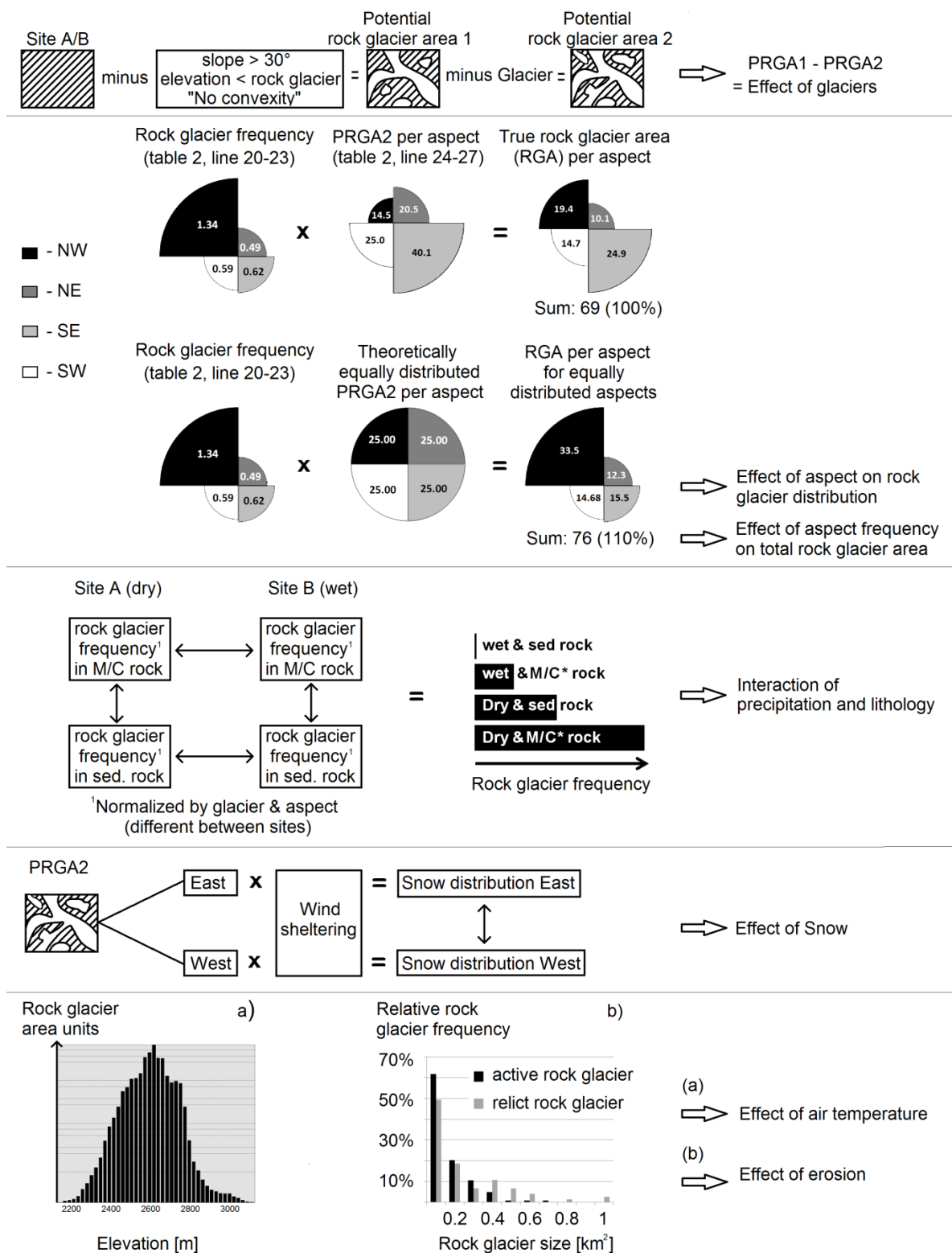
Figure 20: Rock glacier surface distribution and aspect in the Glarner Alps. (a) Definition of the potential rock glacier area (PRGA) and the effect of glacier coverage. (b) Relation between rock glacier frequency, PRGA and true rock glacier area (RGA) (measured). (c) True RGA for an equally distributed PRGA according to aspect. (d) Definition of the effect of mean annual precipitation in metamorphic/crystalline (M/C) rock and sedimentary (sed.) rock. (e) Definition of the effect of snow in different aspects. (f) Histograms showing the effect of temperature and head wall erosion.

5.3.1 Slope angle

Methods

To define a maximum slope angle of the underlying terrain for rock glaciers, rock glacier shapes were again defined, excluding the steep front and side walls and steep scree slopes between the head wall and creeping form. Slope angles for these areas were determined using the digital elevation model DEM25 (Table 4).

Results

Ninety-five per cent of the analysed rock glacier creep forms are on slopes gentler than 30°. This value is therefore considered as being the threshold slope angle for rock glacier formation. Although some parts of rock glaciers are steeper than 30° (e.g. the upper talus), the erosion of such steep slopes is probably too strong to allow the development of characteristic creep forms.

5.3.2 Glacier coverage

Methods

First, we defined an area of potential rock glacier occurrence. An elevation limit was defined by the condition that 95 per cent of the area occupied by active rock glaciers is situated above this limit. Subsequently, all slopes steeper than the maximal slope angle of 30° were excluded. Rock glaciers mainly occur in concave or smooth terrain where avalanche snow and rocks are deposited. The potential rock glacier area was thus confined to the condition 'no convex curvature'. A threshold of convexity was defined by the condition that 95 per cent of the true rock glacier area is either below the threshold, or is concave or smooth (see Figure 20).

We assume that increased glacier cover affects the true rock glacier area to the same extent as this potential rock glacier area. We therefore calculated the percentage of the potential rock glacier area that is currently occupied by glaciers to interpret the effect of the factor 'glacier coverage'.

The potential rock glacier area was now supplemented by the condition 'no glaciers' and was used as the basic unit area when analysing the remaining factors. In this way the influence of glaciation on rock glacier frequency was excluded from the following analysis.

Results

The lowest limit of rock glacier occurrence was approximately 2300 m asl in the Albula Alps and 2100 m asl in the Glarner Alps. Comparing the study regions, 8 per cent (23.4 km2) more of the potential rock glacier terrain is glaciated in the high-precipitation Glarner Alps than in the dry Albula Alps (Table 6, line 29). Hence, 8 per cent less potential rock glacier area is available for the Glarner Alps due to glaciation and so 8 per cent fewer rock glaciers are estimated.

5.3.3 Aspect

Methods

We computed the aspect of the observed rock glacier surfaces divided into four aspect sectors (N-E, E-S, S-W and W-N). Subsequently, the fraction of each direction of the true rock glacier surface was calculated to define the influence of aspect on rock glaciers. However, the four aspect sectors can themselves have different frequencies within the study areas, influencing the total area of rock glaciers in each sector. To rule out the influence of varying aspect frequency and the influence of the factors elevation, slope and glaciers, the percentage of the true rock glacier area on the potential rock glacier area of an aspect sector was calculated. This value is called the rock glacier frequency (Figure 20).

Results

Aspect is another factor clearly influencing rock glacier distribution. All aspect sectors have the same frequency within the potential rock glacier area of the Albula Alps (Table 6, lines 24–27). This region is thus appropriate for the analysis of the aspect effect. Three times more rock glaciers exist in the northern aspects than in the southern ones here. However, western and eastern aspects also show differences with a rock glacier ratio of 2:3 (Table 6, lines 16–19 and 20–23), which corresponds to the permafrost distribution described by Keller *et al.* (1998) and Gruber and Hoelzle (2001). Haeberli (1975) considered diurnal variations in solar radiation as an explanation for this E-W ratio. Referring to data from five MeteoSwiss mountain weather stations (Table 4), there is 5 per cent less incoming global radiation in the afternoon after the solar zenith than before. On the other hand, the difference between GIS-derived potential solar radiation values in the Albula Alps in north-facing and south-facing slopes in summer is more than 20 per cent. If a 20 per cent difference in solar radiation leads to a rock glacier ratio of 3:1, it is questionable whether a 5 per cent difference in solar radiation on eastern and western aspects alone can cause a rock glacier ratio of 2:3.

Aspect sectors in the Glarner Alps have different frequencies (Table 6, lines 24–27). Accordingly, the distribution of rock glaciers with relation to aspect is distorted here, as shown in Table 6, lines 16–19. Instead, the rock glacier frequency shown in Table 6 (lines 20–23) must be analysed. This value shows a cumulation of rock glaciers in the sector W-N, similar to the Albula Alps. The different frequency of aspect sectors in the potential rock glacier area of the Garner Alps also affects the total amount of rock glacier surface here. The sector W-N is clearly under-represented but has the highest rock glacier frequency. The total amount of rock glacier surface in the Glarner Alps would be 10 per cent higher if all aspect sectors had the same frequency. This issue is shown in Figure 20.

5.3.4 MAP

Methods

To analyse the effect of MAP, we focus on the differences in rock glacier frequency between the wetter Glarner Alps and the drier Albula Alps (Table 6, lines 9 and 10).

However, three other factors differ between the Albula Alps and Glarner Alps: frequency of the lithology classes, glacier coverage and aspect (Table 6, line 1; 24–29). To exclude the influence of lithology when analysing MAP, both lithology classes were compared separately for both regions. The regionally different effect of glaciation was eliminated using the potential rock glacier area as the basis of computation. The effect of unequal aspect distribution remained an uncertainty in this calculation.

Results

The rock glacier frequency in the potential rock glacier area of the wetter Glarner Alps in comparison to the Albula Alps was 65 per cent lower for metamorphic/crystalline rock and 96 per cent lower for sedimentary rock (Table 6, line 5). The overall effect of MAP is therefore very strong and the intensity of the effect seems to be related to the lithology. This will be analysed in the Discussion section.

5.3.5 Lithology

Methods

To determine the effect of lithology, the frequency of rock glacier surface occurrence was compared for the potential rock glacier area in sedimentary rock and metamorphic/crystalline rock separately in both regions.

Results

In the Albula Alps, the frequency of rock glaciers in sedimentary rock areas was 38 per cent lower than in metamorphic/crystalline rock areas, whereas in the Glarner Alps it was 91 per cent lower compared to the metamorphic/crystalline rock areas (Table 6, line 5). Again, the mutual reinforcement of the two rock glacier adverse factors is evident (high MAP and sedimentary rock). In sedimentary areas, rock glaciers were not only less frequent, but they were also considerably smaller (Table 6, line 6) and their morphology less clearly defined. Furthermore, they show that rock type has a strong influence on rock glacier development, comparable to that of MAP.

5.3.6 Head wall erosion

Methods

Frauenfelder *et al.* (2003) established correlations between the length of rock glaciers and debris supply. Degenhardt (2009) showed the relation between individual rock glacier lobes and catastrophic rock fall events. This underlines the dependency of active rock glaciers on an ongoing debris supply, the intensity of which is a limiting factor for the size of a rock glacier. In addition to the size of the rock glacier head wall, head wall erosion is crucial for the intensity of the debris supply. However, there are no GIS data on the spatial differences of long-term head wall erosion processes. We therefore analysed two groups of rock glaciers that represent different periods of head wall erosion: relict and active rock glaciers of the Albula Alps. Differences in size between these groups include three effects: The effect of different head wall erosion intensity, the effect of different durations of the active phase and differences in head wall size. To exclude the effect of the head wall size, the ratio between the 2D rock glacier area and the 3D head wall area was compared between relict and active rock glaciers.

Results

The entire relict rock glacier surface is just slightly larger than the active rock glacier surface in the Albula Alps (Table 6, line 4). However, the individual relict rock glaciers are much larger than the active ones. The mean size of the relict Albula rock glaciers is over 70 per cent greater than the mean size of their active counterparts (Table 6, lines 6 and 7). The rock glacier/head wall ratio is 35 per cent higher for relict Albula rock glaciers (Table 6, line 8). The lower elevation boundary for relict Albula rock glaciers is approximately 200 m lower than that for the active ones.

5.3.7 Snow cover

Methods

The different frequencies of rock glacier occurrence in western and eastern aspects were mentioned above. Different amounts of incoming solar radiation (5%) were found for western and eastern slopes but their influence on a rock glacier ratio of 2:3 between E and W was questioned. Snow cover was considered as another factor contributing to this distortion. To validate the influence of snow on different aspects, possible snow deposition/erosion zones within the Albula Alps were analysed. Schirmer *et al.* (2011) showed that the snow distribution in alpine terrain at the end of the accumulation period is mainly influenced by the effect of a few major winter storms. Erickson *et al.* (2005) verified the terrain parameters introduced by Winstral *et al.* (2002) as being most influential for snow distribution, with the wind sheltering index being the most significant parameter. For the following analysis, the sheltering index proposed by Winstral *et al.* (2002) was used for identifying deposition/erosion zones of snow.

We analysed the predominant wind directions in the Albula Alps based on the two wind measurement stations on the summits of Chrachenhorn and Piz Müra (Figure 18), differentiating between half-hourly mean wind speed and half-hourly mean wind exceeding 5 m/s. The wind sheltering index was computed for these predominant wind directions. This index provides a value of wind exposure for each grid cell of the DEM24. Positive values represent wind-sheltered areas and negative values indicate wind-exposed regions. We computed the wind sheltering index using the input parameters given by Plattner *et al.* (2006) (wind directional tolerance 10°, maximum range 250 m). We defined terrain that is wind sheltered for all main wind directions as being a necessary condition for a regular deep snow cover. Areas that are exposed to at least one main wind direction were treated as being prone to snow redistribution and having an irregular small-scale snow cover distribution. Translating this into the GIS data, we calculated a grid representing the minimum wind sheltering index of all main wind directions for each grid cell. The spatial averages of the minimum wind sheltering indices in the aspects W-N, N-E, E-S and S-W were compared for the potential and the true rock glacier areas.

Results

The analysis of the wind fields showed two predominant wind directions, SSW and NNW (Figure 21). The wind speed ranges were identical for both wind directions. Both wind directions occurred with similar frequency and should therefore have a similar influence on snow redistribution.
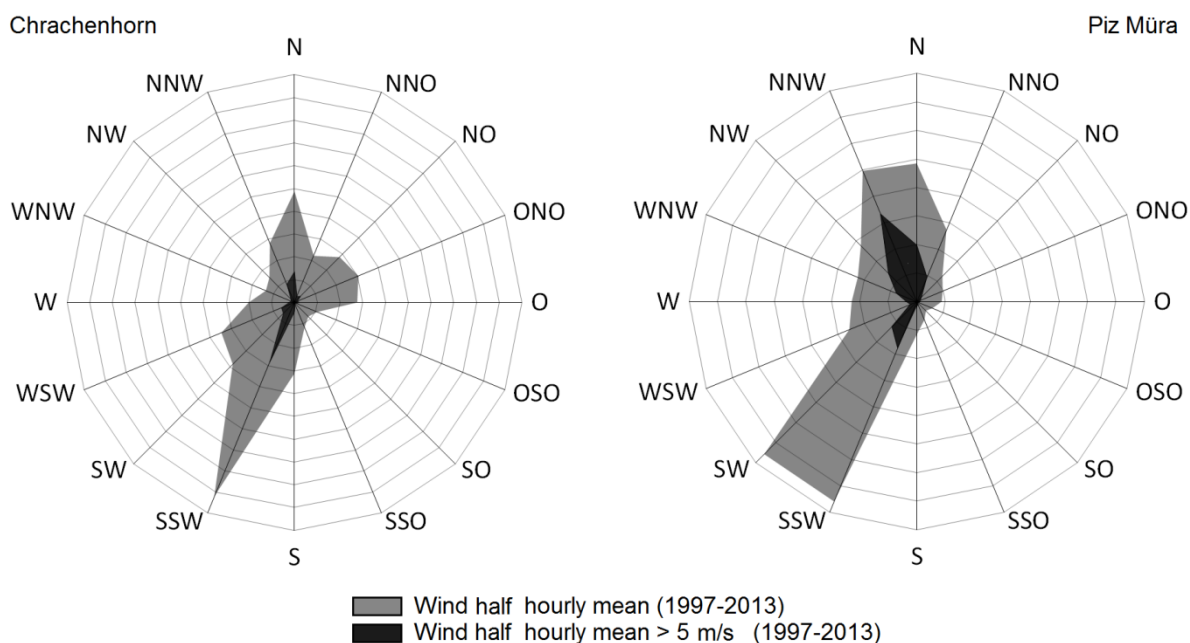
Figure 21: Wind rose diagrams showing dominant wind directions in the Albula Alps.

For both the potential rock glacier area and the true rock glacier area, the spatial average of the resulting wind sheltering indices was negative in the western sectors (wind exposed, low snow accumulation) and positive in the eastern sectors (wind sheltered, high snow accumulation) (Table 7; Figure 19).

Table 7. Spatial average of the minimum wind sheltering indices for different aspects in the Albula Alps.

	Wind sheltering index			Wind sheltering index		
	W-N	N-E	Difference	E-S	S-W	Difference
Potential rock glacier area	-0.11	0.08	0.19	0.04	-0.13	0.17
True rock glacier area	-0.14	0.06	0.20	0.13	-0.03	0.16

5.3.8 MAAT

Methods

The MAAT (MeteoSwiss 1961–90) (Begert *et al.*, 2003) was compared between the study regions. The MeteoSwiss MAAT grid uses a nonlinear parametric function to model the vertical temperature profiles (Frei, 2014). Systematic large-scale nonlinearities in alpine regions are mainly limited to lower elevations close to the valley bottoms. Apart from random small-scale effects, temperature lapse rates are approximately linear between 2000 and 3000 m asl (Frei, 2014). We therefore extracted linear lapse rates for each region from the grid data: temperature-elevation pairs of values were ordered by elevation and a linear trend was calculated through the temperature values. In addition, the lapse rates were used to calculate a MAAT normalised by elevation for each entire region. The mean elevation of the MAAT grid of the Glarner Alps was used as a reference elevation. After verifying the comparability of the regions regarding MAAT, we analysed the distribution of rock glacier surface against elevation for both regions.

Results

The air temperature lapse rates calculated from the grid data are 0.52 °C/100 m for the Albula Alps and 0.62 °C/100 m for the Glarner Alps, and they intersect at around 2700 m asl. The regionally specific MAAT normalised by elevation differs by 0.5 °C (Table 6, line 11). The distribution of MAAT with regard to elevation is shown in Figure 22 for both regions. Although there is a considerable variance in the elevation signal, which is the expression of local small-scale temperature anomalies (Begert *et al.*, 2003), the large-scale temperature distribution is quite similar for both regions. Thus, the effect of MAAT on rock glaciers mainly becomes apparent with regard to their elevation distribution within the regions.

The mean elevation of rock glaciers is generally around 2600 m asl (Table 6, line 13). Referring to the calculated linear temperature lapse rate, this is the exact level of the 0 °C MAAT isotherm approximation. Hence, approximately half of the rock glacier surfaces lie above the 0 °C isotherm and the other half below it. Rock glaciers in the Glarner Alps do not occur above 2800 m asl, which can be explained by the higher degree of glaciation. Three very small rock glaciers in the Glarner Alps are clearly lower than any Albula rock glacier and decrease the lower limit of rock glacier occurrence. In both regions, the elevation of rock glaciers is highly variable: rock glaciers occur within an elevation belt of 850 m in the Albula Alps and 750 m in the Glarner Alps. Individual rock glaciers exist below the current 0 °C isotherm (Table 6, line 13). Marchenko (2001) showed that permafrost can occur at sites

with a positive MAAT. The large elevational distribution of rock glaciers suggests that within a certain interval they are not highly sensitive to MAAT. In addition, many other factors influence the elevation distribution of rock glaciers, such as aspect (Table 6, lines 14 and 15), MAP or head wall erosion (Table 6, line 13).
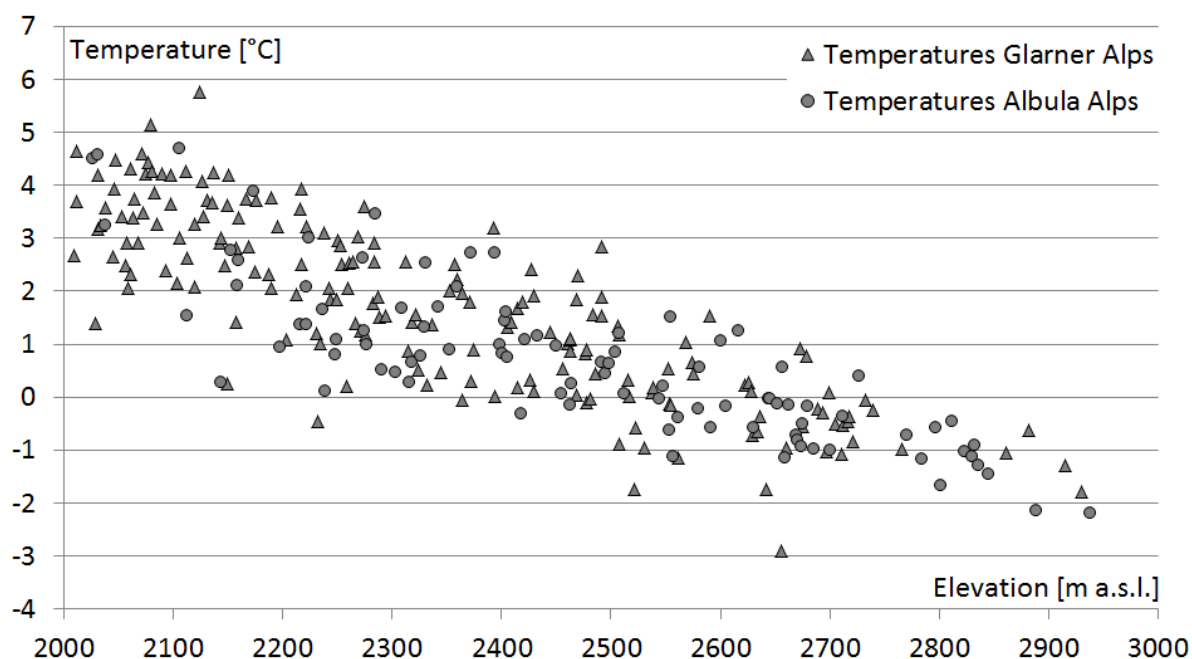
Figure 22: Relationship between mean annual air temperature (MAAT) and elevation for both study regions.

5.4 Discussion

The study shows that all the factors analysed influence rock glacier development. Nevertheless, only the slope factor has a sharp delimiting value (30°) for rock glacier occurrence. The delimiting values for all other factors vary according to the local characteristics of their counterparts. For example, the lower elevational border for rock glacier occurrence depends on aspect, lithology and erosion.

The combination of MAP and lithology was found to have the strongest impact on rock glacier development. Dry areas with metamorphic/crystalline lithology favour rock glacier development, whereas wet sedimentary mountain ranges virtually exclude it.

5.4.1 Precipitation, rock debris grain size and their interaction

Rainfall directly transports energy through the insulating coarse surface boulder layer to the ice. Rist and Phillips (2005) described how refreezing of a water-saturated zone above the permafrost layer can rapidly transfer latent heat into the permafrost body. In addition, thick snow reduces ground cooling in winter (Keller and Gubler, 1993) and counteracts permafrost conservation (Zhang, 2005). In flat ice-rich terrain, meltwater runoff is slow and ponding can rapidly degrade permafrost bodies (Haeberli et al., 2001).

Ikeda and Matsuoka (2006) distinguished between pebbly and bouldery rock glaciers. Pebbly rock glaciers have smaller dominant grain sizes (<20 cm), rounder and more strongly eroded features and are shorter (length < 200 m) than bouldery rock glaciers. Ikeda and Matsuoka (2006) showed that pebbly rock glaciers occur mostly in areas of sedimentary rock, indicating the strong influence of lithology on scree grain size. The smaller the grain size, the less air is contained and the greater the conductive heat transfer within the ground (Putkonen, 1998). Pebbly rock glaciers also contain more water, thus delaying winter freezing of the ground (Boike et al., 1998). In contrast, a coarse layer of boulders is a good insulator in summer (Gruber and Hoelzle, 2008) and delays the formation of a closed snow cover in winter (Keller and Gubler, 1993).

The strong interaction between high MAP and sedimentary rock is notable. Both reduce rock glacier frequency, but their combined effect clearly exceeds the sum of both factors. The smaller grain sizes in sedimentary rock debris compared to metamorphic/crystalline debris are more prone to water erosion and so are the steep front or side walls of pebbly rock glaciers. This makes them sensitive to strong precipitation. Furthermore, throughflow within the active layer is slower in smaller grain sizes (Bodman and Harradine, 1939), which can increase the energy exchange between the water and the permafrost.

5.4.2 Head wall erosion rates control rock glacier size, velocity and front elevations

To quantify the effect of head wall erosion on rock glacier size, we analysed the rock glacier-head wall ratio. This ratio is controlled by head wall erosion rates (specific to individual rock walls) and the duration of the active phase of the rock glacier. Comparing active and relict Albula rock glaciers, we found that the rock glacier-head wall ratio for relict rock glaciers was distinctly higher than that for active ones. Following Böhlert et al. (2011), this is not a result of a longer active phase of relict rock glaciers. Böhlert et al. (2011) dated rock glaciers in the Albula Alps and attributed the main phase of activity of the relict rock glaciers to between

the end of the Younger Dryas and the early Holocene. In contrast, today's active features developed during the entire Holocene. The active phase of the relict Albula rock glaciers investigated was therefore much shorter than those of currently active rock glaciers. Accordingly, Böhlert *et al.* (2011) estimated a mean creep velocity of 30 cm/a for the active phase of the relict rock glaciers. If this value were applied to currently active rock glaciers, which started creeping in the beginning of the Holocene (Böhlert *et al.*, 2011), they would now be 3 km long. In our data-set, very few, exceptionally long rock glaciers currently have a maximum length of 1 km. Consequently, relict rock glaciers reached larger sizes in a shorter time span, which can only be explained by very high head wall erosion rates.

Indeed, Böhlert et al. (2011) postulated a rapid glacier retreat at the end of the Younger Dryas, which resulted in smaller glacier extents than during the Little Ice Age maximum. This implies that huge amounts of debris were available due to deglaciation, debuttressing and head wall warming, leading to permafrost thaw; it also indicates climate conditions comparable with the current situation. Other investigations on climate history in central Europe and the Alps also suggest a rapid and strong warming at the end of the Younger Dryas (Dansgaard *et al.*, 1989). High head wall erosion rates in permafrost rock walls during phases of atmospheric warming are mentioned by Fischer *et al.* (2006), Gruber and Haeberli (2007) and Noetzli *et al.* (2003). Hales and Roering (2005) showed for timescales of 10–15 ka that erosion rates are lower in permafrost rock walls than in neighbouring permafrost-free rock walls. It is therefore likely that warming-induced high head wall erosion rates favour larger and faster rock glaciers.

Moreover, as the lower elevation limit of rock glaciers is also a function of creep length and velocity, strong warming with high head wall erosion rates rather than colder climate conditions could have forced the presence of rock glacier fronts at lower elevations. The absolute size difference between relict and active features is much greater than the difference in the rock glacier-head wall ratio (Table 6, lines 6–8). This implies a high frequency of relict rock glaciers under very large rock walls. It is conceivable that the combined effect of large rock walls and high head wall erosion rates led to rock glacier advances in elevation ranges that were otherwise unsuitable for long-term rock glacier existence. This is supported by Figure 6 in Frauenfelder and Kääb (2000) which shows that the elevational differences between active/relict rock glaciers vary substantially in neighbouring regions, despite a similar MAAT history.

5.4.3 Wind-driven snow redistribution affects rock glacier frequency

At scales of a few hundred metres, the wind sheltering index has proved to be the most significant factor describing snow distribution close to crests (Plattner *et al.*, 2006). This scale is also relevant for rock glaciers. Our study showed that the wind sheltering index differed between eastern and western aspects but was similar for southern and northern aspects (Table 7). The comparison of northern and southern aspects therefore reflects the undistorted influence of insolation (rock glacier ratio 3:1). The influence of snow cover becomes evident in the rock glacier ratio between eastern and western slopes (rock glacier ratio 2:3). In other studies (Gruber and Hoelzle, 2001; Nyenhuis *et al.*, 2005), a significant accumulation of rock glaciers and permafrost in the northwestern aspect is evident too. This corresponds to the higher wind sheltering on eastern slopes (Table 7). A deeper snow cover there reduces the effect of atmospheric cooling of the ground during winter and large amounts of meltwater transport energy in taliks on and within the permafrost body (Zenklusen Mutter and Phillips, 2012b). The contrasting snow accumulation on western and eastern slopes can thus explain the differences in permafrost and rock glacier occurrence between these aspects.

5.4.4 MAAT: An indistinct threshold for rock glacier development

Overall, we suggest that MAAT defines an elevational range for rock glacier occurrence that depends on the influencing factors mentioned previously. However, we found no sharp MAAT threshold value for rock glacier occurrence, which implies that MAAT is not the only limiting factor for the lower boundary of rock glaciers. In addition, MAAT did not prove to be a clearly definable reference value. In alpine terrain, MAAT is highly influenced by local conditions such as long- and shortwave radiation and wind exposure. Accordingly, the location of air temperature measurements has a considerable influence on the MAAT data and might lead to inconsistencies between specifications for individual rock glaciers or between different studies. Although the MAAT range of over 5 °C determined for the occurrence of active rock glaciers in the Albula Alps is an approximation, it indicates a relatively high tolerance of rock glaciers to air temperature variations. Borehole temperatures in alpine rock glaciers have increased to just below 0 °C during the last two decades without displaying widespread permafrost thaw (Haeberli *et al.*, 2006; PERMOS, 2013). This might be a response to the current atmospheric warming, the end of the Little Ice Age or another influence; the time series are still too short for definitive conclusions. It is not clear how stable the current isothermal state of ice-rich rock glacier permafrost is in the Alps. An interruption of response has probably been reached here for the moment, which explains

how rock glacier ice outlasted former warming periods during the Holocene and reached ages of several millennia (Haeberli *et al.*, 1999; Böhlert *et al.*, 2011).

5.4.5 Rock glacier development and its controlling factors

What do the results for the individual influencing factors imply about rock glacier genesis? Konrad *et al.* (1999) showed that the sensitivity of rock glaciers to climate forcing is strongest in the root zone (where accumulation takes place) and that effective insulation by rock debris reduces this sensitivity to almost zero towards the terminus. On the one hand, this supports our results showing a nonlinear sensitivity of rock glaciers to air temperature. On the other, it highlights the fact that the root zone of rock glaciers is both the zone of accumulation and potentially the zone of highest mass loss. This observation mainly favours the accumulation of talus and avalanche snow under steep alpine rock walls as dominant processes of ice formation in rock glaciers. The snow is either conserved and transformed into ice under a layer of insulating rock debris or slowly melted if the debris cover is not thick enough to insulate against atmospheric warming and solar radiation. This process is certainly not the only source of ice in rock glaciers but probably the most relevant one. It explains that rock glacier development can differ considerably under equal temperature conditions, depending on other factors, the significance of which was shown in our study:

1. The intensity of head wall erosion processes and grain size control (a) the formation time of an insulating debris layer superimposed on avalanche snow in the accumulation area, and (b) the accumulation mass that determines rock glacier length and long-term creep velocity.
2. The amount of precipitation that can infiltrate the debris layer and supply a constant energy input, independent of the thickness of the insulating debris layer.

5.5 Conclusions

Rock glacier distribution and characteristics in two regions of the Swiss Alps are influenced by MAP, lithology, MAAT, head wall erosion rates, glacier coverage, slope, aspect and snow cover. Some of these factors interact in a nonlinear way, precluding simple explanations for rock glacier development. High values of MAP (both in terms of summer rainfall and winter snow accumulation) disfavour rock glaciers. Differences in snow distribution on small and medium scales due to wind sheltering lead to lower frequencies of rock glaciers on snow-rich slopes. At regional scales, winter precipitation is the dominant factor controlling snow depth on rock glaciers and therefore influences rock glacier frequency. Head wall erosion

and lithology also strongly influence rock glaciers. The influence of the lithology on rock glaciers clearly increases with increasing MAP. In contrast, the response of permafrost in rock glaciers to MAAT is less linear than in other landforms and is sometimes overemphasised in the literature. Rock glacier growth probably increases during warming periods due to higher head wall erosion rates. Next to MAAT, head wall erosion and MAP are temporally variable factors that influenced rock glacier development during the Holocene. The reaction of rock glaciers to atmospheric warming must therefore be interpreted carefully due to multiple uncertainties and the fact that the effects of temporally variable influencing factors are hard to distinguish.

Acknowledgements

6. Factors controlling velocity variations at short-term, seasonal and multiyear time scales, Ritigraben rock glacier, Western Swiss Alps

Robert Kenner[1], Marcia Phillips1, Jan Beutel[2], Martin Hiller[1], Philippe Limpach[3], Eric Pointner[4], Martin Volken[5]

[1] WSL Institute for Snow and Avalanche Research SLF, Davos, Switzerland
[2] Computer Engineering and Networks Laboratory, ETH Zürich, Switzerland
[3] Institute of Geodesy and Photogrammetry, ETH Zürich, Switzerland
[4] Rovina & Partner AG, Varen/Visp, Switzerland
[5] Aufdenblatten GEOMATIK AG, Zermatt, Switzerland

Personal contributions:

Robert Kenner: Paper concept; Data collection, consolidation and analysis; TLS acquisition and processes; Discussion

Marcia Phillips: Paper idea; Idea and installation of automatic camera, long-term borehole temperature measurements

Jan Beutel: Design of the GNSS Sensor

Martin Hiller: Technical support for the automatic camera

Philippe Limpach: GNSS processing

Eric Pointner: Borehole deformation measurements

Martin Volken: Tachymetric terrain monitoring

Abstract

This study analyses the factors controlling variations in short-term, seasonal and multiyear deformation velocity of an alpine rock glacier from data obtained over periods of 1–20 years. The Ritigraben rock glacier, in the western Swiss Alps, was monitored using tacheometry, terrestrial laser scanning, an in situ global positioning system and borehole deformation measurements. Rock glacier stratigraphy and ground temperature data were obtained from boreholes, and long-term meteorological data (temperature, precipitation, snow water equivalent) from nearby weather stations. Shearing within a distinct water-bearing layer represents the major component of the displacement. Short-term accelerations and seasonal velocity patterns of the rock glacier deformation appear to have been triggered by water supply to this layer. A long-term acceleration of the rock glacier was probably also caused by increased water supply. Permafrost temperature in the rock glacier has increased slightly since 2002, yet no direct causality could be established between this limited warming and rock glacier acceleration.

6.1 Introduction

Alpine rock glaciers have generally accelerated during recent decades (Kaufmann and Ladstädter, 2007; PERMOS, 2016). Such accelerations have often been directly attributed to the increasing temperature of permafrost ice induced by climate warming (Kääb *et al.*, 2007; Ikeda *et al.*, 2008). Hydrological factors have also been proposed as driving mechanisms (Krainer and Mostler, 2006) and exceptionally strong velocity variations have been attributed to topographical conditions or to overloading by major rock fall events (Delaloye *et al.*, 2013). Despite such explanations, clear evidence about the processes leading to rock glacier accelerations is still rare. In particular, little is known about short-term velocity fluctuations of rock glaciers. Here we analyse the variations in rock glacier velocity at three different time scales and discuss the influence of spring snow melt, summer rainfall, subsurface water fluxes and permafrost temperatures on these variations. Our study is based on geodetic measurements, meteorological and subsurface data measured at and near the Ritigraben rock glacier, Switzerland.

6.2 Study site

The active, ice-rich Ritigraben rock glacier has an area of 0.25 km^2 and is located approximately 2 km south of Grächen, Canton Valais, in the western Swiss Alps. The rock glacier originates at the western base of the Gabelhorn and flows into the upper end of the Ritigraben gully, its front around 2600 m above sea level (asl) (Figure 23). Here the topography steepens and the rock glacier forms a detachment zone. The central part of the rock glacier has slope angles below 20°, whereas the front and root zones slope between 30 and 35°. Boulders with a maximum size of a few cubic metres cover the rock glacier surface (Figure 24). As our datasets are mostly limited to the rock glacier front, we focus on this part of the landform (Figure 23). In the 1990s large debris flows originated from the detachment zone at the front of the rock glacier in the uppermost part of the Ritigraben gully, damaging roads and infrastructure below (Lugon and Stoffel, 2010; Stoffel, 2010). Further debris flows are likely after intense rainfall within the next few years, due to debris accumulating in the gully below the rock glacier.
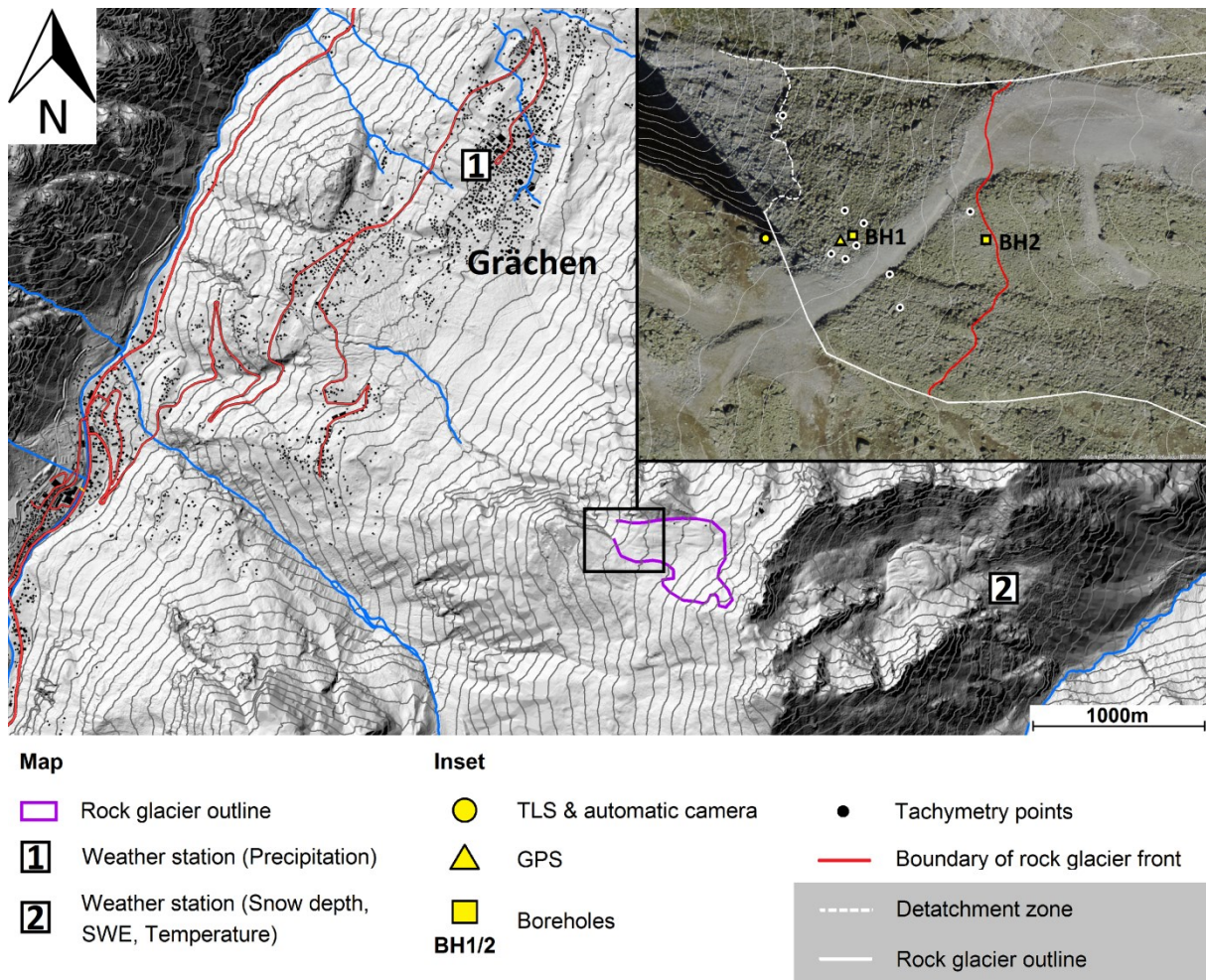
Figure 23: Location map showing the study site and the measurement setup. Inset: Orthophotograph from 20 August 2013, showing a close up of the rock glacier area. The red line indicates the upper limit of the lower part of the rock glacier that is referred to in the text as the "rock glacier front" [Orthofoto: Swissimage (2016) swisstopo 5704000000].
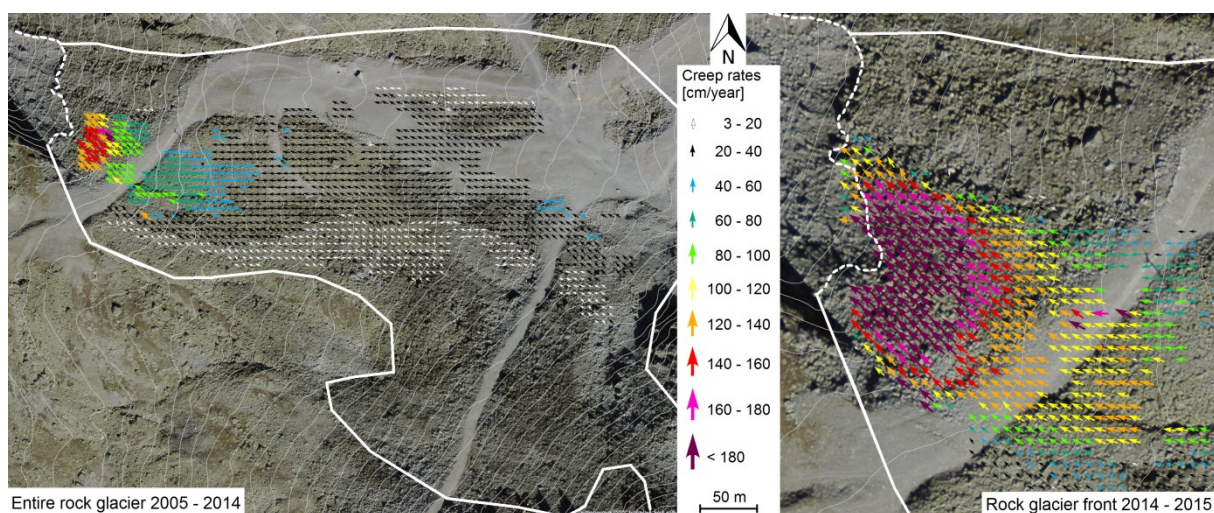

Figure 24: Deformation rates calculated from the Swissimage orthophotographs from 2005 and 2014 (left) and the TLS measurements from 2014 and 2015 (right). The solid white line marks the extent of the rock glacier, and the dashed white line shows the detachment zone [Orthofoto: Swissimage (2016) swisstopo 5704000000].

6.3 Methods and information provided

We used terrestrial laser scanning (TLS), an in-situ global positioning system (GPS) and georeferenced time-lapse photography to acquire data on the surface movement of the Ritigraben rock glacier. Tachymetric monitoring of surface points, carried out between 1995 and 2014, was incorporated in the analysis. Swissimage orthophotographs were analysed to obtain information on the rock glacier deformation between 2005 and 2014. The dates of the measurement campaigns are summarized in Table 8.

6.3.1 Terrestrial laser scanning

Terrestrial laser scanning of the rock glacier surface was carried out once a year between 2012 and 2016 using the Riegl VZ6000 long-range scanner (Figure 23). The laser scanning point clouds were transformed into digital elevation models (DEMs) with 20 cm resolution. Vertical changes between the measurements were defined by calculating differences between DEMs. Horizontal changes (i.e. the expression of displacement at the rock glacier surface) were tracked by correlating surface structure patterns of the rock glacier between two measurements. The surface structure was extracted from the DEMs using a high-pass filter. The resulting displacement vectors were filtered to remove single mismatches or zones in which the whole vector field was chaotic (Kenner *et al.*, 2014). The smallest remaining vectors after this filter process approximate well with the accuracy obtained for calculating displacement rates (Kenner *et al.*, 2014). In the case of Ritigraben this was 3cm.

6.3.2 Continuous differential L1-GPS

In 2012 an in-situ L1-GPS device was installed on a boulder of the southern side of the rock glacier front (Figure 23). The GPS data were processed with the Bernese GNSS Software (Dach *et al.*, 2007) using reference data from a local base station with a baseline distance of 5.845 km and an elevation difference of 102 m (WGS84: N 46.12350, E 7.82129). The daily GPS coordinates are estimated with an error (standard deviation) of approximately 1-2 mm horizontally and 2-3 mm vertically. Velocities were calculated from the daily coordinate series between the first and last values of an 11-day window. For analysing individual short-term accelerations this window was reduced to 3 days, taking into consideration that GPS measurement errors can distort the velocity signal during such a short time period. GPS velocity time series are used to identify accelerations in the order of a couple of days to a few weeks. These short-term accelerations were checked for obvious error influences such as coordinate shifts in varying directions. The GPS data also display a seasonal pattern of the deformation velocity. Interannual differences can be captured but long-term trends have to

be interpreted carefully, as the GPS device moves with the rock glacier (5.5 m displacement between 2012 and 2016).

6.3.3 Time-lapse photography

A time-lapse camera was installed 10 m south of the Ritigraben rock glacier front in July 2015 (Figure 23) to photograph the front and the detachment zone at 3-hour intervals. The photogrammetric matching algorithm introduced by Roesgen and Totaro (1995) was used to calculate translation vectors between the time-lapse images, which represent the displacements of the rock glacier surface. The translation vectors were automatically georeferenced, scaled, and oriented in global coordinates, and velocities were calculated from them using a monoplotting algorithm developed using the MathWorks MATLAB software package. Faulty correlations were eliminated from the results using the same filter algorithm as for the TLS data (Kenner *et al.*, 2014). When processing an image time series (3 days temporal resolution) for summer 2015, the relative velocity of each displacement vector relative to its initial velocity between the first two images was calculated. These relative velocities were averaged for each image step to obtain a relative rock glacier velocity for the entire image section. The velocity data obtained from time-lapse photography have a higher temporal resolution than the GPS data and are, in addition, spatially resolved. Relative velocity time series obtained from two image time series showed a root mean square error of 5.6% between them, which indicates a high precision of the method. However, these time series can be interrupted by thick snow cover or long periods of poor visibility. We used these data to analyse spatial and temporal short-term variations of the deformation process, and provide information on the weather conditions and the snow cover.

6.3.5 Borehole measurements

Two vertical boreholes, B1 (48 m deep) and B2 (30 m deep), were drilled in 2002 on the Ritigraben rock glacier to provide information on the rock glacier stratigraphy, internal deformation and subsurface temperatures (Figure 23). Inclinometer measurements were carried out in borehole B1 using a Slope Indicator Digitilt inclinometer revealing the internal deformation patterns. Borehole B2 was equipped with 30 YSI 44006 thermistors with a calibrated accuracy of ±0.02°C. Borehole temperatures were measured daily and registered using a Campbell Scientific CR1000 data logger. The borehole is gradually being sheared off from the base upwards and all thermistors below 13 m depth have been cut off. The borehole temperature data provide point information on the active-layer thickness, permafrost temperature and the size, position, temperature and occurrence of a talik located between 10 and 13 m depth, described by Zenklusen Mutter and Phillips (2012b).

6.3.4 Total station and orthophotograph monitoring

A network of 22 points on the rock glacier surface and nearby was monitored between 1995 and 2014 using a Leica TCA 2003 total station. Data were acquired in annual or multi-annual resolution (Table 8). Nine of these points are located on the rock glacier front (Figure 23) and were used to define multiannual velocity variations of the rock glacier.Swisstopo provides Swissimage orthophotographs for all of Switzerland, with a spatial resolution of 50 cm in alpine terrain. For smooth terrain, the position accuracy of the orthophotographs is specified to be 50 cm from 2005 onwards. Based on these orthophotographs (Table 8) we calculated multi-annual deformation velocities of the rock glacier between 2005 and 2014, using the same correlation method as applied for the time-lapse images.

6.3.6 Meteorological data

Meteorological data were obtained from two automatic weather stations. A Meteoswiss station in Grächen is located at 1600 m a.s.l., 2.5 km northwest of Ritigraben, and an IMIS (Intercantonal Measurement and Information System) station (Russi *et al.*, 2003) is located at 2500 m a.s.l. in the Seetal valley 2 km east of the Ritigraben catchment, on the eastern side of the Seetal ridge (Figure 23). Liquid summer precipitation is measured only at the Grächen station and the absolute values are probably lower here than at Ritigraben, due to the elevation difference. Snow depth and air temperature are measured at the Seetal weather station, which we consider to represent the Ritigraben site. Using temperature, wind and radiation data from the Seetal station, the simulation model Snowpack continuously calculates the snow water equivalent (SWE) at this station (Lehning *et al.*, 1999). We removed all decreases of the SWE time series during winter, which can occur due to melt or wind erosion, and thus obtained the total SWE for winter. This corresponds to the maximum amount of water that can potentially infiltrate the rock glacier during snow melt.

Table 8: Acquisition time of datasets

Dataset	Time of acquisition
Meteorological data	Daily mean values
Swissimage orthophotographs	1999; 2005; 2008; 2011; 2014
Borehole temperature	Since 27.03.2002, daily mean values
TLS	12.07.2012; 13.09.2013; 20.08.2014; 11.08.2015
GPS position data	Since 20.07.2012, daily mean values,
Time-lapse photography	Since 03.07.2015; every 3 hours
Total station	13.10.1995; 09.10.1996; 01.09.1998; 07.09.1999; 26.09.2000; 03.09.2003; 06.09.2006; 07.10.2010; 21.10.2014

6.4 Results

6.4.1 Rock glacier velocity and velocity variations

The surface displacements derived from the Swissimage data and from the TLS measurements provide a good overview of the deformation velocities at the Ritigraben rock glacier (Figure 24). The moving part of the upper rock glacier was up to 150 m wide and moved up to 40 cm/y. The rock glacier accelerated strongly towards the front, reaching velocities of over 200 cm/y close to the detachment zone.

Rock glacier velocity varied over short-term, seasonal and multi-year time scales. Short-term accelerations usually lasted about one day. Such surges are evident in both the GPS time series and the time-lapse images (Figures 25 and 26). It is difficult to specify the exact duration of most of these events, as the GPS time-series is temporally smoothed. However, some surges are perfectly documented by the time-lapse image data (Figure 26), such as the one on 9 August 2015. During the course of one day only, the rock glacier front moved 16 times faster compared to its previous velocity (Figure 26, inset). With two exceptions (30 November 2013 and 13 February 2014), these short-term accelerations occurred during the snow-free summer period or during the snow melt season.

A pronounced seasonal pattern in the deformation velocity of the rock glacier is recorded by the GPS time series (Figure 25). Maximum velocity was reached between August and November. During winter the rock glacier decelerated slowly and smoothly until a fast and strong acceleration coincided with the onset of snow melt in spring. This acceleration decreased after the snow melt ended but continued until the maximum velocity recurred.
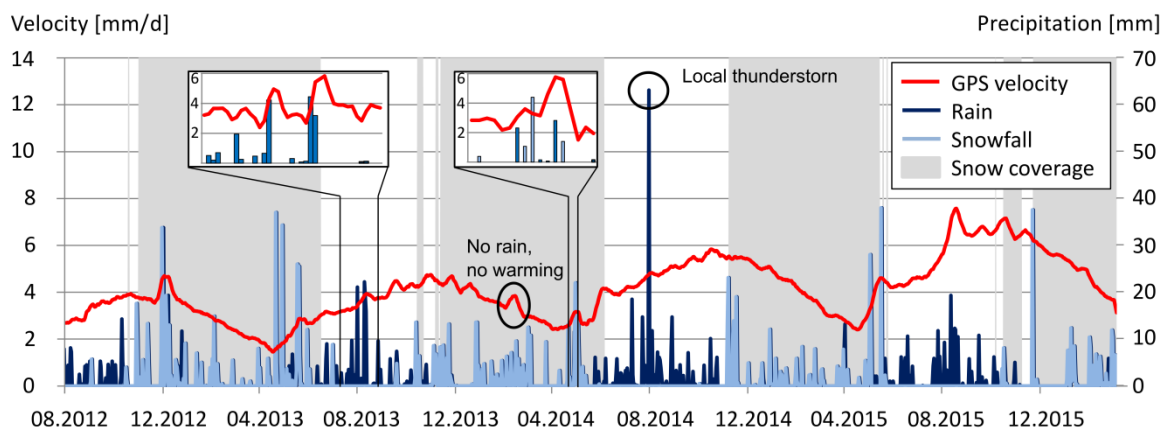

Figure 25: Time series showing the GPS-based deformation velocity and precipitation events. Periods with snow cover are highlighted in grey. The velocity values in the main plot are based on an 11-day window, and the values in the insets on a 3-day window.
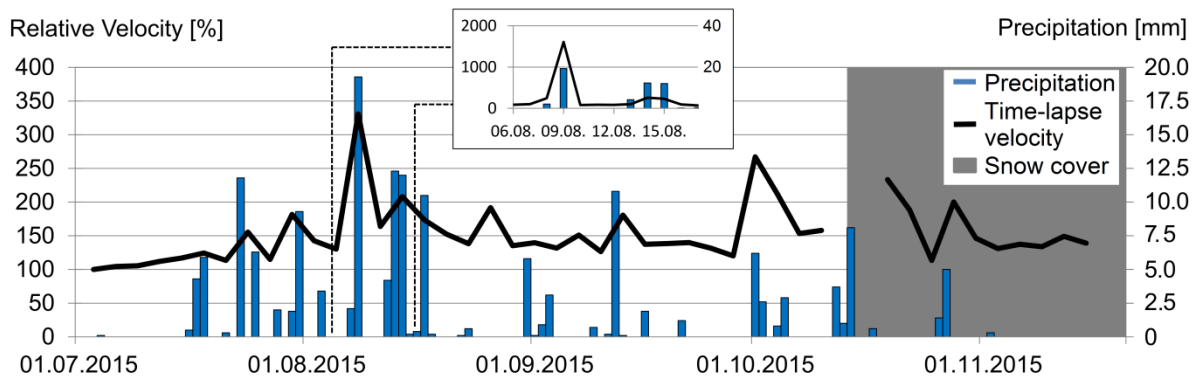
Figure 26: Time series showing relative deformation velocity (derived from time-lapse photography) and precipitation. A strong deformation surge coincided with a heavy precipitation event between 9 and 10 August 2015. The velocity values in the main plot are based on a 3-day window, and the values in the inset on a 1-day window.

Multi-year acceleration of the rock glacier, relative to the period 1999-2000, is evident in the results of all three geodetic measurement systems (total station, TLS and GPS) (Figure 27). As the TLS and GPS data series began in summer 2012, their initial relative velocity was compared with the relative velocity in 2012 defined by the total station. The rock glacier has accelerated by 400% since 1999-2000 (Figure 27). The acceleration is also confirmed by the mean annual deformation rates obtained from the Swissimage dataset between 2005 and 2014 when compared with the TLS values from 2014-2015 (Figure 24).
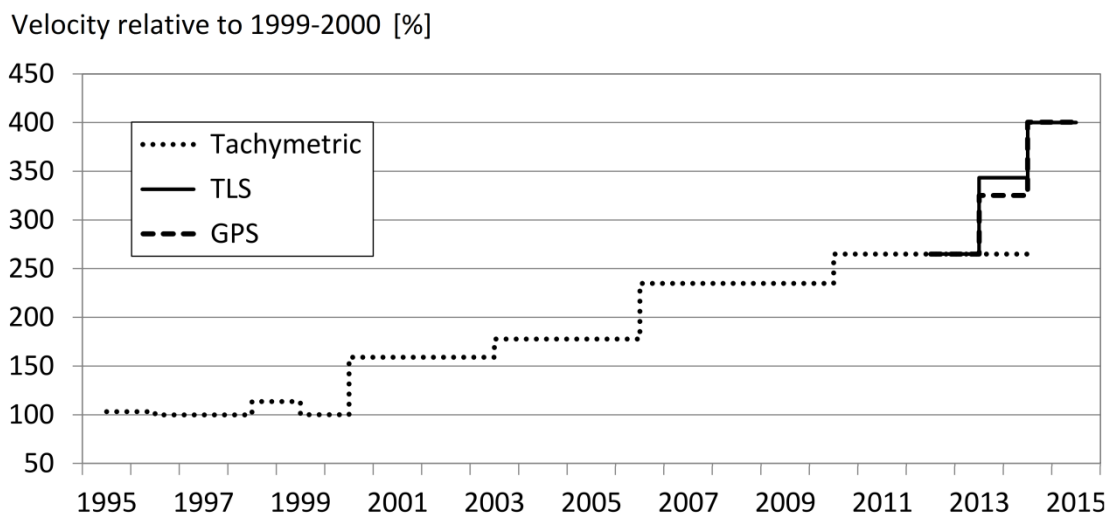

Figure 27: Multiyear velocity variations of the Ritigraben rock glacier front, relative to the period 1999-2000. The initial relative GPS- and TLS-derived velocities have been fitted to the relative tachymetric velocity at the relevant date.

6.4.2 Borehole stratigraphy and deformation

The active layer in borehole B1 was approximately 5 m thick and consisted of a blocky layer with large pore spaces, overlying a permafrost body that contained a mixture of fine material to large blocks (Figure 28). Ice and frozen sand were evident to 21 m depth. Below this was a 16-m-thick, ice-free layer, consisting of blocks and fine material. The zone between 20.8 and 30.2 m was very wet, with water encountered at depths of 22, 24, 25.9, 27.2 and 28 m. Between 37 and 41 m depth the ground was frozen again. Massive gneiss bedrock occurred below 41 m.
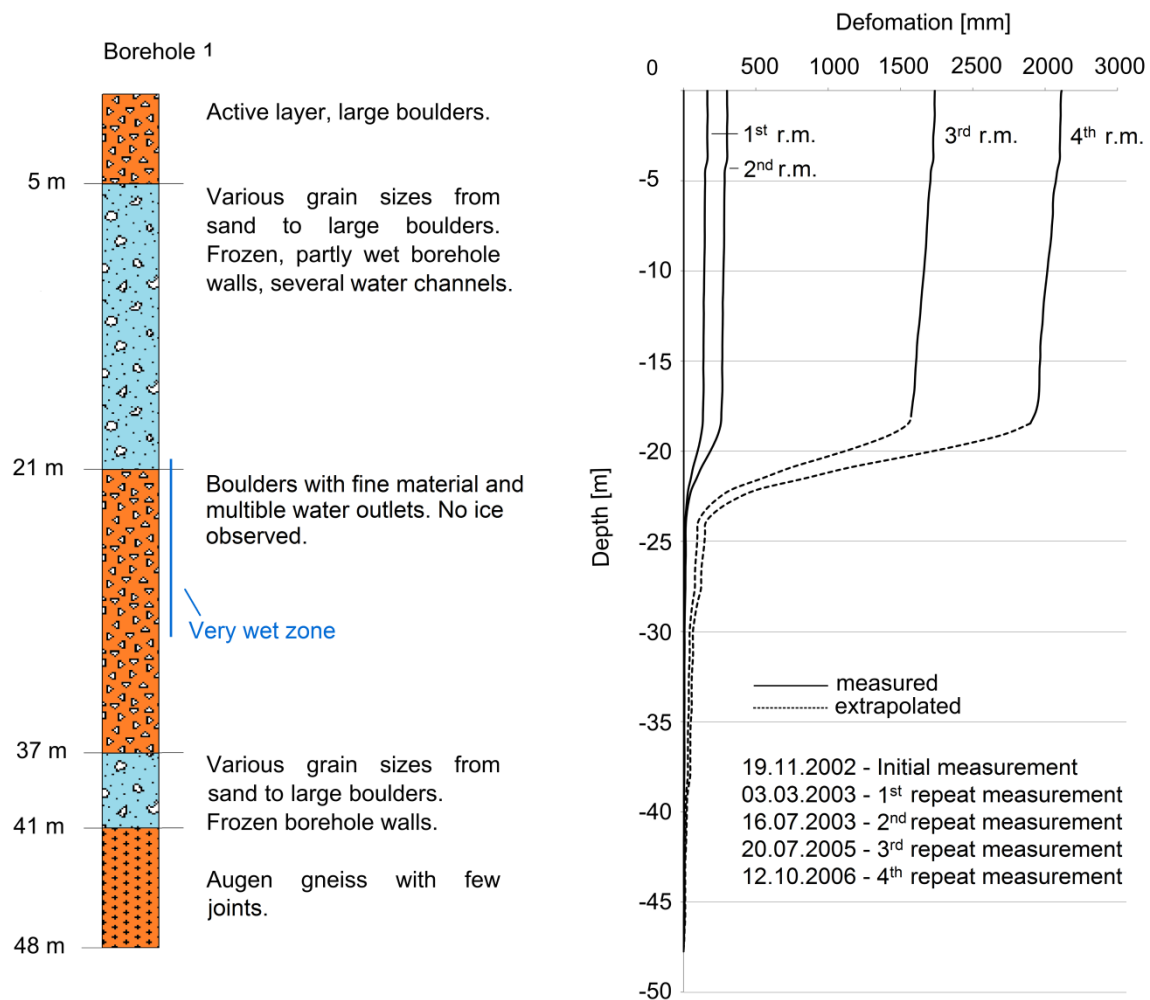
Figure 28: Left: Stratigraphy in borehole B1. Blue colours indicate the presence of ice, and orange ones ice-free rock debris. Right: Inclinometer data from borehole B1 between 2002 and 2006. Data could not be acquired below 19 m during the third and fourth repeat measurements as the shearing process had destroyed the borehole tubing. The surface displacement of the borehole is known from tachymetric measurements. The dashed lines below 19 m in 2005 and 2006 are extrapolated, assuming a fixed ratio relative to the values of the second repeat measurement.

The inclinometer measurements in B1 showed a distinct shear layer at 18-24 m depth, which corresponds to the top of the ice-free layer and the water encountered. In 2003, about 80% of the total deformation occurred in this shear layer, increasing constantly to 93% in 2006 (Figure 28). Below, the deformation was minimal, whereas above a slight deformation between 18 and 4 m was evident, contributing about 20 % to the total deformation in 2003 and 7 % in 2006. The ratio between the deformation in the shear layer and above was measured directly by the first two repeat measurements in 2003. Afterwards, the borehole was destroyed at about 19 m depth and the deformation within the shear horizon was defined by the difference of the surface displacement of the borehole and the deformation in the upper 18 m.

6.4.3 Borehole temperatures

The borehole temperature data (Figure 29) show that the active-layer thickness has remained constant at around 4 m, indicating the presence of ice-rich permafrost below. The lowest thermistor at 30 m depth measured temperatures indicating permafrost before being sheared off. At 11-12 m depth, a seasonal talik has developed since 2007 (Figure 29). Associated with this, an abrupt warming occurred in the permafrost above the talik and a persistent warming trend started below the talik. The occurrence of positive temperatures at 12 m depth were originally attributed to the infiltration of snow melt water and precipitation in summer (Zenklusen Mutter and Phillips, 2012b). However, since 2012 talik temperatures at 12 m depth have increased and remained more or less constantly positive in summer and sporadically positive in winter. Individual snow melt or precipitation events can no longer be discerned thermally. Simultaneously, talik temperatures at 11 m depth have decreased since 2012, whereas permafrost temperatures at the first thermistor below the talik at 13 m depth continued to increase. This indicates downward growth of the talik.
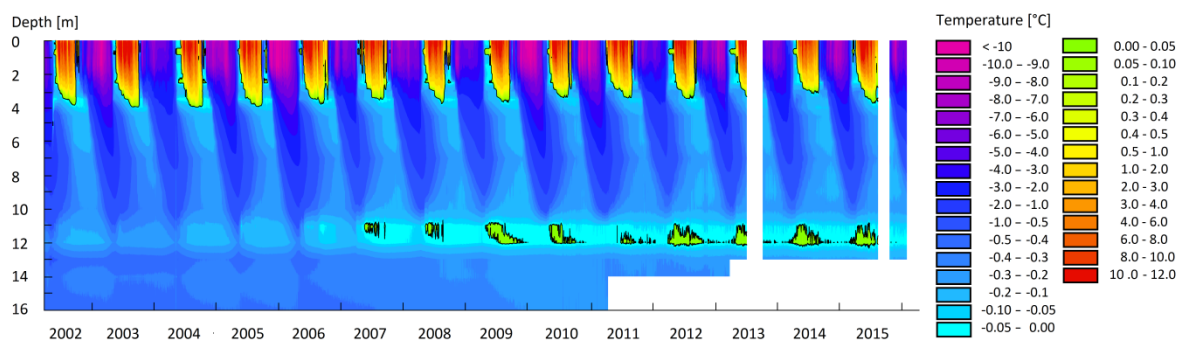

Figure 29: Contoured time series showing ground temperature in borehole B2 between 2002 and 2016.

6.5 Discussion

6.5.1 Seasonal acceleration

The seasonal pattern of the rock glacier velocity at Ritigraben appears to be controlled by water, either from snow melt or rainfall. Conductive energy input at the rock glacier surface reaches the shear layer at approximately 20 m depth with a considerable delay. However, the sudden and sharp acceleration of the rock glacier every spring coincides with the start of snow melt and an increase of temperature in the talik (Figure 30). The laterally induced warming in the talik starts earlier than the conductive warming at the first thermistor above the talik, which indicates that the seasonal acceleration is not controlled by conductive heat transfer. Rock glacier acceleration declines after the end of snow melt and ceases with the onset of the autumn snow cover. During winter, the rock glacier velocity decreases. This seasonal velocity pattern corresponds to observations made on other rock glaciers by Delaloye *et al.* (2010a) or (2006).
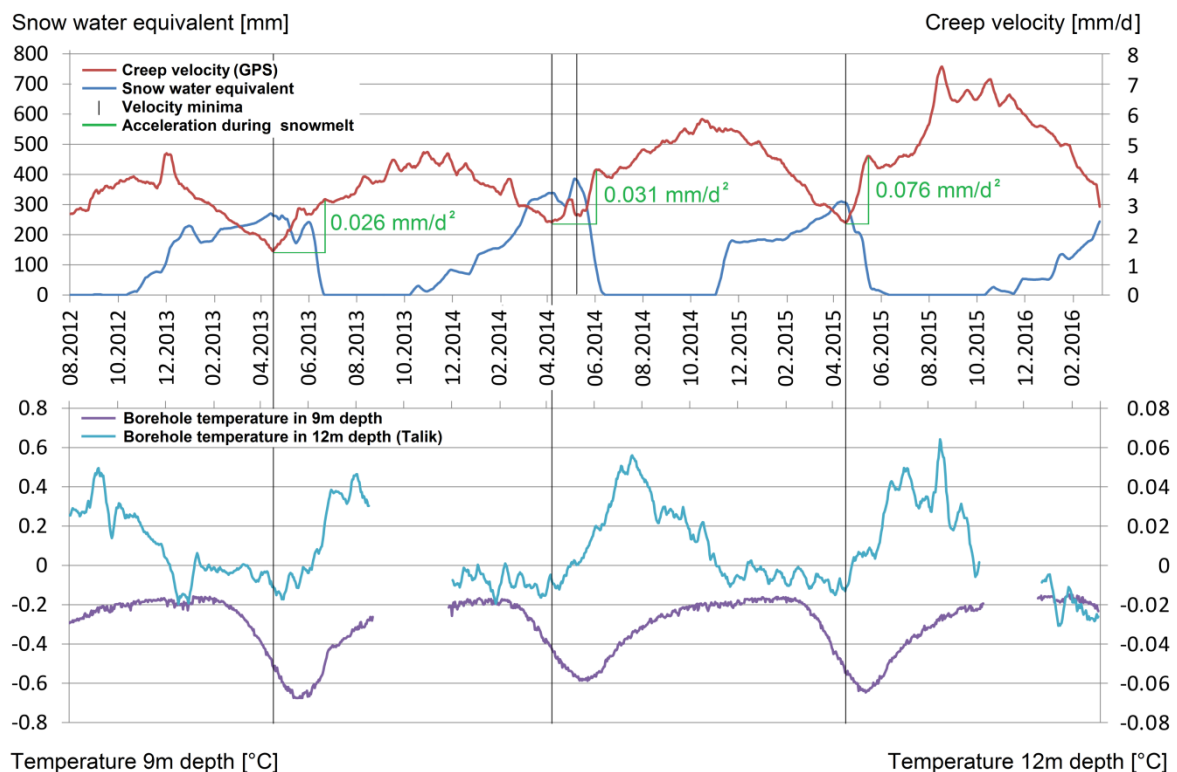

Figure 30: Time series showing the simultaneous onset of snow melt, talik warming and rock glacier acceleration between 2012 and 2016. These accelerations increased during this period despite similar SWE maxima.

6.5.2 Short-term acceleration

In most cases, heavy rainfall triggered short-term acceleration of the rock glacier, although in a few cases the triggering mechanism is unknown. On 9 August 2015, the weather station in Grächen recorded 20 mm of rainfall, an exceptional amount in this dry inner-alpine region, with a return period of 100 days between 2012 and 2016. Simultaneously, the rock glacier moved 16 times faster for just one day before slowing to its former velocity (Figure 26). Other short-term accelerations linked to precipitation are shown in Figure 26 and the two inserts in Figure 25. Two distinct velocity peaks immediately followed heavy rainfall on 29 July and 8 August 2013, and a velocity peak resulting from warming by intense rainfall at high elevations occurred in the last days of April 2014 (Figure 25). However, some rock glacier accelerations are not linked to precipitation, and one surge occurred in winter, on 13 February 2014 (marked with a black ellipse in Figure 25). Abrupt surges such as that on 09 August 2015 suggest that states of internal stress may develop in the rock glacier during the deformation process and are compensated by these surges.

6.5.3 Multiyear acceleration

The displacement data reveal a strong multiyear acceleration of the Ritigraben rock glacier front since 2000. Two triggering factors may explain such acceleration: an increase in permafrost temperature (Ikeda *et al.*, 2003; Kääb *et al.*, 2003) and an increase in water supply from precipitation, or melt of snow or ground ice (Krainer and Mostler, 2006; Roer *et al.*, 2008; Delaloye *et al.*, 2010a). Both factors relate to two processes that are known to deform rock glaciers: shearing within a distinct layer, and internal plastic deformation of the rock glacier body due to the viscosity of the permafrost ice (Hausmann *et al.*, 2007; Roer *et al.*, 2008; Delaloye *et al.*, 2010a). Shearing is influenced by water supply and water pressure controlling the frictional resistance in the shearing zone (Harbor *et al.*, 1997). Plastic deformation depends on the mechanical characteristics of the permafrost ice: warming can cause significant changes in the viscosity, hardness, shear- and crushing strength of polycrystalline ice (Barnes *et al.*, 1971; Hobbs, 1974; Arenson and Springman, 2005) and, theoretically, can therefore trigger rock glacier acceleration. Both shearing and plastic deformation are indicated by inclinometer measurements in rock glacier boreholes (Arenson *et al.* (2002).

At the front of the Ritigraben rock glacier shearing has dominated movement. Its contribution to the total surface displacement increased between 2002 and 2006: 1st repeat measurement (r.m.) 81% contribution; 2nd r.m. 87%; 3rd r.m. 91%; 4th r.m. 93% (Figure 28). Consequently, the shearing process has accelerated and contributed to the overall

acceleration of the rock glacier. Shearing is controlled by water supply, as shown for the short-term and seasonal accelerations, discussed above. This interpretation is supported by the stratigraphic data in borehole B1 (Figure 28), which show that the shear layer is located in a very wet transition zone between the permafrost body and an unfrozen zone below, containing several water-bearing horizons. We assume that this shear layer represents a partly water-saturated continuum between ice-rich permafrost and ice-free rock debris.

Plastic deformation seems to have played no role in the long-term acceleration, although a slight permafrost warming of 0.2°C below 10 m depth occurred since 2002. Between 2002 and 2006 the absolute borehole displacement values due to plastic deformation did not increase significantly (1st r.m. 107 mm/a; 2nd r.m. 106 mm/a; 3rd r.m. 80 mm/a; 4th r.m. 146 mm/a; see Figure 28). The slight permafrost warming in borehole B2 was at least partly induced by the talik formation and it is unclear whether conductive heat flow resulting from atmospheric warming contributed to it.

Although water seems to control the long-term acceleration of the rock glacier, no obvious increase in water supply to it is evident. Annual precipitation sums in Grächen decreased during the GPS/TLS monitoring period (2013: 630.7 mm; 2014: 588.1 mm; 2015: 531.5 mm), and SWE maxima did not increase significantly (Figure 30). A large input of water from subsurface ice melt can also be excluded because the active-layer thickness in borehole B2 was constant and the TLS data showed no signs of surface subsidence in the small catchment above Ritigraben. We therefore considered an alternative explanation: increasingly long periods with rainfall (instead of snowfall) might lead to longer periods with liquid water in the system and so to longer periods of rock glacier acceleration and shorter periods of deceleration. Surprisingly, the opposite applied at Ritigraben. During the three seasonal cycles with GPS measurements the duration of deceleration per cycle increased, despite the overall acceleration trend.

Although the seasonal duration of rock glacier acceleration did not increase, its magnitude did. The GPS velocity time series shows that the multiyear acceleration is manifested mainly by a strong increase of the maximum velocities in summer and autumn, and less by the winter velocities (Figure 30). Simultaneously, the strong acceleration during snow melt as well as the surges during rainfall events increased in magnitude during the observation period (see acceleration values in Figure 30). Although the water supply did not increase, the efficiency of acceleration triggered by the same amount of water clearly increased. This can be explained by an increasing amount of runoff reaching the shear layer of the rock glacier via flow channels, evident in the Ritigraben borehole data in the form of a water-bearing talik

(Zenklusen Mutter and Phillips, 2012b). This new drainage system most likely explains the higher sensitivity of the rock glacier velocity to water supply and hence the acceleration.

Internal drainage development may help explain the overall acceleration trend of most rock glaciers in the European Alps. Borehole temperatures show that most Swiss rock glaciers have reached temperatures close to 0°C in the last decades (PERMOS, 2016). At these temperatures no refreezing can occur and additional energy input contributes to ice melt. These are optimal conditions for the development of taliks in the form of new runoff channels permeating the permafrost body and ensuring a more effective supply of water to the shear layer or the base. Ground-ice melt may also increase the water supply in some cases. Rising temperature of permafrost ice may indirectly influence acceleration but does not directly force it, at least where shearing dominates. Temporal correlations between mean annual air- or permafrost temperatures and rock glacier deformation velocity (Kellerer-Pirklbauer and Kaufmann, 2012; Nickus *et al.*, 2015) are therefore reasonable but do not necessarily occur, as shown by Roer *et al.* (2005) or this study.

Changes in viscosity due to higher ice temperature would cause a more constant and smoother long-term acceleration. Studies which attribute rock glacier acceleration to higher permafrost temperature focus on the internal plastic deformation of the permafrost (Kääb *et al.*, 2007; Ikeda *et al.*, 2008). But this is usually the less dominant process contributing to rock glacier deformation (Arenson *et al.*, 2002; Krainer *et al.*, 2015). Internal plastic deformation is linked to a local overloading of a viscous material (Jiskoot, 2011), and this overloading most likely occurs in the root zone of a rock glacier, where snow and rock material accumulate. As a consequence, internal plastic deformation is likely to be most pronounced close to the rock glacier root zone and act as a "pushing force", initiating the more important process of shearing (Figure 31).

6.6 Conclusions

Water fluxes in the permafrost of the Ritigraben rock glacier appear to influence rock glacier velocity variations at short-term, seasonal and multiyear time scales. The rapid and pronounced acceleration of the rock glacier during rainfall or snow melt suggest a decrease in the frictional resistance in the shear layer by water, which favours shearing. This shear layer is located at the base of an ice-rich permafrost body and several water-bearing horizons were found when drilling through it.

The long-term acceleration of the rock glacier is likely affected not by the amount of water entering it, but by the efficiency of funnelling water towards the shear layer. This funnelling

is controlled by the development of run-off channels inside the permafrost body, such as the talik depicted by the borehole B2 temperature data. Changes in permafrost temperature only affect deformation velocity indirectly at this site: the warming of permafrost close to 0°C favours the development of new runoff channels towards the shear horizon and expedites water supply to this zone. This explains the increasingly higher sensitivity of the Ritigraben rock glacier to rainfall or snow melt. This might be similar for other rock glaciers with a dominant shearing component in the deformation movement and may help explain the widespread rock glacier acceleration during the last decades in the European Alps.
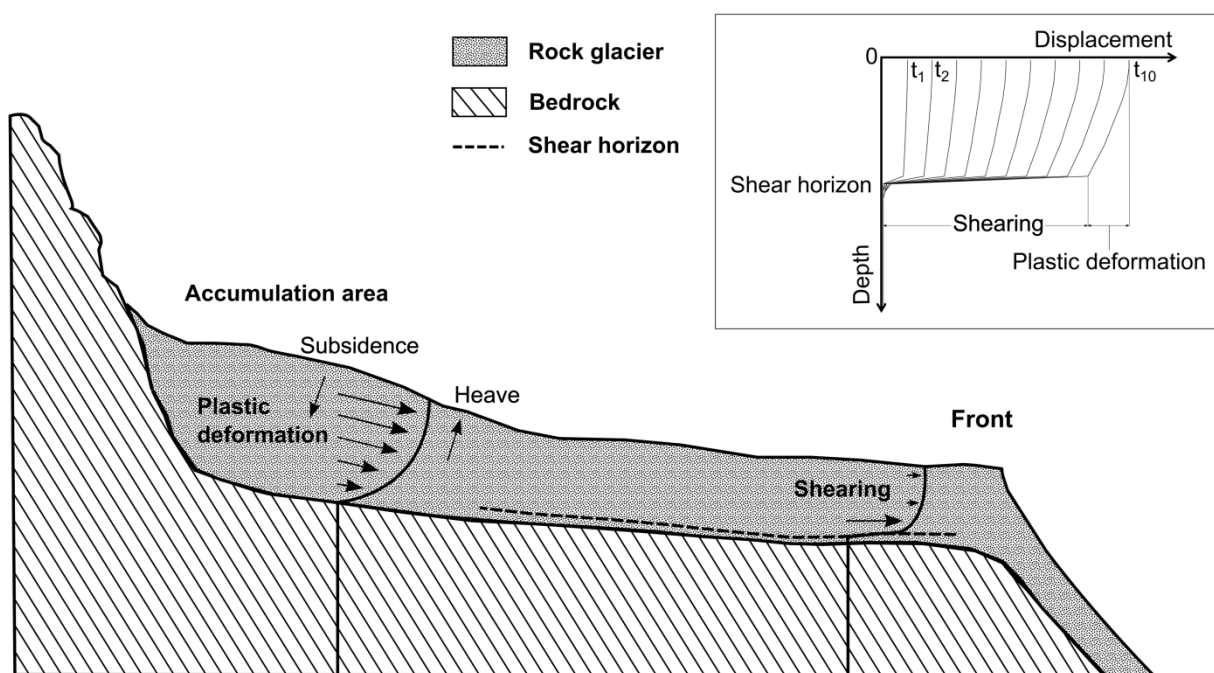

Figure 31: Schematic diagram showing a deformation profile of an idealised rock glacier. Close to the root zone, plastic deformation dominates due to the local overloading by rock fall deposits. The internal deformation of the viscous material corresponds to a gravitationally influenced power law fluid. The deformation rates increase towards the surface, causing surface subsidence in the area of overloading and surface heave at the front of the downslope propagating mass. Due to the thinning of the moving layer, plastic deformation decreases further downslope and basal shearing becomes the dominant deformation process.

Acknowledgements

7. The influence of precipitation on ice-rich permafrost: consolidation of the findings and paleo-geomorphologic implementations

Focusing on the factor precipitation, the last two studies revealed two interesting effects. On the one hand, high precipitation values arrest the formation of rock glaciers. On the other hand, high water supply, e.g. by precipitation can cause a considerable acceleration of rock glaciers. This might have a strong effect on the size and distribution of active and relict rock glaciers in the Alps.

In our GIS analysis on rock glacier influencing factors (Chapter 5) we recorded relict rock glaciers in the Albula Alps. This work was extended to the Plessura Alps. The Plessura Alps border on the Albula Alps in the North and receive more precipitation than the Albula Alps, especially from northern currents (Figure 32). Differences in precipitation are also present within the Albula Alps. As it constitutes the main Alpine ridge, the northern parts receive more precipitation from northern currents, while the southern parts are more strongly affected by southern currents.
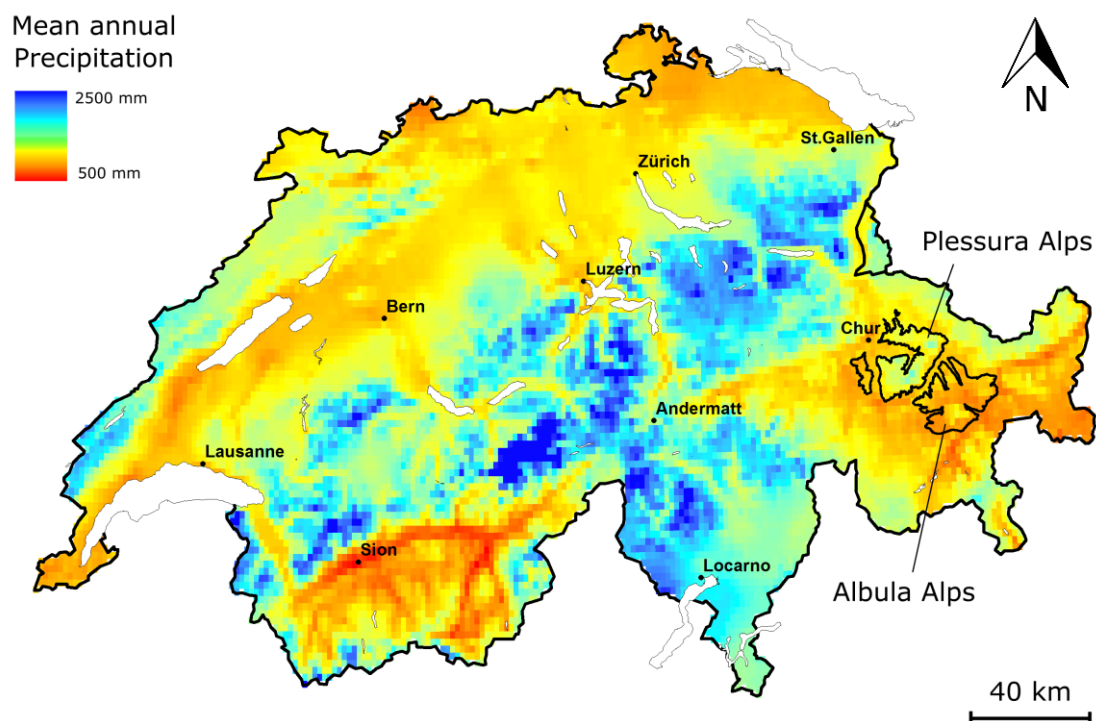

Figure 32: Mean annual precipitation sums in the Albula Alps and Plessura Alps (Data: Norm value charts (1981-2010) provided by Meteoswiss)

Interestingly, the ratio relict to active rock glaciers is much higher in the northern parts of the Albula Alps. Even stronger is the contrast between the Plessura Alps and the Albula Alps: Relict rock glaciers are much more common in the Plessura range, both absolutely and relative to their active neighbours (Table 9). Additionally the elevation difference between the lower borders of relict and active rock glaciers is much higher in the Plessura Alps compared with the Albula Alps (Table 9). Frauenfelder and Kääb (2000) made similar observations. They also measured the difference in front elevation between active and relict rock glaciers and interpreted this difference as sign of climate warming since the active phase of the relict rock glaciers. They did this for different regions and the elevation differences varied considerably between these regions: The highest elevation differences were found for the northern regions of the Prealps (corresponds to a temperature increase of 5°C) and Bernese Alps, the lowest for the inner alpine regions (corresponds to a temperature increase of 1°C, see Figure 6 in Frauenfelder and Kääb, 2000). It is rather unlikely that the temperature increase since the active phase of relict rock glaciers was five times higher in the Prealps than in the inner alpine regions. However, the current climate is characterised by clearly different precipitation rates in inner alpine regions and the northern edge of the Alps. The question therefore arises whether it is possible that precipitation is the deciding factor for the elevational distribution of active and relict rock glaciers, rather than air temperature.

Table 9: Size and spatial distribution of relict versus active rock glaciers differ considerably between the Albula Alps and the Plessura Alps.

	Albula active rock glaciers	Albula relict rock glaciers	Plessura active rock glaciers	Plessura relict rock glaciers
Elevation belt of rock glaciers (mean) [m.a.s.l.]	2260 - 3110 (2650)	2070 - 2910 (2456)	2273 – 2760 (2525)	1759 - 2767 (2290)
Elevation difference between relict and active rock glaciers: Δ lowest occurrence (Δ mean altitude)	+190 (+194)	-190 (-194)	+515 (+235)	-515 (-235)
Rock glacier surface, absolute [km²] (Relative to site area [%])	13.552 (3.75)	14.109 (3.91)	1.060 (0.29)	19.512 (5.42)
Active rock glacier area relative to relict rock glacier area [%]	96	100	5	100

At the end of the Younger Dryas large parts of northern Europe lay under an ice shield. The Baltic and the North Seas were considerable smaller than today and the British Islands were part of the continent (Adams, 1997). The North Atlantic was colder and covered with sea ice at latitudes over 55° (Dansgaard *et al.*, 1989). During the transition to the subsequent Preboreal Interval the climate system of the North Atlantic changed rapidly within a few decades following Dansgaard *et al.* (1989). Decreasing sea ice and warming of sea water led to a doubling of snow accumulation on the Greenland ice sheet as described by Alley *et al.* (1993). In the ongoing Holocene, large sea areas developed in northern Europe due to the melting polar ice shields and the 60 m global sea level rise during the early and middle Holocene (Smith *et al.*, 2011). Combined with higher air temperatures these changes led to a higher supply of moisture, especially for currents reaching the Alps from the North. Higher precipitation rates in the Alps could initially have led to higher rock glacier creep velocities. This could have contributed to relatively low front elevations. In the long term, a secondary effect of the high precipitation rates could have become effective: an increased evolution of rock glaciers from the active to the relict state. As higher precipitation rates from the North affected the northern Prealps strongest, this process was much more intense here, compared with the inner Alpine regions. This might explain the differences between both regions regarding the spatial distribution and frequency of active and relict rock glaciers.

Concluding our findings, precipitation influences the deformation velocity, the size and the spatial distribution of rock glaciers. This distinct effects of precipitation should be carefully considered by rock glacier research.

8. New insights on permafrost genesis and conservation in talus slopes based on observations at Flüelapass, Eastern Switzerland

Robert Kenner[1], Marcia Phillips[1], Christian Hauck[2], Christin Hilbich[2], Christian Mulsow[3], Yves Bühler[1], Andreas Stoffel[1], Manfred Buchroithner[4]

[1] WSL Institute for Snow and Avalanche Research SLF, Davos Switzerland
[2] Department of Geosciences University of Fribourg, Switzerland
[3] Institute of Photogrammetry and Remote Sensing, Dresden University of Technology, Germany
[4] Institute of Cartography, Dresden University of Technology, Germany

Personal contributions:

Robert Kenner: Paper idea and concept; Data collection and analysis; TLS acquisition and processing; Geomorphological analyses; Discussion

Marcia Phillips: Borehole temperature measurements; Geomorphological analyses, Automatic photographs; Scientific assistance

Christian Hauck: Geophysical measurements; Scientific assistance

Christin Hilbich: Geophysical measurements; Scientific assistance

Christian Mulsow: Subaquatic DEM processing

Yves Bühler: Aerial image acquisition

Andreas Stoffel: Aerial image acquisition

Manfred Buchroithner: Idea of Subaquatic DEM; Scientific assistance

Abstract

The talus slope at Flüelapass was the first mountain permafrost study site in Switzerland in the 1970s and the presence of ice-rich permafrost at the foot of the slope has been investigated in the context of several studies focusing on the role of snow cover distribution. We carry out a review of previously developed hypotheses and present new ones using various data sources, such as borehole temperature measurements, a subaquatic DEM generated from unmanned aerial system (UAS) photogrammetry, terrestrial laser scan measurements of snow depth, geophysical ground investigations and automatic time-lapse photography. Together with observations in the field, this combination of data sources allows to establish an interesting sequence of geomorphologic processes at Flüelapass. As a result we show how mass wasting processes can initiate the genesis and long-term conservation of ice-rich permafrost at the base of talus slopes.

8.1 Introduction

The lower fringe of mountain permafrost is often characterized by permafrost talus slopes or by rock glaciers with the root zone located in ice-rich permafrost talus slopes (Delaloye and Lambiel, 2005; Lambiel and Pieracci, 2008; Gruber and Haeberli, 2009). Permafrost in these landforms is, therefore, preferentially used to calibrate models of the local distribution of permafrost (Etzelmüller *et al.*, 2001; Gruber and Hoelzle, 2001; Boeckli *et al.*, 2012; Sattler *et al.*, 2016) or to analyse the consequences of climate change on mountain permafrost (Springman *et al.*, 2012; Monnier and Kinnard, 2016). The processes controlling the presence of permafrost in talus slopes, especially at elevations in the lower belt of the local permafrost environment are, thus, of particular interest. The talus slope at Flüelapass was the first site at which systematic research into mountain permafrost was carried out in the Swiss Alps and was first investigated by Haeberli (1975). Haeberli carried out extensive refraction surveys here and discovered the presence of ice-rich permafrost along the foot of the talus slope. This was later confirmed by vertical electrical soundings carried out by King et al. (1987). Furthermore, Haeberli (1975) showed a spatial correlation between thaw depth and perennial avalanche snow deposits: At the time of observation, the thaw depth was thinner at locations with perennial avalanche snow. This observed spatial relation led to the hypothesis that permafrost at the foot of talus slopes is present because of the insulating effect of superimposed perennial snow fields against radiation and atmospheric warming (Haeberli, 1975). We henceforth refer to this as the "insulation theory". This was adopted by other studies carried out at Flüelapass. Lerjen *et al.* (2003) supplemented the hypothesis by adding the effect of soil properties (organic material vs. rock and gravel) on the thermal regime of the ground. Luetschg *et al.* (2004) analysed ground temperature simulations, ground surface and borehole temperature measurements and found that a delay in snow melt influences the active layer temperatures. This was interpreted as a confirmation of the insulation theory. Lerjen *et al.* (2003) and Luetschg *et al.* (2004) cited the effect of snow erosion by wind as a ground cooling factor in the Flüela talus slope but did not specifically show a spatial correlation between the distribution of permafrost and the spatial pattern of wind erosion.

Ice-rich permafrost often occurs at the foot of talus slopes (e.g. Lambiel and Pieracci, 2008; Scapozza *et al.*, 2011). The insulation theory is one of two general explanations for this spatial niche of permafrost. The second explanation refers to air ventilation in talus slopes. Several studies have shown that ventilation can lead to substantial ground cooling in talus slopes and might contribute to permafrost conservation or development (Delaloye and Lambiel, 2005; Zacharda *et al.*, 2007; Morard *et al.*, 2010; Gadek, 2012; Schneider *et al.*,

2012; Niu *et al.*, 2016; Wicky and Hauck, 2016). On the basis of borehole temperature measurements Phillips et al. (2009) also demonstrated the occurrence of a ventilation effect underneath the perennially frozen part in the Flüela talus slope, but showed that it mostly causes positive temperatures in the voids in winter, thus contradicting a development of permafrost by ventilation at this site.

Snow coverage has changed at the Flüela site in recent decades: whereas perennial avalanche deposits at the base of the slope were the normal case in the 1970s according to Haeberli (1975), no perennial snow has occurred for the last 14 years at least, according to time-lapse images taken by an automatic camera. Data availability has significantly improved since the 1970s; e.g. borehole temperatures, geophysical soundings or remote sensing data and the length of observation periods have increased, allowing a critical verification of the hypotheses made in the past. It is still unclear whether a substantial effect of avalanche snow or wind driven snow redistribution occurs on the presence of ice-rich permafrost. Based on the improved dataset presented here, we will discuss whether the insulation theory is indeed the most relevant explanation for permafrost in the Flüelapass talus slope and present an alternative hypothesis which may be relevant for other sites with ice-bearing talus slopes. A key question here: what is the origin of the excess ice in the Flüela talus slope?

8.2 Site description and geomorphological history

The talus slope at Flüelapass is located on the NE flank and at the base of the summital rock wall of "Chlein Schwarzhorn", a 2986 m high peak in the eastern Swiss Alps (46°44'37.804"N 9°56'13.758"E). The foot of the talus slope at 2375 m a.s.l. forms the eastern shore of lake Schottensee, which has an area of 83'000 m^2 (Figure 33). Two 20 m vertical boreholes were drilled in the slope in 2001; the upper one (B1) is 125 m above the lake at 2501 m a.s.l., and the lower one (B2) is 20 m above the lake at 2394 m a.s.l. Around B1 the slope is covered with soil and grass and positive temperatures are registered throughout the borehole (no permafrost), whereas the foot of the slope around B2 is devoid of vegetation, covered in talus and has negative temperatures between 3 and 10 m depth (permafrost). The stratigraphies of both boreholes are presented in Phillips et al. (2009) and apart from the surface and the ice content they are very similar, with rocks and gravel and a very blocky layer that is a few metres thick around 10 m (B1) and 15 m (B2) depth, respectively. The grain sizes of the talus at the surface of B2 range between 10 and 40 cm.

The lower quarter of the slope is a snow avalanche deposit zone and avalanche snow often persists here for long periods of the summer.

A series of interesting landforms at Flüelapass reveal the history of the site and help to elucidate the genesis of permafrost ice at the bottom of the talus slope. These landforms are highlighted on the orthophoto in Figure 34. There is a conspicuous shallow channel around B2, delimited by two sharply defined parallel escarpments. These escarpments are oriented parallel to the slope and reach from the lower third of the talus slope to the lake shore. We have observed similar channels with sharply defined escarpments in talus slopes at other sites. Figure 35 shows a similar feature at a talus slope at Piz Corvatsch (Eastern Swiss Alps), close to the Murtèl rock glacier (Haeberli *et al.*, 1998). A distinct lobe is evident directly below the shallow channel at Piz Corvatsch. Unpublished terrestrial laser scanning (TLS) and electric resistivity tomography (ERT) measurements we carried out indicate that the Corvatsch lobe is creeping downslope and contains ice. It is, therefore, very likely that the loose rock material forming the lobe originates from the shallow channel above and was displaced by permafrost creep.
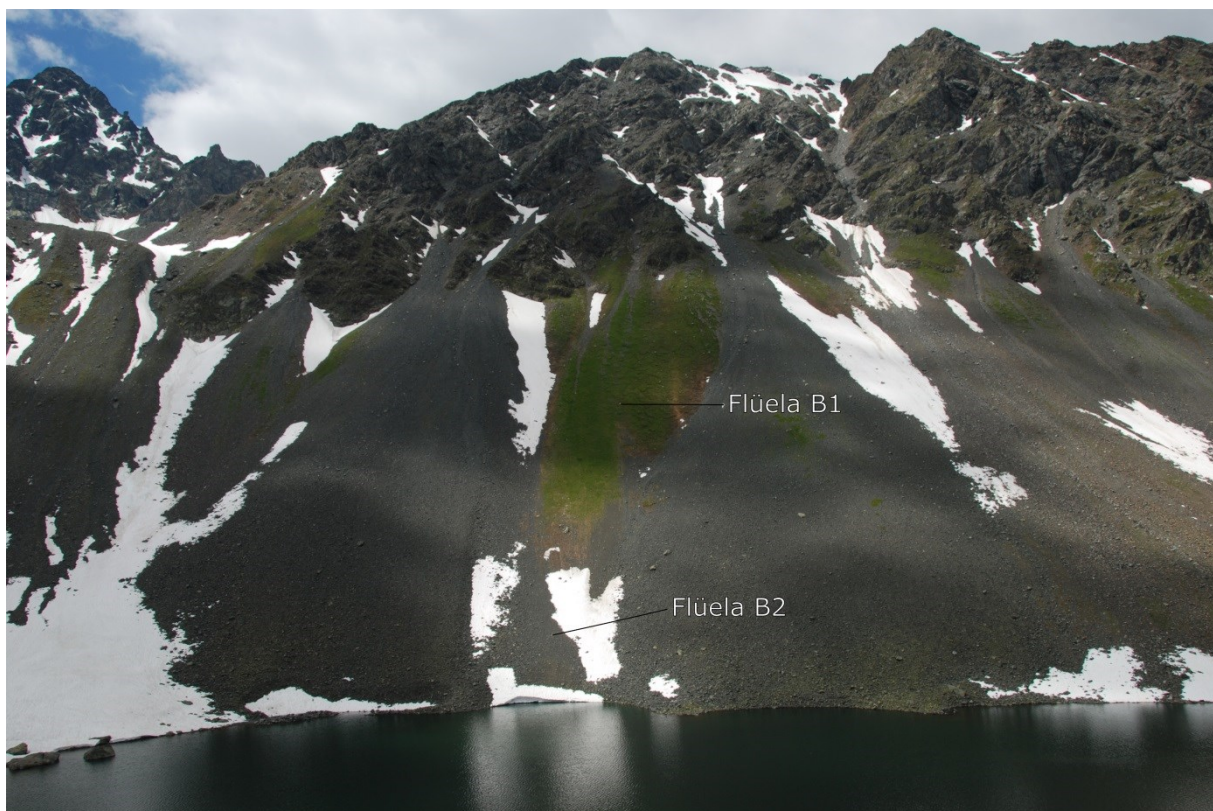
Figure 33: Photograph showing the Flüela talus slope on 13.07.2009 with the positions of the two boreholes. The pattern of snow melt out is quite complex (Photograph: M. Phillips).

Spring

Mega ripples
(Figure 6)

Rock fall
deposit

Current lake outflow

Debris flow deposits

Schottensee

Flüela talus slope

Thermokarst
depression*

Lobe*

B2

Shallow channel

Escarpments

B1

swissimage©2014 swisstopo (5704 000 000)
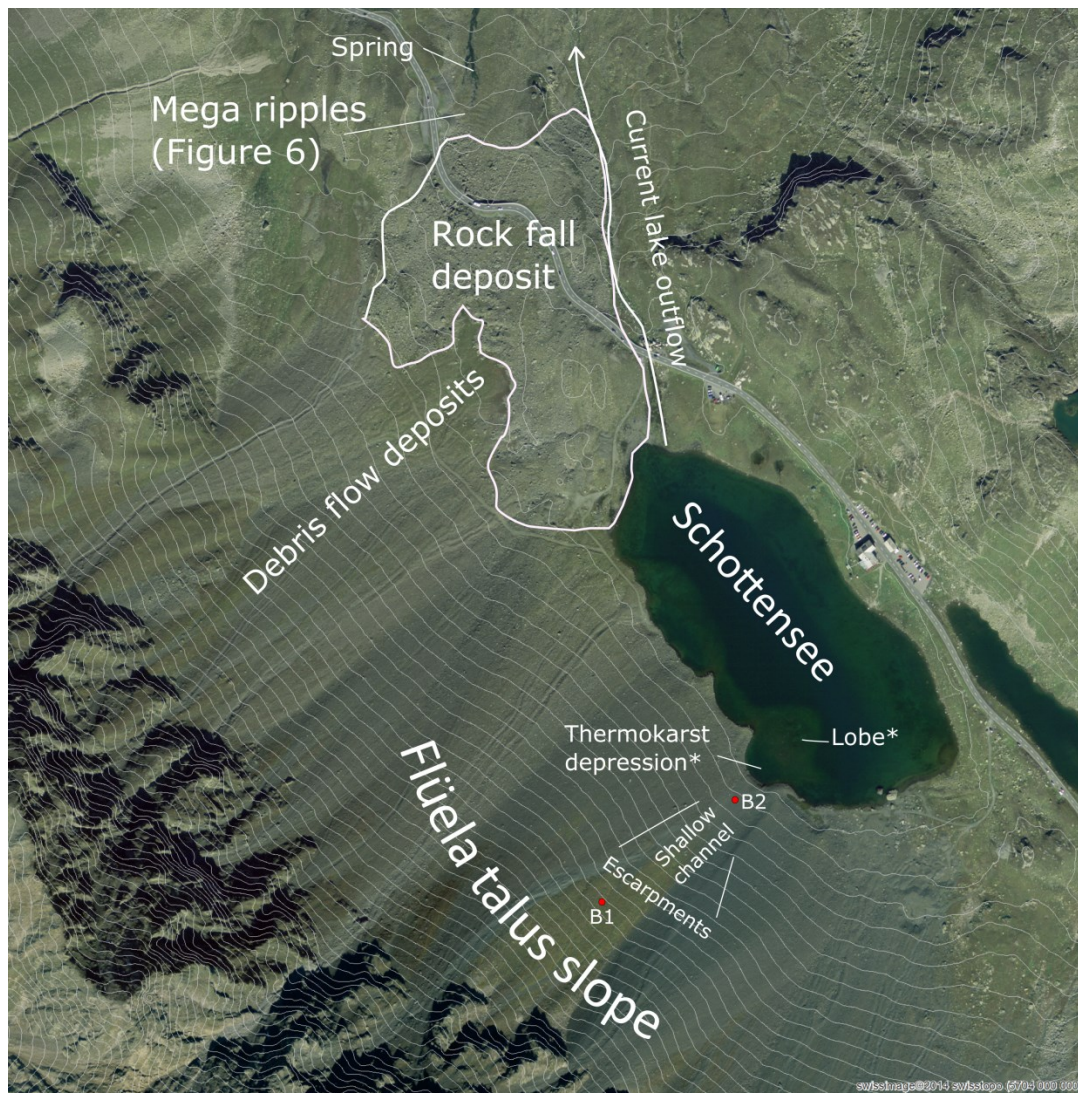
↑ *Figure 34: Orthophoto of the Flüelapass site with mapped landforms. Each of these features is discussed in the study (orthofoto: swissimage©2014 swisstopo (5704 000 000).*

Creeping lobe

Shallow channel

Edges of channel
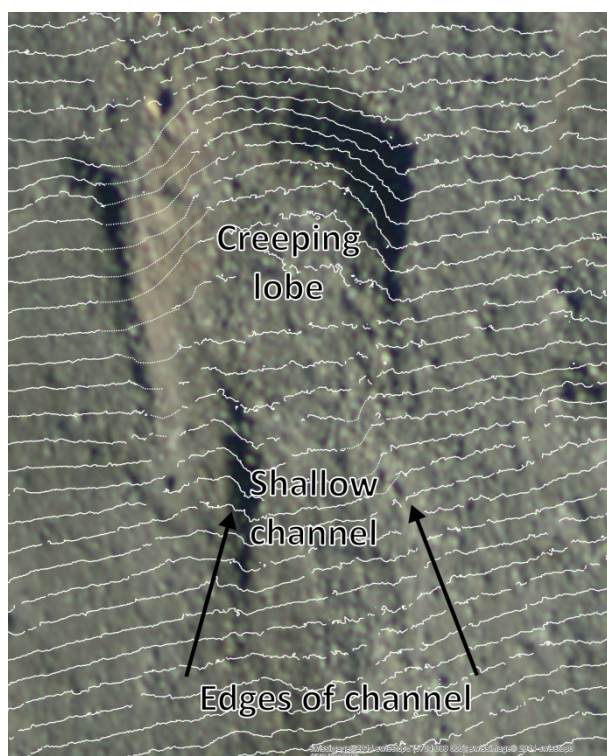
← *Figure 35: Example of a creep lobe at Piz Corvatsch, which is similar to that at Flüelapass (orthofoto: swissimage©2014 swisstopo (5704 000 000).*

116

At Flüelapass a similar lobate form is also evident below the shallow channel, at the lake bottom. The orthophoto in Figure 36, acquired by UAS borne photogrammetry shows this lobe, which encloses a deep depression in the lake. Based on the morphology (Haeberli, 1985) we consider both lobate features at Piz Corvatsch and Flüelapass as being small rock glaciers.

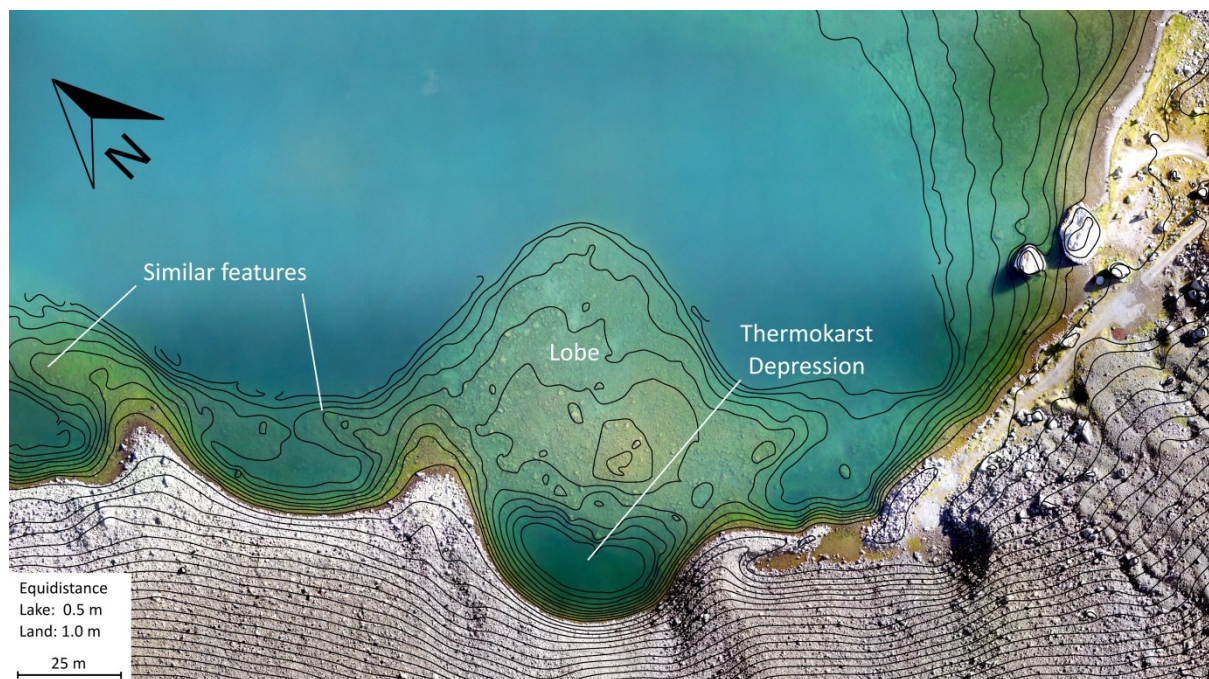*Figure 36: Orthophoto created from UAS imagery with the contour lines of the corresponding (subaquatic) DEM. The underwater lobe constitutes the front of a relict rock glacier with a deep thermokarst sink in its centre (Photograph SLF UAS, 2016). Similar features are visible along the lake shore.*

Rock glaciers cannot form under water, as the water temperature would lead to ice melt (Haeberli *et al.*, 2001). The only explanation for the underwater rock glacier at Flüelapass is, therefore, that the lake is younger than the rock glacier. This in turn explains the deep depression in the underwater lobe. After the lake flooded the rock glacier, the ground ice melted and a thermokarst depression developed. The rock glacier front and side walls which contained less or no ice now form the underwater lobe with 45° steep side walls (Figure 37). Similar features are visible all along the SW lakeshore, indicating widespread permafrost creep at the base of the talus slope in the past (Figure 34 and 36). The sizes and positions of the lobes correspond to the main deposition areas of snow avalanches.

At the NW end of the lake there is a field of large rocks and boulders with a distinctly rougher texture than the neighbouring talus slopes (Figure 34). This area is clearly the deposition zone of a large rock fall originating from the rock wall NW of the lake. This deposit likely blocked the northward runoff from Flüelapass and dammed the lake (Suchlandt and

Schmassmann, 1936) which then flooded the rock glacier. At the Eastern side of the rock fall deposit a new stream channel has developed (Figure 34). A part of the lake runoff is however still discharged under the rock fall deposit and is released by a spring at the N lower end of the rock fall deposit. Directly around and below the spring, a series of ripple-like features are evident with a wave length of approximately 6 m (Figure 38). These are probably mega-ripples, which are formed by flood waves released during a lake outburst (Burr *et al.*, 2009). Hence, rock fall event(s) and the subsequent lake formation were probably followed by a partial lake outburst here. Similar ripples are also known to be formed by permafrost creep (Frehner *et al.*, 2015). Other geomorphologic characteristics of a relict rock glacier are however missing here.

← Figure 37: The steep front of the flooded rock glacier at the foot of the Flüela talus slope (Photograph: M. Schaer, 08.10.2012).

↓ Figure 38: Mega-ripples around the spring below the rock fall deposit at Flüelapass, which may have been formed by a lake outburst after the rock fall which dammed the lake (Photograph: R. Kenner, 28.09.2016).

8.3 Methods:

8.3.1 Temperatures in boreholes

The boreholes at Flüelapass were equipped with thermistor chains (with 12 YSI 44008 thermistors) and a Campbell CR10X data logger. Temperatures are measured every 2 hours at 0.25, 0.5, 1.0, 1.5, 2.0, 3.0, 4.0, 6.0, 8.0, 10.0, 15.0 and 20.0 m depth. In February 2016 the thermistor chain was removed from B2 for recalibration and it was found that the thermistors at 6.0, 8.0, 10.0 and 15.0 m depth had been subject to a slow but distinct temperature drift (causing artificially high temperatures to be registered). This problem can be induced by moisture in the thermistors and tends to start slowly and increase exponentially (Luethi and Phillips, 2016). Recalibration of this thermistor chain and measurements made from July 2016 onwards with a new thermistor chain indicate that the drift was such that the postulation made by Phillips *et al.* (2009) regarding the occurrence of permafrost degradation from the base upwards is likely wrong and that the ground ice is still intact to a depth of approximately 10 m. It is difficult to determine the exact time at which drift started.

Borehole temperatures are used to define the thickness of permafrost and active layer (AL). Furthermore, we calculated thermal orbits by plotting temperatures of neighbouring thermistors against each other. The shape of these orbits gives indications on the type of heat transfer occurring (Beltrami, 1996; Smerdon *et al.*, 2009; Zenklusen Mutter and Phillips, 2012b). The end of snow melt dates are defined by the date at which the spring zero curtain ends at 0.25 m depth. We defined the maximal thickness of the AL by linear interpolation between the lowest thermistor in the AL and the uppermost thermistor in the permafrost. Linear interpolation might not be appropriate to find the absolute thickness of the AL but gives an indication of the variability of AL thickness over time.

8.3.2 Geophysics

In addition to early refraction seismic surveys (Haeberli 1975) and vertical electrical soundings (King, 1987) at the Flüela talus slope, new geophysical surveys were conducted in summer 2009 with the aim to map the spatial distribution of ground ice in the talus slope in more detail. We used electrical resistivity tomography (ERT) and refraction seismic tomography (RST), as both methods are highly sensitive to the transition from unfrozen to frozen materials and, thus, well suited to identify ice-rich permafrost (e.g.Kneisel and Schwindt, 2008).

ERT data were obtained along a vertical profile that crossed both borehole positions and three parallel horizontal profiles in the lower part of the talus slope. The measurements were carried out using a *Geotom* multi-electrode instrument (Geolog) and 75 electrodes with 4 m spacing (resulting in 296 m profile lines). Measurements were performed in the Wenner-Schlumberger configuration, as a good compromise between spatial resolution and high signal-to-noise ratio. Data processing was conducted with filtering procedures and choice of inversion parameters as detailed e.g. in (Hilbich *et al.*, 2011). Data inversion (i.e. the calculation of the specific resistivity model of the subsurface based on the measured apparent resistivities) was performed using the Software *Res2DInv* (Loke 2012).

In addition, RST data were collected parallel to selected ERT profiles, but with smaller extent and penetration depth. We used a 24 channel *Geode* instrument (Geometrics) with a sensor spacing of either 4 or 5 m (resulting in 92 and 115 m profile lines) and shot points every 8 or 10 m, respectively. Tomographic inversion was performed using the software ReflexW (Sandmeier, 2014). First arrival picking and choice of inversion parameters were conducted as described in Hilbich (2010).

Although the RST method often reveals less detailed structural information of the subsurface, it provides valuable complementary data in ambiguous situations (e.g. Hilbich, 2010). Especially in talus slopes (or other coarse blocky landforms) resistive anomalies can usually be interpreted as zones with high porosity, but it cannot always be determined whether they are predominantly air- or ice-filled voids. In contrast, seismic velocities of air and ice differ by one order of magnitude and ice-rich anomalies can usually be well distinguished from zones with air-filled voids (Kneisel and Hauck, 2003; Hauck and Kneisel, 2008; Kneisel and Schwindt, 2008).

8.3.3 Subaquatic digital elevation model from UAS borne photogrammetry

A digital elevation model (DEM) and an orthophoto of the base of the talus slope and of parts of the lake bottom were calculated from aerial images acquired with a Sony NEX-7 camera (24 Mp, 20 mm F/2.8 optical lens), mounted on an Ascending Technologies (AscTec) Falcon 8 octocopter (Bühler *et al.*, 2016). We obtained a DEM resolution of 4 cm and an orthophoto resolution of 2 cm. The images were taken on 08.09.2016 from around 100 m above ground with an overlap of approximately 75% along track and 65% across track. Eight ground control points were integrated in the set of images, whose coordinates were defined using a Topcon GR5 GNSS receiver in real time kinematic mode. For image orthorectification and the generation of a georeferenced 3D point cloud of the ground surface the Agisoft software

PhotoScan Pro v1.2.6 was used. Additionally we carried out point reference measurements of the water depth, using a sounding pole and the Topcon GR5 GNSS receiver.

When comparing the reference depth measurement with the 3D-data derived from aerial images, the effects of optical refraction on the water surface are quite prominent (Rinner, 1969). This leads to an underestimation of water depth, because the image ray path is assumed to be a straight line in PhotoScan, which is only valid for land-points (Buchroithner, 1991). In our case, the differences reached values from ~ 0.3 m for water depths of about 1.3 m up to ~ 0.8 m for depths of 2.8 m. This means that the refraction has to be considered for subaquatic points. Unfortunately, most commercial software cannot provide this function. Therefore a special software was developed at the Institute for Photogrammetry and Remote Sensing at TU-Dresden (Mulsow, 2010) for the processing.

The results from PhotoScan were used as initial values for image orientation, camera calibration data and the DEM. New image points were automatically measured in the photographs and classified as subaquatic or land-points. The water surface was modelled as a plane, with its height determined from the GNSS measurements and its surface normal in vertical direction. For the refraction index of water, a tabular value of 1.33 was assumed. Finally, the data were processed simultaneously in a bundle-adjustment to calculate the image orientation, the camera calibration data as well as the surface points. In contrast to a standard bundle adjustment, our software was extended with a multimedia-module. In the standard pinhole camera model the image ray path is defined as a straight line between the object point, the projection centre of the camera and the image point. In the case of a subaquatic point, the ray path is a polygon between an object point, the penetration point through the water, the projection centre and the image point. The implemented multimedia-module calculates the refraction at the interface between water and air and provides the image ray direction between the image point and the projection centre for the bundle adjustment. For land-points the direction is given by the vector between the projection centre and the point itself. In the case of a subaquatic point it is given by the projection centre and the penetration point of the image ray through the water surface. A detailed description can be found in (Mulsow, 2010). When comparing the photogrammetrically derived DEM with reference lake depth measurements, an RMS of 10 cm could be obtained (9 check points). This corresponds to the relative accuracy of the subaquatic reference points, obtained from the adjustment (9 cm).

8.3.4 Terrestrial laser scanning

Terrestrial laser scans were carried out yearly in summer between 2009 and 2016 to capture potential surface deformations and to obtain a detailed DEM of the Flüela talus slope. An additional scan was carried out on 23.01.2013 to determine the distribution of snow depth over the talus slope. The laser scans were performed using a Riegl VZ6000 long range laser scanner. The point clouds showed a spatial resolution of 10 cm and were georeferenced by control points (Kenner *et al.*, 2014). The co-registration of the scans was verified in snow free areas like rock walls or on boulders.

8.3.5 Time-lapse camera

A time-lapse camera (Panasonic Lumix DMC FZ100) is located on a small rock wall opposite the talus slope. It takes photographs of the lake and of the talus slope on a two-hourly basis from 06.00 am until 22.00 pm. The pictures allow the distribution of snow cover and avalanche activity to be determined.

8.4 Results

8.4.1 Ground temperatures in the Flüela boreholes

The ground temperatures measured in B2 from 2002 to 2016 are shown in Figure 39. The rectangle marks the artefact caused by thermistor drift between 6 and 10 m depth which falsely indicates permafrost thaw. These depths were excluded from the analysis. The thickness of the AL is constant over the whole time series and is shown in Table 10, together with the end of snow melt dates. The stable ground ice conditions are also indicated by the TLS measurements which show no signs of ground deformation. The dates of snow disappearance, deduced from the uppermost borehole temperatures, are confirmed by the snow melt progression visible in the time-lapse images. The permafrost is warm with maximum temperatures around -0.1°C at all depths.

Table 10: End of spring zero curtain at 0.25 m depth (date of end of snow melt) and maximum active layer thickness at B2

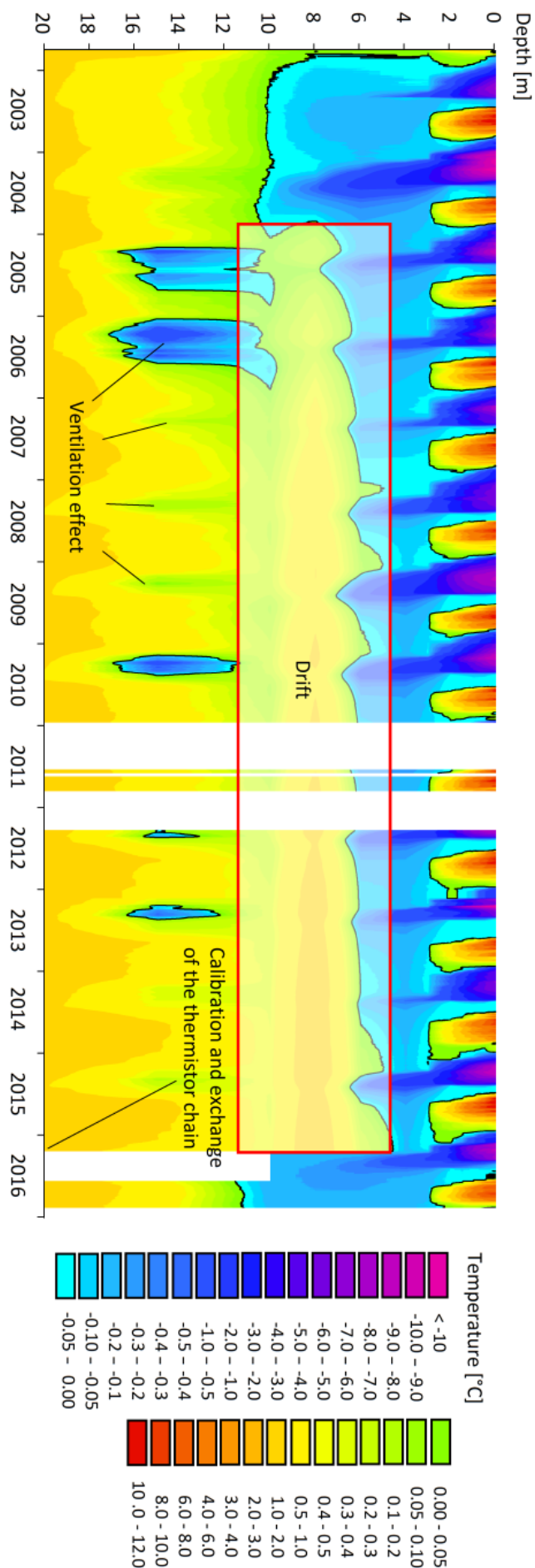|	2003	2004	2005	2006	2007	2008	2009	2010	2012	2013	2014	2015
Active layer depth	2.96	2.90	2.93	2.96	2.97	2.96	2.95	2.96	2.96	2.95	2.96	2.96
End of snow melt	12.06.	17.07.	28.06.	26.06.	03.06.	24.06.	03.07.	02.07.	29.06.	22.07.	17.06.	13.06.

Figure 39: Contour plot of the borehole temperature time series in B2. Some thermistors were subject to thermal drift. In spring 2016 the thermistor chain was exchanged and the new data reveal that no change in permafrost extent occurred since the beginning of the time series (Data: SLF/PERMOS).

The thermal orbits of the thermistors at 15 m and 20 m depth (Figure 40, top) are chaotic and indicate the ventilation analysed by Phillips *et al.* (2009). The seasonal thermal effect of ventilation underneath the permafrost is also clearly visible in Figure 39. It causes a cooling of the ground below the permafrost body and, thus, probably influences the lower border of the permafrost. However as the temperatures are mostly positive throughout the year in the ventilation zone, they are too high to cause the presence of permafrost on their own. The thermal orbits of the thermistors at 3 m and 4 m depth, both located in permafrost, show ellipsoidal shapes and indicate the dominance of conductive heat transfer initiated from the top (Figure 40, bottom). In contrast, in borehole B1 positive temperatures are recorded at all depths throughout the year. Only the thermistor at 0.25 m depth measured slightly negative temperatures during a few winters.
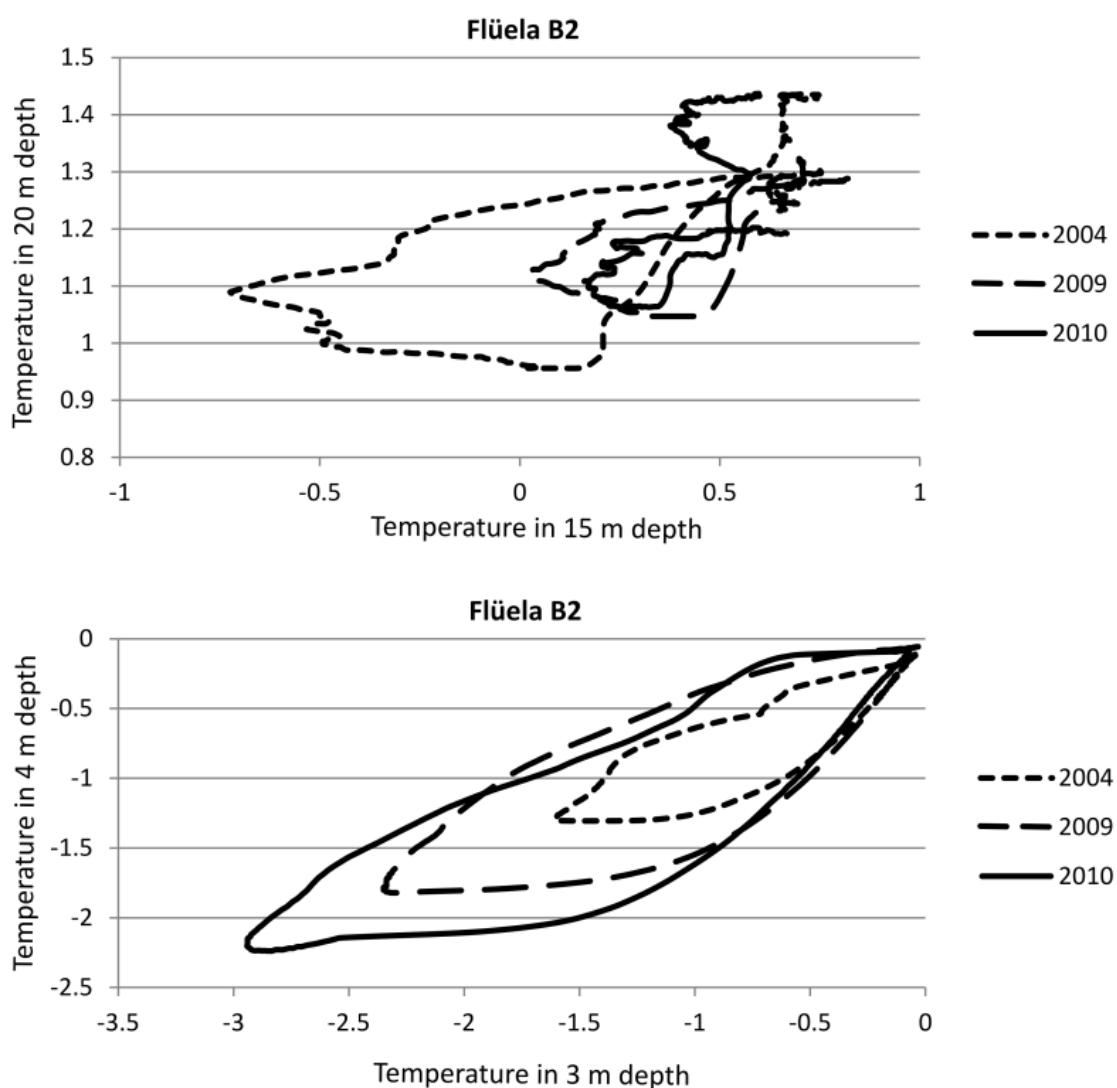

Figure 40: Thermal orbits of neighbouring thermistors in the borehole B2. Elliptic orbits indicate purely conductive heat transfer (Data: SLF/PERMOS)

8.4.2 Geophysics

In accordance with the results of the earlier seismic refraction soundings (Haeberli, 1975) and vertical electrical soundings (King et al. 1987), our ERT data indicate ice-rich permafrost at the base of the talus slope, which slowly thins out upslope (Figure 41). This interpretation is also supported by our refraction seismic data, which show high P-wave velocities in this area indicating ground ice occurrence as opposed to air-filled voids, which would lead to lower P-wave velocities (Figure 42). Three horizontal ERT profiles (Figure 41; Figure 42) indicate that the ice-rich permafrost is present all along the lake shore. Further upslope, in the central part of the longitudinal profile, a layer with high resistivities (10000-20000 Ωm) is visible at 10 – 30 m depth, which can be interpreted as a blocky substrate with high air- or low to moderate ice content. Bedrock was detected at approximately 30 – 40 m depth in the central part of the profile and at 15 m depth at borehole B1 (Figure 41). In general, our results largely confirm the findings of Haeberli (1975) and King et al. (1987), partly with a remarkable correspondence, given the differences in measurement geometry, acquisition parameters and data processing. This relates especially to the spatial extent of the confined ice-rich permafrost body at the foot of the talus slope. Solely, the thickness of the ground ice was estimated larger by Haeberli (1975) compared to our results.
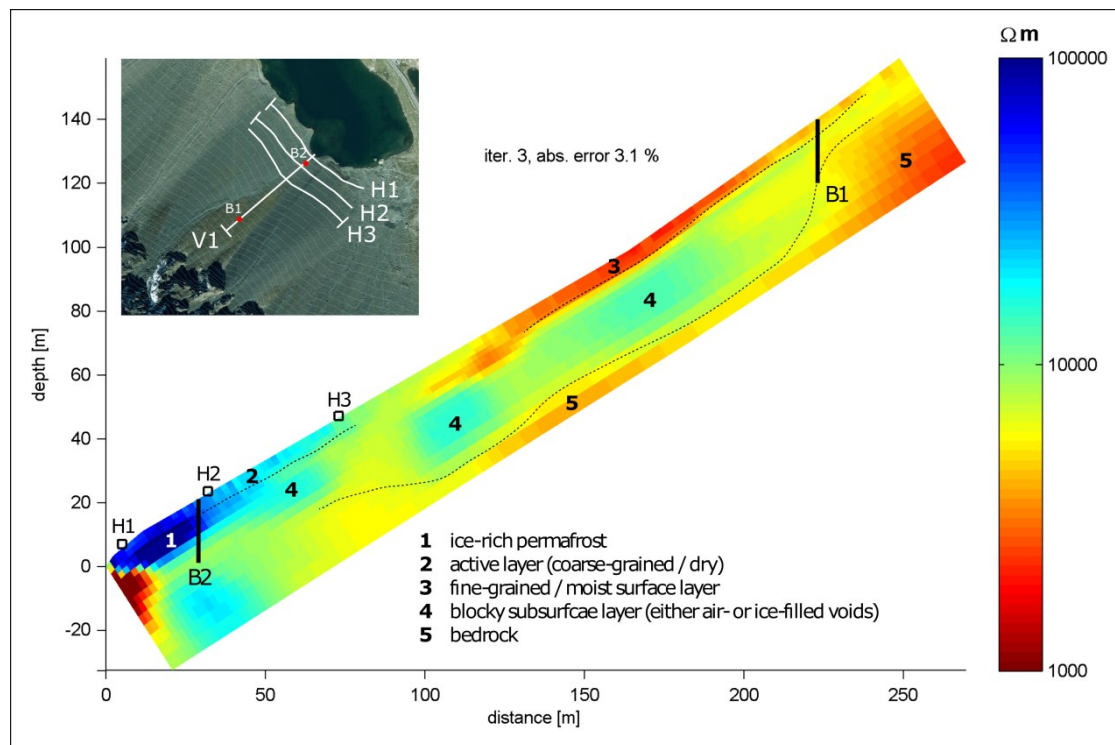
Figure 41: Electrical resistivity tomography profile of the Flüela talus slope. The white lines in the orthophoto indicate the position of the profiles. The 3 cross section profiles are included in the appendix. The red circles mark the positions of the boreholes. The high resistivity values in the lower part of the talus slope indicate ice-rich ground.

Figure 42: Horizontal ERT profiles and the vertical RST profile (bottom) acquired in the Flüela talus slope.

8.4.3 Subaquatic DEM

The orthophoto and the correspondent DEM acquired using unmanned aerial system UAS photogrammetry is shown in Figure 36. The elevation model sho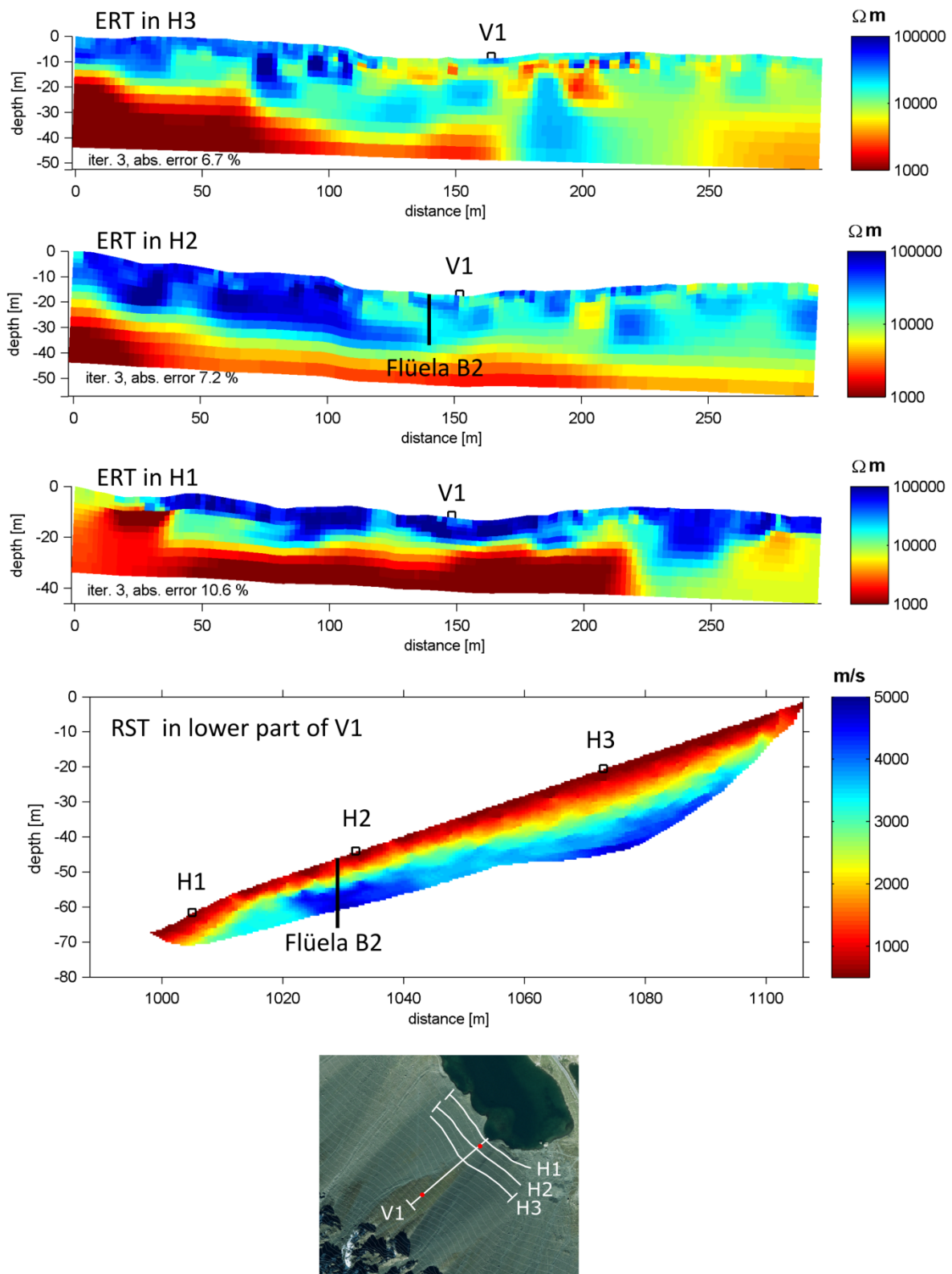ws that the thermokarst depression is approximately 4.5 m deep in relation to the surrounding lobe. The absolute water depth in the depression is approximately 7 m at a distance of 11 m from the shore and the highest point of the lobe is 0.5 m under water at a distance of 33 m from the shore.

8.5 Interpretation and Discussion

8.5.1 The genesis of excess ice permafrost in the Flüela talus slope

The geomorphological analysis of the Flüela site indicates the former occurrence of permafrost creep in the talus slope. This process is caused by excess ice (Arenson *et al.*, 2002; Kääb and Reichmuth, 2005; Haeberli *et al.*, 2006). The presence of excess ice at the foot of the talus slope indicates a possibly important if not dominant process of ground ice formation: the burial and/or embedding of (avalanche) snow deposits below steep rock walls or talus slopes by rock fall or scree slides (Potter, 1972; Isaksen *et al.*, 2000; Humlum *et al.*, 2007; Kenner and Magnusson, 2017). Sanders *et al.* (2014) presented a case study of such a rock fall on snow, directly above a relict rock glacier. At the Flüela site the avalanche snow

deposits easily reach 7 m thickness. Thin debris layers of a couple of cm can already delay the melt of such snow deposits (Nicholson and Benn, 2006; Reznichenko *et al.*, 2010; Evatt *et al.*, 2015). Thus, in addition to one large rock fall, a sequence of smaller events would suffice to effectively insulate snow remains. Another means of debris layer formation on avalanche snow can be the melt out of scree, which is incorporated in the avalanche snow. Figure 43 shows an avalanche deposit at B2 in March 2017 which is interspersed with

Figure 43: Avalanche deposit interspersed with scree around the Borehole B2 (Photograph:M. Phillips, 02.03.2017).

scree. In case of multiple perennial avalanche layers, the scree can form a closed layer at the surface due to melt out. This activates a positive feedback, as firn melt is reduced by the scree, thus enabling scree accumulation on top of the firn for a longer period of time.

During the last glaciation, the maximal ice coverage reached approximately 2600 m a.s.l. at Flüelapass, as is demonstrated by the presence of polished rocks to this elevation E of the lake. In its present form, the investigated talus slope must, therefore, have developed postglacially (Phillips *et al.*, 2009). The formation of talus slopes like the one at Flüelapass would, however, not have been possible during the Holocene, taking current rates of erosion as a reference (Ballantyne, 2002). Instead, rock fall activity was generally much more intense at the beginning of the Holocene than today (e.g. Haeberli *et al.*, 1999). This might mainly have been caused by the strong warming (Noetzli *et al.*, 2003; Fischer *et al.*, 2006; Gruber and Haeberli, 2007) after the last glaciation. During periods with frequent rock fall during which the talus slope developed, the burial of avalanche snow, leading to ground ice formation is likely (Phillips *et al.*, 2009) and explains the correlation of avalanche depositions and subaquatic creep lobes in terms of their size and position.

There are some other indications for the relevance of excess ice formation because of the burial of avalanche snow in alpine permafrost in general. Kenner and Magnusson (2017) highlighted these processes by analysing an inventory of rock glaciers in the Swiss Albula mountain range. We have since analysed the avalanche snow coverage of all 122 rock glaciers in this inventory: Aerial images taken in four different years between 2006 and 2015 were analysed to define the number of talus slopes in the root zone of rock glaciers covered with avalanche snow (Table 11). On average, 71% of the rock glaciers still had snow in the root zones at the time of image acquisition in autumn or late summer. Rock fall can, therefore, potentially cover avalanche snow at these locations at any time of year. Furthermore snow avalanche deposits are limited to slope angles below 30° because avalanches do not stop in steeper slopes (Munter, 2003). The same slope limitation is valid for ice-rich permafrost (Kenner and Magnusson, 2017), which applies to the Flüela talus slope but also for example to the talus slopes investigated by Lambiel and Pieracci (2008). Figure 44 shows the zones of high electrical resistivity (indicative for ice-rich permafrost) in the Mont Dolin talus slope adopted from Lambiel and Pieracci (2008) and areas with slope angles steeper than 30°. In contrast to a typical talus slope, the slope angle does not increase homogenously with elevation at this site. Accordingly, the ground ice distribution shows no typical "base of talus slope" pattern but follows the 30° slope limit.

Table 11: Percentage of 122 rock glaciers in the Albula Range with avalanche snow deposits in the root zone in autumn or late summer.

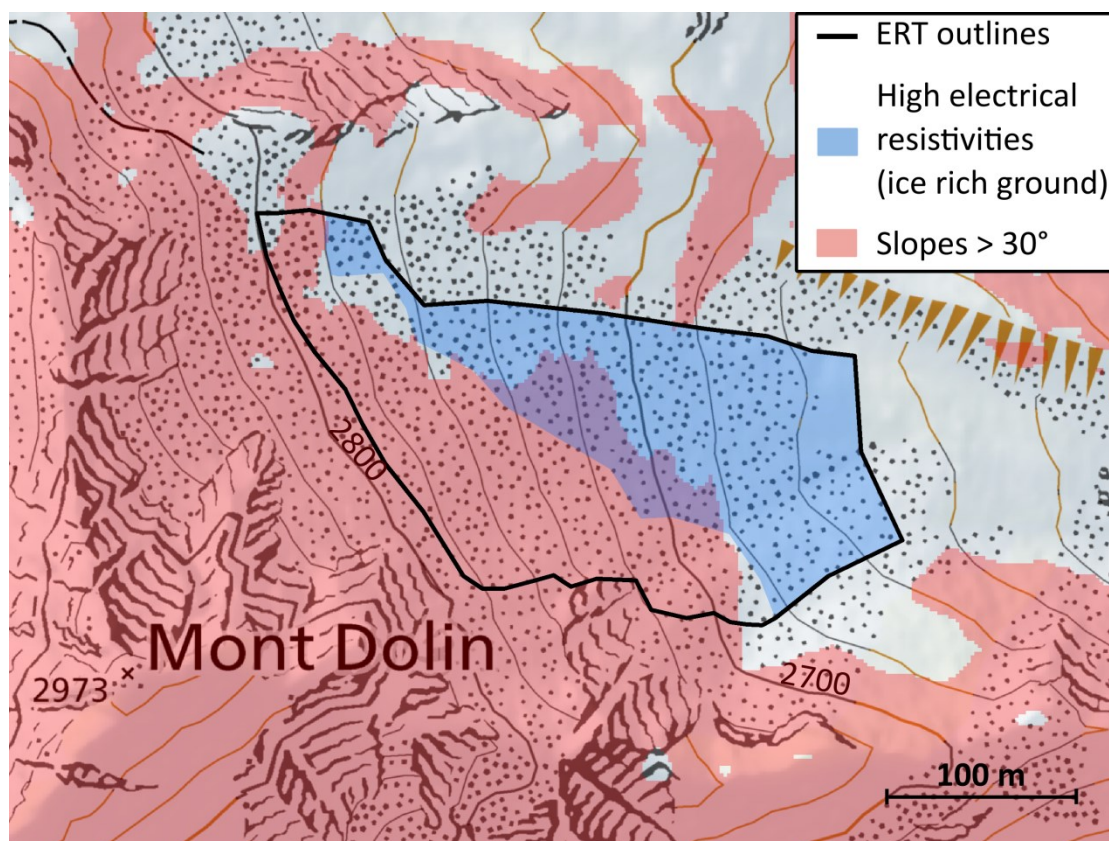| Date	27.08.2015	19.08.2012	20.08.2009	09.09.2006
Percentage of rock glaciers with avalanche snow in root zone	63%	80%	84%	57%

Figure 44: Adapted approximation of the ERT measurement results in Lambiel and Pieracci (2008) for the Mont Dolin talus slope in spatial comparison to areas with slope angles over 30°.

8.5.2 The thermal influence of wind- or avalanche driven snow redistribution on permafrost in the Flüela talus slope

Former studies focused on the redistribution of snow as the explanation for the permafrost distribution at the Flüela site (Lerjen *et al.*, 2003; Luetschg *et al.*, 2004). The insulation theory focusses on snow redistribution by avalanches, causing ground cooling by long lasting or perennial snow deposits at the base of the slope, whereas areas above melt out earlier. Time-lapse images demonstrate that this typical melt out pattern does not occur every year (see for example Figure 33). The date at which snow melt at B2 ends differs by up to 50

days within the 14 year time series we analysed (Table 10). Additionally there has no longer been any perennial snow as was documented by Haeberli (1975) for the early 1970s. Neither the interannual variation of the snow melt date, nor the long term changes regarding perennial snow patches have had a strong impact on AL thickness in B2, which has stayed very constant at circa 2.95 m for the entire time series. The limited sensitivity to interannual variations is typical for ice-rich permafrost (Zenklusen Mutter and Phillips, 2012a), as is present at B2 (Phillips et al. 2009, ERT results Figure 41). If the insulation theory applies, long term changes in the date of snow melt should cause some reactions in permafrost.

A comparison of the temperatures in both boreholes might explain the absence of such reactions: the delay in snow melt at B2 has only a small effect on the ground temperatures near the permafrost table. Figure 45 shows temperature differences between B1 and B2 for the AL and the uppermost permafrost thermistor in B2. The zero curtain during snow melt starts simultaneously in both boreholes but ends earlier in B1, which causes a steep peak in AL temperature differences. These peaks show a short delay with increasing depth but become considerably smaller towards the depth of permafrost in B2 (red dashed line in Figure 45). If the duration of avalanche snow coverage were decisive for the thermal conditions in both boreholes, this peak should represent the maximum temperature difference between B1 and B2 at 2 or 3 m depth. According to the logic of the insulation theory, ground temperatures should converge again after the end of snow melt at B2. The temperatures continue to diverge, however, after this peak of snow melt (Figure 45). The snow cover duration, thus, only has a subordinate effect on ground temperature in B2.

Furthermore, the insulation theory implies that the absence of permafrost in the upper talus slope should be caused by a stronger surface warming in summer because of the lack of insulation by avalanche snow. This effect, however, is rather small compared to the large differences in surface temperature regime between both boreholes in winter. Figure 46 shows that ground temperatures at 0.25 m depth are quite similar in B1 and B2 after snowmelt in summer, but show differences of up to 10°C during the whole winter season. Lerjen et al. (2003) and Luetschg et al. (2004) supposed that winter snow erosion by wind contributes to these differences in winter ground cooling. A TLS survey from January 2013, however, shows much more snow already at the base of the talus slope where permafrost is present than in the upper permafrost-free parts (Figure 47). We consider the snow distribution in Figure 47 as being representative for early winter, because snow distribution patterns are particularly constant over the years, especially in pass regions (Mott et al., 2010). Wind driven snow erosion, therefore, does not seem to play a role for permafrost

conservation. We hypothesize that the presence of permafrost is more likely influenced by the thermal characteristics of the ground than by snow redistribution.
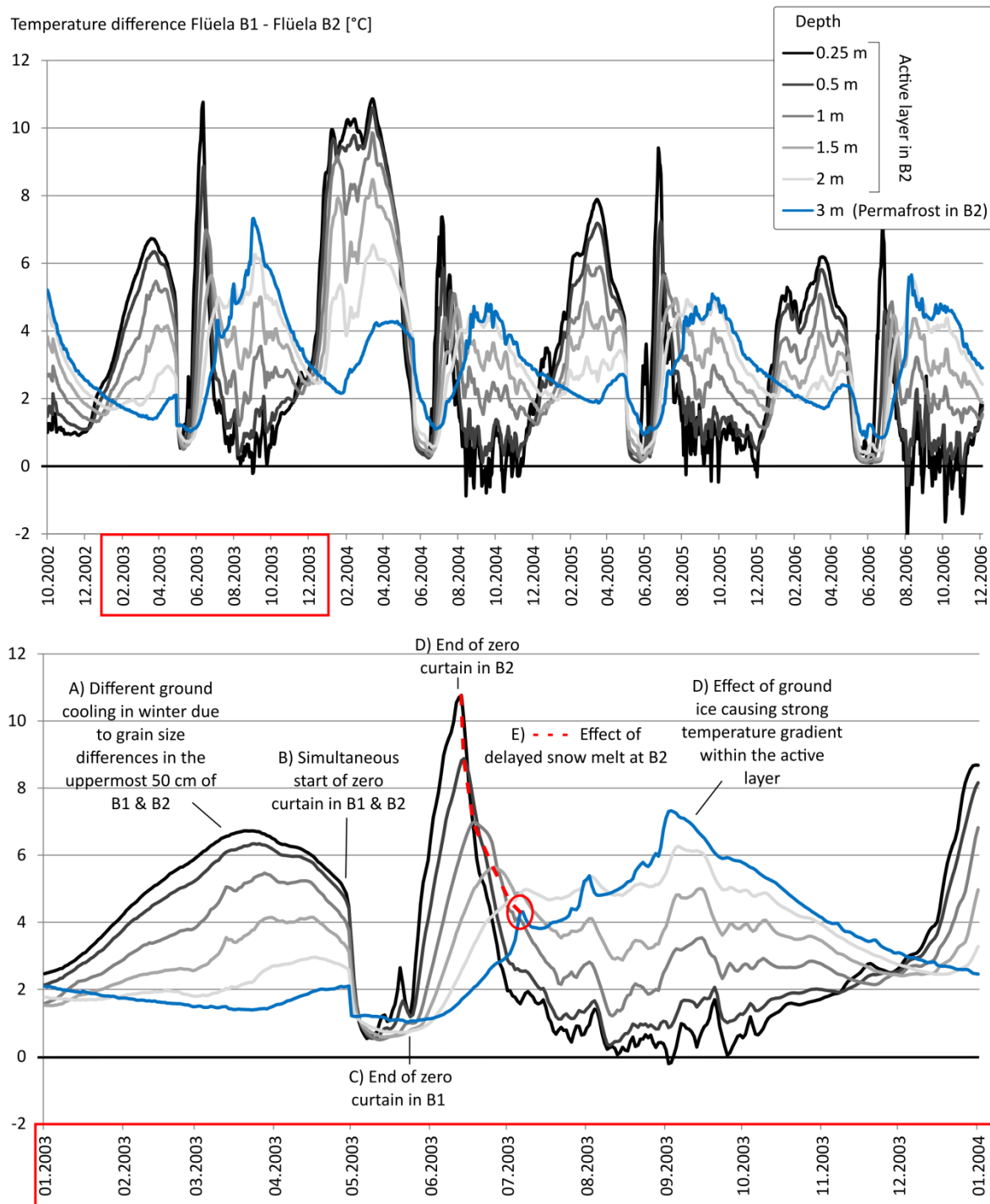

Figure 45: Temperature differences between the boreholes B1 and B2 for different depths. Whereas temperatures differ strongest close to the surface in winter, the largest differences in summer occur at 3 m, close to the permafrost table in B2. The effect of different melt out dates is limited (Data: SLF/PERMOS).
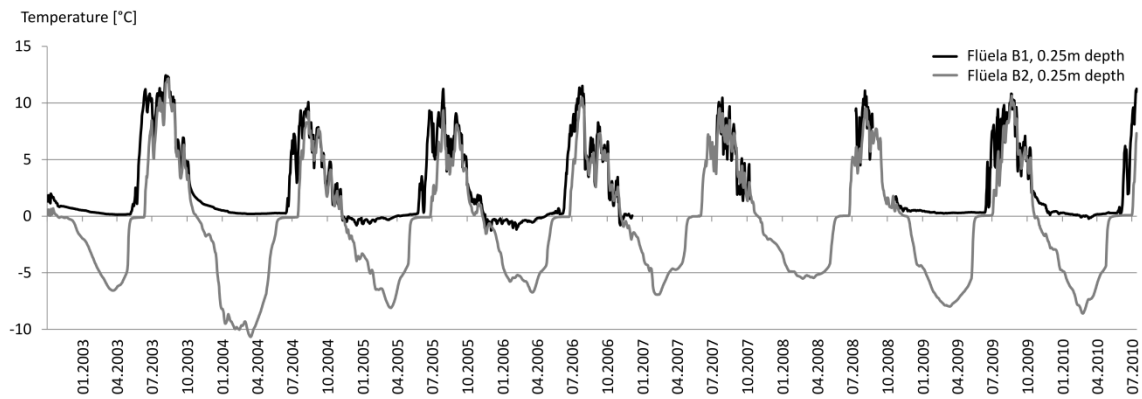
131

Figure 46: Temperatures measured in B1 and B2 at 0.25 m depth. Whereas they are similar in summer, large differences are evident in winter and during snow melt (Data: SLF/PERMOS).
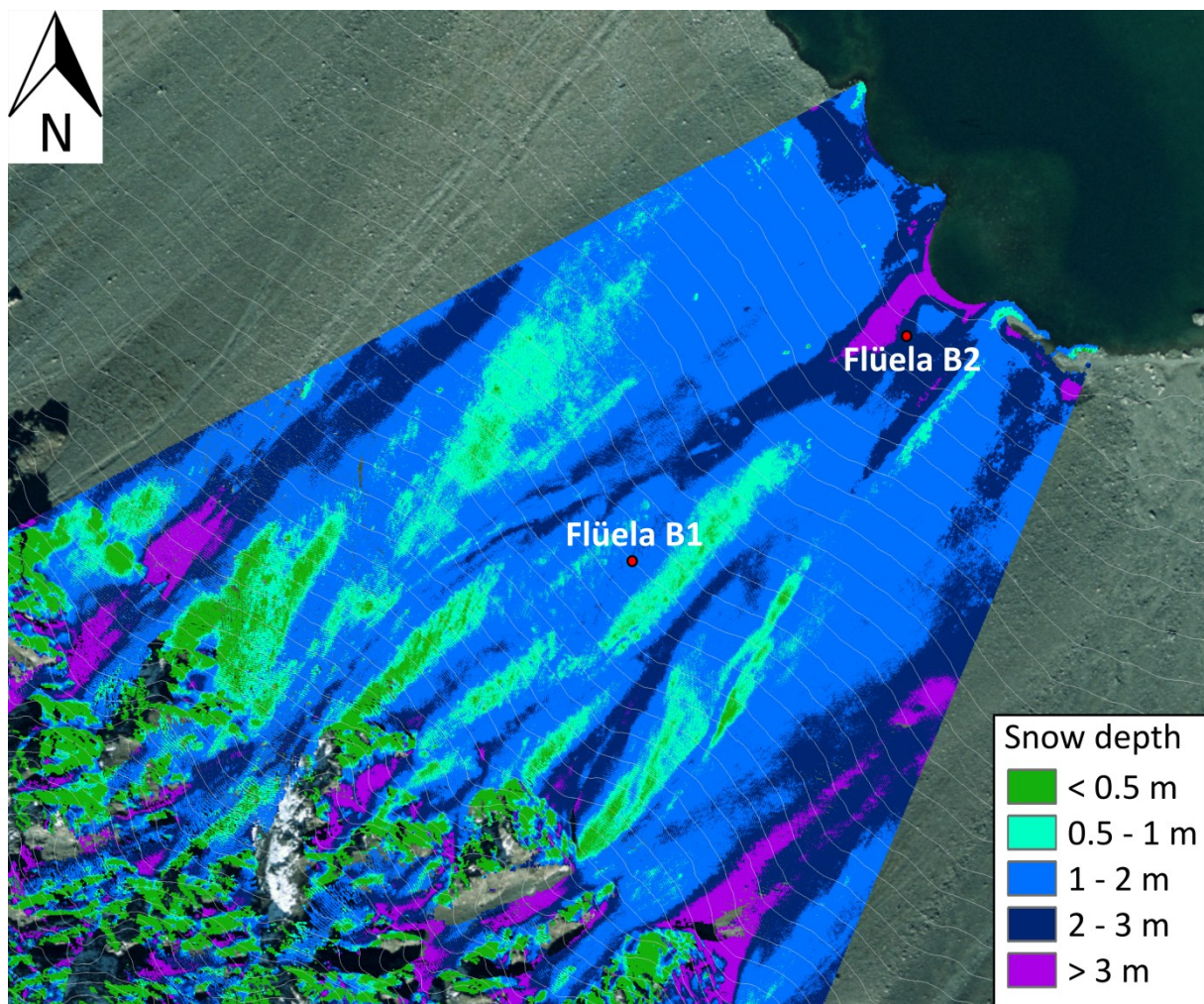

Figure 47: Snow depths measured using terrestrial laser scanning in the Flüela talus slope on 23.01.2013. The borehole positions are shown.

8.5.3 The effect of soil/talus grain size and ground ice on the thermal characteristics of the ground

One explanation for the different ground surface cooling in winter in B1 and B2 is the difference in grain sizes and was described by all of the former studies at the Flüela site (Lerjen *et al.*, 2003; Luetschg *et al.*, 2004; Phillips *et al.*, 2009). The upper 50 cm in borehole B1 consist of grass covered organic soils and sand, whereas coarse grained talus occurs at the surface at B2. As fine grained and vegetated soils have a higher water retention capacity, the water content can be higher and they cool down slower in autumn because of the release of latent heat during freezing (Schneider *et al.*, 2012).

Coarse grained talus at the surface is also known to cause a cooling effect in summer (Gruber and Hoelzle, 2008; Schneider *et al.*, 2012), however, this effect is not dominant here. In contrast to winter, the highest temperature differences in summer between B1 and B2 do not occur in the upper 0.5 m, which have different grain sizes - but they increase towards the depth of the permafrost in B2 (Figure 45). This increase in temperature differences below 0.5 m depth occurs despite a very similar stratigraphy in both boreholes (Phillips *et al.*, 2009). This implies that the thermal effect of the ground ice dominates the effect of the surface soil properties in summer and vice versa in winter.

Considering that permafrost is also absent in parts of the upper slope that have talus at the surface (Haeberli, 1975; Lerjen *et al.*, 2003; Luetschg *et al.*, 2004), the ground ice content appears to be the most relevant difference between both boreholes concerning the thermal regime. One common point of view is that perennial ground ice can develop because of permafrost conditions (Scapozza *et al.*, 2011); this process was described by Haeberli and Vonder Mühll (1996) under the term congelation ice. We suggest that the opposite is also possible, i.e. that long term stable permafrost conditions can develop in a talus slope at or below the lower fringe of mountain permafrost because of the incorporation of snow or ice into the ground by mass wasting processes as explained in Section 8.5.1 This process of ground ice genesis is to a certain extent independent from the thermal ground conditions reigning at the time of deposition. As well as the soil grain sizes, the presence of ground ice, however, can change the thermal regime of the ground after its formation (Schneider *et al.*, 2012).

Ice-rich permafrost is characterized by soil pore spaces that are completely filled or even oversaturated with ice (excess ice) (Ferrians Jr, 1989). In contrast, ground devoid of ice contains air instead. The ice content increases the heat capacity of the ground, its thermal

conductivity (Côté and Konrad, 2005) and its emissivity. In winter the high conductivity of ice saturated ground favours heat transfer upwards to the permafrost table and the heat emission towards the AL is faster. In summer energy is absorbed by the ice and rapidly distributed downward through the ice body, which is an efficient heat conductor. As long as the ice is not isothermal at 0°C, it can absorb a large amount of energy without undergoing melt because of its high heat capacity in comparison to air-filled pore spaces (Figure 48).
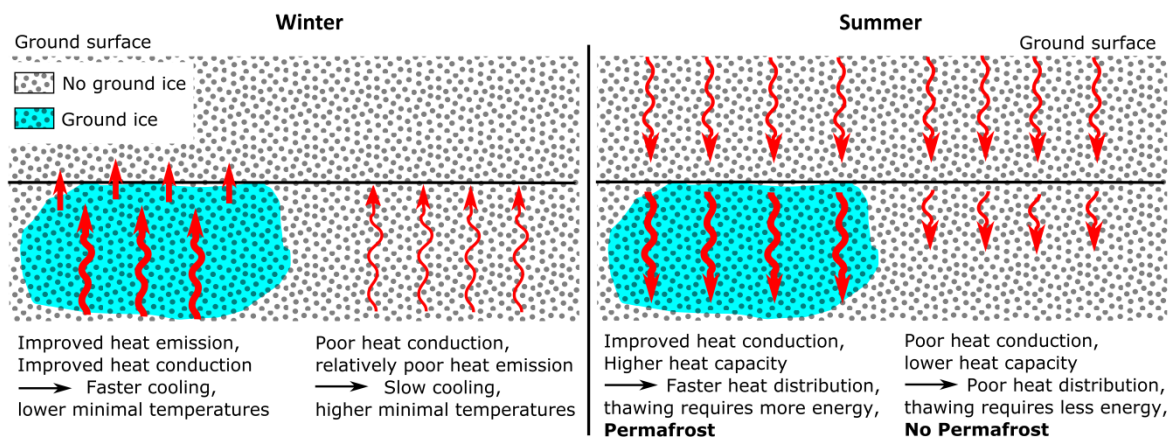

Figure 48: Sketch showing the changes in the thermal characteristics of the ground caused by ground ice and how they contribute towards the presence of permafrost and its conservation.

Ground ice acts as an effective heat sink: it rapidly absorbs and emits heat and distributes it over a larger area in ground. Incorporation of ice into the ground can, thus, allow the formation and conservation of permafrost in contrast to ice free ground, despite a similar energy budget at the surface. This implies that the thermally defined state of permafrost can be reached by the (non-thermal) process of ground ice formation.

8.6 Conclusions and implications for permafrost research

We postulate that the avalanche snow deposits located on permafrost ground at the foot of the Fluëla talus slope indicate the formation of ice-rich frozen ground by burial and/or embedding of avalanche snow into coarse-grained debris, perhaps at times of more intense rock fall activity during the distant past (Late-glacial/early Holocene?). This process may have occurred in combination with insulation effects against radiation and atmospheric influences as earlier suggested by the insulation theory but could also have played a predominating role. The formation of ground ice initiated long-term thermally self-stabilising permafrost. Additional factors contributing to a contrasting thermal regime over the slope are the intra-

talus ventilation and the different soil properties at the surface. The ventilation cools the ground below the permafrost and, thus, influences the lower edge of the permafrost body. The finer grained organic soil around B1 particularly reduces ground cooling in winter. The influence of these factors on the present day permafrost conditions, however, is limited: the ventilation only has a barely traceable effect on the permafrost temperatures and the permafrost distribution is not correlated with the presence of superficial talus.

Existing knowledge about the process of permafrost formation by mass movements, which probably dominates the lower belt of mountain permafrost is of particular relevance, because the coupling of these processes to climate change is not straightforward. Increases in rock fall activity induced by climate change might even favour the process of ground ice formation because of mass wasting processes. Paleoclimatic reconstructions related to permafrost and future permafrost distribution modelling should carefully consider these aspects. Furthermore we conclude that:

- The effect of long lasting avalanche snow on ground temperature is indisputable but its effect on permafrost conservation is probably limited and may previously have been overestimated at the Flüela talus slope. Differences in surface heat exchange between B1 and B2, resulting from delayed snow melt at B2, have a relatively small influence on the temperatures close to the permafrost table. Strong temporal variabilities of the snow cover are neither reflected by the permafrost extent nor by the permafrost temperatures, at annual and multiannual scales.
- At the Flüelapass site, wind driven snow redistribution does not appear to influence the distribution of permafrost.
- The presence of a relict rock glacier at the lake bottom is additional proof of the existence of excess ice in the Flüela talus slope. The "Schottensee" lake at Flüelapass is younger than the relict subaquatic rock glacier and was dammed by a rock fall. Mega-ripples located below the rock fall deposit are an interesting indicator of a subsequent lake outburst.

Acknowledgements

9. Geomorphological analysis on the interaction of glaciers and rock glaciers

Robert Kenner

WSL Institute for Snow and Avalanche Research SLF

Abstract

The interaction of glaciers and rock glaciers is still an incompletely investigated field of periglacial geomorphology. This study presents examples of glacier - rock glacier interactions in the Swiss and French Alps, based on sequences of current and historical maps and orthophotos. It is concluded from these examples that creeping permafrost features, which were widely specified as "glacier derived" in the literature appear to be much older than the glacier itself and constitute the remains of rock glaciers which were disrupted by glaciers. Furthermore, the environmental conditions causing an alternation of glaciers and rock glaciers at the same location are analysed and the processes leading to a transition from one landform to the other are identified in the examples given.

9.1. Introduction

Glaciers, debris covered glaciers and rock glaciers are geomorphologic features which are sometimes difficult to distinguish. Especially in arid or polar regions, continuum features exist which are often hard to categorise (Ackert, 1998; Monnier and Kinnard, 2015). In the Alps, the geomorphological differences between these features are generally more pronounced. Our study focusses on glacier – rock glacier interactions in the Swiss and French Alps. Rock glaciers are specified by their morphology here, and have bulgy and steep fronts and sidewalls, ridges and furrows or lobate superficial creep forms and have blocky talus at their surface (Potter, 1972). To illustrate this, see for example rock glacier Muragl in Figure 51. Debris covered glaciers in the Alps are similar to dead ice structures: no creep forms are visible, they are often fractured by crevasses, have rock islands, superficial melt water runoff channels and subglacial flow system outlets. Their fronts are either flat or a massive ice core is exposed in steep flanks, as the examples in Figure 49 show. The transition between glaciers and debris covered glaciers is in fact also in the Alps fluent and it is hardly possible to define a threshold in debris coverage to clearly distinguish between them.

Glacier and rock glacier interactions have been the subject of controversy in the literature for a long time. Some authors supported a glacier to rock glacier mutation (Whalley, 1983; Humlum, 1996; Whalley and Palmer, 1998; Baroni *et al.*, 2004; Berger *et al.*, 2004), whereas others doubt this type of genesis and support the formation of ground ice by segregation or burial of surface snow and ice (Haeberli *et al.*, 2006; Berthling, 2011). The intense discussion and investigations on the role of glaciers in rock glacier genesis is briefly summarized below.

Glaciers and rock glaciers can alternatingly occur at the same site, depending on climatic and climate related (i.e. rock wall erosion rates) conditions (Ackert, 1998; Ribolini *et al.*, 2010). As rock glaciers depend on debris supply by rock fall (Haeberli *et al.*, 2006), the environments shared by glaciers and rock glaciers over time are typically located at the base of rock walls. Rock glaciers can, but do not have to contain ice of glacial origin (Potter *et al.*, 1998; Ribolini *et al.*, 2010). Rock glacier ice is often mixed with rock debris (Arenson *et al.*, 2002; Hausmann *et al.*, 2007) but some rock glaciers also have thick massive ice layers (Haeberli *et al.*, 1998), as was recently observed during the drilling of a borehole in the rock glacier Murtèl in Switzerland in 2015, with a 30 m thick layer of massive ice (Bast *et al.*, 2016). Furthermore Ribolini *et al.* (2010) and Reynard *et al.* (2003) showed on the basis of geophysical measurements that subsequent glacier advances are disruptive for the overridden permafrost structures. This was shown for alpine isothermal glaciers but might

be different for cold polar glaciers. Nevertheless, glacier – rock glacier interactions have received comparatively little attention and need more systematic investigation according to Haeberli *et al.* (2010).

The sequence and types of processes taking place during the recent interaction of glaciers and rock glaciers since the little ice age (LIA) are investigated in this study, based on an interesting set of examples from the Swiss and French Alps. This study discusses the following questions: What kind of geomorphologic evidence is there for glacier – rock glacier interactions? How does the transition from one feature to the other occur? How can glacier ice be incorporated in rock glaciers? What are the driving environmental factors leading to an alternation of rock glaciers and glaciers at the same location?
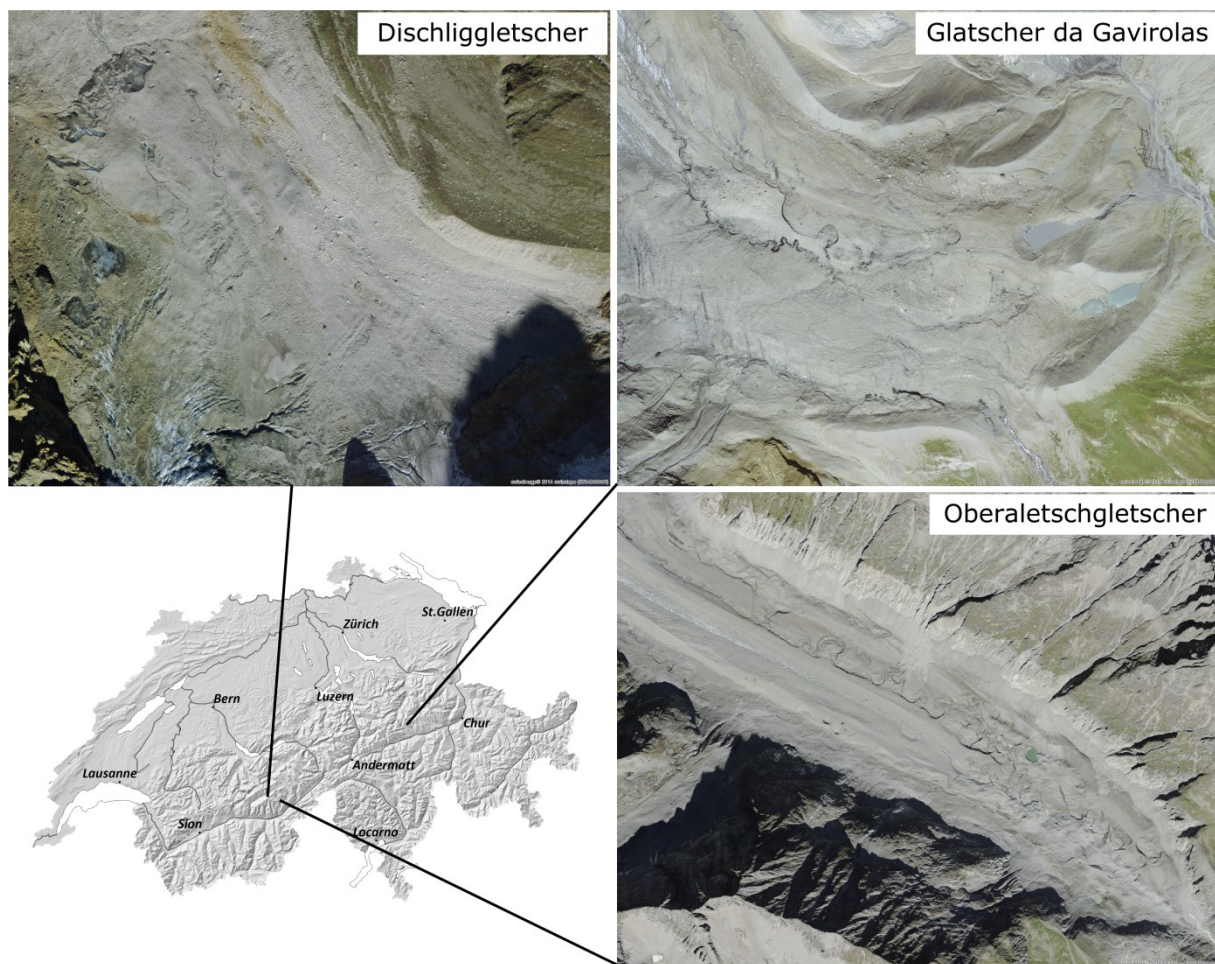
Figure 49: Examples showing the morphology of debris covered glaciers from the Swiss Alps.

9.2. Methods

In this study a geomorphological analysis is carried out on the basis of multi-temporal aerial photographs and historical topographic maps. This data covers the period from the maximum glaciation of the Alps during the LIA in the second half of the 19th century until present. The data are provided by the Swisstopo products Swissimage and Siegfried map. Swissimage is a countrywide orthophoto of Switzerland with regular updates since 1998. The Siegfried map is the first modern map of Switzerland and the parts relevant for this study were produced in 1875. All orthofotos and the Siegfried map were reproduced with the permission of Swisstopo (permission no. 5704 000 000). The study shows examples of glacier – rock glacier interactions at 8 sites, whose locations are mapped in Figure 50.

Figure 50: Geographical overview of the example sites presented in this study.

9.3. Geomorphological reconstructions of glacier – rock glacier interactions

The interaction of rock glacier Muragl and glacier Vadret Muragl (Figures 51 and 53) is used here as a prime example. The glacier Vadret Muragl reached its maximum extent during the LIA around 1850 (Figure 51). The Muragl rock glacier is located to the north west of Vadret Muragl and has been described by Kääb and Kneisel (2005), Maisch *et al.* (2003) and Arenson *et al.* (2002). Adjacent to it in the east and in the forefield of the glacier Vadret da Muragl there is a steep and bulgy debris front (Figure 51 and 53). This debris front is specified by Maisch *et al.* (2003) as being the 1850 moraine of Vadret da Muragl. Kääb and Kneisel (2005) carried out further investigations of the front and measured surface creep rates of up to 50 cm/a and the presence of ground ice in the front and the adjacent glacier forefield. They concluded from their results, that "permafrost and ground ice aggrades, after exposure of the ground to the atmosphere due to glacier retreat."
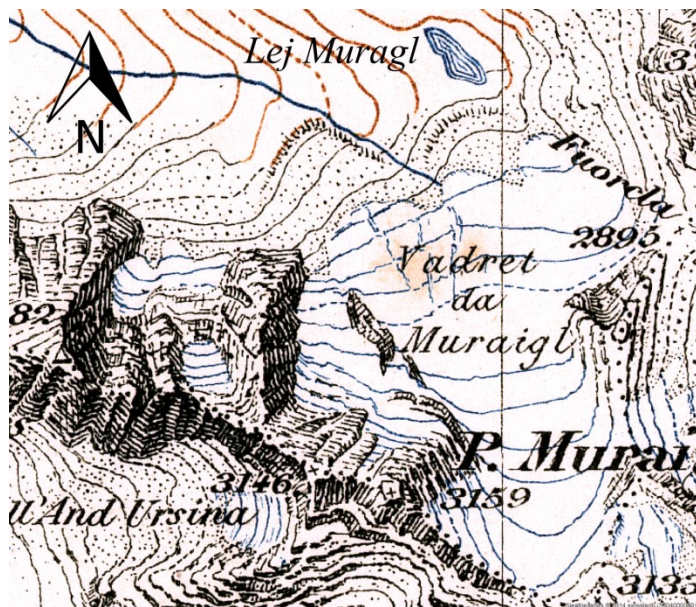
← *Figure 51: Overview of the site of rock glacier Muragl and glacier Vadret Muragl. The map (top) shows the area during the mapping campaign for the 1875 release. The debris front marked in the 2016 orthophoto (bottom) is already present in the forefield of the glacier, mapped as escarpment hatching.*
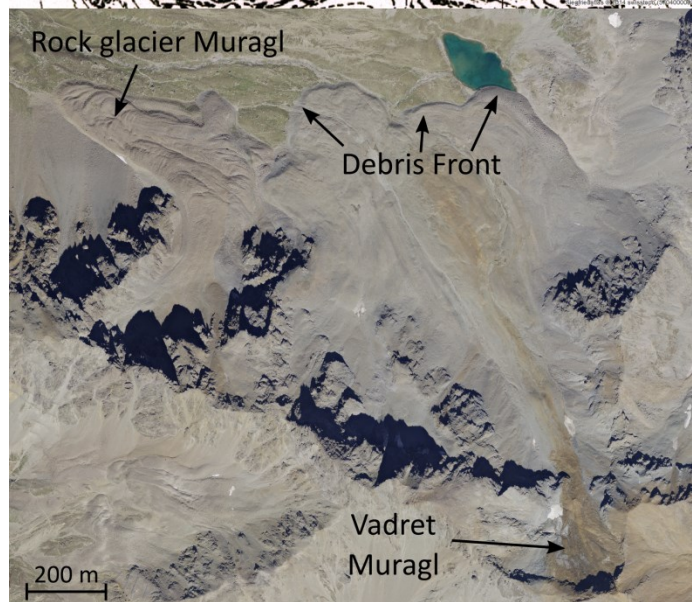
↓ *Figure 52: Schematic profile of a typical moraine dam and a typical rock glacier front.*
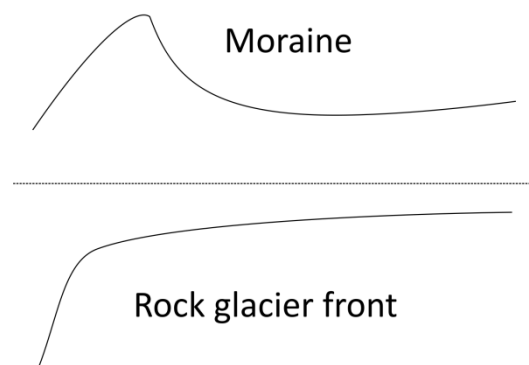
9.3.1 Transition from rock glacier to glacier coverage

Interestingly however, the morphology of the lobes of the Vadret da Muragl debris front is typical for a rock glacier but not for a moraine. The front is not shaped like a typical moraine dam - i.e. subsiding in both directions, to the valley side and to the glacier side (Figure 52). In contrast, above the steep front the terrain continues to ascend slightly in a convex manner, as in the case of a rock glacier tongue (Figure 53a). The region was mapped in detail in 1875 for the Swiss Siegfried map. According to this map the debris front already existed during the LIA (Figure 51). The distance between the debris front and the glacier tongue was about 230 m in 1875. However, other glaciers of the same size and orientation in the closer surroundings were mapped very close to their maximal front moraines in 1875, which are visible in the current orthophoto (e.g. glaciers in the northern surroundings of Piz Vadret, see mapped front moraines in the uppermost example in Figure 54). A retreat of 230 m between 1850 and 1875 would therefore be exceptional for this region.
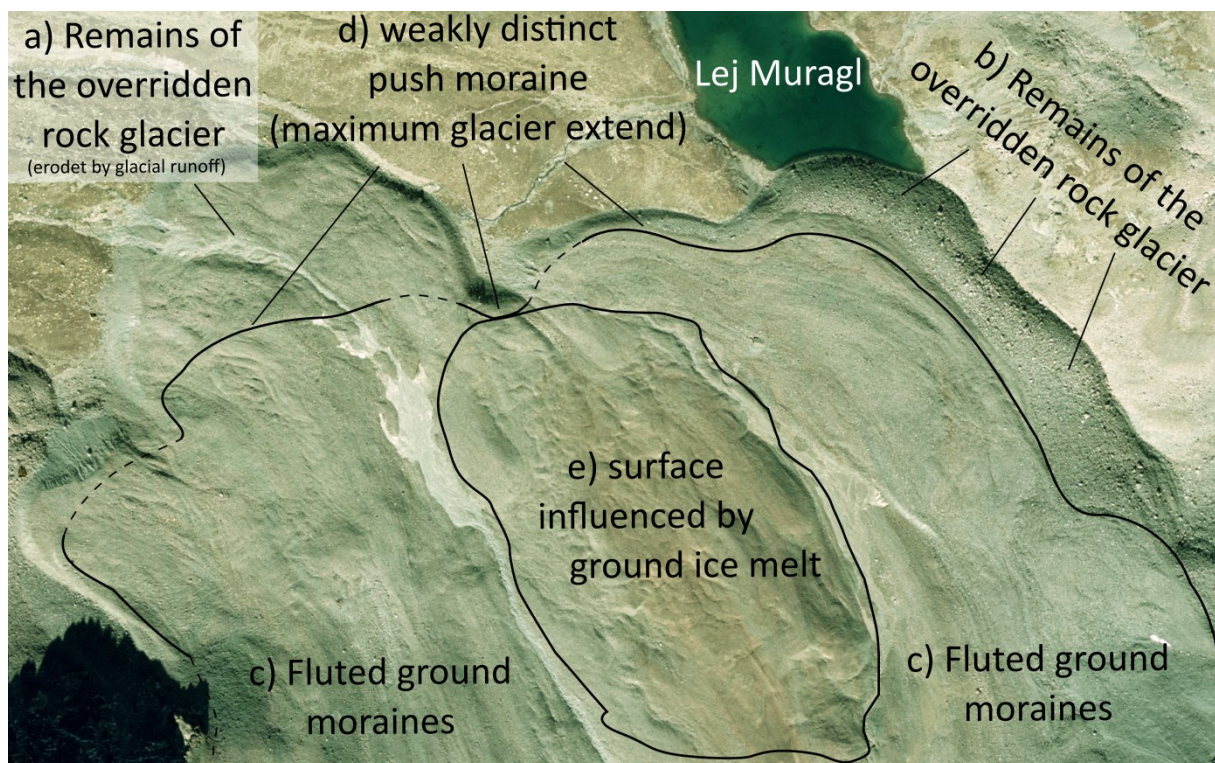
Figure 53: Close up of the debris front in the forefield of Vadret Muragl, with labelled geomorphological key features. The dashed line indicates zones in which the location of the push moraine of Vadret Muragl is not discernible.

→ Figure 54: Examples of Swiss rock glaciers which were overridden by glaciers in their upper parts. On the left current orthophotos of the example sites are shown and on the right the Siegfried map of the same area. The uppermost example, Piz Vadret is located just 600 m to the North of our prime example, rock glacier Muragl. In the Piz Vadret orthophoto (top, left), the maximum moraines of some other LIA glaciers are mapped in red, to show that the maximal glaciation in this region corresponds to the glacier extent on the Siegfried map.
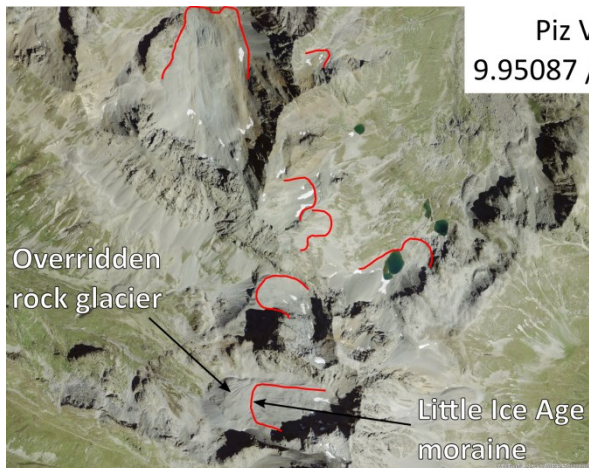
Piz Vadret
9.95087 / 46.50896

Overridden rock glacier

Little Ice Age moraine
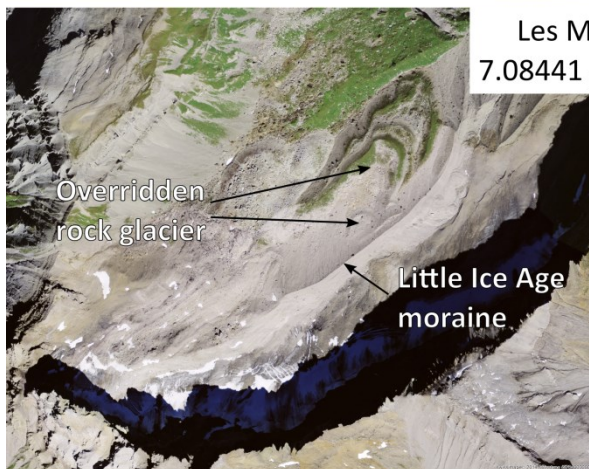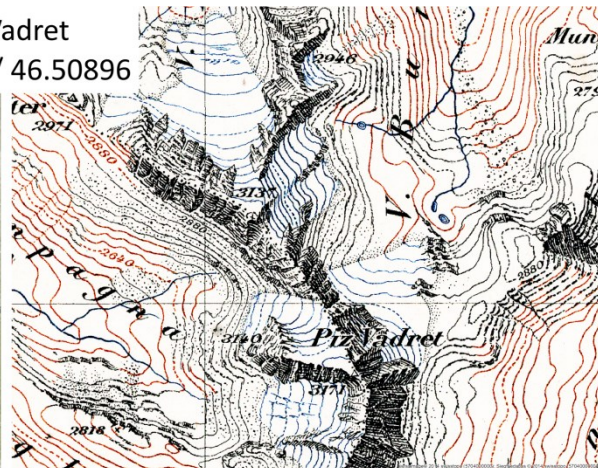
Les Martinets
7.08441 / 46.20704

Overridden rock glacier

Little Ice Age moraine
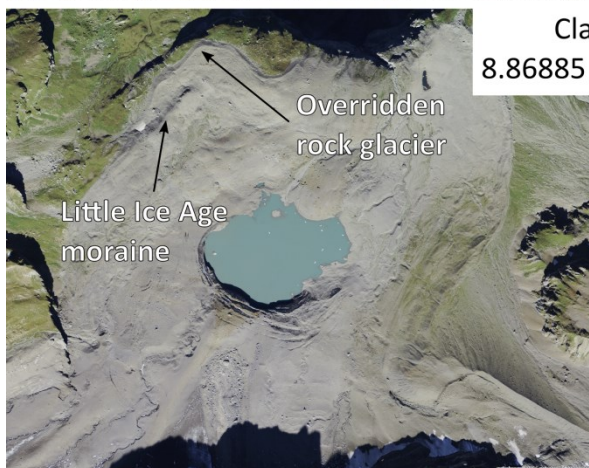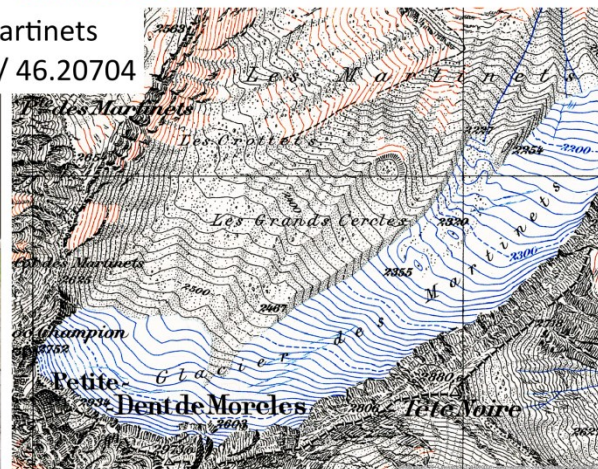
Clariden
8.86885 / 46.86132

Overridden rock glacier

Little Ice Age moraine
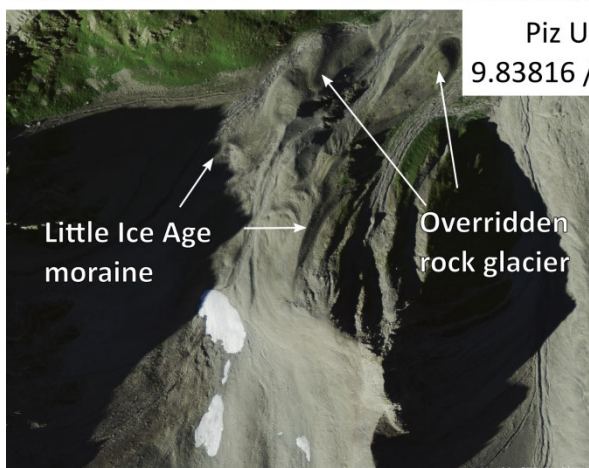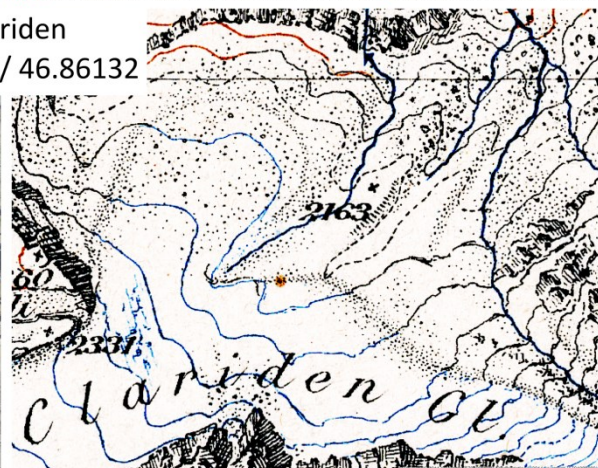
Piz Uertsch
9.83816 / 46.60740

Little Ice Age moraine

Overridden rock glacier
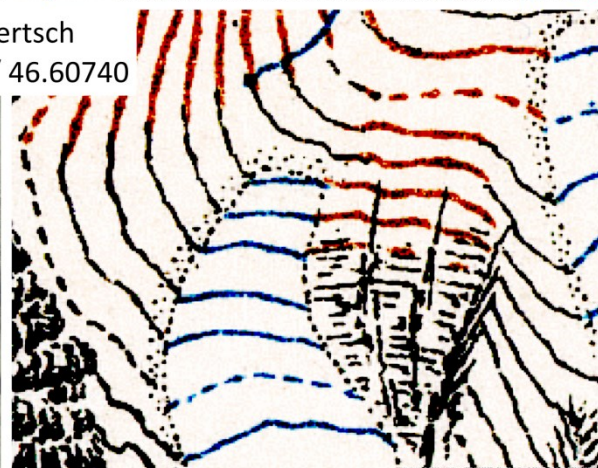
Consequently, the debris front is not considered as being the moraine of Vadret Muragl here but as constituting the remains of the large eastern part of Muragl rock glacier which was widely overridden by glacier Vadret Muragl during the LIA and hence disrupted. Only the front of the former eastern part was preserved, still containing ground ice and displaying creep movements (Figure 53a,b). There are further morphological indications supporting this assumption: The front part of the feature close to Lej Muragl, which is described as a push moraine by Kääb and Kneisel (2005) consists of rough blocks and not of finer grained moraine material (Figure 53b). This zone has a very different surface texture than the fluted ground moraines to the West (Figure 53c). This feature might actually be a small remainder of the former rock glacier. A weakly defined push moraine (Figure 53d) indicates the maximal extent of the glaciation. The absence of fluted ground moraines in some areas of the old glacier bed was explained in Kääb and Kneisel (2005) as sectors in which the glacier was frozen to its bed. These zones might rather correspond to formerly very ice-rich ground, on which debris was rearranged due to ground ice melt as a consequence of glaciation or glacial runoff (Figure 53e). In contrast to the surrounding areas with fluted moraines, ground ice melt may have continued here until the end of the LIA glaciation and the surface was not completely reshaped by glacial erosion.

Referring to the Swiss Siegfried map, other examples of partly overridden rock glaciers with preserved fronts can be identified. Examples of such rock glaciers are shown in Figure 54 and their locations are summarized in Figure 50. The uppermost example shows a rock glacier beneath Piz Vadret just 600 m to the N of the Muragl site. The example "Les Martinets" shows a push moraine superimposed on multiple rock glacier lobes, of which the smaller, non-vegetated one might still be active as the moraine dam above this lobe is slightly deformed. The examples "Clariden" and "Piz Uertsch" also show distinct rock glacier fronts clearly downslope of the maximum LIA glaciation. The example "Glacier de la Réchasse" in Figure 55 is impressive, particularly with regard to the destructive effect of glacier advances on rock glaciers.
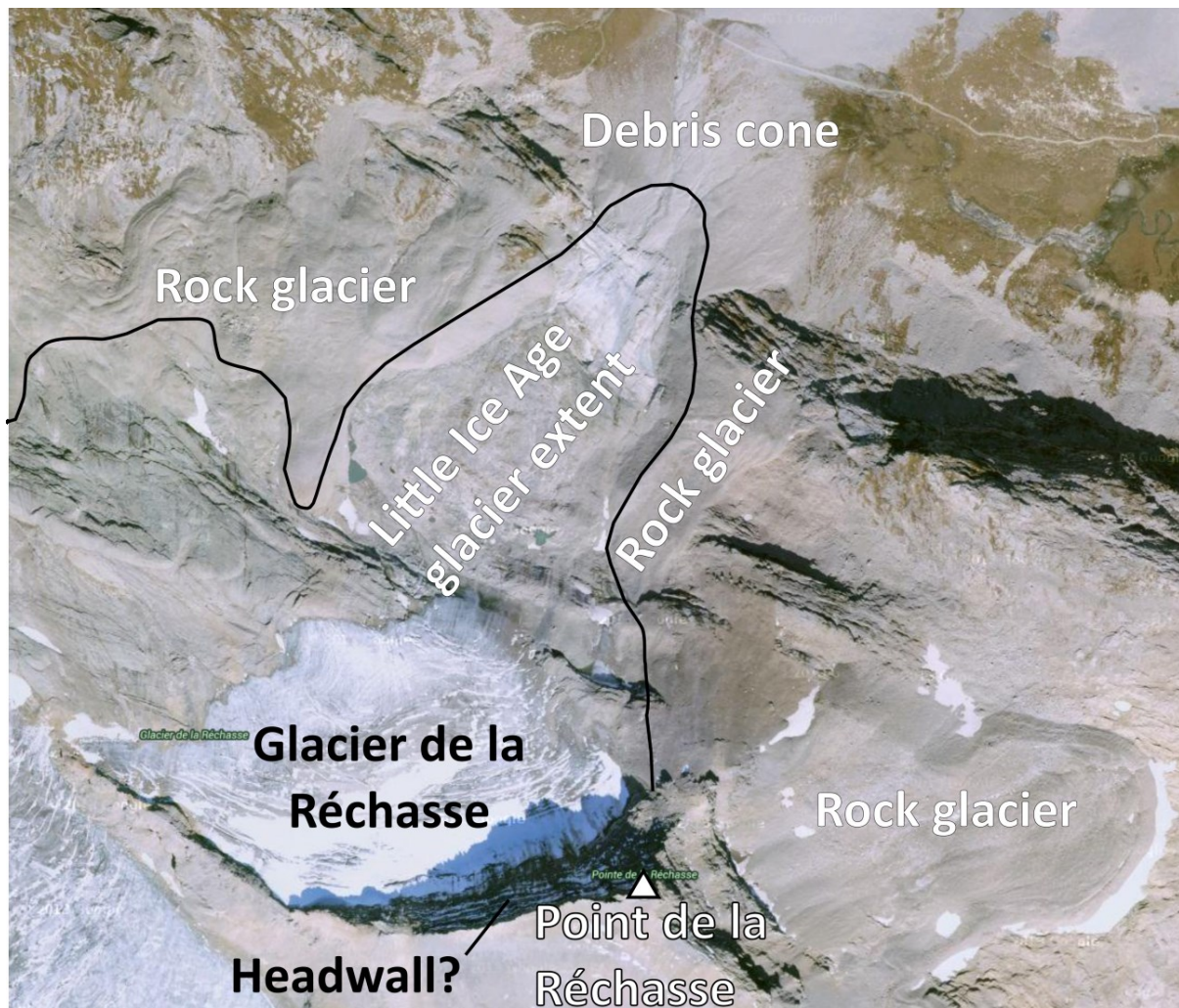
Figure 55: The former extent of Glacier de la Réchasse is clearly visible on the orthophoto (© Google Maps). The moraine dam marked with the black line is surrounded by rock glacier remains. The rock glacier probably occupied the entire area below the north facing rock wall of Pointe de la Réchasse (headwall) before the glaciation or it developed from rock fall which was released from the glacier when advancing close to the little terrain step in the glacier forefield. Regardless of its former extent, large parts of the rock glacier were eroded up to the bed rock by the glacier, which build a large debris cone from the rock glacier material below.

Sites similar to those in Figures 54 and 55 were described and interpreted by Reynard *et al.* (2003) and Ribolini *et al.* (2010) in a similar manner. However, there is a much larger part of literature, which describes such preserved front parts of glacially overridden rock glaciers as creeping, ice-cored moraines (Östrem, 1971; Barsch, 1988; Clark *et al.*, 1994; Etzelmüller and Hagen, 2005; Etzelmüller and Frauenfelder, 2009). This term implies that rock glaciers can develop out of the push moraines of glaciers or constitute the remains of debris covered glacier termini and are therefore glacier derived. The process chain presented here indicates that many of these creeping fronts are indeed glacier disrupted and not glacier derived. For

example the rock glaciers presented by Clark *et al.* (1994) and described there as flowing moraines might also be amongst these examples. The creep forms in front of the Goethe Glacier (Figure 5 in Clark et al., 1994) or North Palisade Glacier (Figure 6 in Clark et al., 1994) all show the morphological characteristics of rock glacier like creep structures with rough boulders at the surface and steep bulging side walls. Between the glacier tongue and these creep forms, the surface is in contrast depressed and smooth, indicating the past maximal extent of the glacier. This study also considers these creep features as being glacially overridden rock glaciers. Exposures of massive glacier ice, which were found by Clark *et al.* (1994) at the transition between the eroded glacier fore field and the rock glacier do not contradict this theory. Dead ice structures in push moraines are a common phenomenon and are likely to occur in this transition zone (Östrem, 1959; Schomacker and Kjaer, 2008). This does not however imply that the glacier is the source of ice for the entire rock glacier front. The same conclusions probably also apply to the Norwegian rock glacier in Sunndalsfjella presented by (Berthling, 2011).

9.3.2 Transition from glacier to rock glacier coverage

Since 1875, the extent of glacier Vadret Muragl has been significantly reduced and only small glacierets still exist. Figure 56 shows orthophotos of the glacier between 2003 and 2016. In addition to the glacier retreat, the ongoing scree coverage of initially clean glacier ice is evident. There are two processes contributing to the scree coverage: On the one hand the burial of glacier ice and seasonal snow patches / avalanche deposits by rock slides beneath a rock wall located to the South. Multiple ice-debris layers can thus develop on the glacier ice. On the other hand the melt out of scree contained by the glacieret is also evident. The ice releasing this scree is located in a depression and belongs to the deepest ice layers in the uppermost parts of the former glacier Vadret Muragl. Glacier ice in such positions is not very strongly affected by glacier flow (Schwikowski, 2004). Hence, the scree incorporated in this ice most likely originates from rock fall and scree slides released before or at the very beginning of the glaciation. This in turn indicates that the mutual burial of snow, ice and scree already occurred here before the formation of the Vadret Muragl glacier and continues after its retreat. The LIA was probably a brief interruption of the rock glacier and permafrost history at this site. The colder climate during the LIA led to an increase in snow accumulation and a decrease in rock fall activity, favouring the temporary development of a glacier. Meanwhile the processes have reversed and increased rock fall activity and decreased snow accumulation are initiating a new phase of permafrost genesis by snow and ice incorporation into the ground. The glacieret of Vadret Muragl will probably constitute the basis of a new rock glacier here in the future.
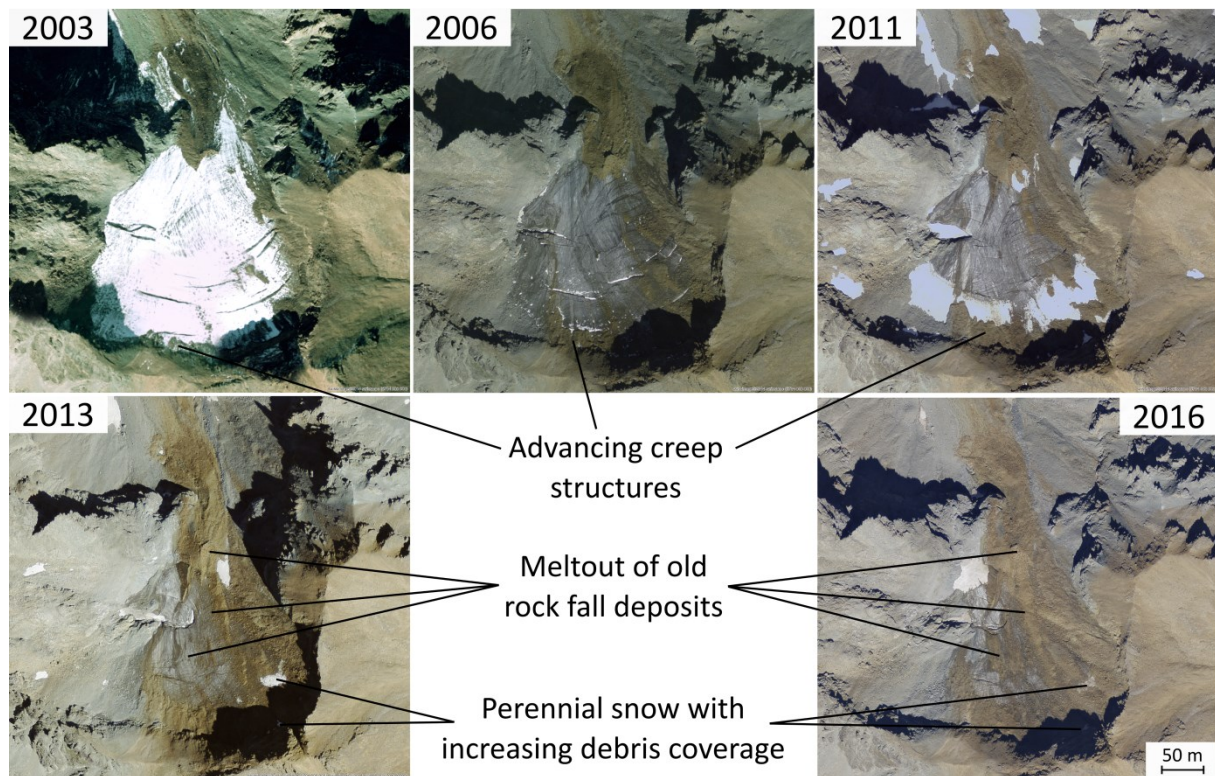
Figure 56: Glacieret Vadret Muragl between 2003 and 2016. The ongoing debris coverage by rock fall, creeping loose material and melt out is clearly visible. Perennial snow patches are buried by these processes.

This example shows that debris covered glacierets can in some cases constitute an intermediate state during the transition from glacier to rock glacier coverage. A prerequisite is that the whole remaining ice layer is subject to ongoing rock debris and snow accumulation. This is only the case for small glacierets, yet not for larger debris covered valley glaciers. Without an insulating ice-debris mixture at the surface, the remaining glacier ice will either melt or form a stable dead ice body under its debris cover. As small glacierets only provide a limited amount of ice and have very low flow rates, it is rather unlikely that they provide the entire ice supply for future centuries or millennia of rock glacier development. It is more probable that additional rock glacier ice develops from alternating accumulation of snow and talus on top of the glacierets or in formerly glaciated terrain. Figure 57 shows an example of multiannual snow covered with talus and large boulders below a steep rock wall in the glacier forefield of Vadret da las Maisas (Figure 50). This is most probably the most dominant source of ground ice in rock glaciers and explains rock glacier genesis beyond formerly glaciated terrain.

Figure 57: Debris covered multiannual snow in the glacier forefield of Vadret da las Maises (Photo: Robert Kenner, 26.06.2017). This site shows frequent rock fall activity and long lasting avalanche snow and is therefore appropriate for future rock glacier formation.

In the current period of climate warming, multiple examples of deglaciation favouring rock glacier development can be found: the initial formation of ice-rich permafrost due to the burial of dead ice structures and seasonal snow patches is shown in Figure 58. The ice of a former glacier (nameless) under the west slope of Piz Kesch (Figure 50) is rapidly being covered with rapidly creeping loose material originating from the surrounding scree flanks. The elongated shape of the tongue-like creep structures suggests an interspersion of the loose material with ice or snow, as observed by (Phillips *et al.*, 2016).
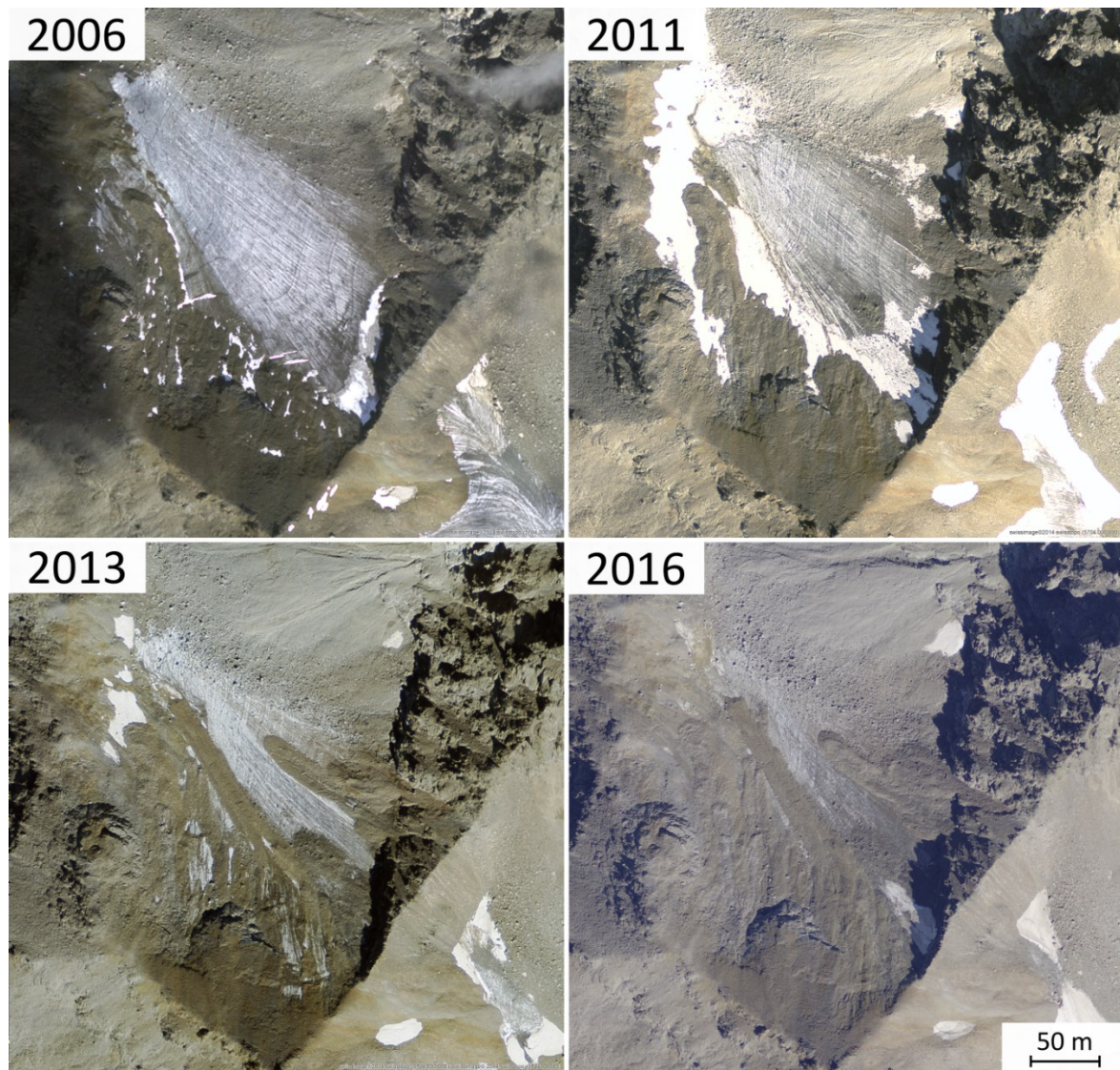
Figure 58: Example of a glacieret to the West of Piz Kesch, similar to that in Figure 56, where periglacial processes are starting, superimposed on the glacier ice, including creeping debris, debris melt out and the burial of surface snow.

Further examples are shown in Figures 59 and 60. They show glacierets in Valais and Grisons (Figure 50), remainings of former glaciers, which have been covered by scree slides or rock fall deposits over time and have developed a rock glacier like, creep-induced morphology. Figure 60 shows another example of a rapidly changing glacier - rock glacier interaction under the north face of Grand Muveran (Figure 50). Here a rock glacier is currently reoccupying an old glacier bed with a characteristic push moraine. Several large boulders located on the rock glacier could be tracked on orthophotos taken between 2003 and 2016: they moved over 10 m in 13 years. However the upper part of this rock glacier is already being disrupted again by a recent glacier advance, probably in the 1980s (Figure 60, right) which has formed a second moraine on top of the rock glacier.

1956

1959

2000

Glacieret

Glacieret

1968

2000

2013

Creep rates of several meters per year

2016

recent
rock falls
on snow
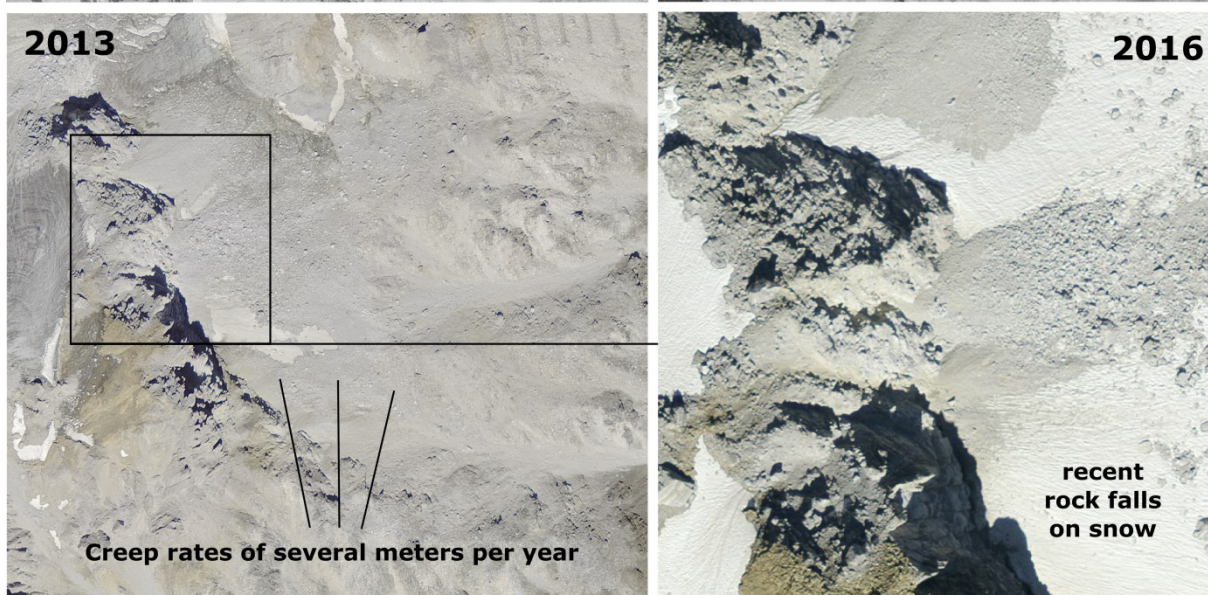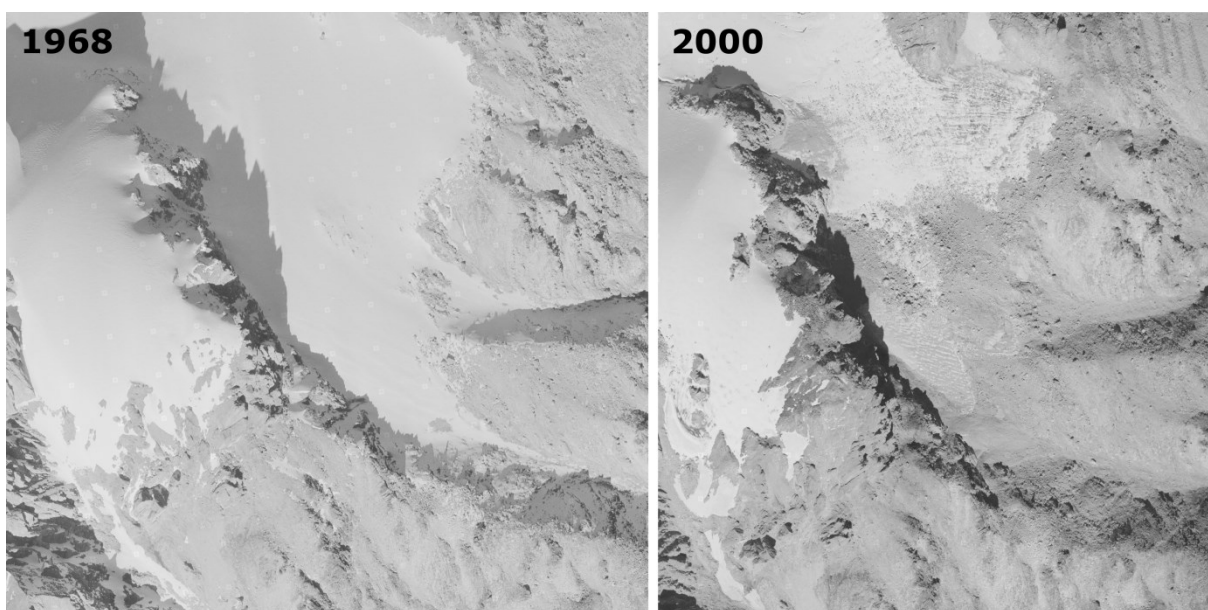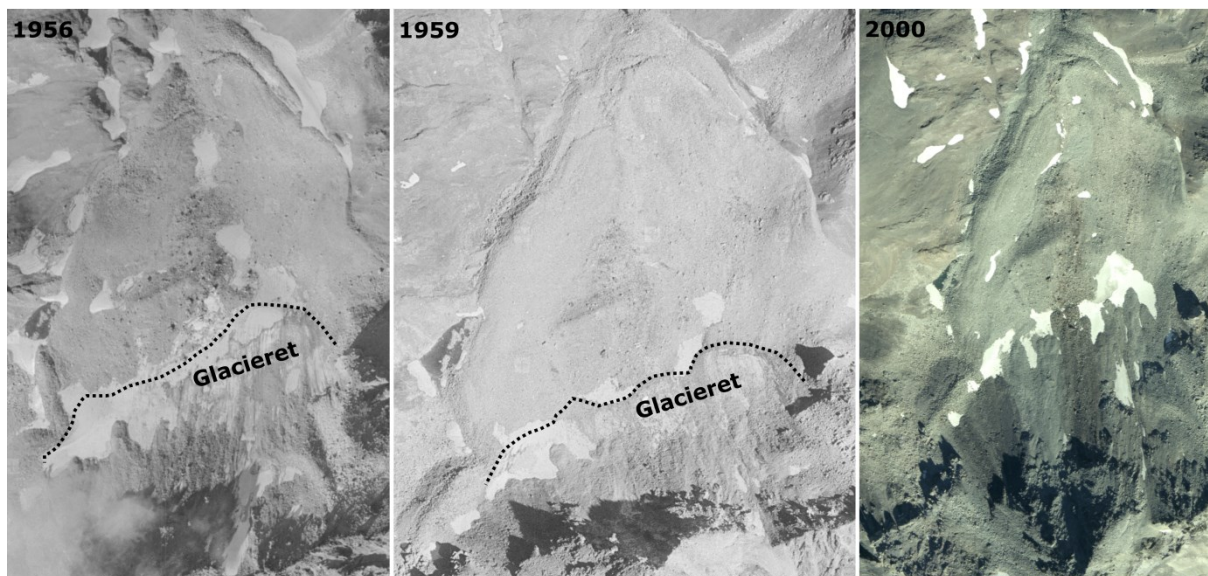
Figures on the last page:

Top: Figure 59: Glacieret in the north slope of Piz Val Lunga which is replaced by rock glacier like creep structures over time. The scree cover originates from the rock wall upslope.

Bottom: Figure 60: Part of Schmalgletscher below the summit of Wisse Schijen which was completely covered by scree from the surrounding rock walls during the last decades. The ongoing coverage of snow by rock material leads to the formation of new ground ice.

Further upslope, orthophotos between 1998 and 2016 indicate a very high supply of avalanche snow and rock avalanches. This high mass turn over probably caused the fast sequence of rock glacier and glacier advances. Years with extraordinary snow avalanches can favour extreme ice accumulation rates below a rock wall and thus promote a glacier advance. Less snow accumulation or large rock falls can switch the process towards rock glacier formation. Interestingly, there is no glacier at this site on the 1880 Siegfried map and the interannual summer snow coverage, visible in multiannual orthophotos, varies drastically. Apparently, the site is less influenced by climate but more by local effects like avalanche activity or rock fall. Consequently variations in the ice/debris ratio of the accumulating mass can occur in short-term, tipping the process towards glacier or rock glacier formation. Similar sites, showing extraordinary high accumulation rates of snow and debris and a competitive existence of glacier and rock glacier related morphology over time have been described by Monnier and Kinnard (2015) or Ackert (1998).
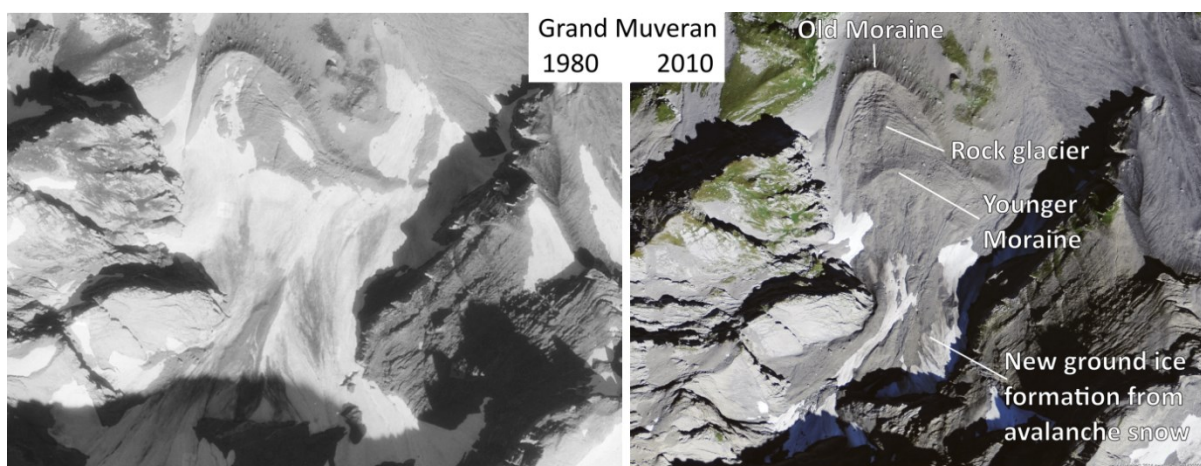
Figure 61: Example of rapidly alternating glacier – rock glacier development in a cirque below the N face of Grand Muveran, which provides large amounts of rock debris and avalanche snow.

In a few cases, such high amounts of rock and snow accumulation can form continuum features which show characteristics of both glaciers and rock glaciers. Such a feature can be found under the 1000 m high north face of Chli Ruchi (Figures 50 and 62). Its size, morphology and debris coverage have not changed since 1958 (earliest aerial image available). Consequently, this landform is also (similar to the one in figure 61) mainly controlled by the very high rates of scree and snow accumulation out of the large rock wall but it is not very sensitive to climate fluctuations.
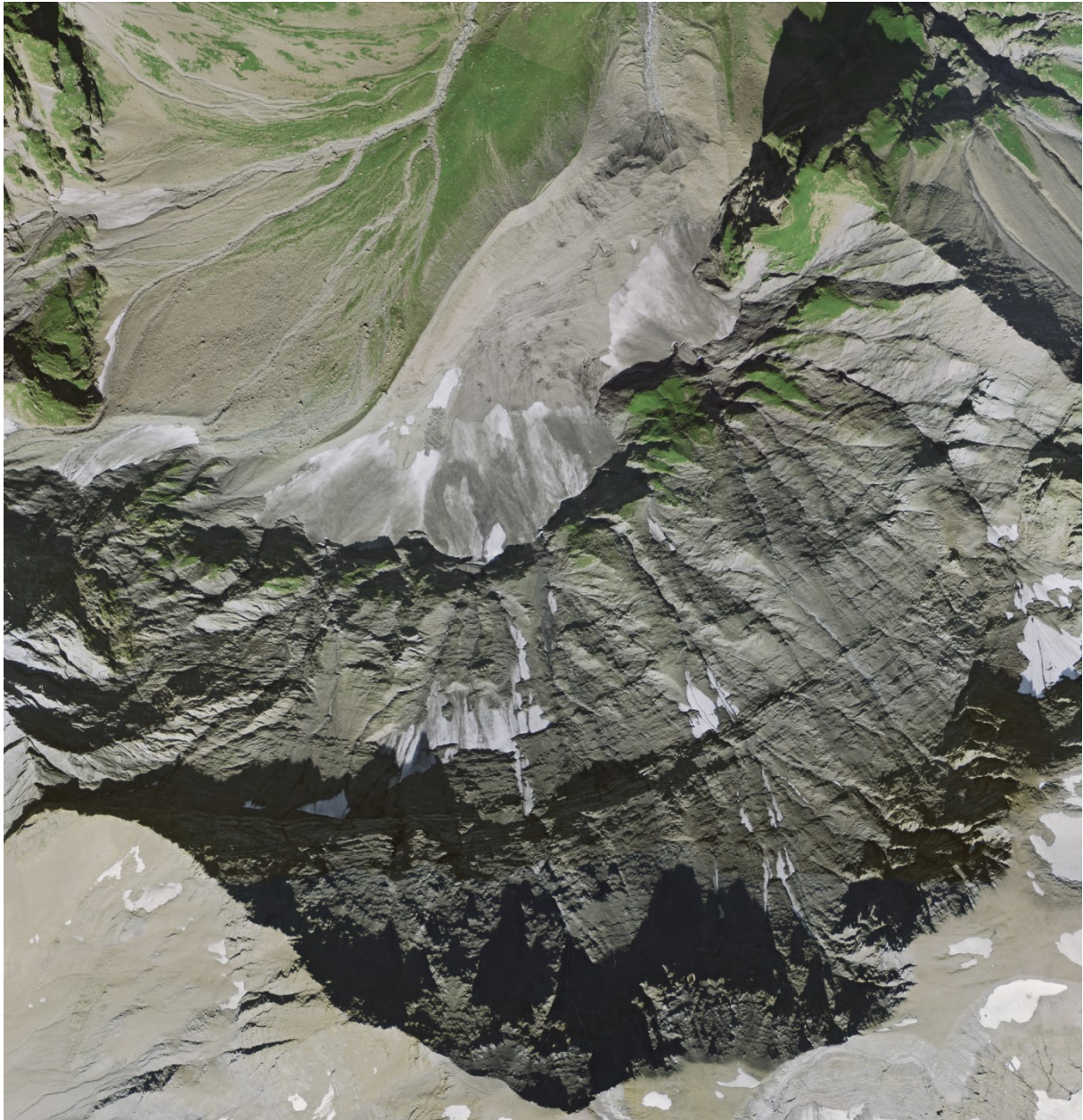
Figure 62: Sulzgletscher below the north face of Chli Ruchi. This ice-rich feature is most similar to a debris covered glacier but also shows rock glacier like characteristics particularly in the orographic right part of its front or in the moraine below the steep front.

9.4. Discussion and conclusions

Some features described as creeping, ice-bearing moraines in the literature are indeed rudiments of rock glaciers which were overridden by glaciers in their upper parts. They are rather glacier disrupted than glacier derived. A final verification of our hypothesis would be feasible by dating the ground ice content in such rock glacier fronts adjacent to the frontal push moraines of glaciers. Ages older than the LIA glaciation would support our findings.

The difference in development towards a glacier or a rock glacier depends on the ratio between rock debris and snow accumulation. If snow accumulation clearly predominates, a glacier will develop. If both materials are accumulated in a ratio typical for the ice/debris content in rock glaciers, a rock glacier will develop. Ice-rich talus slopes exist in places fed by rock fall but with smaller lasting avalanche snow deposits. Although rock glaciers can develop superimposed on glacierets, glacier ice is unlikely to be the exclusive source of ice in a rock glacier.

The reconstructed sequence of glacier versus rock glacier development implies that the development of rock glaciers is favoured during periods of warming. Climate warming, deglaciation and permafrost thaw cause an increase in rock fall activity (Noetzli *et al.*, 2003; Fischer *et al.*, 2006; Gruber and Haeberli, 2007) as well as more intense snow melt and thus change the talus to snow accumulation ratio under rock walls in favour of rock glacier development (Kenner and Magnusson, 2017). In contrast, cooling periods can be disruptive for rock glaciers due to the increased accumulation of snow and the associated glacier formation. The previously established connection of the development of larger and lower reaching rock glaciers in periods with colder climate (Haeberli, 1983; Payne, 1998; Sailer and Kerschner, 1999; Frauenfelder *et al.*, 2001) is therefore not necessarily applicable (Kenner and Magnusson, 2017).

10. Distinguishing ice-rich and ice-poor permafrost to map ground temperatures and -ice content in the Swiss Alps

Robert Kenner

WSL Institute for Snow and Avalanche Research SLF

Abstract

A countrywide permafrost distribution map of Switzerland was created, indicating ground temperatures and ice content. A realistic representation of ground temperatures has been achieved by distinguishing ice-poor and ice-rich permafrost in the modelling process. There is a very strong correlation of ground temperatures with elevation and potential incoming solar radiation in ice-poor and ice-free ground. The distribution of ice-rich permafrost was defined by modelling mass wasting processes and the integration of snow and ice into the ground caused by them. This approach yields a very accurate and largely unambiguous map. Permafrost occurrence is represented by three clearly defined classes: permafrost, possible patchy permafrost and potentially ice-rich permafrost. 58% of all 92 validation sites could be definitively classified as having permafrost or no permafrost. If only ice-poor or –free ground is considered, this value reaches 90%. The rather simple dependency of ice-poor permafrost on two main parameters is not only relevant for mapping approaches but also for a wide range of scientific and engineering purposes.

10.1 Introduction

Permafrost distribution maps are useful products applied in different fields of practice and research. They are used to plan construction work in alpine terrain, to evaluate local slope instability or to estimate large scale permafrost occurrence for scientific purposes. An essential requirement for each permafrost distribution map are reference data provided by monitoring networks such as the Swiss permafrost monitoring network PERMOS (2016) which was also used here. Previous mapping approaches in Switzerland (Keller, 1992; Keller *et al.*, 1998; Gruber and Hoelzle, 2001; Hoelzle *et al.*, 2001; Gruber *et al.*, 2006; Boeckli *et al.*, 2012; Deluigi *et al.*, 2017) have in common that they represent a statistically based permafrost likelihood for different terrain forms. Predictor variables for this likelihood are basically mean annual air temperature represented by elevation and potential incoming solar radiation. Further adjustment parameters are vegetation coverage or terrain characteristics such as slope or curvature (Boeckli *et al.*, 2012; Deluigi *et al.*, 2017). This approach has the advantage that uncertainties in the mapping of permafrost are clearly evident for the map user. However, the probability classes given are difficult to interpret and a clear prognosis about the permafrost conditions is seldom possible.

The permafrost and ground ice map (PGIM) of Switzerland presented here uses a different approach of mapping, which is based on the quintessence of two previous papers (Kenner and Magnusson, 2017; Kenner *et al.*, 2017b). In these papers we highlighted the differences between ice-rich and ice-poor permafrost in terms of their development and conservation. Ice-rich mountain permafrost (permafrost containing excess ice) was considered as being mainly caused by the burial of snow and ice into the ground, i.e. permafrost occurrence as a result of ground ice formation. This confirms the recognition of the characteristic occurrence of ice-rich permafrost at the base of talus slopes made by (Haeberli, 1975). Ice-poor permafrost (permafrost without excess ice) was focussed on as being controlled by atmospherically driven thermal processes and solar radiation, (where limited amounts of ground ice exist as a result of permafrost conditions). The need to distinguish between ice-poor and ice-rich permafrost becomes apparent in the context of permafrost monitoring and 1D thermal modelling. In general, ice-rich permafrost is less sensitive to climate fluctuations due to thermal characteristics of ice and to latent heat effects (Scherler *et al.*, 2013). Extreme weather events like the summer 2003 and 2015 heat waves in the Alps can however cause active layer thickening (PERMOS, 2016), linked to the melt of considerable amounts of ground ice in ice-rich permafrost. While active layer deepening caused by such extreme events is reversible in ice-poor permafrost (Krautblatter, 2009; Marmy *et al.*, 2013), it can be irreversible in ice-rich permafrost due to the degradation of ground ice (Zenklusen

Mutter and Phillips, 2012a). This highlights ground ice as a requirement for the existence of permafrost at such sites. 1D permafrost modelling considers this deciding relevance of ground ice and relies on a soil stratigraphy including the ice content to reproduce highly accurate ground temperatures (Hipp *et al.*, 2012; Staub *et al.*, 2015). Ice-rich and ice-poor permafrost are therefore already distinguished for the purpose of 1D permafrost modelling. As the need for this distinction has been recognized for local scale thermal modelling, it is logical to adopt this approach for permafrost mapping as well.

The PGIM presented here distinguishes between ice-rich and ice-poor permafrost, thus allowing a higher permafrost prediction accuracy and so a totally different mapping approach: In contrast to other permafrost maps, PGIM does not represent an empirically defined permafrost likelihood of occurrence, but analytically defined ground temperatures and areas with potentially high ground ice content. This type of approach has not previously been implemented by any other permafrost mapping study and is compared here with the performance of existing permafrost maps of Switzerland.

10.2 Methods

The permafrost and ground ice map PGIM of Switzerland consists of 3 zones: Permafrost (Zone 1), possible patchy permafrost (Zone 2) and potentially ice-rich permafrost (Zone 3).

Zones 1 and 2 of the PGIM were derived from modelled ground temperatures. Zone 1 includes all areas with modelled negative ground temperatures. Zone 2 includes the areas with ground temperatures ranging between 0°C and 1°C and is intended as a buffer zone, covering areas which might sporadically be affected by permafrost. The ground temperatures were calculated based on a linear regression analysis using the explanatory variables potential incoming solar radiation and elevation (as proxy for mean annual air temperature). Potential incoming solar radiation was calculated with the ESRI tool "Area solar radiation" with the parameter transmissivity set at 0.4, and diffusity at 0.5, which corresponds to values recommended for moist temperate climates by the software developer. We used ground temperatures measured in 10 reference boreholes as predictor variables. These boreholes were carefully chosen from areas without ice-rich permafrost under the condition that non-ambivalent insolation values can be attributed to them (upper 10 sites in table 12). These boreholes represent the entire set of available ground temperature data in Switzerland meeting this requirement. Temperature is measured in the boreholes at several depths by thermistor chains with a sub-day temporal resolution. The

thermistors commonly have a measurement accuracy of around 0.1°C or better, the types of thermistor and data loggers are specified in (PERMOS, 2016). The mean annual ground temperatures (MAGTs) measured in these boreholes are shown in Figure 63. Extracting a representative mean temperature from them is not straightforward because they have different measurement periods, temperature profiles and depths. The lowest average MAGT is considered to be decisive for the presence of permafrost. We therefore averaged the MAGTs over the entire time series of a thermistor and then chose the lowest average MAGT of all depths (Figure 63). For this we did not consider data from the active layer in permafrost boreholes. All MAGTs are plotted in Figure 63 and the chosen reference temperature is indicated in the charts.

Zone 3 includes all forms of ice-rich permafrost such as rock glaciers, ice-rich talus slopes or ice-bearing moraines and was defined in ERSI ArcGIS. The basic concept was to define areas in which the burial of ice or snow by mass wasting processes can lead to the development of ice rich permafrost.

First the hydrological flow accumulation from rock walls steeper than 40° was calculated on the basis of a 25 m DEM. This was done in areas above 2000 m elevation, as only very few, azonal permafrost sites exist below (Cremonese *et al.*, 2011). The runoff tracks were buffered by a 120 m wide belt and the resulting strips correspond in their upper parts to the main tracks of snow avalanches and rock fall. Further down they represent potential rock glacier creep paths. These areas were then reduced stepwise by deleting spatial intersections with several other datasets from them, namely:

- All areas steeper than 30°

- All vegetation covered areas. The vegetation coverage was deduced from orthophotos using the SAVI Index (Huete, 1988). Areas of vegetation / no vegetation within the resulting 25 m grid were homogenized by iteratively applying a classic 3x3 cell erosion and dilation operation.

- Flood plains, which were defined as being areas with slope < 4° and intersected by rivers.

- Lakes

- Maximal extent of Little Ice Age (LIA) glaciation. This dataset was created by Maisch (1999).

The remaining polygons were then aggregated to fill small gaps, simplified and smoothed. After this, all areas mentioned above were deleted again from the reworked polygons. In a final step, a 50 m buffer zone around the LIA moraines was added to the zone to include ice-bearing moraines.

In a final step, the resulting polygons were edited manually. Some of them still contained areas in which bedrock at the surface excludes the development of ice-rich permafrost development as described above. In a few cases, parts of rock glaciers were missing due to errors in the reproduction of creep paths or to small terrain steps with slopes over 30°. Manual editing included 2 clear tasks: All areas showing a bedrock surface, infrastructure or > 50% vegetation coverage (which was for some reason not captured by the SAVI index) were removed from zone 3. Missing parts of rock glaciers were added to zone 3 if at least parts of them were already captured by the automatic mapping approach. The polygon editor was not aware of the positions of the validation points during this process. The resulting areas form zone 3 are considered to potentially contain ice-rich permafrost.
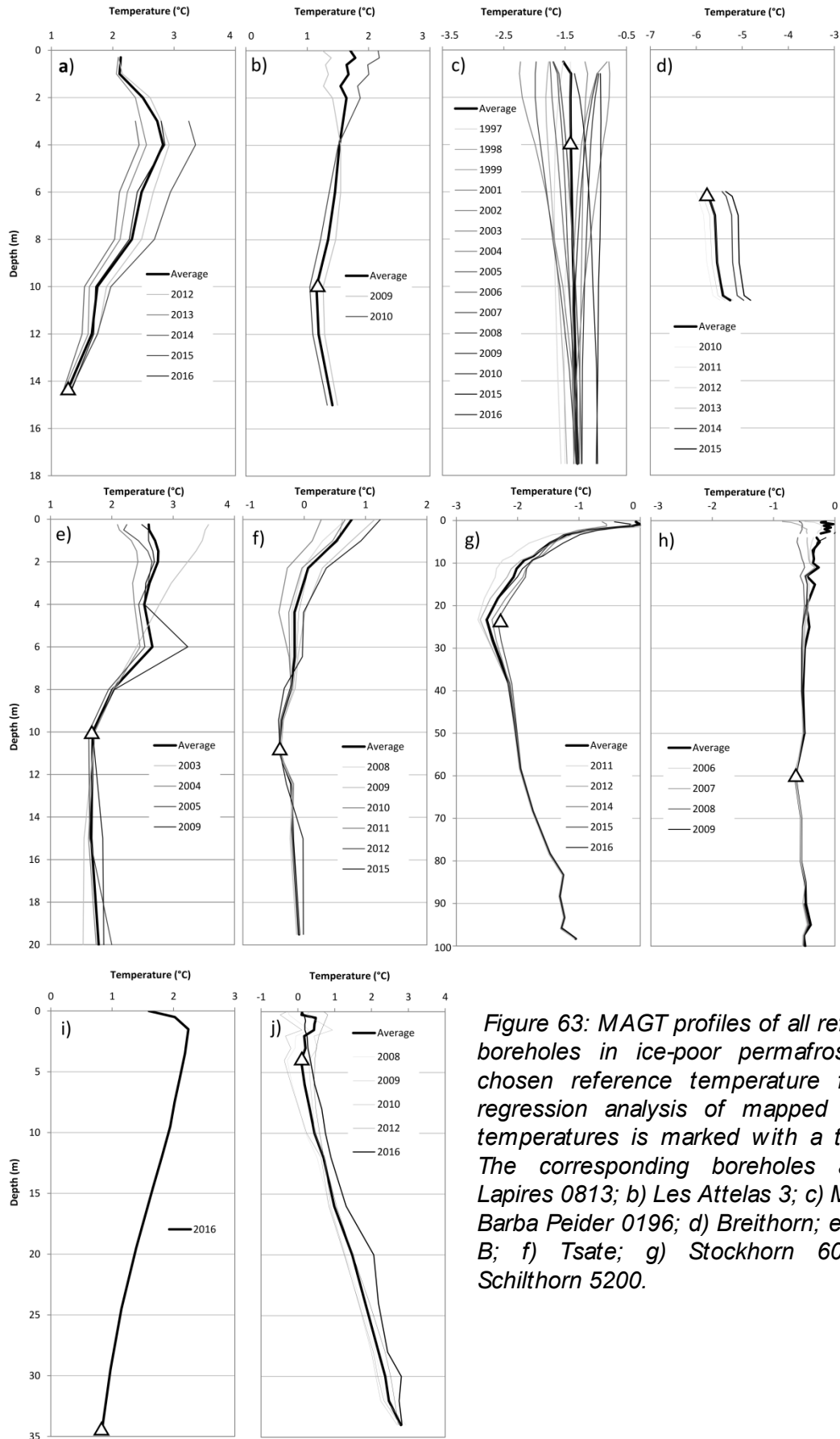
Figure 63: MAGT profiles of all reference boreholes in ice-poor permafrost. The chosen reference temperature for the regression analysis of mapped ground temperatures is marked with a triangle. The corresponding boreholes are: a) Lapires 0813; b) Les Attelas 3; c) Muot da Barba Peider 0196; d) Breithorn; e) Flüela B; f) Tsate; g) Stockhorn 6000; h) Schilthorn 5200.

159

Table 12: Reference boreholes provided by 1 - PERMOS (2016), 2 – WSL Institute for Snow and Avalanche Research SLF, 3 - Swiss Federal Office for the Environment, 4 – University of Fribourg, 5 - University of Lausanne. The uppermost 8 were used for the calculation of ground temperatures in Zones 1 and 2 of the PGIM. The lowermost 8 were used to demonstrate the failure of this calculation if ice-rich and ice-poor boreholes are not distinguished (Table 14). The MAGT value corresponds to the depth at which the lowest MAGT was measured in the boreholes (Figure 63).

Site name & Provider	Ground ice content	Elevation [m a.s.l.]	Insolation [Wh/m^2]	MAGT [°C]	Longitude (WGS 84)	Latitude (WGS 84)
Muot da Barba Peider 0196 [1]	Ice-poor	2946	1038317	-1.41	9.93109	46.49639
Schilthorn 5200 [1]	Ice-poor	2910	1150229	-0.65	7.83442	46.55828
Stockhorn 6000 [1]	Ice-poor	3410	1591939	-2.50	7.82419	45.98678
Tsate [1]	Ice-poor	3040	1635945	-0.4	7.54844	46.10904
Jungfrau [1]	Ice-poor	3590	766101	-5.79	7.97316	46.54617
Flüela B [2]	Ice-free	2501	1075441	1.69	9.94314	46.74687
Breithorn [3]	Ice-free	2865	1595590	0.84	7.81785	46.14010
Lapires 0813 [4]	Ice-free	2559	1079555	1.15	7.28345	46.10526
Les Attelas 3 [5]	Ice-free	2741	1343517	1.04	7.27492	46.09659
Gemsstock Nord [1]	Ice-free	2940	1436194	0.025	8.61043	46.60125
Flüela 0102 [1]	Ice-rich	2394	1144458	-0.3	9.94516	46.74792
Attelas 0108 [1]	Ice-rich	2661	1348729	-1.06	7.27307	46.09677
Attelas 0208 [1]	Ice-rich	2689	1303296	-0.41	7.27368	46.09674
Corvatsch 0287 [1]	Ice-rich	2672	1323424	-1.35	9.82185	46.42878
Lapires 1108 [1]	Ice-rich	2500	1103135	-0.6	7.28435	46.10611
Muragl 0299 [1]	Ice-rich	2539	1324043	-0.2	9.92735	46.50722
Schafberg 0190 [1]	Ice-rich	2754	1502401	-0.77	9.92631	46.49737
Ritigraben 0102 [1]	Ice-rich	2690	1473731	-1.24	7.84983	46.17469

10.3 Validation

The permafrost map was validated using a set of 92 evidence points of permafrost occurrence or permafrost absence. Parts of these validation points correspond to the dataset presented by Cremonese *et al.* (2011). Records from this database were only used if they have exact coordinates and show direct evidence of permafrost occurrence or absence; either based on observations of ice in construction work trenches and rock fall scars or based on ground temperature data measured in boreholes

The records in this database have a clear bias towards permafrost occurrence, as many research sites are included which were intentionally chosen to be included in a permafrost measurement network because of a high probability of permafrost occurrence. We therefore

added a second validation dataset based on continuous ground surface temperature data (GST) measured at 38 automatic weather stations of the Intercantonal Measurement and Information System (IMIS) (Russi *et al.*, 2003). To balance the number of evidence points with and without permafrost, only IMIS stations above 2400 m elevation were chosen, which turned out to be most relevant for validation purposes. These IMIS stations measure the temperature within the uppermost 10 cm of the ground with a Campbell 107 temperature probe. Of these 38 IMIS stations, 33 register a constant zero curtain during winter time and are therefore on permafrost free ground (Hoelzle, 1992). The remaining 5 stations show quite constant winter GST between -3°C and -4°C and are located on active rock glaciers. They were therefore classified as permafrost sites. Furthermore, a few additional borehole sites, which are not included in Cremonese *et al.* (2011) were added to the validation set (Table 13, Appendix).

All three classes of the PGIM were attributed with the number of validation records lying within them indicating permafrost occurrence or permafrost absence. The same validation process was applied to the alpine permafrost index map (APIM) created by Boeckli *et al.* (2012) and the Potential permafrost distribution map (PPDM) created by Gruber *et al.* (2006), available online in the Swisstopo web map service map.geo.admin.ch. A closer methodical background to the PPDM can be found in Haeberli (1975) and (Keller, 1992). Additionally, Zone 3 of the PGIM was validated against a rock glacier inventory of the Albula Alps created by Kenner and Magnusson (2017). With 124 records, the inventory represents all rock glaciers in the 361 km^2 large alpine zone (area above 2000 m a.s.l.) of the Albula Alps.

10.4 Results

Predicting the ground temperatures of the ice-poor reference boreholes on the basis of elevation and potential incoming solar radiation yields a correlation coefficient of 0.998 and a standard error of 0.16°C (Table 14, Figure 64). The strong regression result highlights the rather simple dependency of ice-poor permafrost on elevation and solar radiation and its high and accurate predictability.
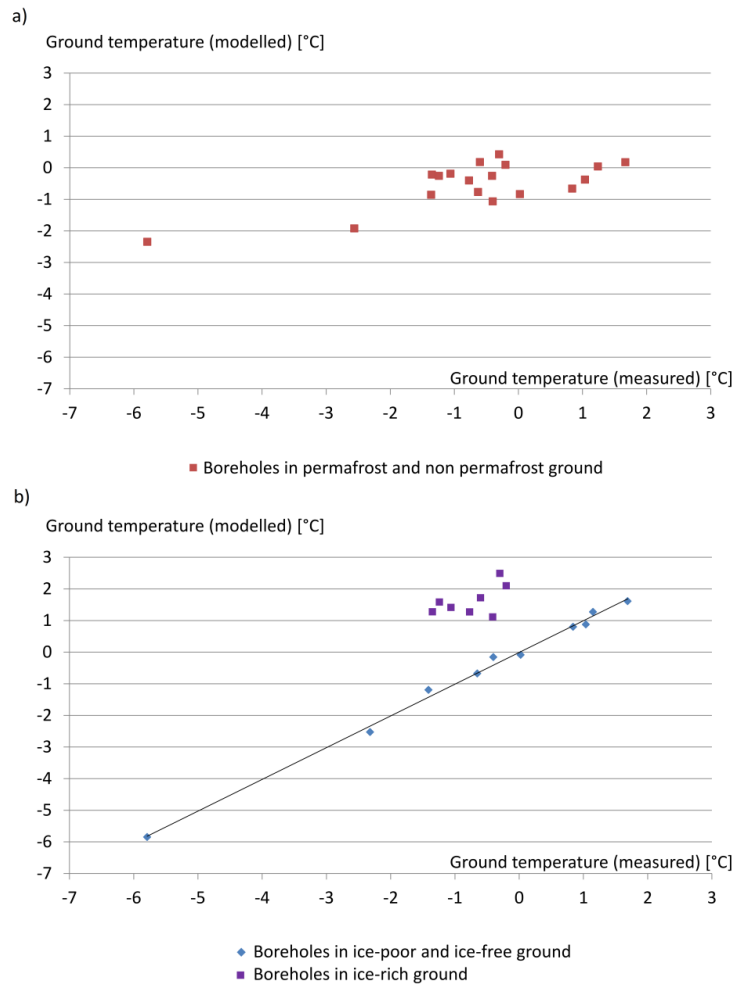
Figure 64: Each data point represents a borehole and its measured and modelled mean ground temperature. The modelled temperatures are calculated using the result of a linear regression based on elevation and potential solar radiation. While there is no systematic relation between these two parameters and the ground temperatures when using both ice-poor and ice-rich boreholes for the regression (a), a clear correlation appears when using only ice-poor or ice-free boreholes (b).

The validation of the PGIM (Figure 65) confirms the high accuracy of ice-poor permafrost prediction. Twenty of 22 validation sites representing ice-poor permafrost are located in Zone 1, one validation point in Zone 2 and one site outside the permafrost zonation. In turn, 0 of 49 sites devoid of permafrost were located in Zone 1 and 4 in Zone 2. Zone 3 (potential ice-rich permafrost) includes 31 sites indicating permafrost and 2 indicating permafrost absence. Zone 3 furthermore includes 95.5% of the rock glacier area registered in the Albula Alps inventory (Kenner and Magnusson, 2017). This value applies to the automatically created version of zone 3 before it was manually edited and some rock glacier outlines were redrawn within zone 3.

Table 14: Results of the regression analysis on ground temperature in dependency of elevation and potential solar radiation.

	Ice-poor permafrost (10 Boreholes)	Ice-poor & ice-rich permafrost together (16 boreholes)
Correlation coefficient	0.998	0.523
Coefficient of determination	0.986	0.274
Standard error	0.16°C	1.02°C

The validation of the APIM is shown in Figure 66. The two zones representing "No Permafrost" and the highest permafrost probability have a similar error rate as the corresponding classes in the PGIM but contain much less validation records. For the remaining classes no systematic relation between the index ranges and the occurrence of permafrost is discernible. The permafrost distribution over the indices is rather homogeneous and an increase in permafrost frequency is only visible within the very high indexed areas > 80.

The validation result of the PPDM is shown in Figure 67. The different probability ranges do not reflect the actual permafrost frequency given by the validation points in each class. Several permafrost evidences even exist outside the permafrost zonation of this map.
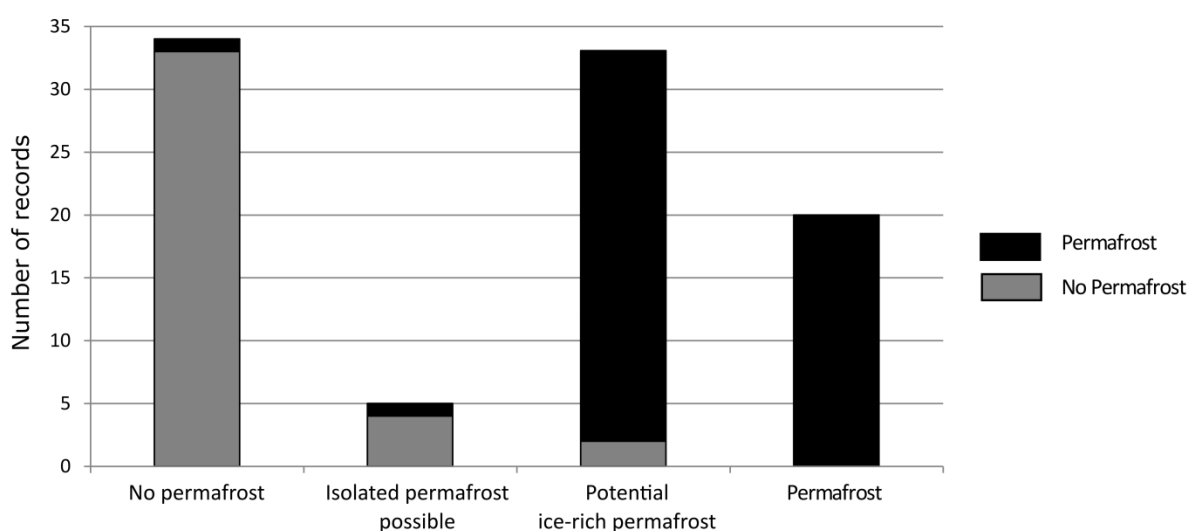
Figure 65: Validation of the PGIM showing the number of sites with permafrost occurrence and permafrost absence in each map class.
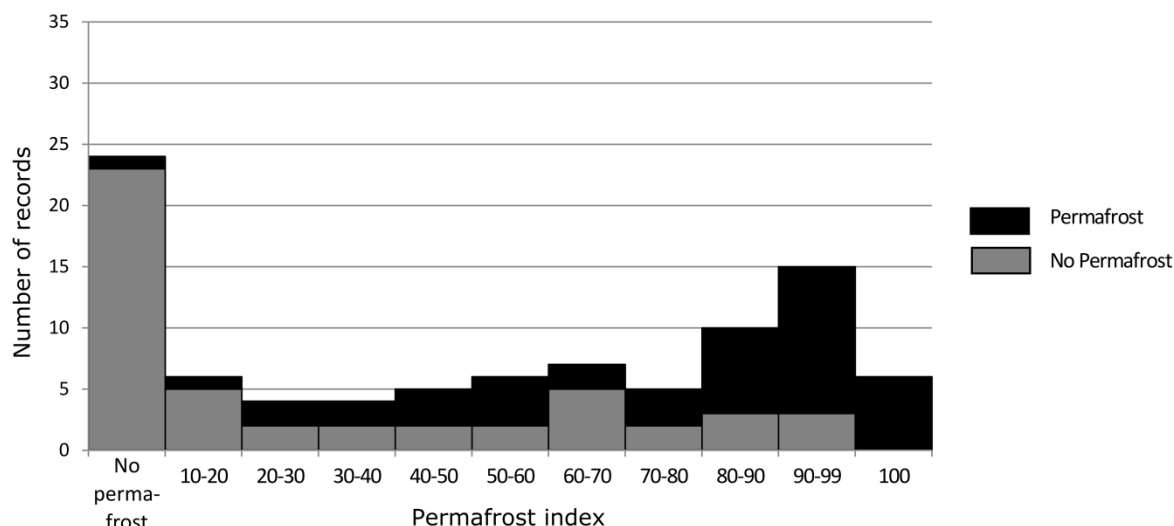
Figure 66: Validation of the APIM showing the number of sites with permafrost occurrence and permafrost absence for different permafrost probability ranges. As the map does not define classes but gives unique index values for each cell of the map, ranging from 0.1 to 1, these values were classified in 10 permafrost classes and a "No permafrost" class including all records outside the permafrost zonation.
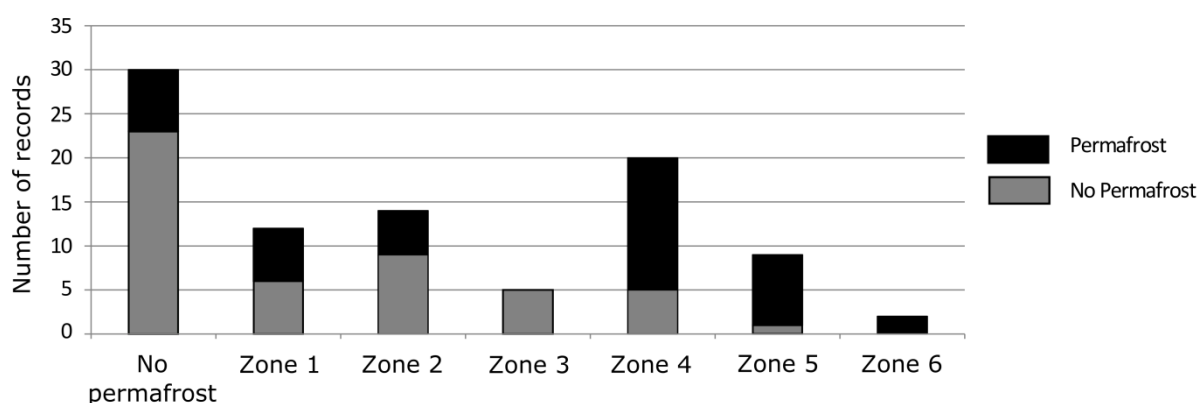
Figure 67: Validation of the PPDM showing the number of sites with permafrost occurrence and permafrost absence in each map class. The zones were originally defined as follows: **Zone 1** *– local permafrost possible (lpp), patchy, discontinuous;* **Zone 2** *- lpp, frequent patchy distribution;* **Zone 3** *- lpp, patchy to extensive;* **Zone 4** *– Extensive permafrost likely (epl);* **Zone 5** *– epl, increasing thickness;* **Zone 6** *– epl, very thick in places, to over 100 m. The class "No Permafrost" includes all records outside the permafrost zonation.*

10.5 Discussion:

10.5.1 Permafrost predictability

The high dependency of ice-poor permafrost on elevation and solar radiation highlights the importance of distinguishing between ice-rich and ice-poor permafrost. The extremely high correlation coefficient is probably caused by the small number of test sites (10) and might rather overestimate the strength of this dependency. Nevertheless, the strong relation is remarkable, in particular when taking into account that the borehole temperatures represent different landforms with strong differences in slope, substrate characteristics and snow coverage. Snow cover timing and thickness is known to have seasonal influences on the ground temperature (Zhang, 2005; Haberkorn *et al.*, 2015). The regression result raises the question on the actual long-term effect of these seasonal influences.

The high predictability of ice-poor permafrost is insufficiently exploited as long as ice-rich permafrost is not treated separately in the data analysis. Table 14 and Figure 64 show how drastically the predictability of permafrost by elevation and solar radiation drops when ice-rich permafrost is included in the regression analysis of ground temperatures. The formerly strong correlation practically disappears. Ice-poor and ice-rich permafrost have different origins, different mechanisms of conservation and different rates of degradation and must therefore be distinguished in permafrost modelling, mapping or climate sensitivity analyses. The predictability of ice-rich permafrost is clearly lower and requires the consideration of mass wasting processes such as rock fall, avalanche activity and varying glaciation during the entire Holocene. The accuracy in reproducing these processes is naturally limited.

10.5.2 Map interpretation, uncertainty and accuracy

In contrast to other maps, the PGIM only has 3 zones, which are easy to interpret: Two zones (1 and 2) represent modelled ground temperatures and the third one specifies areas with potential ground ice content caused by mass movement processes (Figure 68). This enables an improvement in mapping accuracy and reduces uncertainty.
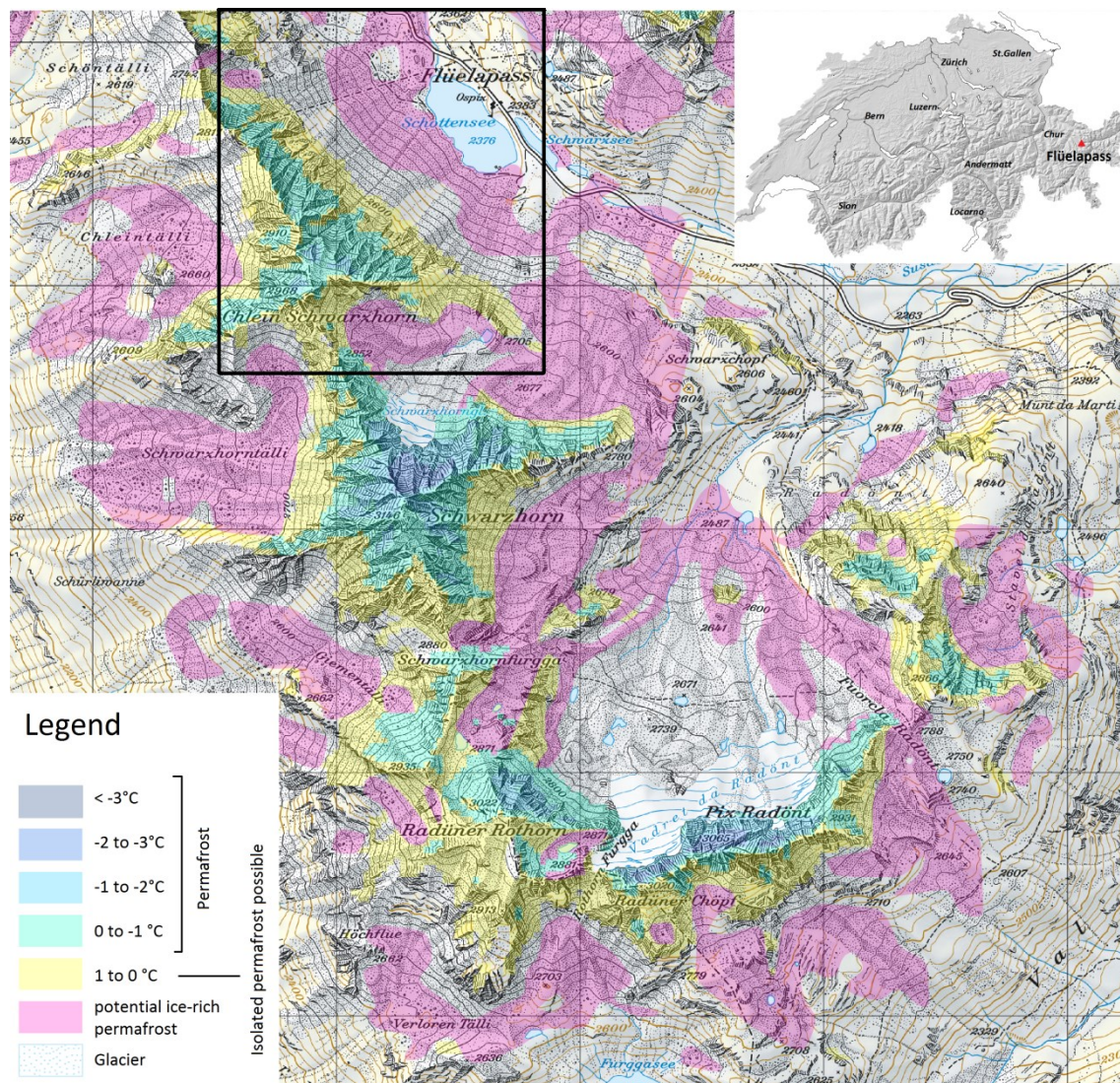
Figure 68: Map section of the PGIM, showing the permafrost distribution in three zones. The black frame is the sector shown in Figure 68. The map grid has a resolution of 1 km. (Map: pixmaps © (2017) swisstopo (5704 000 000))

The uncertainty can be quantified by the validation points, which are clearly attributed by the map as being permafrost or not. In the PGIM, definitive permafrost is indicated by the Zone 1. In the APIM definitive permafrost is indicated by a permafrost index of 1 (for validation, values higher than 0.994 were rounded to 1). The PPDM does not have a zone of definitive permafrost. Definitive permafrost absence is indicated on all three maps for areas outside the permafrost zonation. Compared to the other maps, the PGIM can attribute the most validation points to a definitive class, indicating either permafrost occurrence or permafrost absence (Figures 65-67).

Accuracy can be measured by the number of validation points wrongly attributed to a definitive class or by the plausibility of the description of a class. The accuracy of the PPDM,

166

in which 7 permafrost sites occur out of the permafrost zonation is relatively low. The definitive classes of the APIM and the PGIM predict all validation points contained within them correctly - with the exception of one site (Emshorn-Oberems), which was attributed wrongly on both maps. The definitive classes of the PGIM nevertheless contained more than double the records than the APIM.

Both comparison maps showed weaknesses in the reproduction of permafrost free areas, while PGIM performed better here. This might be caused by a phenomenon which can be described as an 'elevational permafrost gap'. A common permafrost distribution in the Alps is characterised by thermally induced permafrost in the upper parts of a rock wall, with a 'permafrost gap' below and ice-rich permafrost at the base of the underlying talus slopes. Figure 69 shows the example of the research site Flüelapass (Kenner *et al.*, 2017b), showing this pattern of permafrost distribution.
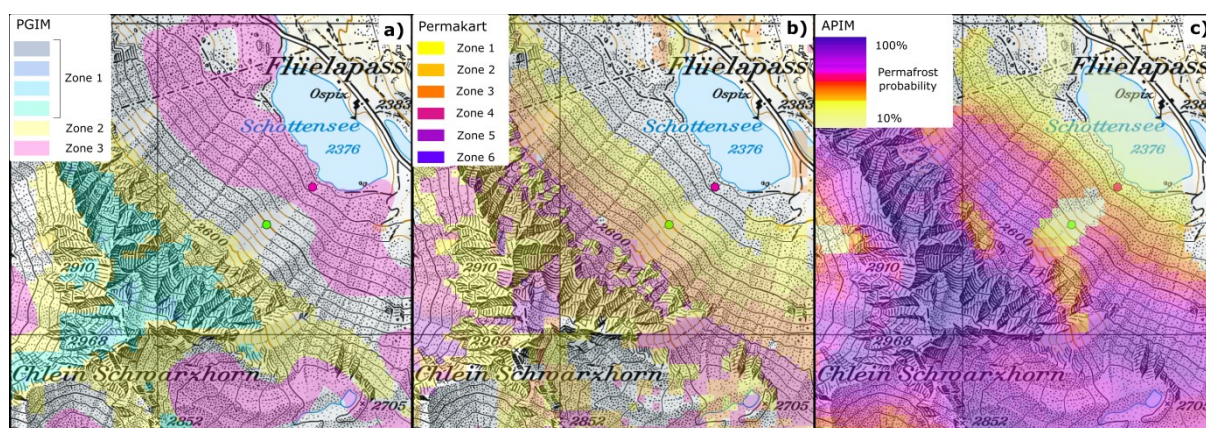
Figure 69: Comparison of three permafrost maps at the research site Flüelapass (a: PGIM, b: PPDM, c: APIM). This site is a typical example showing ice-rich permafrost at the base of a talus slope, a permafrost gap further upslope and most likely permafrost in the rock wall above the talus slope. A borehole without permafrost (green dot) is located in the permfrost gap, another with ice-rich permafrost (pink dot) is located at the base of the slope. (Map: pixmaps © (2017) swisstopo (5704 000 000))

Mapping based on thermal influences only is not able to reproduce the gap and either neglects the permafrost at the base of the talus slope (Figure 69b) or overestimates the permafrost further upslope (Figure 69b and 69c). This problem leads to suspicious peaks of permafrost absence in the zones of the comparison maps which indicate a medium permafrost probability, e.g. the probability zone of 60-70 % on the APIM or the zone "local permafrost possible, patchy to extensive" on the PPDM (Figures 66 and 67). The same reason might cause the rather random distribution of permafrost free validation points over the remaining probability classes of APIM.

The typical azonal permafrost found at low elevations (<2000 m), at sites like Creux du Van (Delaloye *et al.*, 2003) or Dreveneuse (Delaloye and Lambiel, 2007) is not included on any of the Swiss permafrost distribution maps discussed in this paper. The presence of azonal permafrost is enabled by a constellation of processes involving unusually effective advective cooling. These are difficult to implement in a large scale nationwide map.

10.5.3 Challenges and possible future approaches in mapping ice-rich permafrost

Zone 3 representing ice-rich permafrost in the PGIM has a relatively high uncertainty. The low number of permafrost free validation points (2 out of 33, see Figure 65) in this zone might rather overestimate the accuracy of this zone due to a general lack of permafrost free validation points in talus slopes. However, there is very little ice-rich permafrost outside this zone, as indicated by the almost entire representation of the Albula rock glacier inventory within the automatically created raw version of zone 3. Accordingly, zone 3 should not be interpreted as a reliable representation of ice-rich permafrost but more as a best-possible one including almost the entire ice-rich permafrost in Switzerland and some bycatch of permafrost free ground. This area needs to be narrowed down in a common effort by the permafrost community and improved updates of the map are planned for the future. This is however related to certain challenges, which are discussed below.

Rock glaciers are a clearly visible indicator of ice-rich permafrost but are also the most critical ice-rich permafrost features to map, as the creep process has to be considered. The creep paths are sometimes hard to reproduce, as the rock glacier changes the terrain morphology in such a way that the runoff tracks, which are the basis of Zone 3, run laterally to the convex rock glacier body and their buffer zone does not incorporate the whole rock glacier. Additionally, in some cases rock glaciers creep over terrain steeper than 30° and these parts of the rock glaciers are missing in zone 3. A further problem is caused by rock glaciers mapped as LIA glaciers in Maisch (1999) and are thus not included in the map. These problems have largely been solved by the manual editing of zone 3. However further improvements would be possible by merging the large number of existing rock glacier inventories in Switzerland and completing a nationwide inventory by mapping hitherto uninvestigated areas. In this way, rock glaciers can be excluded from the automatic mapping of ice rich ground, which allow focussing on ice-rich talus slopes, which are easier to delimit automatically.

Ice-rich permafrost only occurs in loose rock sediments, thus, the uncertainty in mapping it can radically be lowered by distinguishing loose rock from solid bedrock. Such a dataset does not yet exist on a national scale and in the required accuracy and existing automatic classification algorithms are not able to perform this differentiation. This problem was also improved by manual editing of zone 3. A refinement of the result would nevertheless be useful.

Kenner and Magnusson (2017) highlighted the influence of the combined effect of lithology and precipitation on ice-rich permafrost. As ice-rich permafrost is rarer in sedimentary rock areas with high precipitation rates and relatively frequent in drier areas with crystalline or metamorphic lithology, zone 3 will contain more or less permafrost in the respective regions. These regional climate- and lithology induced differences are difficult to implement in a map and must be carefully interpreted by the user.

10.5.4 Permafrost area in Switzerland

The PGIM indicates a potential permafrost area of 2000 km^2 in the Swiss Alps, which is considerably less than that indicated by the APIM (3710 km^2 (Böckli and Haeberli, 2013)) and also less than on the PPDM (2550 km^2). To estimate the true permafrost area, Böckli and Haeberli (2013) suggested to consider all areas of the APIM with an index value > 0.5. This results in an area of 2160 km^2 for the APIM. The PGIM includes 830 km^2 in Zone 1 and 600 km^2 in Zone 3, of which maximum 90% are expected to include permafrost. This results in an area of ≤ 1400 km^2 of permafrost terrain in the Swiss Alps.

10.5.5 Ground temperatures and ice content

The advantage of the PGIM is not only its relatively high accuracy and low uncertainty. The zonation allows an estimation of the permafrost temperature, as Zones 1 and 2 indicate ground temperatures and the ice-rich permafrost in Zone 3 often has a temperature close to 0°C (PERMOS, 2016). The localisation of ice-rich and warm permafrost is particularly important for engineering purposes as it affects the ground stability and bearing capacity strongest (Bommer *et al.*, 2010). Warm permafrost in rock walls is in addition very sensitive to climate fluctuations and can contribute to rock slope instability (Davies *et al.*, 2001). In cold rock permafrost specially developed construction materials are required (Bommer *et al.*, 2008).

Furthermore, the distinction between ice-rich and ice-poor permafrost can be the basis for a more accurate estimation of the potential water resources stored as ground ice in the Swiss Alps (Jones *et al.*, 2018). Additional information on ground ice content as well as average

permafrost thickness in ice-rich permafrost would be necessary for such a calculation. (Böckli and Haeberli, 2013) deduced these values from ground temperatures. However, in the case of ice-rich permafrost they are largely controlled by mass wasting processes and can only be empirically defined.

10.6 Conclusion:

This study not only presents a new permafrost distribution map for the Swiss Alps but also demonstrates the high predictability of ice-poor permafrost and the need to distinguish it from ice-rich permafrost. This is an important outcome for mapping and local modelling but also for studies of future permafrost scenarios and/or past permafrost evolution. We conclude that:

- Temperatures in ice-poor or ice-free ground can be mapped with high accuracy on a national scale.
- The approach seems to be reliable not only for moderate slopes but also for steep rock walls. This raises questions on the long-term effect of seasonal influences of the snow cover on ground temperatures.
- The distribution of ice-rich permafrost is better predicted and explained by analysing mass wasting processes than thermal ones.
- The permafrost and ground ice map PGIM presented here contributes towards an improvement in the accuracy of permafrost mapping in Switzerland.
- The 3 zones of the map give the reader clear information on their meaning (ground temperatures/ ice content) instead of a probability value and thus enable an easy interpretation with a low uncertainty.
- The future adaptation of the map to higher ground temperatures in the reference boreholes, triggered by climate warming, is easily possible.

Acknowledgements

Appendix

Table 13: Validation sites and the zones assigned to them in the permafrost maps. Type: IMIS - IMIS station, BH - borehole, CS - construction site, RF - rock fall. Data providers: 1 – WSL Institute for Snow and Avalanche Research SLF, 2 - Cremonese et al. (2011), 3 - University of Lausanne, 4 – Swiss Federal Office for the Environment. 5 – University of Fribourg. Zones and probability classes of the maps: see Figures 63-65.

Type/ Provider	Name	Perma frost	PGIM	APIM	PPDM	Elevation [m a.s.l.]	Longitude (WGS 84)	Latitude (WGS 84)
IMIS / 1	Saas - Seetal	No	Zone 3	No perm.	Zone 1	2477	7.87895	46.17137
IMIS / 1	Trubelboden - Trubelboden	No	Zone 3	No perm.	No perm.	2459	7.58558	46.37096
IMIS / 1	Lukmanier - Lai Verd	No	Zone 3	63	No perm.	2554	8.78352	46.60416
IMIS / 1	Fully - Grand Cor	No	Zone 3	46	No perm.	2602	7.08964	46.19469
IMIS / 1	Bernina - Puoz Bass	No	Zone 3	50	No perm.	2629	9.91588	46.44007
IMIS / 1	Boveire - Pointe de Toules	No	Zone 3	43	Zone 4	2687	7.23722	45.98480
IMIS / 1	Gandegg - Gandegg	No	Zone 3	72	No perm.	2710	7.76060	46.42926
IMIS / 1	Kesch - Porta d'Es-cha	No	Zone 3	66	Zone 1	2727	9.89813	46.62132
IMIS / 1	Gornergrat - Gornergratsee	No	Zone 3	98	Zone 5	2952	7.78359	45.98718
BH / 2	Barthélemy les Rochers (Zinal)	No	Zone 3	35	Zone 2	2519	7.59812	46.13660
BH / 2	Neue Monte Rosa Hütte (Zermatt)	No	Zone 3	93	Zone 1	2866	7.81233	45.95795
BH / 3	Lapir2	No	Zone 3	76	Zone 3	2559	7.28345	46.10526
IMIS / 1	Zermatt - Alp Hermetje	No	No perm.	No perm.	No perm.	2409	7.70238	45.99799
IMIS / 1	Goms - Treichbode	No	No perm.	No perm.	No perm.	2428	8.22856	46.48912
IMIS / 1	Julier - Vairana	No	No perm.	No perm.	Zone 1	2426	9.69231	46.47850
IMIS / 1	Oberwald - Jostsee	No	No perm.	No perm.	No perm.	2432	8.31595	46.54522
IMIS / 1	Piz Martegnas – Colms da Prasonz	No	No perm.	No perm.	No perm.	2429	9.53739	46.58009
IMIS / 1	Bedretto - Cavanna	No	No perm.	No perm.	Zone 2	2420	8.51112	46.53268
IMIS / 1	Bernina - Motta Bianca	No	No perm.	No perm.	No perm.	2447	10.02920	46.42057
IMIS / 1	Davos - Hanengretji	No	No perm.	No perm.	No perm.	2456	9.77400	46.78885
IMIS / 1	Goms - Bodmerchumma	No	No perm.	10	Zone 2	2439	8.23251	46.42045
IMIS / 1	Taminatal - Wildsee	No	No perm.	59	No perm.	2468	9.39093	46.96836
IMIS / 1	Eggishorn - Flesch	No	No perm.	No perm.	No perm.	2500	8.09170	46.41680
IMIS / 1	Bever - Valetta	No	No perm.	No perm.	No perm.	2512	9.83713	46.53953
IMIS / 1	Samnaun - Ravaischer Salaas	No	No perm.	No perm.	No perm.	2512	10.33833	46.95637
IMIS / 1	Weissfluhjoch	No	No perm.	34	No perm.	2536	9.80911	46.82955
IMIS / 1	Les Attelas - Lac des Vaux	No	No perm.	No perm.	No perm.	2550	7.26988	46.10529
IMIS / 1	Davos - Barentalli	No	No perm.	No perm.	Zone 3	2557	9.81941	46.69890
IMIS / 1	Les Diablerets - Tsanfleuron	No	No perm.	65	No perm.	2584	7.23939	46.31445
IMIS / 1	Anniviers - Tracuit	No	No perm.	No perm.	No perm.	2589	7.65639	46.12116
IMIS / 1	Arolla - Breona	No	No perm.	No perm.	No perm.	2602	7.56205	46.08742
IMIS / 1	Anniviers - Orzival	No	No perm.	No perm.	Zone 4	2641	7.53536	46.18828
IMIS / 1	Zermatt - Triftchumme	No	No perm.	19	Zone 4	2753	7.72738	46.04217

CS / 2	Speichersee Totalpsee (Davos)	No	No perm.	26	Zone 2	2501	9.81109	46.83724
CS / 2	Herrenabfahrt Corviglia (St. Moritz)	No	No perm.	14	Zone 2	2829	9.80023	46.50610
BH / 2	Catogne (Bovernier)	No	No perm.	21	No perm.	2331	7.10474	46.06012
BH / 2	La Montagnetta (St. Jean/Grimentz)	No	No perm.	0	No perm.	2270	7.55943	46.19472
BH / 2	Barthélemy les Rochers (Zinal)	No	No perm.	0	Zone 2	2519	7.59812	46.13660
BH / 2	Barthélemy les Rochers (Zinal)	No	No perm.	0	Zone 1	2519	7.59812	46.13660
BH / 2	Emshorn (Oberems)	No	No perm.	16	Zone 1	2506	7.67602	46.26670
BH / 2	Emshorn (Oberems)	No	No perm.	0	No perm.	2506	7.67602	46.26670
BH / 2	Felskinnbahn (Saas Fee)	No	No perm.	68	Zone 3	2585	7.91784	46.08137
BH / 2	Flüelapass (Davos)	No	No perm.	18	Zone 2	2500	9.94317	46.74688
BH / 2	Illsee	No	No perm.	0	Zone 2	2359	7.63472	46.25945
BH / 2	Gemsstock (Andermatt)	No	No perm.	97	Zone 2	2911	8.61043	46.60125
IMIS	St. Niklaus – Oberer Stelligletscher	No	Zone 2: 0.4°C	86	Zone 3	2915	7.75054	46.16782
BH / 4	Breithorn	No	Zone 2: 0.7°C	81	Zone 3	2864	7.81785	46.14010
BH / 5	Attelas 3	No	Zone 2: 0.7°C	69	Zone 4	2741	7.27493	46.09660
IMIS / 1	Arolla - Les Fontanesses	No	Zone 2: 0.9°C	83	Zone 4	2857	7.44542	46.02967
IMIS / 1	Finhaut - L'Ecreuleuse	Yes	Zone 3	18	No perm.	2252	6.96409	46.10076
IMIS / 1	Simplon - Wenghorn	Yes	Zone 3	46	No perm.	2424	8.04516	46.17802
IMIS / 1	Piz Lagrev - Tscheppa	Yes	Zone 3	72	Zone 1	2727	9.74488	46.45112
IMIS / 1	Vinadi - Alpetta	Yes	Zone 3	82	Zone 5	2729	10.44286	46.93178
IMIS / 1	Saas - Schwarzmies	Yes	Zone 3	91	Zone 5	2799	7.97436	46.12436
CS / 2	Gruobtagfeld (Turtmanntal)	Yes	Zone 3	21	No perm.	2375	7.71797	46.20474
CS / 2	Wasserscheide (Davos Parsenn)	Yes	Zone 3	56	Zone 4	2620	9.80255	46.83391
BH / 2	Gentianes	Yes	Zone 3	87	Zone 5	2894	7.30226	46.08383
BH / 2	Mont Dolin	Yes	Zone 3	49	Zone 4	2597	7.46188	46.02634
BH / 2	Mont Dolin, (Arolla)	Yes	Zone 3	30	No perm.	2574	7.46330	46.02634
BH / 2	Ritigraben (Grächen)	Yes	Zone 3	51	Zone 4	2639	7.84983	46.17470
BH / 2	Seetalhorn (Grächen)	Yes	Zone 3	92	Zone 5	2862	7.85911	46.17642
BH / 2	Stafel-Seetalhorn (Grächen)	Yes	Zone 3	36	Zone 4	2457	7.86022	46.18694
BH / 2	Flüelapass (Davos)	Yes	Zone 3	29	No perm.	2500	9.94317	46.74688
BH / 2	Lapires	Yes	Zone 3	61	Zone 2	2505	7.28435	46.10612
BH / 2	Schafberg I	Yes	Zone 3	74	Zone 4	2752	9.92701	46.49655
BH / 2	Schafberg II	Yes	Zone 3	61	Zone 1	2729	9.92387	46.49909
BH / 2	Murtèl-Corvatsch	Yes	Zone 3	83	Zone 1	2666	9.82186	46.42879
BH / 2	Muragl I	Yes	Zone 3	60	Zone 4	2536	9.92784	46.50757
BH / 2	Les Attelas1	Yes	Zone 3	47	Zone 4	2661	7.27308	46.09677
BH / 2	Les Attelas2	Yes	Zone 3	55	Zone 4	2689	7.27369	46.09675
BH / 2	Emshorn (Oberems)	Yes	No perm.	0	Zone 2	2506	7.67602	46.26670
BH / 2	Muot da Barba Peider, lower shoulder	Yes	Zone 1: -0.1°C	81	Zone 4	2791	9.92891	46.49583
RF / 2	Gemsstock (Andermatt)	Yes	Zone 1: -0.2°C	99	Zone 1	2911	8.61043	46.60125
RF / 2	Chrachenhorn (Davos Monstein)	Yes	Zone 1: -0.4°C	91	Zone 5	2830	9.81226	46.68836
BH / 2	Pointe du Tsaté	Yes	Zone 1: -0.4°C	94	Zone 5	3028	7.54696	46.10995
BH / 2	Lagalp (Berninapass)	Yes	Zone 1: -0.4°C	97	Zone 2	Restricted	Restricted	Restricted
RF / 2	Kärpf (Elm)	Yes	Zone 1: -0.6°C	74	Zone 4	2654	9.08917	46.91611
CS / 2	Scex Rouge (Les Diablerets)	Yes	Zone 1: -0.6°C	93	No perm.	Restricted	Restricted	Restricted
CS / 2	Diavolezza (Berninapass)	Yes	Zone 1: -0.6°C	98	Zone 5	2993	9.96948	46.40975
BH / 2	Schilthorn 51/98	Yes	Zone 1: -0.7°C	100	Zone 4	2910	7.83462	46.55828
CS / 2	Cabane des Vignettes (Arolla)	Yes	Zone 1: -0.9°C	89	Zone 1	3164	7.47555	45.98865
CS / 2	Rothornhütte (Zermatt)	Yes	Zone 1: -0.9°C	98	Zone 4	Restricted	Restricted	Restricted
CS / 2	Rifugio Camosci (Pizzo Cristallina)	Yes	Zone 1: -0.9°C	94	No perm.	2903	8.53667	46.46444
BH / 2	Muot da Barba Peider I	Yes	Zone 1: -1.0°C	99	6	2938	9.93092	46.49647
BH / 2	Arolla, Mt. Dolin	Yes	Zone 1: -1.0°C	99	Zone 5	2862	7.45473	46.02663
BH / 2	Wisse Schijen (Randa)	Yes	Zone 1: -1.2°C	89	Zone 4	3039	7.74832	46.09635
BH / 2	Hörnligrat (Matterhorn, Zermatt)	Yes	Zone 1: -2.0°C	100	6	3288	7.67605	45.98232
BH / 2	Stockhorn 60/00	Yes	Zone 1: -2.7°C	100	Zone 4	3412	7.82420	45.98679
CS / 2	Cabane Dent Blanche (Ferpècle)	Yes	Zone 1: -3.3°C	100	Zone 2	Restricted	Restricted	Restricted
BH / 2	Jungfraujoch South	Yes	Zone 1: -3.9°C	100	Zone 2	3574	7.97306	46.54548
BH / 2	Jungfraujoch North	Yes	Zone 1: -5.2°C	100	Zone 4	3602	7.97319	46.54611
BH / 2	Eggishorn (Fiesch)	Yes	Zone 2: 0.6°C	88	Zone 1	2847	8.09365	46.42638

11. Overall conclusions

The studies included in this dissertation highlight the particular characteristics of ice-rich mountain permafrost, which differ from those of ice-poor permafrost. In these studies the analysis of rock glacier influencing factors in Chapter 5 has a particular role. It gives an overview of the parameters which have to be considered when investigating ice-rich permafrost. All the subsequent studies are based on the findings of Chapter 5 and analyse the factors influencing permafrost genesis and distribution in more detail: Chapters 6 and 7 discuss the role of precipitation, Chapter 8 the role of head wall erosion, snow and soil properties (which corresponds to the factor lithology presented in Chapter 5) and Chapter 9 discusses the role of glaciers.

Chapter 5 deals with rock glaciers, which are certainly features of ice-rich permafrost but represent only a fraction of the latter. Nevertheless, the author assigned the characteristics found for rock glacier permafrost directly to ice-rich permafrost in general. Other studies even go beyond and focus on rock glaciers e.g. as indicators for local permafrost distribution or as climate indicators (Chapter 5). This thesis attempts to provide justification for the first approach and highlights limitations of the second one. This helps to clarify what rock glaciers and ice-rich permafrost can actually tell us and what not.

The lower fringe of mountain permafrost is dominated by ice-rich permafrost. The mapping study in Chapter 10 shows that this permafrost has clearly different characteristics than ice-poor permafrost at higher elevations and that thermal processes are not the dominant factors controlling its distribution. The studies in Chapters 5 and 8 explain this phenomenon by the process of ground ice formation in ice-rich permafrost. Mass wasting, i.e. rock fall and snow avalanches lead to the incorporation of massive ice within the ground. This is the deciding requirement for permafrost development in slopes where the presence of permafrost is otherwise prevented by too high rates of energy exchange between the ground and the atmosphere. The mechanically generated ground ice raises the heat capacity of the ground and prevents thawing of the ground in summer, despite similar incoming energy fluxes. There is no evidence that there is a difference in ground ice formation between rock glaciers and ice-rich permafrost in other landforms, such as talus slopes. In the Flüelapass talus slope, ice-rich permafrost was not considered to be the root zone of a rock glacier for a long time because the creep morphology is hidden in the lake. This shows, that there is no obvious difference between ice-rich permafrost in rock glaciers and talus slopes except of the landform itself. In contrast, permafrost ice in both landforms

constitutes a continuum in the Flüelapass example. Single rock glacier tongues developed in the ice-rich talus slope in areas with particular high avalanche snow deposition rates, i.e. in places with particularly high ground ice contents. Most likely, the same process leads to ice-rich permafrost in talus slopes and rock glaciers and the amount of ground ice influences whether rock glacier formation occurs or not. Rock fall and snow avalanche deposits might therefore be the most important factors controlling the spatial distribution and morphology of low-elevation permafrost. In contrast, atmospheric conditions and solar radiation, seem to play a secondary role for the genesis of ice-rich permafrost.

These last two factors are certainly more critical for the thermal state and hence the long term conservation of ice-rich permafrost. However, there are other significant factors superimposing the direct influence of atmospheric warming on ice-rich permafrost. The studies in this thesis suggest rock fall activity (Chapter 5 and 9), precipitation (Chapter 6 and 7), and glaciation (Chapter 9) as additional factors, controlling changes over time.

As explained in the previous section, rock fall deposits are crucial for rock glacier genesis. Changes in rock fall intensity can strongly affect this process. Thin rock debris layers can already clearly delay the melt of covered snow. Periodic rock fall over multiple years to decades can thus lead to the formation of a debris layer on snow, thick enough to finally halt snow/ice melt and enable the conservation of a long-term stable permafrost body. Lower rock fall intensities can prevent such processes and the formation of ice-rich permafrost is only sporadically possible, e.g. when large rock fall events occur, which instantly build a sufficiently thick debris layer.

Water influences ice-rich permafrost due to lateral heat fluxes and its high heat capacity. Furthermore it controls the frictional resistance in the shear layers of rock glaciers and causes variations in deformation velocity. The amount of water supply to the permafrost is mainly controlled by precipitation rates and ground ice melt can provide an additional water input. However we demonstrated in Chapter 6 that water supply to deeper permafrost layers can also be influenced by changes in permafrost structure and temperature: Increasing ground ice temperatures can lead to the development of drainage channels through the permafrost and hence to more intense water fluxes. The shearing velocity of rock glaciers is therefore controlled by water but is also indirectly linked to permafrost temperatures.

High precipitation rates in general and high precipitation rates together with small soil grain sizes in particular, were shown to have an adverse effect on rock glacier formation in

Chapter 5. Rainfall provides heat which is directly transported through the otherwise insulating active layer to the ice. The most important reason for the interaction of precipitation and grain size might be the reduced ground cooling of water-bearing, fine grained soils due to latent heat effects, as was shown for the Flüelapass study site and by several other studies (Chapter 8). Changes in the Holocene precipitation regime might therefore have a strong influence on past permafrost evolution, which has barely been considered in the literature so far.

The relevance of snow for ice-rich permafrost is multifaceted. The importance of snow cover timing is a well-known fact. While snow-poor conditions during winter favour ground cooling, a long lasting snow cover in spring and summer insulates the ground from atmospheric warming. Ground cooling can however be considered as more important than spring insulation (Chapter 8) and snow-poor conditions are generally more favourable for permafrost. Snow is also the most relevant source of ground ice in ice-rich permafrost. This points out the relevance of snow avalanche deposit zones, which often are the only places in snow poor environments at which snow is concentrated in amounts high enough to produce excess ice. The conspicuous limitation of ice-rich permafrost to zones of avalanche deposits, shown in the mapping study in Chapter 10, underlines this observation.

Glaciation was described in Chapter 5 as being a generally rock glacier adverse factor. It covers terrain which could probably be occupied by rock glaciers under drier climate conditions. Chapter 9 highlighted the interaction of glaciers and rock glaciers and their oscillating occurrence at the same location. Glacier advances could be shown as being disruptive for rock glaciers. Many rock glaciers, whose upper parts were overridden by glaciers in the Little Ice Age outlasted the glaciers in their lower parts in front of their frontal moraines. Such rock glaciers are sometimes misleadingly attributed as being "glacier derived" or as "ice-bearing, creeping moraines" (Chapter 9). Glacier retreat in combination with intense rock fall activity can lead to the incorporation of glacier ice in a newly developing rock glacier. However, this source of ice probably only plays a secondary role in rock glacier formation. The increasing development of ice-rich permafrost on top of the remains of retreated glaciers or in former glacier beds is currently occurring, as shown by several examples in Chapter 9. Further examples suggest that the course of development towards a glacier, a rock glacier or towards ice-rich permafrost in talus slopes is mainly controlled by the ratio of rock and snow deposition in the accumulation zones. If snow clearly dominates, a glacier develops, smaller amounts of snow deposition can lead to rock glacier formation or to ice-rich permafrost in talus slopes.

Considering the factors mentioned above as crucial for ice-rich permafrost implies a considerable conflict with other approaches, which consider ice-rich permafrost as a thermal phenomenon. Factors like rock fall activity or glaciation favour the development of ice-rich permafrost in periods of climate warming. However, climate warming causes exactly the opposite in ice-poor permafrost: a degradation. Processing both types of permafrost together can cause a clear loss in validity, as is clearly demonstrated in the mapping study in Chapter 10. This problem especially affects the modelling of permafrost distribution in the past, present and future. Modelling inaccuracies of permafrost distribution may often be due to the insufficient consideration of the special characteristics of ice-rich permafrost. Furthermore the use of rock glaciers as climate indicators appears to be problematic.

In summary, the most important findings in this dissertation are:

- Ice-rich mountain permafrost is mainly a result of mass wasting processes and would not be present without ground ice formation from buried avalanche snow or glacier ice.

- Ice-poor mountain permafrost is highly correlated to elevation and potential incoming solar radiation and can thus be delimited relatively accurately.

- The sensitivity of ice-rich mountain permafrost to atmospheric warming is limited. Additional factors with a high influence over time are changes in precipitation, rock fall activity and glaciation. The last two can favour the genesis of ice-rich permafrost in periods of climate warming.

- The combination of sedimentary rock (associated with small grain sizes) and precipitation is particularly unfavourable for ice-rich permafrost. Slower subsurface runoff and reduced winter cooling may explain this.

- The deformation velocity of rock glaciers is controlled by the water supply to the shear horizon. Long term accelerations of rock glaciers might be caused by a more effective funnelling of water to the shear horizon, as a consequence of permafrost warming.

- Time-lapse images can be an efficient low cost method to monitor rock glaciers and similar mass wasting processes with a very high spatial and temporal resolution.

Acknowledgements

References

Abellán A, Calvet J, Vilaplana JM, Blanchard J. 2010. Detection and spatial prediction of rockfalls by means of terrestrial laser scanner monitoring. *Geomorphology* 119(3–4): 162-171. doi: 10.1016/j.geomorph.2010.03.016

Ackert JRP. 1998. A rock glacier/debris-covered glacier system at Galena Creek, Absaroka Mountains, Wyoming. *Geografiska Annaler: Series A, Physical Geography* 80(3-4): 267-276. doi: 10.1111/j.0435-3676.1998.00042.x

Adams JM. 1997. *Global land environments since the last interglacial*. Oak Ridge National Laboratory, TN, USA

Alley RB, Meese DA, Shuman CA, Gow AJ, Taylor KC, Grootes PM, White JWC, Ram M, Waddington ED, Mayewski PA, Zielinski GA. 1993. Abrupt increase in Greenland snow accumulation at the end of the Younger Dryas event. *Nature* 362(6420): 527-529

Angeli M-G, Pasuto A, Silvano S. 2000. A critical review of landslide monitoring experiences. *Engineering Geology* 55(3): 133-147. doi: 10.1016/S0013-7952(99)00122-2

Arenson L, Hoelzle M, Springman S. 2002. Borehole deformation measurements and internal structure of some rock glaciers in Switzerland. *Permafrost and Periglacial Processes* 13: 117-135

Arenson LU, Springman SM. 2005. Mathematical descriptions for the behaviour of ice-rich frozen soils at temperatures close to 0 °C. *Canadian Geotechnical Journal* 42(2): 431-442. doi: 10.1139/t04-109

Ballantyne CK. 2002. Paraglacial geomorphology. *Quaternary Science Reviews* 21(18–19): 1935-2017. doi: 10.1016/S0277-3791(02)00005-7

Bamler R, Hartl P. 1998. Synthetic aperture radar interferometry. *Inverse Problems* 14

Barboux C, Delaloye R, Strozzi T, Lambiel C, Collet C, Raetzo H. 2012. Monitoring active rock glaciers in the Western Swiss Alps: Challenges of Differential Sar Interferometry and solutions to estimate annual and seasonal displacement rates. In, *Geoscience and Remote Sensing Symposium (IGARSS), 2012 IEEE International*, 5210-5213. doi: 10.1109/IGARSS.2012.6352435

Barboux C, Strozzi T, Delaloye R, Wegmüller U, Collet C. 2015. Mapping slope movements in Alpine environments using TerraSAR-X interferometric methods. *ISPRS Journal of Photogrammetry and Remote Sensing* 109: 178-192. doi: 10.1016/j.isprsjprs.2015.09.010

Barnes P, Tabor D, Walker JCF. 1971. The Friction and Creep of Polycrystalline Ice. *Proceedings of the Royal Society of London A: Mathematical, Physical and Engineering Sciences* 324(1557): 127-155. doi: 10.1098/rspa.1971.0132

Baroni C, Carton A, Seppi R. 2004. Distribution and behaviour of rock glaciers in the Adamello–Presanella Massif (Italian Alps). *Permafrost and Periglacial Processes* 15(3): 243-259. doi: 10.1002/ppp.497

Barsch D, 1988. Rockglaciers. In: M.J. Clark (Editor), *Advances in Periglacial Geomorphology*. John Wiley & Sons, pp. 69-90

Barsch D, 1996. *Rock-glaciers. Indicators for the Present and Former Geoecology in High Mountain Environments.* Springer, Heidelberg

Bast A, Noetzli J, Gärtner-Roer I, Hoelzle M, Hauck C, Vonder Mühll D, Müller J, Phillips M, Wasser D, Vieli A. 2016. And it continues: A new borehole extends the longest mountain permafrost temperature record on rock glacier Murtèl, Swiss Alps. In: Exploring Permafrost In a Future Earth, *XI. International Conference on Permafrost - Book of Abstracts*, Potsdam, Germany, F. Günther, A. Morgenstern (eds). Bibliothek Wissenschaftspark Albert Einstein,. doi: 10.2312/GFZ.LIS.2016.001

Bauer A, Paar G, Kaufmann V. 2003. Terrestrial laser scanning for rock glacier monitoring, *8th International Conference on Permafrost*, Zurich, Switzerland, Phillips, Springman, Arenson (eds), Swets & Zeitlinger, pp. 55-60

Begert M, Seiz G, Schlegel T, Musa M, Baudraz G, Moesch M, 2003. Homogenisierung vom Klimareihen der Schweiz und Bestimmung der Normwerte 1961 - 1990. Schlussbericht des Projekts NORM90., Veröffentlichung der MeteoSchweiz. MeteoSchweiz

Beltrami H. 1996. Active layer distortion of thermal orbits. *Permafrost and Periglacial Processes* 7: 101-110

Berger J, Krainer K, Mostler W. 2004. Dynamics of an active rock glacier (Ötztal Alps, Austria). *Quaternary Research* 62(3): 233-242. doi: 10.1016/j.yqres.2004.07.002

Berthling I. 2011. Beyond confusion: rock glaciers as cryo-conditioned landforms. *Geomorphology* 131: 98-106. doi: 10.1016/j.geomorph.2011.05.002

Bingyuan H, Chao M, Guifang Z, Lixun K. 2008. Analyzing Decorrelation of Multi-temporal SAR Data on InSAR. In, *Image and Signal Processing, 2008. CISP '08. Congress on*, 452-461. doi: 10.1109/CISP.2008.383

Böckli L, Haeberli W, 2013. *Characterizing Permafrost in the Entire European Alps: Spatial Distribution and Ice Content*

Bodman GB, Harradine EF. 1939. Mean Effective Pore Size and Clay Migration during Water Percolation in Soils. *Soil Science Society of America Journal* 3(C): 44-51. doi: 10.2136/sssaj1939.036159950003000C0009x

Boeckli L, Brenning A, Gruber S, Noetzli J. 2012. Permafrost distribution in the European Alps: calculation and evaluation of an index map and summary statistics. *The Cryosphere* 6(4): 807-820. doi: 10.5194/tc-6-807-2012

Böhlert R, Egli M, Maisch M, Brandova D, Ivy-Ochs S, Kubik PW, Haeberli W. 2011. Application of a combination of dating techniques to reconstruct the Lateglacial and early Holocene landscape history of the Albula region (eastern Switzerland). *Geomorphology* 128(1-2): 1-13

Boike J, Roth K, Overduin PP. 1998. Thermal and hydrologic dynamics of the active layer at a continuous permafrost site (Taymyr Peninsula, Siberia). *Water Resources Research* 34(3): 355-363. doi: 10.1029/97WR03498

Bollmann E, Klug C, Sailer R, Stötter J, Abermann J. 2012. Quantifying Rock Glacier Creep Using Airborne Laser Scanning: A Case Study from Two Rock Glaciers in the Austrian Alps, *10th International Conference on Permafrost.*, Salekhard, Russia, K.M. Hinkel (eds), The Northern Publisher, pp. 49-54

Bommer C, Keusen H-R, Phillips M. 2008. Engineering solutions for foundations and anchors in mountain permafrost. In, *9th International Conference on Permafrost*, Fairbanks, Alaska, D.L. Kane, K.M. Hinkel (eds). Institute of Northern Engineering, University of Alaska Fairbanks, 159-163

Bommer C, Phillips M, Arenson LU. 2010. Practical recommendations for planning, constructing and maintaining infrastructure in mountain permafrost. *Permafrost and Periglacial Processes* 21: 97-104. doi: 10.1002/ppp.679

Bozzini C, Conedera M, Krebs P. 2012. A New Monoplotting Tool to Extract Georeferenced Vector Data and Orthorectified Raster Data from Oblique Non-Metric Photographs. *International Journal of Heritage in the Digital Era* 1(3): 499-518. doi: 10.1260/2047-4970.1.3.499

Brutsaert W, 2005. *Hydrology*. Cambridge University Press, Cambridge

Buchroithner MF. 1991. Three-dimensional survey of submarine sedimentary trails by means of spaceborne remote sensing. *GeoJournal* 24(1): 93-101. doi: 10.1007/bf00213061

Bühler Y, Adams MS, Bösch R, Stoffel A. 2016. Mapping snow depth in alpine terrain with unmanned aerial systems (UASs): potential and limitations. *The Cryosphere* 10(3): 1075-1088. doi: 10.5194/tc-10-1075-2016

Bühler Y, Marty M, Ginzler C. 2012. High resolution DEM generation in high-alpine terrain using airborne remote sensing techniques. *Transactions in GIS* 16: 635-647

Burr DM, Baker VR, Carling PA, 2009. *Megaflooding on Earth and Mars*. Cambridge University Press

Carson MA. 1977. Angles of repose, angles of shearing resistance and angles of talus slopes. *Earth Surface Processes* 2(4): 363-380. doi: 10.1002/esp.3290020408

Chen Y, Medioni G. 1991. Object modeling by registration of multiple range images. In, *Robotics and Automation, 1991. Proceedings., 1991 IEEE International Conference on*, 2724-2729 vol.3. doi: 10.1109/ROBOT.1991.132043

Chueca J. 1992. A statistical analysis of the spatial distribution of rock glaciers, Spanish Central Pyrenees. *Permafrost and Periglacial Processes* 3(3): 261-265. doi: 10.1002/ppp.3430030316

Clark DH, Clark MM, Gillespie AR. 1994. Debris-Covered Glaciers in the Sierra Nevada, California, and Their Implications for Snowline Reconstructions. *Quaternary Research* 41(2): 139-153. doi: 10.1006/qres.1994.1016

Clark DH, Steig EJ, Potter JN, Gillespie AR. 1998. Genetic variability of rock glaciers. *Geografiska Annaler: Series A, Physical Geography* 80(3-4): 175-182. doi: 10.1111/j.0435-3676.1998.00035.x

Colesanti C, Ferretti A, Prati C, Rocca F. 2003. Multi-image satellite SAR interferometry: state of the art and future trends. In, *Radar Conference, 2003. Proceedings of the International*, 239-244. doi: 10.1109/RADAR.2003.1278746

Colesanti C, Wasowski J. 2006. Investigating landslides with space-borne Synthetic Aperture Radar (SAR) interferometry. *Engineering Geology* 88(3–4): 173-199. doi: 10.1016/j.enggeo.2006.09.013

Côté J, Konrad J-M. 2005. A generalized thermal conductivity model for soils and construction materials. *Canadian Geotechnical Journal* 42(2): 443-458. doi: 10.1139/t04-106

Cremonese E, Gruber S, Phillips M, Pogliotti P, Boeckli L, Noetzli J, Suter C, Bodin X, Crepaz A, Kellerer-Pirklbauer A, Lang K, Letey S, Mair V, Morra di Cella U, Ravanel L, Scapozza C, Seppi R, Zischg A. 2011. Brief Communication: "An inventory of permafrost evidence for the European Alps". *The Cryosphere* 5(3): 651-657. doi: 10.5194/tc-5-651-2011

Dach R, Hugentobler U, Fridez P, Meindl M. 2007. Bernese GPS software version 5.0. *Astronomical Institute, University of Bern* 640: 114

Dansgaard W, White JWC, Johnsen SJ. 1989. The abrupt termination of the Younger Dryas climate event. *Nature* 339(6225): 532-534

Davies MCR, Hamza O, Harris C. 2001. The effect of rise in mean annual temperature on the stability of rock slopes containing ice-filled discontinuities. *Permafrost and Periglacial Processes* 12: 137-144

Degenhardt J. 2009. Development of tongue-shaped and multilobate rock glaciers in alpine environments – Interpretations from ground penetrating radar surveys. *Geomorphology* 109(3–4): 94-107. doi: 10.1016/j.geomorph.2009.02.020

Delaloye R, Lambiel C. 2005. Evidences of winter ascending air circulation throughout talus slopes and rock glaciers situated in the lower belt of alpine discontinuous permafrost (Swiss Alps). *Norsk geogr. Tidsskr.* 59: 194-201

Delaloye R, Lambiel C. 2007. Drilling in a low elevation cold talus slope (Dreveneuse, Swiss Prealps). *Geophysical Research Abstracts* 9: 10907

Delaloye R, Lambiel C, Gärtner-Roer I. 2010a. Overview of rock glacier kinematics research in the Swiss Alps: seasonal rhythm, interannual variations and trends over several decades. *Geographica Helvetica* 65: 135-145

Delaloye R, Morard S, Abbet D, Hilbich C. 2010b. The Slump of the Grabengufer Rock Glacier (Swiss Alps). In, *3rd European Conference on Permafrost (EUCOP III)*, Svalbard, Norway,

Delaloye R, Morard S, Barboux C, Abbet D, Gruber V, Riedo M, Gachet S. 2013. Rapidly moving rock glaciers in Mattertal, *Mattertal - ein Tal in Bewegung*, St. Niklaus, C. Graf (eds), Eidg. Forschungsanstalt WSL, pp. 21-31

Delaloye R, Perruchoud E, Avian M, Kaufmann V, Bodin X, Hausmann H, Ikeda A, Kääb A, Kellerer-Pirklbauer A, Krainer K, Lambiel C, Mihajlovic D, Staub B, Roer I, Thibert E. 2008. Recent interannual variations of rock glacier creep in the European Alps, *9th International Conference on Permafrost* Fairbanks, Alaska, D.L. Kane, K.M. Hinkel (eds), pp. 343-348

Delaloye R, Reynard E, Lambiel C, Marescot L, Monnet R. 2003. Thermal anomaly in a cold scree slope (Creux du Van, Switzerland). In, *Eighth International Conference on Permafrost*, Zurich, M. Phillips, S.M. Springman, L.U. Arenson (eds). Zwets & Zeitlinger, 175-180

Deluigi N, Lambiel C, Kanevski M. 2017. Data-driven mapping of the potential mountain permafrost distribution. *Science of The Total Environment* 590: 370-380

Dramis F, Giraudi C, Guglielmin M, 2003. Rock glacier distribution and paleoclimate in Italy. In: Phillips, Springman, Arenson (Editors), *Permafrost*. A.A. Balkema Publishers, Lisse, pp. 199-204

Echelard T, Krysiecki J, Gay M, Schoeneich P. 2013. Détection des mouvements de glaciers rocheux dans les Alpes françaises par interférométrie radar différentielle (D-InSAR) dérivée des archives satellitaires ERS (European Remote Sensing). *Geomorphology* 3: 231-242

Eisenbeiß H, 2009. *UAV photogrammetry*, ETH Mitteilungen Nr.105. ETH Zurich, Zurich, Switzerland. doi: 10.3929/ethz-a-005939264

Erickson TA, Williams MW, Winstral A. 2005. Persistence of topographic controls on the spatial distribution of snow in rugged mountain terrain, Colorado, United States. *Water Resources Research* 41(4): W04014. doi: 10.1029/2003wr002973

Etzelmüller B, Frauenfelder R. 2009. Factors Controlling The Distribution of Mountain Permafrost in The Northern Hemisphere and Their Influence on Sediment Transfer. *Arctic, Antarctic, and Alpine Research* 41(1): 48-58. doi: 10.1657/1523-0430-41.1.48

Etzelmüller B, Hagen JO. 2005. Glacier-permafrost interaction in Arctic and alpine mountain environments with examples from southern Norway and Svalbard. *Geological Society, London, Special Publications* 242(1): 11-27. doi: 10.1144/gsl.sp.2005.242.01.02

Etzelmüller B, Hoelzle M, Flo Heggem ES, Isaksen K, Mittaz C, Mühll DV, Ødegård RS, Haeberli W, Sollid JL. 2001. Mapping and modelling the occurrence and distribution of mountain permafrost. *Norsk Geografisk Tidsskrift - Norwegian Journal of Geography* 55: 186-194

Evatt GW, Abrahams ID, Heil M, Mayer C, Kingslake J, Mitchell SL, Fowler AC, Clark CD. 2015. Glacial melt under a porous debris layer. *Journal of Glaciology* 61(229): 825-836. doi: 10.3189/2015JoG14J235

Fabris M, Dipartimento di Fisica SG, Università degli Studi di Bologna, Italy, Pesci A, Istituto Nazionale di Geofisica e Vulcanologia SB, Bologna, Italia. 2005. *Automated DEM extraction in digital aerial photogrammetry: precisions and validation for mass movement monitoring*

Ferrians Jr OJ. 1989. Glossary of permafrost and selected ground-ice terms. *Canadian Geotechnical Journal* 26(4): 769-769. doi: 10.1139/t89-097

Fischer L, Kääb A, Huggel C, Noetzli J. 2006. Geology, glacier retreat and permafrost degradation as controlling factors of slope instabilities in a high-mountain rock wall: the Monte Rosa east face. *Natural Hazards and Earth System Sciences* 6(5): 761-772

Frauenfelder R, Haeberli W, Hoelzle M, 2003. Rockglacier occurrence and related terrain parameters in a study area of the Eastern Swiss Alps. In: M. Phillips, S. Springman, L. Arenson (Editors), *Permafrost*. A.A. Balkema Publishers, Lisse, pp. 253-258

Frauenfelder R, Haeberli W, Hoelzle M, Maisch M. 2001. Using relict rockglaciers in GIS-based modelling to reconstruct Younger Dryas permafrost distribution patterns in the Err-Julier area, Swiss Alp. *Norsk Geografisk Tidsskrift - Norwegian Journal of Geography* 55(4): 195-202. doi: 10.1080/00291950152746522

Frauenfelder R, Kääb A. 2000. Towards a palaeoclimatic model of rock-glacier formation in the Swiss Alps. *Annals of Glaciology* 31(1): 281-286. doi: 10.3189/172756400781820264

Frauenfelder R, Schneider B, Kääb A. 2008. Using dynamic modelling to simulate the distribution of rockglaciers. *Geomorphology* 93: 130-143. doi: 10.1016/j.geomorph.2006.12.023

Frehner M, Ling AHM, Gärtner-Roer I. 2015. Furrow-and-Ridge Morphology on Rockglaciers Explained by Gravity-Driven Buckle Folding: A Case Study From the Murtèl Rockglacier (Switzerland). *Permafrost and Periglacial Processes* 26(1): 57-66. doi: 10.1002/ppp.1831

Frei C. 2014. Interpolation of temperature in a mountainous region using nonlinear profiles and non-Euclidean distances. *International Journal of Climatology* 34(5): 1585-1605. doi: 10.1002/joc.3786

Gadek B. 2012. Debris slopes ventilation in the periglacial zone of the Tatra Mountains (Poland and Slovakia): The indicators. *Cold Regions Science and Technology* 74–75: 1-10. doi: 10.1016/j.coldregions.2012.01.007

Gischig V, Loew S, Kos A, Moore J, Raetzo H, Lemy F. 2009. Identification of active release planes using ground-based differential InSAR at the Randa rock slope instability, Switzerland. *Natural Hazards and Earth System Science* 9(6): 2027-2038

Gruber S, Haeberli W. 2007. Permafrost in steep bedrock slopes and its temperature-related destabilization following climate change. *Journal of Geophysical Research: Earth Surface* 112(F2). doi: 10.1029/2006JF000547

Gruber S, Haeberli W, 2009. Mountain permafrost. In: R. Margesin (Editor), *Permafrost Soils*. Springer

Gruber S, Haeberli W, Krummenacher B, Keller F, Mani P, Hunziker G, Hölzle M, Vonder Mühll D, Zimmermann M, Keusen H-R, A. G, Rätzo H, 2006. Erläuterungen zur Hinweiskarte der potentiellen Permafrostverbreitung in der Schweiz 1:50'000. Swiss Federal Office for the Environment (FOEN)

Gruber S, Hoelzle M. 2001. Statistical modelling of mountain permafrost distribution: local calibration and incorporation of remotely sensed data. *Permafrost and Periglacial Processes* 12: 69-77

Gruber S, Hoelzle M. 2008. The cooling effect of coarse blocks revisited: a modeling study of a purely conductive mechanism. In, *9th International Conference on Permafrost*, Fairbanks, Alaska, D.L. Kane, K.M. Hinkel (eds). Institute of Northern Engineering, University of Alaska Fairbanks, 557-561

Haberkorn A, Phillips M, Kenner R, Rhyner H, Bavay M, Galos SP, Hoelzle M. 2015. Thermal Regime of Rock and its Relation to Snow Cover in Steep Alpine Rock Walls: Gemsstock, Central Swiss Alps. *Geografiska Annaler: Series A, Physical Geography* 97(3): 579-597. doi: 10.1111/geoa.12101

Haeberli W, 1975. *Untersuchungen zur Verbreitung von Permafrost zwischen Flüelapass und Piz Grialetsch (Graubünden).* Mitteilungen der Versuchsanstalt für Wasserbau, Hydrologie und Glaziologie der ETH Zürich, 17, Zurich, 221 pp

Haeberli W. 1983. Permafrost–glacier relationships in the Swiss Alps today and in the past. In, *Fourth International Conference on Permafrost*, Washington D.C. National Academy Press, 415–420

Haeberli W, 1985. *Creep of mountain permafrost: Internal structure and flow of alpine rock glaciers*. Mitteilung der VAW/ETH Zürich, 77

Haeberli W, Guodong C, Gorbunov A, Harris S. 1993. Mountain permafrost and climatic change. *Permafrost and Periglacial Processes* 4(2): 165-174

Haeberli W, Hallet B, Arenson L, Elconin R, Humlum O, Kääb A, Kaufmann V, Ladanyi B, Matsuoka N, Springman S, Vonder Mühll D. 2006. Permafrost creep and rock glacier dynamics. *Permafrost and Periglacial Processes* 17: 189-214. doi: 10.1002/ppp.561

Haeberli W, Hoelzle M, Kääb A, Keller F, Vonder Mühll D, Wagner S. 1998. Ten years after drilling through the permafrost of the active rock glacier Murtèl, eastern Swiss Alps: answered questions and new perspectives. In: Collection Nordicana, *7th International Conference on Permafrost*, Yellowknife, Canada, A.G.L.a.M. Allard (eds). Université Laval, Canada, 403-410

Haeberli W, Kääb A, Vonder Mühll D, Teysseire P. 2001. Prevention of outburst floods from periglacial lakes at Grubengletscher, Valais, Swiss Alps. *Journal of Glaciology* 47(156): 111-122

Haeberli W, Kääb A, Wagner S, Vonder Mühll D, Geissler P, Haas JN, Glatzel-Mattheier H, Wagenbach D. 1999. Pollen analysis and ^{14}C age of moss remains in a permafrost core recovered from the active rock glacier Murtèl-Corvatsch, Swiss Alps: geomorphological and glaciological implications. *Journal of Glaciology* 45(No. 149): 1-8

Haeberli W, Noetzli J, Arenson L, Delaloye R, Gärtner-Roer I, Gruber S, Isaksen K, Kneisel C, Krautblatter M, Phillips M. 2010. Mountain permafrost: development and challenges of a

young research field. *Journal of Glaciology* 56(200): 1043-1058. doi: 10.3189/002214311796406121

Haeberli W, Vonder Mühll D. 1996. On the characteristics and possible origins of ice in rock glacier permafrost. *Zeitschrift für Geomorphologie* 104: 43-57

Hales TC, Roering JJ. 2005. Climate controlled variations in scree production, Southern Alps, New Zealand. *Geology* 33: 701-704

Harbor J, Sharp M, Copland L, Hubbard B, Nienow P, Mair D. 1997. Influence of subglacial drainage conditions on the velocity distribution within a glacier cross section. *Geology* 25(8): 739-742. doi: 10.1130/0091-7613(1997)025<0739:iosdco>2.3.co;2

Hauck C, Kneisel C, 2008. Quantifying the ice content in low-altitude scree slopes using geophysical methods. In: C. Hauck, C. Kneisel (Editors), *Applied geophysics in periglacial environments*. Cambridge University Press, pp. 153-164

Hausmann H, Krainer K, Brückl E, Mostler W. 2007. Internal structure and ice content of Reichenkar rock glacier (Stubai Alps, Austria) assessed by geophysical investigations. *Permafrost and Periglacial Processes* 18(4): 351-367. doi: 10.1002/ppp.601

Hilbich C. 2010. Time-lapse refraction seismic tomography for the detection of ground ice degradation. *The Cryosphere* 4: 243-259. doi: 10.5194/tc-4-243-2010

Hilbich C, Fuss C, Hauck C. 2011. Automated Time-lapse ERT for Improved Process Analysis and Monitoring of Frozen Ground. *Permafrost and Periglacial Processes* 22(4): 306-319. doi: 10.1002/ppp.732

Hipp T, Etzelmüller B, Farbrot H, Schuler TV, Westermann S. 2012. Modelling borehole temperatures in Southern Norway – insights into permafrost dynamics during the 20th and 21st century. *The Cryosphere* 6(3): 553-571. doi: 10.5194/tc-6-553-2012

Hobbs PV, 1974. *Ice Physics*. Oxford University Press Inc., New York

Hoelzle M. 1992. Permafrost occurrence from BTS measurements and climatic parameters in the Eastern Swiss Alps. *Permafrost and Periglacial Processes* 3: 143-147

Hoelzle M, Mittaz C, Etzelmüller B, Haeberli W. 2001. Surface energy fluxes and distribution models of permafrost in European mountain areas: an overview of current developments. *Permafrost and Periglacial Processes* 12(1): 53-68

Huete AR. 1988. A soil-adjusted vegetation index (SAVI). *Remote Sensing of Environment* 25(3): 295-309. doi: 10.1016/0034-4257(88)90106-X

Humlum O. 1996. Origin of rock glaciers: Observations from Mellemfjord, Disko Island, Central West Greenland. *Permafrost and Periglacial Processes* 7(4): 361-380. doi: 10.1002/(sici)1099-1530(199610)7:4<361::aid-ppp227>3.0.co;2-4

Humlum O, Christiansen HH, Juliussen H. 2007. Avalanche-derived rock glaciers in Svalbard. *Permafrost and Periglacial Processes* 18(1): 75-88. doi: 10.1002/ppp.580

Ikeda A, Matsuoka N. 2006. Pebbly versus bouldery rock glaciers: Morphology, structure and processes. *Geomorphology* 73(3–4): 279-296. doi: 10.1016/j.geomorph.2005.07.015

Ikeda A, Matsuoka N, Kääb A. 2003. A rapidly moving small rock glacier at the lower limit of the mountain permafrost belt in the Swiss Alps. In, *Proceedings of the Eighth International Conference on Permafrost*, 455-460

Ikeda A, Matsuoka N, Kääb A. 2008. Fast deformation of perennially frozen debris in a warm rock glacier in the Swiss Alps: An effect of liquid water. *Journal of Geophysical Research: Earth Surface* 113(1): F01021. doi: 10.1029/2007jf000859

Isaksen K, Ødegård RS, Eiken T, Sollid JL. 2000. Composition, flow and development of two tongue-shaped rock glaciers in the permafrost of Svalbard. *Permafrost and Periglacial Processes* 11(3): 241-257. doi: 10.1002/1099-1530(200007/09)11:3<241::AID-PPP358>3.0.CO;2-A

Jansson P-E. 2012. CoupModel: model use, calibration, and validation. *Transactions of the ASABE* 55(4): 1335-1344

Jansson P-E, Karlberg L, 2004. *Coupled heat and mass transfer model for soil-plant-atmosphere systems.* Royal Institute of Technology, Dept of Civil and Environmental Engineering, Stockholm

Jiskoot H, 2011. Dynamics of Glaciers, *Encyclopedia of snow, ice and glaciers*. Springer Netherlands, pp. 245-256

Johnson BG, Thackray GD, Van Kirk R. 2007. The effect of topography, latitude and lithology on rock glacier distribution in the Lemhi Range, central Idaho, USA. *Geomorphology* 91: 38-50. doi: 10.1016/j.geomorph.2007.01.023

Jones DB, Harrison S, Anderson K, Selley HL, Wood JL, Betts RA. 2018. The distribution and hydrological significance of rock glaciers in the Nepalese Himalaya. *Global and Planetary Change* 160: 123-142. doi: 10.1016/j.gloplacha.2017.11.005

Kääb A. 1999. Photogrammetry for Early Recognition of High Mountain Hazards: New Techniques and Applications. *Physics and Chemistry of the Earth* 25: 765–770

Kääb A, Frauenfelder R, Roer I. 2007. On the response of rockglacier creep to surface temperature increase. *Global and Planetary Change* 56: 172-187. doi: 10.1016/j.gloplacha.2006.07.005

Kääb A, Kaufmann V, Ladstädter R, Eiken T. 2003. Rock glacier dynamics: implications from high-resolution measurements of surface velocity fields, *8th International Conference on Permafrost*, Zurich, Switzerland, Phillips, Springman, Arenson (eds), A.A. Balkema Publishers, pp. 501-506

Kääb A, Kneisel C. 2005. Permafrost creep within a recently deglaciated glacier forefield: Muragl, Swiss Alps. *Permafrost Periglac* 17(1): 79-85. doi: 10.1002/ppp.540

Kääb A, Reichmuth T. 2005. Advance mechanisms of rock glaciers. *Permafrost and Periglacial Processes* 16(2): 187-193. doi: 10.1002/ppp.507

Kaufmann V. 2012. The evolution of rock glacier monitoring using terrestrial photogrammetry: the example of Äußeres Hochebenkar rock glacier (Austria). *Austrian Journal of Earth Sciences* 105(2)

Kaufmann V, Ladstädter R. 2003. Quantitative analysis of rock glacier creep by means of digital photogrammetry using multi-temporal aerial photographs: two case studies in the Austrian Alps, *8th International Conference on Permafrost*, Zurich, Switzerland, Phillips, Springman, Arenson (eds), A.A. Balkema Publishers, pp. 525-530

Kaufmann V, Ladstädter R. 2007. Mapping of the 3D surface motion field of Doesen rock glacier (Ankogel group, Austria) and its spatio-temporal change (1954-1998) by means of digital photogrammetry. In, *Proceedings of the 9th International Symposium of High Mountain Remote Sensing Cartography*, Graz, Austria, 127-144

Keller F. 1992. Automated mapping of mountain permafrost using the program PERMAKART within the Geographical Information Systems ARC/INFO. *Permafrost and Periglacial Processes* 3: 133-138

Keller F, Frauenfelder R, Gardaz JM, Hoelzle M, Kneisel M, Lugon R, Phillips M, Reynard E, Wenker L. 1998. Permafrost map of Switzerland. In, *Seventh International Conference on Permafrost*, Yellowknife Canada, A.G. Lewkowicz, M. Allard (eds). Collection Nordicana, 557-562

Keller F, Gubler H. 1993. Interaction between snow cover and high mountain permafrost. In, *6th International Conference on Permafrost*, Beijing, China, C. Goudong (eds). South China University of Technology Press, 332-337

Kellerer-Pirklbauer A, Kaufmann V. 2012. About the relationship between rock glacier velocity and climate parameters in central Austria. *Austrian Journal of Earth Sciences* 105(2): 94-112

Kenner R, Bühler Y, Delaloye R, Ginzler C, Phillips M. 2014. Monitoring of high alpine mass movements combining laser scanning with digital airborne photogrammetry. *Geomorphology* 206(0): 492-504. doi: 10.1016/j.geomorph.2013.10.020

Kenner R, Magnusson J. 2017. Estimating the effect of different influencing factors on rock glacier development in two regions in the Swiss Alps. *Permafrost and Periglacial Processes* 28(1): 195-208. doi: 10.1002/ppp.1910

Kenner R, Phillips M, Beutel J, Hiller M, Limpach P, Pointner E, Volken M. 2017a. Factors Controlling Velocity Variations at Short-Term, Seasonal and Multiyear Time Scales, Ritigraben Rock Glacier, Western Swiss Alps. *Permafrost and Periglacial Processes* 28(4): 675-684. doi: 10.1002/ppp.1953

Kenner R, Phillips M, Danioth C, Denier C, Zgraggen A. 2011. Investigation of rock and ice loss in a recently deglaciated mountain rock wall using terrestrial laser scanning: Gemsstock, Swiss Alps. *Cold Regions Science and Technology* 67: 157-164. doi: 10.1016/j.coldregions.2011.04.006

Kenner R, Phillips M, Hauck C, Hilbich C, Mulsow C, Bühler Y, Stoffel A, Buchroithner M. 2017b. New insights on permafrost genesis and conservation in talus slopes based on observations at Flüelapass, Eastern Switzerland. *Geomorphology* 290: 101-113. doi: 10.1016/j.geomorph.2017.04.011

Kerschner H. 1978. Paleoclimatic Inferences from Late Würm Rock Glaciers, Eastern Central Alps, Western Tyrol, Austria. *Arctic and Alpine Research* 10(3): 635-644. doi: 10.2307/1550684

King L. 1987. Comparison of resistivity and radio-echo soundings on rock glacier permafrost. *Zeitschrift für Gletscherkunde und Glazialgeologie* 23(1): 77-97

Kneisel C, Hauck C. 2003. Multi-method geophysical investigation of a sporadic permafrost occurrence. *Z. Geomorph. N.F.* 132: 145-159

Kneisel C, Schwindt D. 2008. Geophysical mapping of isolated permafrost lenses at a sporadic permafrost site at low altitude in the Swiss Alps, *9th International Conference on Permafrost*, Fairbanks, Alaska, D.L. Kane (eds), INE-UAF, pp. 959-964

Konrad SK, Humphrey NF, Steig EJ, Clark DH, Potter NJ, Pfeffer WT. 1999. Rock glacier dynamics and paleoclimatic implications. *Geology* 27(12): 1131-1134

Kos A, Strozzi T, Stockmann R, Wiesmann A, Werner C, 2013. Detection and characterization of rock slope instabilities using a portable radar interferometer (GPRI), *Landslide Science and Practice*. Springer Berlin Heidelberg, pp. 325-329

Krainer K, Bressan D, Dietre B, Haas JN, Hajdas I, Lang K, Mair V, Nickus U, Reidl D, Thies H, Tonidandel D. 2015. A 10,300-year-old permafrost core from the active rock glacier Lazaun, southern Ötztal Alps (South Tyrol, northern Italy). *Quaternary Research* 83(2): 324-335. doi: 10.1016/j.yqres.2014.12.005

Krainer K, Mostler W. 2006. Flow velocities of active rock glaciers in the Austrian Alps. *Geografiska Annaler: Series A, Physical Geography* 88(4): 267-280. doi: 10.1111/j.0435-3676.2006.00300.x

Krautblatter M, 2009. *Detection and Quantification of Permafrost Change in Alpine Rock Walls and Implications for Rock Instability*

Lambiel C, Delaloye R. 2004. Contribution of Real-time Kinematic GPS in the Study of Creeping Mountain Permafrost: Examples from the Western Swiss Alps. *Permafrost and Periglacial Processes* 15: 229-241

Lambiel C, Pieracci K. 2008. Permafrost distribution in talus slopes located within the alpine periglacial belt, Swiss Alps. *Permafrost and Periglacial Processes* 19: 293-304

Lanari R, Mora O, Manunta M, Mallorqui JJ, Berardino P, Sansosti E. 2004. A small-baseline approach for investigating deformations on full-resolution differential SAR interferograms. *Geoscience and Remote Sensing, IEEE Transactions on* 42(7): 1377-1386. doi: 10.1109/TGRS.2004.828196

Lehning M, Bartelt P, Brown B, Russi T, Stöckli U, Zimmerli M. 1999. SNOWPACK model calculations for avalanche warning based upon a new network of weather and snow stations. *Cold Regions Science and Technology* 30: 145-157

Lerjen M, Kääb A, Hoelzle M, Haeberli W. 2003. Local distribution of discontinuous mountain permafrost. A process study at Flüela Pass, Swiss Alps. In, *Eighth International Conference on Permafrost*, Zurich, M. Phillips, S.M. Springman, L.U. Arenson (eds). Swets & Zeitlinger, 667-672

Loup C. 2008. SWISSIMAGE – das Schweizer Orthophotomosaik in ständiger Weiterentwicklung. *Kartographische Nachrichten* 5: 268-271

Luethi R, Phillips M. 2016. Challenges and solutions for long-term permafrost borehole temperature monitoring and data interpretation. *Geogr. Helv.* 71(2): 121-131. doi: 10.5194/gh-71-121-2016

Luethi R, Phillips M, Lehning M. 2017. Estimating Non-Conductive Heat Flow Leading to Intra-Permafrost Talik Formation at the Ritigraben Rock Glacier (Western Swiss Alps). *Permafrost and Periglacial Processes* 28(1): 183-194. doi: 10.1002/ppp.1911

Luetschg M, Stoeckli V, Lehning M, Haeberli W, Ammann W. 2004. Temperatures in two boreholes at Flüela Pass, Eastern Swiss Alps: the effect of snow redistribution on permafrost distribution patterns in high mountain areas. *Permafrost and Periglacial Processes* 15: 283-297

Lugon R, Stoffel M. 2010. Rock-glacier dynamics and magnitude-frequency relations of debris flows in a high-elevation watershed: Ritigraben, Swiss Alps. *Global and Planetary Change* 73: 202-210. doi: 10.1016/j.gloplacha.2010.004

Maas HG, Casassa G, Schneider D, Schwalbe E, Wendt A. 2010. Photogrammetric determination of spatio-temporal velocity fields at Glaciar San Rafael in the Northern Patagonian Icefield. *The Cryosphere Discuss.* 2010: 2415-2432. doi: 10.5194/tcd-4-2415-2010

Maisch M, 1999. *Die Gletscher der Schweizer Alpen: Gletscherhochstand 1850, aktuelle Vergletscherung, Gletscherschwund-Szenarien ; [Projektschlussbericht im Rahmen des Nationalen Forschungsprogrammes "Klimaänderungen und Naturkatastrophen", NFP 31]*. vdf, Hochsch.-Verlag an der ETH

Maisch M, Haeberli W, Frauenfelder R, Kääb A, Rothenbühler C, 2003. Lateglacial and Holocene evolution of glaciers and permafrost in the Val Muragl, Upper Engadin, Swiss Alps. In: M. Phillips, S. Springman (Editors), *Permafrost*. A.A. Balkema Publishers, Lisse, pp. 717-722

Marchenko SS. 2001. A model of permafrost formation and occurrences in the intracontinental mountains. *Norsk Geografisk Tidsskrift - Norwegian Journal of Geography* 55(4): 230-234. doi: 10.1080/00291950152746577

Marmy A, Salzmann N, Scherler M, Hauck C. 2013. Permafrost model sensitivity to seasonal climatic changes and extreme events in mountainous regions. *Environmental Research Letters* 8(3): 035048

Monnier S, Kinnard C. 2015. Reconsidering the glacier to rock glacier transformation problem: New insights from the central Andes of Chile. *Geomorphology* 238: 47-55. doi: 10.1016/j.geomorph.2015.02.025

Monnier S, Kinnard C. 2016. Interrogating the time and processes of development of the Las Liebres rock glacier, central Chilean Andes, using a numerical flow model. *Earth Surface Processes and Landforms* 41(13): 1884-1893. doi: 10.1002/esp.3956

Morard S, Delaloye R, Lambiel C. 2010. Pluriannual thermal behaviour of low elevation cold talus slopes in western Switzerland. *Geographica Helvetica* 65(2): 124-134

Morris SE. 1981. Topoclimatic Factors and the Development of Rock Glacier Facies, Sangre de Cristo Mountains, Southern Colorado. *Arctic and Alpine Research* 13(3): 329-338. doi: 10.2307/1551039

Mott R, Schirmer M, Bavay M, Grünewald T, Lehning M. 2010. Understanding snow-transport processes shaping the mountain snow-cover. *The Cryosphere* 4(4): 545-559. doi: 10.5194/tc-4-545-2010

Mulsow C. 2010. A flexible multi-media bundle approach. *Int. Arch. Photogramm. Remote Sens. Spat. Inf. Sci* 38: 472-477

Munter W, 2003. *3x3 Lawinen: Risikomanagement im Wintersport*. Pohl & Schellhammer, 223 pp

Neyer F, Limpach P, Gsell T, Geiger G, Beutel J. 2014. Permanent rock glacier monitoring with a stereo pair of optical cameras. In, *Swiss Geoscience Meeting*, Fribourg, Switzerland, N. Oesterling, A. Wiget, M. Cannata (eds), 381

Nicholson L, Benn DI. 2006. Calculating ice melt beneath a debris layer using meteorological data. *Journal of Glaciology* 52(178): 463-470. doi: 10.3189/172756506781828584

Nickus U, Abermann J, Fischer A, Krainer K, Schneider H, Span N, Thies H. 2015. Rock Glacier Äußeres Hochebenkar (Austria) - Recent results of a monitoring network. *Zeitschrift für Gletscherkunde und Glazialgeologie* 47/48: 43-62

Niu F, Cheng G, Niu Y, Zhang M, Luo J, Lin Z. 2016. A naturally-occurring 'cold earth' spot in Northern China. *Scientific Reports* 6: 34184. doi: 10.1038/srep34184

Noetzli J, Hoelzle M, Haeberli W. 2003. Mountain permafrost and recent Alpine rock-fall events: a GIS-based approach to determine critical factors. In, *8th International Conference on Permafrost*, Zurich, Switzerland, M. Phillips, Springman, S.M., Arenson, L.U. (eds). Balkema, 827-832

Noetzli J, S. G, Kohl T, Salzmann N, Haeberli W. 2007. Three-dimensional distribution and evolution of permafrost temperatures in idealized high-mountain topography. *Journal of Geophysical Research* 112

Nyenhuis M, Hoelzle M, Dikau R. 2005. Rock glacier mapping and permafrost distribution modelling in the Turtmanntal, Valais, Switzerland *Zeitschrift für Geomorphologie* 49(3): 275-292

Östrem G. 1959. Ice Melting under a Thin Layer of Moraine, and the Existence of Ice Cores in Moraine Ridges. *Geografiska Annaler* 41(4): 228-230

Östrem G. 1971. Rock Glaciers and Ice-Cored Moraines, a Reply to D. Barsch. *Geografiska Annaler. Series A, Physical Geography* 53(3/4): 207-213. doi: 10.2307/520791

Payne D. 1998. Climatic implications of rock glaciers in the arid Western Cordillera of the Central Andes. *Glacial Geology and Geomorphology* rp03

PERMOS, 2013. Permafrost in Switzerland 2008/2009 and 2009/2010, J. Noetzli (eds), Glaciological Report Permafrost. University of Zurich

PERMOS, 2016. Permafrost in Switzerland 2010/2011 to 2013/2014, J. Noetzli, Luethi, R., and Staub, B. (eds), Glaciological Report Permafrost No. 12–15 of the Cryospheric Commission of the Swiss Academy of Sciences

Phillips M, Wolter A, Lüthi R, Amann F, Kenner R, Bühler Y. 2016. Rock slope failure in a recently deglaciated permafrost rock wall at Piz Kesch (Eastern Swiss Alps), February 2014. *Earth Surface Processes and Landforms*: n/a-n/a. doi: 10.1002/esp.3992

Phillips M, Zenklusen Mutter E, Kern-Luetschg M, Lehning M. 2009. Rapid degradation of ground ice in a ventilated talus slope: Flüela Pass, Swiss Alps. *Permafrost and Periglacial Processes* 20: 1-14. doi: 10.1002/ppp.638

Plattner C, Braun L, Brenning A. 2006. The spatial variability of snow accumulation at Vernagtferner, Austrian Alps, in winter 2003/2004. *Zeitschrift für Gletscherkunde und Glazialgeologie* 39: 43-57

Potter JN. 1972. Ice-Cored Rock Glacier, Galena Creek, Northern Absaroka Mountains, Wyoming. *Geological Society of America Bulletin* 83: 3025-3058

Potter JN, Steig EJ, Clark DH, Speece MA, Clark GM, Updike AB. 1998. Galena Creek rock glacier revisited—new observations on an old controversy. *Geografiska Annaler: Series A, Physical Geography* 80(3-4): 251-265. doi: 10.1111/j.0435-3676.1998.00041.x

Pradhan B, Buchroithner M, 2012. *Terrigenous Mass Movements*. Springer-Verlag Berlin Heidelberg, 400 pp

Pritchard ME, Simons M. 2002. A satellite geodetic survey of large-scale deformation of volcanic centres in the central Andes. *Nature* 418(6894): 167-171

Putkonen J. 1998. Soil thermal properties and heat transfer processes near Ny-Alesund, northwestern Spitsbergen, Svalbard. *Polar Research* 17(2): 165-179. doi: 10.1111/j.1751-8369.1998.tb00270.x

Putnam AE, Putnam DE. 2009. Inactive and relict rock glaciers of the Deboullie Lakes Ecological Reserve, northern Maine, USA. *Journal of Quaternary Science* 24(7): 773-784. doi: 10.1002/jqs.1252

Reynard E, Lambiel C, Delaloye R, Devaud G, Baron L, Chapellier D, Marescot L, Monnet R. 2003. Glacier/permafrost relationships in forefields of small glaciers (Swiss Alps). In, *Proceedings 8th International Conference on Permafrost, Zurich, Switzerland*, 947-952

Reznichenko N, Davies T, Shulmeister J, McSaveney M. 2010. Effects of debris on ice-surface melting rates: an experimental study. *Journal of Glaciology* 56(197): 384-394. doi: 10.3189/002214310792447725

Ribolini A, Guglielmin M, Fabre D, Bodin X, Marchisio M, Sartini S, Spagnolo M, Schoeneich P. 2010. The internal structure of rock glaciers and recently deglaciated slopes as revealed by

geoelectrical tomography: insights on permafrost and recent glacial evolution in the Central and Western Alps (Italy–France). *Quaternary Science Reviews* 29(3–4): 507-521. doi: 10.1016/j.quascirev.2009.10.008

Rinner K. 1969. Problems of Two-Medium-Photogrammetry. *Photogrammetric Engineering* 35(2): 275-282

Rist A, Phillips M. 2005. First results of investigations on hydrothermal processes within the active layer above alpine permafrost in steep terrain. *Norsk Geografisk Tidsskrift* 59: 177-183

Roer I, Haeberli W, Avian M, Kaufmann V, Delaloye R, Lambiel C, Kääb A. 2008. Observations and considerations on destabilizing active rock glaciers in the European Alps, *9th International Conference on Permafrost*, Fairbanks, D.L. Kane, K.M. Hinkel (eds), Institute of Northern Engineering, University of Alaska Fairbanks, pp. 1505-1510

Roer I, Kääb A, Dikau R. 2005. Rockglacier acceleration in the Turtmann valley (Swiss Alps): Probable controls. *Norsk Geografisk Tidsskrift - Norwegian Journal of Geography* 59(2): 157-163. doi: 10.1080/00291950510020655

Roesgen T, Totaro R. 1995. Two-dimensional on-line particle imaging velocimetry. *Experiments in Fluids* 19: 188-193

Russi T, Ammann W, Brabec B, Lehning M, Meister R, 2003. Avalanche Warning Switzerland 2000. In: J. Zschau, A. Küppers (Editors), *Early Warning Systems for Natural Disaster Reduction*. Springer Berlin Heidelberg, Berlin, Heidelberg, pp. 569-577. doi: 10.1007/978-3-642-55903-7_77

Sailer R, Bollmann E, Hoinkes S, Rieg L, Sproß M, StÖTter J. 2012. QUANTIFICATION OF GEOMORPHODYNAMICS IN GLACIATED AND RECENTLY DEGLACIATED TERRAIN BASED ON AIRBORNE LASER SCANNING DATA. *Geografiska Annaler: Series A, Physical Geography* 94(1): 17-32. doi: 10.1111/j.1468-0459.2012.00456.x

Sailer R, Kerschner H. 1999. Equilibrium line altitudes and rock glaciers in the Ferwall-Group (Western Tyrol, Austria) during the Younger Dryas cooling event. *Annals of Glaciology* 28: 141-145

Sanders D, Widera L, Ostermann M. 2014. Two-layer scree/snow-avalanche triggered by rockfall (Eastern Alps): Significance for sedimentology of scree slopes. *Sedimentology* 61(4): 996-1030. doi: 10.1111/sed.12083

Sandmeier K, 2014. REFLEXW-Software for the processing of seismic, acoustic or electromagnetic reflection, refraction and transmission data

Sattler K, Anderson B, Mackintosh A, Norton K, de Róiste M. 2016. Estimating permafrost distribution in the maritime southern alps, New Zealand, based on climatic conditions at rock glacier sites. *Frontiers in Earth Science* 4(4). doi: 10.3389/feart.2016.00004

Scapozza C, Lambiel C, Baron L, Marescot L, Reynard E. 2011. Internal structure and permafrost distribution in two alpine periglacial talus slopes, Valais, Swiss Alps. *Geomorphology* 132(3–4): 208-221. doi: 10.1016/j.geomorph.2011.05.010

Scapozza C, Lambiel C, Bozzini C, Mari S, Conedera M. 2014. Assessing the rock glacier kinematics on three different timescales: a case study from the southern Swiss Alps. *Earth Surface Processes and Landforms* 39(15): 2056-2069. doi: 10.1002/esp.3599

Scherler M, Hauck C, Hoelzle M, Salzmann N. 2013. Modeled sensitivity of two alpine permafrost sites to RCM-based climate scenarios. *Journal of Geophysical Research: Earth Surface* 118(2): 780-794. doi: 10.1002/jgrf.20069

Scherrer SC, Fischer EM, Posselt R, Liniger MA, Croci-Maspoli M, Knutti R. 2016. Emerging trends in heavy precipitation and hot temperature extremes in Switzerland. *Journal of Geophysical Research: Atmospheres* 121(6): 2626-2637. doi: 10.1002/2015JD024634

Schirmer M, Wirz V, Clifton A, Lehning M. 2011. Persistence in intra-annual snow depth distribution: 1. Measurements and topographic control. *Water Resources Research* 47(9): W09516. doi: 10.1029/2010wr009426

Schneider S, Hoelzle M, Hauck C. 2012. Influence of surface and subsurface heterogeneity on observed borehole temperatures at a mountain permafrost site in the Upper Engadine, Swiss Alps. *The Cryosphere* 6: 517-531. doi: 10.55194/tc-6-517-2012

Schomacker A, Kjaer KH. 2008. Quantification of dead-ice melting in ice-cored moraines at the high-Arctic glacier Holmströmbreen, Svalbard. *Boreas* 37(2): 211-225. doi: 10.1111/j.1502-3885.2007.00014.x

Schröter B, Buchroithner M. 2015. Time-lapse camera images for observtion and visualisation of snow lines on glaciers in high asia, *International Cartographic Conference*, Rio de Janeiro / Brazil,

Schwikowski M, 2004. Reconstruction of European Air Pollution from Alpine Ice Cores. In: L. DeWayne Cecil, J.R. Green, L.G. Thompson (Editors), *Earth Paleoenvironments: Records Preserved in Mid- and Low-Latitude Glaciers*. Springer Netherlands, Dordrecht, pp. 95-119. doi: 10.1007/1-4020-2146-1_6

Scotti R, Brardinoni F, Alberti S, Frattini P, Crosta GB. 2013. A regional inventory of rock glaciers and protalus ramparts in the central Italian Alps. *Geomorphology* 186: 136-149. doi: 10.1016/j.geomorph.2012.12.028

Skolnik M, 1980. *Introduction to Radar Systems*. McGraw-Hill Kogakusha Ltd., New York NY

Smerdon JE, Beltrami H, Creelman C, Stevens MB. 2009. Characterizing land surface processes: A quantitative analysis using air-ground thermal orbits. *Journal of Geophysical Research* 114: D15102. doi: 10.1029/2009JD011768

Smith DE, Harrison S, Firth CR, Jordan JT. 2011. The early Holocene sea level rise. *Quaternary Science Reviews* 30(15–16): 1846-1860. doi: 10.1016/j.quascirev.2011.04.019

Speck R, Turchi P, Süß H. 2007. An end-to-end simulator for high-resolution spaceborne SAR systems. In, 65680H-65680H-8

Springman SM, Arenson LU, Yamamoto Y, Maurer H, Kos A, Buchli T, Derungs G. 2012. Multidisciplinary investigations on three rock glaciers in the swiss alps: legacies and future perspectives. *Geografiska Annaler: Series A, Physical Geography* 94: 215-243. doi: 10.1111/j.1468-0459.2012.00464.x

Staub B, 2015. The evolution of mountain permafrost in the context of climate change Alps, Université de Fribourg

Staub B, Marmy A, Hauck C, Hilbich C, Delaloye R. 2015. Ground temperature variations in a talus slope influenced by permafrost: a comparison of field observations and model simulations. *Geogr. Helv.* 70(1): 45-62. doi: 10.5194/gh-70-45-2015

Stoffel M. 2010. Magnitude-frequency relationships of debris flows - A case study based on field surveys and tree-ring records. *Geomorphology* 116: 67-76

Stoffel M, Lièvre I, Conus D, Grichting MA, Raetzo H, Gärtner HW, Monbaron M. 2005. 400 Years of Debris-Flow Activity and Triggering Weather Conditions: Ritigraben, Valais, Switzerland. *Arctic, Antarctic, and Alpine Research* 37(3): 387-395. doi: 10.1657/1523-0430(2005)037[0387:yodaat]2.0.co;2

Strozzi T, Delaloye R, Kääb A, Ambrosi C, Perruchoud E, Wegmüller U. 2010. Combined observations of rock mass movements using satellite SAR interferometry, differential GPS, airborne digital photogrammetry, and airborne photography interpretation. *Journal of Geophysical Research: Earth Surface* 115(F1): n/a-n/a. doi: 10.1029/2009JF001311

Strozzi T, Farina P, Corsini A, Ambrosi C, Thüring M, Zilger J, Wiesmann A, Wegmüller U, Werner C. 2005. Survey and monitoring of landslide displacements by means of L-band satellite SAR interferometry. *Landslides* 2(3): 193-201. doi: 10.1007/s10346-005-0003-2

Strozzi T, Kääb A, Frauenfelder R. 2004. Detecting and quantifying mountain permafrost creep from in situ inventory, space-borne radar interferometry and airborne digital photogrammetry. *International Journal of Remote Sensing* 25(15): 2919-2931. doi: 10.1080/0143116042000192330

Stubenrauch C, Rossow W, Kinne S, 2012. WCRP Report No. 23/2012: Assessment of Global Cloud Data Sets from Satellites

Suchlandt O, Schmassmann W. 1936. Limnologisehe Beobachtungen an acht Hochgebirgsseen der Landschaft Davos. *Zeitschrift für Hydrologie,* 7(1+2)

Swisstopo. 2005. *DHM25 Das digitale Höhenmodell der Schweiz*. Bundesamt für Landestopografie Swisstopo, Wabern

Swisstopo. 2007. *VECTOR25 Das digitale Landschaftsmodell der Schweiz*. Bundesamt für Landestopografie Swisstopo, Wabern

Teng Y, Stanier SA, Gourvenec SM. 2017. Synchronised multi-scale image analysis of soil deformations. *International Journal of Physical Modelling in Geotechnics* 17(1): 53-71. doi: 10.1680/jphmg.15.00058

Tobler D, Kull I, Hählen N. 2012. Gefahrenmanagement der Murgänge im Spreitgraben, Guttannen. *Swiss bulletin für angewandte Geologie* 17/2: 53-61

Travelletti J, Delacourt C, Allemand P, Malet J-P, Schmittbuhl J, Toussaint R, Bastard M. 2012. Correlation of multi-temporal ground-based optical images for landslide monitoring: Application, potential and limitations. *ISPRS Journal of Photogrammetry and Remote Sensing* 70: 39-55. doi: 10.1016/j.isprsjprs.2012.03.007

van Herwijnen A, Berthod N, Simenhois R, Mitterer C. 2013. Using time-lapse photography in avalanche research. In, *Proceedings ISSW*, 950-954

Veulliet E, Stötter J, Weck-Hannemann H, 2009. *Sustainable Natural Hazard Management in Alpine Environments.* Springer-Verlag Berlin, Heidelberg, 403 pp

Whalley WB. 1983. Rock glaciers - permafrost features or glacial relicts. In, *Permafrost fourth international conference*, Washington D.C. National Academy Press, 1396-1401

Whalley WB, Palmer CF. 1998. A glacial interpretation for the origin and formation of the Marinet Rock Glacier, Alpes Maritimes, France. *Geografiska Annaler: Series A, Physical Geography* 80(3-4): 221-236. doi: 10.1111/j.0435-3676.1998.00039.x

Wicky J, Hauck C. 2016. Numerical modelling of convective heat transport by air flow in permafrost-affected talus slopes. *The Cryosphere Discuss.* 2016: 1-29. doi: 10.5194/tc-2016-227

Winstral A, Elder K, Davis RE. 2002. Spatial Snow Modeling of Wind-Redistributed Snow Using Terrain-Based Parameters. *Journal of Hydrometeorology* 3(5): 524-538. doi: 10.1175/1525-7541(2002)003<0524:ssmowr>2.0.co;2

Wirz V, Beutel J, Gruber S, Gubler S, Purves RS. 2014. Estimating velocity from noisy GPS data for investigating the temporal variability of slope movements. *Nat. Hazards Earth Syst. Sci.* 14(9): 2503-2520. doi: 10.5194/nhess-14-2503-2014

Wirz V, Geertsema M, Gruber S, Purves R. 2015. Temporal variability of diverse mountain permafrost slope movements derived from multi-year daily GPS data, Mattertal, Switzerland. *Landslides*: 1-17. doi: 10.1007/s10346-014-0544-3

Zacharda M, Gude M, Vlastimil R. 2007. Thermal regime of three low elevation scree slopes in Central Europe. *Permafrost and Periglacial Processes* 18: 301-308

Zenklusen Mutter E, Blanchet J, Phillips M. 2010. Analysis of ground temperature trends in Alpine permafrost using generalized least squares. *Journal of Geophysical Research*(115): F004009. doi: 10.1029/2009JF001648

Zenklusen Mutter E, Phillips M. 2012a. Active layer characteristics at ten borehole sites in Alpine permafrost terrain, Switzerland. *Permafrost and Periglacial Processes* 23(2): 138-151. doi: 10.1002/ppp.1738

Zenklusen Mutter E, Phillips M. 2012b. Thermal evidence of recent talik formation in Ritigraben rock glacier: Swiss Alps. In, *10th International Conference on Permafrost*, Salekhard, Russia, M. Hinkel (eds). The Northern Publisher, 479-483

Zhang T. 2005. Influence of the seasonal snow cover on the ground thermal regime: an overview. *Reviews of Geophysics* 43(RG4002): 1-23

Erklärung des Promovenden

Die Übereinstimmung dieses Exemplars mit dem Original der Dissertation zum Thema:

„Genesis, conservation and deformation of ice-rich mountain permafrost: Driving factors, mapping and geodetic monitoring"

wird hiermit bestätigt.

Dresden, 29.01.2018

Robert Kenner